Halogen (F, Cl, Br, I) cycling in the critical zone:

Formation of primary ore deposits, their supergene weathering and the fate of halogens in soil and along the hydrological flow path

Dissertation

der Mathematisch-Naturwissenschaftlichen Fakultät

der Eberhard Karls Universität Tübingen

zur Erlangung des Grades eines

Doktors der Naturwissenschaften

(Dr. rer. nat.)

vorgelegt von

M.Sc. Tatjana Epp

aus Reutlingen

Tübingen

2020

Gedruckt mit Genehmigung der Mathematisch-Naturwissenschaftlichen Fakultät der Eberhard Karls Universität Tübingen.

Tag der mündlichen Qualifikation:	17.06.2020
Dekan:	Prof. Dr. Wolfgang Rosenstiel
1. Berichterstatter:	Prof. Dr. Gregor Markl
2. Berichterstatter:	Prof. Dr. Yvonne Oelmann
3. Berichterstatter:	PD Dr. Michael Marks

Danksagung

Mein größter Dank gilt zunächst Prof. Dr. Yvonne Oelmann, Prof. Dr. Gregor Markl und PD Dr. Michael Marks für die Vergabe meines Promotionsthemas und meine Betreuung während der drei Jahre meiner Doktorarbeit. Des Weiteren, möchte ich mich für die unzähligen konstruktiven Diskussionen, Anregungen und die Hilfsbereitschaft während dieser Zeit herzlich bedanken, die alle mit in die vorliegende Arbeit eingeflossen sind. An dieser Stelle auch vielen Dank für die immer zeitnahe Bearbeitung meiner Manuskripte.

Bei Dr. Harald Neidhardt möchte ich mich für seine vielseitige Hilfe, Betreuung und immerwährende Hilfsbereitschaft während meiner Arbeit bedanken.

Weiterer Dank geht an PD. Dr. Thomas Wenzel für die Betreuung der Mikrosondenmessungen, die zahlreichen Diskussionen und allzeit hilfreichen Gespräche. Bei Dr. Udo Neumann möchte ich mich herzlich für seine Hilfe bei der Mikroskopie, aber auch für das entgegengebrachte jahrelange Vertrauen bei der praktischen Übung der Auflichtmikroskopie bedanken.

Für die Hilfe und Unterstützung bei der Analytik gilt mein großer Dank Gabriele Stoschek und Bernd Steinhilber, für die vielen Messungen und die Bereitschaft jederzeit Probleme gemeinsam anzugehen und zu beheben. In dem Rahmen möchte ich auch dem gesamten Ionenchromatographie Team, insbesondere Andreas Walter, Stefan Rosanowski und Tanja Zimmer, der Firma Metrohm in Filderstadt danken, die sich immer sofort unserer Schwierigkeiten angenommen haben und bei allen Fragen immer hilfreich zur Verfügung standen. Bei Simone Schafflick möchte ich mich ganz herzlich für die immer schnelle und sorgfältige Bearbeitung und Präparation meiner Proben bedanken. Für die Betreuung der XRD Messungen und anschließenden Diskussionen gilt mein Dank Dr. Christoph Berthold und Frieder Lauxmann. Bei Dr. Peter Kühn möchte ich mich für die konstruktiven Gespräche bezüglich der Aufbereitung bedanken. Mein weiterer Dank gilt Prof. Dr. Christian Mikutta und PD Dr. Stefan Dultz für ihre Hilfsbereitschaft und die konstruktiven Diskussionen.

Den Koautoren meiner Publikationen Prof. Dr. Gregor Markl, Prof. Dr. Yvonne Oelmann, PD Dr. Michael Marks, Dr. Harald Neidhardt, Dr. Mark Kendrick, Thomas Ludwig, Prof. Dr. Nelson Eby, Prof. Dr. Wolfgang Bach, Manuel Scharrer, Dr. Benjamin Walter, Gabriel Lehmann, Christian Heimgärtner, Katharina Henze und Norina Pagano danke ich für die gute Zusammenarbeit.

Für das Korrekturlesen dieser Dissertation möchte ich mich bei Manuel Scharrer, Dr. Sebastian Staude und PD Dr. Thomas Wenzel bedanken.

Auch bei meinen Kollegen und ehemaligen Kollegen Manuel Scharrer, Anja Allabar, Rebekka Reich, Frieder Lauxmann, Dr. Maximilian Keim, Dr. Stefan Kreißl, Dr. Sebastian Staude, Johannes Hecker, Dr. Johannes Giebel, Katharina Sandritter, Aylin Polat, Tim Kristandt, Gabriel Lehmann, Christian Dietzel, Simon Braunger und Dr. Benjamin Walter möchte ich mich zum einen für die vielen hilfreichen Diskussionen, aber auch für die immer gute und sehr unterhaltsame Arbeitsatmosphäre bedanken.

Mein ganz besonderer Dank gilt meiner Familie und meinen Freunden. Danke, dass ihr mich zu jeder Zeit unterstützt und immer an mich geglaubt habt.

Abstract

The halogens fluorine (F), chlorine (Cl), bromine (Br) and iodine (I) are ubiquitous in nature and are involved in a vast number of processes in terrestrial environments. They are not only important for humans, animals and plants as micro-nutrients, but also play an important role in for example metal transport in fluids or in mobilizing and re-precipitation of toxic trace elements such as lead (Pb) or arsenic (As). Therefore, halogens are in the scope of important environmental interests and a detailed understanding of halogen distribution and behavior in natural environments is essential in order to prevent potentially harmful impacts. This thesis deals with the formation of primary Pb-deposits, the subsequent supergene weathering with a specific focus on the halogen distribution in thereby formed secondary Pb-minerals and the fate of the halogens (F, Cl, Br and I) in the critical zone, including the pedosphere and the hydrological flow path. The Schwarzwald in SW-Germany provides an ideal area since numerous primary formed hydrothermal veins, their supergene weathering zone and well-developed soil profiles are easily accessible.

Polymetallic Sb-Pb(-Ag±Au) deposits have been formed by various fluids with specific physico-chemical conditions and were subject to intense remobilization processes. However, the formation of this vein type within the entire Schwarzwald has not been comprehensively investigated in detail. Based on mineral textures, formation temperature, fluid and mineral composition and stability diagrams, this work revealed, that this vein type typically formed over four mineralization stages. The primary mineralization was formed by cooling of high temperature, low salinity fluids. It was overprinted subsequently by at least three further hydrothermal phases, driven by high salinity and medium to low temperature fluids. The results observed showed increased complex mineral associations over time, associated with an increased importance of halogens within the hydrothermal processes.

Exposed to near-surface conditions by uplift and erosion, supergene weathering of such primary hydrothermal Pb-deposits leads to the formation of pyromorphite-group minerals (PyGM) in nearly all cases. These minerals incorporate halogens in up to weight percent ranges and immobilize Pb and As. Bulk geochemical mineral analyses showed that halogen incorporation (especially Br and I) is mineral specific and is less related to crystal chemical controls. Spatially resolved analyses revealed variable halogen ratios in different crystal growth zones independent of major element composition. This implies that the halogen composition is not governed by a crystal-chemical control (alone), but more substantially by external factors such as fluid composition. Halogen distribution in natural fluids and soils above a weathering zone has been shown to be influenced by halogen-specific processes. Simultaneously F, Cl, Br and I have been analyzed in ecosystem solutions and vertical soil profiles at one site for the

first time, in order to investigate the near-surface halogen cycle. It was depicted that this cycle is controlled by a complex interaction of biotic and abiotic processes and that these processes differed for each halogen. Accumulation of Cl in the topsoil could be shown to be caused by chlorination processes and nutrient uplift by roots. The cycling of F, Br and I was rather controlled by pH-related weathering and high solubility in combination with sorption processes to pedogenic oxides or incorporation into clay minerals. Furthermore, it was shown that also vegetation and soil external processes such as atmospheric halogen input had an influence on halogen composition along the hydrological flow path, due to the wash-off of dry deposition and foliage leaching. Overall, it was shown that the halogen cycling in the critical zone is governed by coupled biological, mineralogical, chemical and physical processes.

Kurzzusammenfassung

Die Halogene Fluor (F), Chlor (Cl), Brom (Br) und Iod (I) sind in der Natur allgegenwärtig und an einer Vielzahl von Prozessen innerhalb des terrestrischen Milieus beteiligt. Sie sind dabei nicht nur für Menschen, Tiere und Pflanzen als Mikronährstoffe wichtig, sondern spielen auch eine wichtige Rolle z.B. beim Metalltransport in Fluiden, oder bei der Mobilisierung und anschließenden Wiederausfällung von toxischen Spurenelementen wie Blei (Pb) oder Arsen (As). Dies sind nur wenige Gründe, warum Halogene heutzutage beispielsweise im Umweltsektor von Bedeutung sind. Deswegen ist ein detailliertes Verständnis der Verteilung und des Verhaltens von Halogenen in der Umwelt unerlässlich, um potenziell schädlichen Auswirkungen vorbeugen zu können. Diese Arbeit beschäftigt sich mit der Bildung primärer Pb-Lagerstätten, der anschließenden supergenen Verwitterung mit einem spezifischen Fokus auf die Halogenverteilung in den dadurch gebildeten sekundären Pb-Mineralen, sowie dem Halogenverhalten in der kritischen Zone, einschließlich der Pedosphäre und dem hydrologischen Kreislauf. Da zahlreiche primär gebildeten hydrothermalen Gänge, ihre supergene Verwitterungszone, sowie ausgeprägte Bodenprofile im Schwarzwald in Südwest Deutschland gut zugänglich sind, bietet dieser hierfür ein ideales Studiengebiet.

Bei der Bildung von polymetallischen Sb-Pb(-Ag±Au) Lagerstätten spielen Fluide mit spezifischen physiko-chemischen Zusammensetzungen, sowie verschiedene Remobilisierungsprozesse eine zentrale Rolle. Allerdings ist die Bildung dieses Lagerstättentyps noch nicht umfassend im gesamten Schwarzwald untersucht worden. Basierend auf der Grundlage von Mineraltexturen, Fluid- und Mineralchemie, sowie Stabilitätsdiagrammen, zeigte diese Arbeit, dass typischerweise vier Mineralisationsphasen diesen Lagerstättentyp charakterisieren. Die primäre Mineralisation wurde durch Hochtemperatur-Fluide mit geringer Salinität gebildet. Diese wurde anschließend in mindestens drei weiteren hydrothermalen Phasen von hochsalinaren, mittel- bis niedertemperierten Fluiden überprägt. Die Ergebnisse der Studie zeigten, dass mit der Zeit komplexere Mineralvergesellschaftungen mit einer zunehmenden Bedeutung von Halogenen innerhalb hydrothermaler Prozesse einhergegangen sind.

Durch Hebung und Erosion den oberflächennahen Bedingungen ausgesetzt, führt die supergene Verwitterung solcher primärer hydrothermalen Pb-Lagerstätten in fast allen Fällen zur Bildung von Pyromorphit-Gruppen Mineralen (PyGM). Die Halogengehalte in diesen Mineralen können Größenordnungen von mehreren Gewichtsprozent erreichen, außerdem können sie Pb und As immobil machen. Geochemische Analysen zeigten, dass der Halogeneinbau (insbesondere der von Br und I) mineralspezifisch erfolgte und weniger durch die Kristallchemie kontrolliert wurde. Darüber hinaus zeigten ortsaufgelöste Analysen in

unterschiedlichen Kristallwachstumszonen variable Halogenverhältnisse unabhängig von der Hauptelementchemie. Diese Ergebnisse implizieren, dass die Halogenchemie von PyGM vermutlich nicht durch eine rein kristallchemische Kontrolle, sondern vielmehr durch externe Faktoren wie beispielsweise die Fluidzusammensetzung bestimmt wurde. Des Weiteren hat sich gezeigt, dass die Halogenverteilung in natürlichen Fluiden und Böden oberhalb einer Verwitterungszone durch halogenspezifische Prozesse beeinflusst wird. Zum ersten Mal wurden F, Cl, Br und I gleichzeitig in Ökosystemlösungen und vertikalen Bodenprofilen an einem gemeinsamen Standort analysiert, um den oberflächennahen Halogenkreislauf zu untersuchen. Dabei konnte gezeigt werden, dass dieser Kreislauf durch ein komplexes Zusammenspiel von biotischen und abiotischen Prozessen gesteuert wird und dass sich die Prozesse für die einzelnen Halogene unterscheiden. Es konnte gezeigt werden, dass die Anreicherung von Cl im Oberboden durch Chlorierung und den Nährstofftransport durch Wurzeln zustande kommt. Wohingegen der Kreislauf von F, Br und I im Boden vorwiegend durch pH-abhängige Verwitterung und eine hohe Löslichkeit in Kombination mit Sorption an pedogene Oxide oder den Einbau in Tonminerale gesteuert wird. Darüber hinaus konnte gezeigt werden, dass auch die Vegetation und bodenexterne Prozesse wie der atmosphärische Halogeneintrag einen Einfluss auf die Halogenzusammensetzung im hydrologischen Kreislauf haben. Dabei spielen vor allem das Abwaschen von Trockenablagerungen auf Blättern und die Auslaugung von Laub durch den Niederschlag eine große Rolle. Insgesamt konnte veranschaulicht werden, dass der Halogenkreislauf in der kritischen Zone durch eine Kopplung von biologischen, mineralogischen, chemischen und physikalischen Prozessen gesteuert wird.

List of publications in this thesis

The results, discussion and concluding remarks of the following individual studies are included in this thesis:

Study A

Epp, T., Walter, B. F., Scharrer, M., Lehmann, G., Henze, K., Heimgärtner, C., Bach, W. & Markl, G. (2019). Quartz veins with associated Sb-Pb-Ag±Au mineralization in the Schwarzwald, SW Germany: a record of metamorphic cooling, tectonic rifting, and element remobilization processes in the Variscan belt. Mineralium Deposita, 54(2), 281-306. DOI: 10.1007/s00126-018-0855-8

Study B

Epp, T., Marks, M. A., Ludwig, T., Kendrick, M. A., Eby, N., Neidhardt, H., Oelmann, Y. & Markl, G. (2019). Crystallographic and fluid compositional effects on the halogen (Cl, F, Br, I) incorporation in pyromorphite-group minerals. American Mineralogist, 104(11), 1673-1688. DOI: 10.2138/am-2019-7068

Study C

Epp, T., Neidhardt, H., Pagano, N., Marks, M. AW., Markl, G. & Oelmann, Y. (2020). Vegetation canopy effects on total and dissolved Cl, Br, F and I concentrations in soil and their fate along the hydrological flow path. Science of the Total Environment, 712, 135473. DOI: 10.1016/j.scitotenv.2019.135473

Study D

Epp, T., Marks, M. AW., Neidhardt, H., Oelmann, Y. & Markl, G. (submitted). Halogen (F, Cl, Br, I) sorption in silt and clay fractions of a Cambisol from a temperate forest, SW Germany.

Personal contribution

The following tables explain in detail the author's contributions in publications included in the thesis.

Author	Author position	Scientific ideas %	Data generation %	Analysis and interpretation %	Paper writing %
Epp, T	1	30	30	40	60
Walter BF	2	20	20	15	10
Scharrer, M	3	15	10	20	10
Lehmann, G	4	0	15	5	0
Henze, K	5	0	10	5	0
Heimgärtner, C	6	0	10	5	0
Bach, W	7	0	5	0	5
Markl, G	8	35	0	10	15
Title of paper:		Quartz veins with associated Sb-Pb-Ag±Au mineralization in the Schwarzwald, SW Germany: a record of metamorphic cooling, tectonic rifting, and element remobilization processes in the Variscan belt			
Status in publication process		Accepted and published			

Author	Author position	Scientific ideas %	Data generation %	Analysis and interpretation %	Paper writing %
Epp, T	1	50	75	50	65
Marks, MAW	2	15	0	15	10
Ludwig, T	3	0	15	10	5
Kendrick, MA	4	10	5	10	5
Eby, N	5	0	5	0	5
Neidhardt, H	6	5	0	0	0
Oelmann, Y	7	5	0	0	0
Markl, G	8	15	0	15	10
Title of paper:		Crystallographic and fluid compositional effects on the halogen (Cl, F, Br, I) incorporation in pyromorphite-group minerals			
Status in publication process		Accepted and published			

Author	Author position	Scientific ideas %	Data generation %	Analysis and interpretation %	Paper writing %
Epp, T	1	50	95	50	50
Neidhardt, H	2	20	0	20	20
Pagano, N	3	0	5	0	0
Marks, MAW	4	5	0	5	5
Markl, G	5	5	0	5	5
Oelmann, Y	6	20	0	20	20
Title of paper:		Vegetation canopy effects on total and dissolved Cl, Br, F and I concentrations in soil and their fate along the hydrological flow path			
Status in publication process		Accepted and published			

Author	Author position	Scientific ideas %	Data generation %	Analysis and interpretation %	Paper writing %
Epp, T	1	60	100	70	80
Marks, MAW	2	15	0	5	5
Neidhardt, H	3	5	0	10	5
Oelmann, Y	4	5	0	10	5
Markl, G	5	15	0	5	5
Title of paper:		Halogen (F, Cl, Br, I) sorption in silt and clay fractions of a Cambisol from a temperate forest, SW Germany			
Status in publication process		Manuscript submitted			

Table of content

1. Introduction

The critical zone describes a “heterogeneous, near-surface environment in which complex interactions involving rock, soil, water, air and living organisms regulate the natural habitat and determine the availability of life sustaining resources” (NRC 2001). It comprises the entire pedosphere, as well as the near-surface biosphere, hydrosphere, atmosphere and lithosphere (LIN 2010). The understanding of the halogen (F, Cl, Br, I) cycling in the critical zone requires the linking of different research areas to investigate the coupling of mineralogical, biological and physical processes. Halogens are omnipresent in the environment and are important micro-nutrients for humans, animals and plants (FUGE 1988; KABATA-PENDIAS 2011). Although, relatively extensive research on chlorine and fluorine has been carried out in the fields of the geochemistry of igneous and sedimentary environments (FUGE 1988; KENDRICK 2018), information on the distribution of halogens in soils and biosphere has been lacking. In the past few years however, considerable research has been done in exactly this area but a detailed understanding of processes involving F, Cl, Br and I in the terrestrial halogen cycle is still sparse. This work focuses on the halogen distribution in the near-surface environment and processes influencing their fate in the halogen cycle. Furthermore, halogen systematics can be source indicative as is, for example, the case with Cl/Br ratios or total salinity in hydrothermal solutions (FRAPE et al. 1984; KENDRICK AND BURNARD 2013; KENDRICK et al. 2017; WALTER et al. 2017). Halogens, due to its general abundance especially chlorine, can act as an important complexing agent as it, for example, enables the transport of Pb in hydrothermal solutions (e.g., WOOD et al. 1987). Due to supergene weathering of Pb-deposits secondary Pb-minerals such as pyromorphite-group minerals form, which are known to incorporate high amounts of Cl or F (MARKL et al. 2014). Processes that lead to the formation of primary Pb-bearing deposits as well as the halogen geochemistry in secondary Pb-minerals, will be also investigated in this thesis.

1.1. Halogens in general

The halogens (group VII of the periodic table) comprise the elements fluorine (F), chlorine (Cl), bromine (Br), iodine (I) and astatine (At; WIBERG 1985). Whereas, F, Cl, Br and I are stable elements, At only occurs as a radioactive decay product of uranium, thorium and actino-uranium (WIBERG 1985; FUGE 1988), and is thus not regarded further. Fluorine has the highest electronegativity and is by far the most reactive halogen (GREENWOOD AND EARNSHAW 1984). From F to I the electronegativity and their reactivity decrease, while the ionic radius increases (DOWNS AND ADAMS 1975; GREENWOOD AND EARNSHAW 1984). Chlorine is of great importance since it is the dominant ligand that facilitates metal transport in most of the hydrothermal fluids (BISCHOFF AND DICKSON 1975; SEYFRIED JR AND BISCHOFF 1981; YARDLEY 2005; KENDRICK 2018).

Fluorine and Cl are the most abundant halogens in nature, but they occur almost exclusively as aqueous halide ions fluoride (F^-) and chloride (Cl^-), respectively (HALKA AND NORDSTROM 2010) and are rarely rock-forming mineral constituents, as it is the case in for example fluorite (CaF_2) and NaCl (FUGE 1988). Fluorine and Cl have similar overall abundances on Earth with concentrations of ~15-300 mg kg^{-1} in the primitive mantle (PYLE AND MATHER 2009; KENDRICK et al. 2017) and 625 to 640 mg kg^{-1} on average in the Earth's crust (KABATA-PENDIAS 2011 and references therein). Generally, Cl is the dominant halogen in various types of waters, rocks or soils although F is more abundant in specific rock types such as e.g., in leucogranites (e.g., LÅG AND STEINNES 1976; GÖB et al. 2013; BURISCH et al. 2016). By far the highest Cl concentrations can be found in seawater with up to 19,000 ppm Cl, whereas F only occurs up to 1.3 ppm (WILSON 1975; WHITFIELD AND TURNER 1979; LI 1991; HALKA AND NORDSTROM 2010). Whole-rock analyses from various igneous, metamorphic and sedimentary rock types show variable Cl concentrations but are similar to the range observed in soils (e.g., BEHNE 1953; LÅG AND STEINNES 1976; MURAMATSU AND WEDEPOHL 1998; REDON et al. 2013).

In contrast, Br and I occur in much lower concentrations in nature (WIBERG 1985). Similar to F and Cl they can be found as bromide (Br^-) and iodide (I^-) ions, or in organic compounds (FUGE 1988; HALKA AND NORDSTROM 2010). Bromine and I are only trace element constituents in the primitive mantle with concentrations of ~76 ppb for Br and ~7 ppb of I (MCDONOUGH AND SUN 1995; PYLE AND MATHER 2009; KAMENETSKY AND EGGINS 2012; KENDRICK et al. 2017) and primary iodide or bromide minerals are exceptionally rare (FUGE 1988). Interestingly, the highest I concentrations can be found in coastal environments in Kelp, a type of seaweed, and at sea in phytoplankton (LEBLANC et al. 2006; IWAMOTO AND SHIRAIWA 2012). In Kelp, I concentrations of up to 6 wt% (KÜPPER et al. 2013) with an average of around 1 wt% (GALL et al. 2004) have been reported. Excluding the mantle, the ocean is the largest reservoir for Br with concentrations of 65 ppm in seawater, whereas I is only up to 0.06 ppm (WONG AND BREWER 1974; WILSON 1975; WHITFIELD AND TURNER 1979; LI 1991; HALKA AND NORDSTROM 2010).

1.2. Terrestrial halogen reservoirs and systematics

Halogen distribution in terrestrial ecosystems is influenced and monitored by a vast number of small and large scale biotic, abiotic and also anthropogenic factors and processes. In the following, a summary of the complete earth halogen cycle and biosphere are described, where a special focus was given to the earth's crust, hydrosphere and biosphere as they are most relevant to this study.

During the subduction of halogen-bearing pore fluids, sediments or altered oceanic crust (BARNES et al. 2018 and references therein), the halogens can be reintroduced into the mantle

environment. The mineral-bound halogens can be released during subduction zone metamorphism and were assumed to be a dominant enrichment source of halogens in the Earth's mantle (KENDRICK et al. 2014; BARNES et al. 2018). Generally, Cl, Br and I are rather strongly partitioned into aqueous fluids, whereas F is preferably incorporated into solid phases when stable (ZHU AND SVERJENSKY 1991). Furthermore, water is subducted into the mantle, chemically bound in hydrous mineral phases within the hydrated oceanic lithosphere (KENDRICK et al. 2011 and references therein), and is also an important volatile source for the mantle (HOLLAND AND BALLENTINE 2006). These processes produce a very heterogeneously composed mantle with respect to halogens (HOFMANN 2003 and references therein). During partial melting of the mantle (at various tectonic settings) the halogens can be remobilized and transported by the melt into crustal levels. Furthermore, crustal level metamorphism can redistribute and concentrate these halogens in e.g., newly formed minerals (HAMMERLI et al. 2016).

These halogens can be recycled to the Earth's surface by either volcanism (FUGE 1988; BARNES et al. 2018), hydrothermal activity or temporary stored within crystallized rocks and subsequently released due to weathering processes. During volcanism, enormous amounts of halogens can be emitted as HF, HCl, HBr and HI into the atmosphere (FUGE 1988; WEBSTER et al. 2018). At least part of these near-surface halogens will be eventually washed into the ocean, which is a further important halogen reservoir. Evaporation successively leads to the emission of halogens into the atmosphere, mostly in the form of aerosols (FUGE 1988; WORDEN 2018). However, it was reported that Cl and F could also occur in their particulate form (FUGE 1988), whereas Br and I can be present in a gaseous form (DUCE et al. 1965). Furthermore, anthropogenic sources such as biomass burning, coal combustion, waste incineration and other industrial processes increase the halogen content in the atmosphere drastically (KEENE et al. 1999). Due to wet and dry deposition halogens are transported to continental surfaces. Locations close to coastal areas receive distinctly higher halogen amounts originating from atmospheric deposition compared to distant locations (LÅG AND STEINNES 1976; STEINNES AND FRONTASYEVA 2002; JOHANSSON et al. 2003; MONTELIUS et al. 2015). These dry depositions of halogens on needles and leaves may enrich rainfall halogen concentrations when passing through a canopy (throughfall). Accordingly, this was observed for dissolved Cl and I, where higher concentrations in throughfall were detected compared to rainfall, due to leaching from organic compounds in the canopy and dissolution of dry deposition (e.g., LOVETT et al. 2005; MONTELIUS et al. 2015; ROULIER et al. 2019). To sum this up, halogen input into near-surface terrestrial ecosystems occurs by halogen release due to host rock weathering and atmospheric input in the form of dry (aerosols, dust) and wet deposition (rainfall).

Subsequently, throughfall and rainfall percolate through the soil and the underlying host rock. Transformation and retention processes in the soil play an important role in the

biogeochemistry and availability of F, Cl, Br and I in natural ecosystems. Biological transformations of inorganic halogens to organic halogens in soils take place by halogenation (i.e., chlorination, bromination, fluorination and iodination) of organic matter (e.g., ÖBERG AND SANDÉN 2005; LERI AND MYNENI 2010; ÖBERG AND BASTVIKEN 2012). Such transformations are governed by the amount of atmospheric input, nutrient and seasonal availability, redox conditions, or microbial activity (JOHANSSON et al. 2003; REDON et al. 2011; ÖBERG AND BASTVIKEN 2012). These halogenation processes lead to an accumulation of for example Cl in the organic soil layer (FUGE 1988; BASTVIKEN et al. 2007; REDON et al. 2011) and different depth distribution patterns were reported for Cl, F, Br and I (CORTIZAS et al. 2016; TAKEDA et al. 2018; ROULIER et al. 2019; WANG et al. 2019). A further important process influencing the halogen distribution in the soil column is adsorption on e.g., positively charged iron (Fe), manganese (Mn) and aluminum (Al) oxides and (oxy) hydroxides. For dissolved F_{inorg} and I_{inorg} strong adsorption to oxides and Fe-, Al-hydroxides was found (MCLAUGHLIN et al. 1996; GERZABEK et al. 1999; LOGANATHAN et al. 2007). However, since soils are heterogeneously composed (also with respect to depth; IUSS-WORKING-GROUP-WRB 2015), it is not very surprising that halogen distribution varies with respect to soil horizon and soil composition.

Furthermore, halogens are not only accumulated in the organic soil horizons, but can also be released by leaching from decomposing litter into the soil solution, as has been shown for Cl (LOVETT et al. 2005). Halogen release from the organic soil layer leads to a halogen enrichment of the soil solution compared to rainfall concentrations (LOVETT et al. 2005). So far, a vertical depth profile for soil solutions was only described for Cl_{inorg}, where a dependence of halogen concentration on increased adsorption and nutrient uptake by plants resulted in decreasing dissolved Cl_{inorg} concentrations with increasing depth (LOVETT et al. 2005). To conclude, a lot of research on halogen systematics in terrestrial ecosystems has been done so far. Nevertheless, relatively little is known about systematic halogen variations concerning all four halogens F, Cl, Br and I in rainwater, and their dependence on canopy presence and soil depth in soil profiles or soil solutions. It will be a major aspect of this work to focus on exactly this topic, i.e., the halogen distribution in the near-surface halogen cycle.

1.3. Formation and weathering of hydrothermal Pb-deposits and halogen systematics in pyromorphite-group minerals

During the Variscan orogeny and subsequent large-scale tectonic events (e.g., the opening of the Atlantic Ocean and the Upper Rhine Graben rifting), complex tectonic fault patterns were created in the Schwarzwald (SW Germany), and reactivated multiple times (BAATARTSOGT et al. 2007). These can act as suitable pathways for fluid circulation (KNIPE 1993; WERNER AND FRANZKE 2001). Since 310 Ma repeated Permian and Tertiary volcanic activity, ongoing basement subsidence during the Jurassic and the opening of the Upper Rhine Graben in the

Cenozoic in combination with suitable precipitation mechanisms led to periodically formation of abundant mineralized veins (SCHUMACHER 2002; WETZEL et al. 2003; STAUDE et al. 2007; 2009; WALTER et al. 2016; 2018). A lot of these hydrothermal veins have been mined during medieval times (especially for Ag) since these veins bear a large variety of different metals such as Pb, Ag, Au, Sb, Zn, Cu, Ni or Co (METZ AND RICHTER 1957). Metals are transported as e.g., Cl complex (WOOD et al. 1987) and therefore, halogens in hydrothermal solutions are of great interest, but also because of very high Cl and Br concentrations due to remarkable high salinities to some extent (BAATARTSOGT et al. 2007; WALTER et al. 2017). In total, there were five peaks of hydrothermal activity in the late Carboniferous, Permian, Triassic-Jurassic, Jurassic-Cretaceous and in the post-Cretaceous (PFAFF et al. 2009; STAUDE et al. 2009; WALTER et al. 2016). The chemical (e.g., Cl/Br ratios, metal content) and physical characteristics of the fluids which formed new and remobilized old hydrothermal veins varied with age between these periods of increased hydrothermal activity (e.g., BEHR AND GERLER 1987; STAUDE et al. 2009; WALTER et al. 2016). Carboniferous quartz-tourmaline veins occur spatially associated with granitic intrusions and were formed by low salinity (< 4.5 wt% NaCl eq.) magmatic fluids with temperatures up to 550 °C (MARKS et al. 2013; WALTER et al. 2016). Permian Sb±Ag±Au veins were formed by cooling of late metamorphic fluids. These were characterized by high temperatures of up to 440 °C and low salinities < 5 wt% NaCl eq. with Cl/Br ratios of ~90 (WAGNER AND COOK 2000; BAATARTSOGT et al. 2007; WALTER et al. 2016). Triassic-Jurassic quartz-hematite±barite veins precipitated from medium temperature fluids with variable salinities (BRANDER 2000; WALTER et al. 2016). In contrast, quartz-fluorite-barite veins with chemically and texturally complex mineral assemblages in the Jurassic-Cretaceous were formed by fluids with variable temperatures (50 – 150 °C) and high salinities (20 - 28 wt% NaCl eq.; BAATARTSOGT et al. 2007; STAUDE et al. 2009; WALTER et al. 2016). These fluids had characteristic Cl/Br ratios of up to 800 (WALTER et al. 2016). The halogens play a vital role during vein formation, not only due to the abundance of complexing Cl which enables metal transport, but also due to the high F concentrations that led to enormous quantities of fluorite precipitation (BEHR AND GERLER 1987; STAUDE et al. 2009). Veins formed in post-Cretaceous times precipitated from fluids with variable temperatures (50 – 150 °C) and variable salinities with Cl/Br ratios of up to 150 (1 - 23 wt% NaCl eq.; LÜDERS 1994; WALTER et al. 2016). Several fluid origins and metal provenances have been proposed for many of the veins so far: (1) leaching of crystalline basement rocks by sedimentary brines, (2) hydrothermal exsolution from magmatic intrusions or (3) introduction of juvenile solutions from the crust-mantle boundary (YARDLEY 2005; FUSSWINKEL et al. 2013; BURISCH et al. 2016; SCHARRER et al. 2019 and references therein). Within these fluids, the metals are predominantly transported as either chloride- (YARDLEY 2005), sulfide- (SHERMAN et al. 2000), or hydroxide complexes and can be precipitated through several mechanisms. These include fluid cooling, boiling, fluid dilution,

fluid mixing, host rock interaction, or fluid reduction by hydrocarbons, sulfides or reaction with ferrous minerals (SVERJENSKY 1981; DRUMMOND AND OHMOTO 1985; FONTBOTÉ et al. 2017; SCHARRER et al. 2019 and references therein).

During the exhumation of these veins and their weathering at surface conditions due to the presence of oxidizing meteoric fluids, the primary hydrothermal minerals can be dissolved and/or replaced. In general, galena (PbS) is the most abundant primary hydrothermal Pb-bearing ore mineral. At ambient conditions, it is most commonly replaced by pyromorphite-group minerals (PyGM; which host halogen concentrations up to wt%) and other secondary Pb-minerals (e.g., anglesite or cerussite; WERNER 2002; MARKL et al. 2014; KEIM AND MARKL 2015). The supergene weathering zone is typically restricted to the upper few meters of an ore deposit below the surface (AGUE AND BRIMHALL 1989; SILLITOE 2005; REICH AND VASCONCELOS 2015; REICH et al. 2019). Dissolution and transport processes are strongly climate-dependent, thus, reflect for instance temperature conditions, water and or other species availability, biological or microbiological activity (REICH AND VASCONCELOS 2015; REICH et al. 2019). The recent growth of PyGM crusts on for example medieval dumps shows that the weathering of the ore deposits is still ongoing (BURMANN et al. 2013). Calculations of KEIM AND MARKL (2015) indicated that millimeter-thick PyGM crusts can form in a few tens toa hundred years. This in combination with an extremely low solubility emphasizes their importance in immobilizing harmful toxins such as As and Pb (SCHECKEL et al. 2005; KUMPIENE et al. 2008).

In general, PyGMs are minerals of the apatite supergroup with an ideal formula of Pb_5A_3L, where A represents PO_4^{3-} (pyromorphite), AsO_4^{3-} (mimetite), or VO_4^{3-} (vanadinite). The dominant L anion is Cl^-, but substitutions with F^-, OH^-, Br^- and/or I^- occur to some degree (e.g., WONDRATSCHEK 1963; PASERO et al. 2010; KNYAZEV et al. 2011; MARKL et al. 2014). Furthermore, at least a partial solubility exists with the structurally very similar members of the hedyphane group (phosphohedyphane, hedyphane, and fluoro-phosphohedyphane) which have the following formula: $Ca_2Pb_3A(Cl^-, OH^-, F^-)$ with A either composed of $PO4^{3-}$ or $AsO4^{3-}$ (PASERO et al. 2010). Complete miscibilities were described for pyromorphite-mimetite, pyromorphite-phosphohedyphane and mimetite-hedyphane (DENNEN 1960; WONDRATSCHEK 1963; FÖRTSCH AND WONDRATSCHEK 1965; FLIS et al. 2011; MARKL et al. 2014). In natural PyGM samples Cl^- concentrations can reach up to more than 2 wt% while, although less, significant amounts of F^- and OH^- can also be incorporated (MARKL et al. 2014). However, phosphohedyphane is the only F-dominated endmember that occurs in nature (PASERO et al. 2010; KAMPF AND HOUSLEY 2011). Two further naturally occurring endmembers of this mineral group have been described, i.e., hydroxylpyromorphite (HÅLENIUS et al. 2017) and hydroxylmimetite, where the L site is dominated by an OH-endmember (MARKL et al. 2014).

Furthermore, PyGMs with compositions close to Pb_5A_3L are dominated by Cl^-, whereas the L site of phospho-/ hedyphane $Ca_2Pb_3A_3L$ compositions is preferably occupied by F^- (PASERO et al. 2010; MARKL et al. 2014). This is due to the fact that Pb^{4+} has a larger ionic radius compared to Ca^{2+}, compositions of Pb_5A_3L have larger cell unit dimensions and thus favor the incorporation of Cl^- which has a larger ionic radius than F^- (PASERO et al. 2010; MARKL et al. 2014). This observation was made in Ca-rich hedyphane samples where higher F amounts were detected compared to pyromorphite, mimetite, or vanadinite (MARKL et al. 2014). However, less information about Br and I distribution in natural occurring PyGM exist, due to the general lacking information about these heavy halogens in natural systems due to analytical difficulties. Several studies synthesized halogen (F, Cl, Br) PyGM endmembers (in exception I-pyromorphite) and thus proved, that these mineral phases are thermodynamically stable and could theoretically occur at near-surface conditions (WONDRATSCHEK 1963; JANICKA et al. 2012).

2. Objectives

In this work the formation of primary Pb-deposits, the subsequent supergene weathering with a specific focus on the halogen distribution in thereby formed secondary Pb-minerals and the fate of the halogens (F, Cl, Br and I) in the critical zone, including the pedosphere and the hydrological flow path, are addressed.

The formation of primary Pb-deposits was studied on veins distributed in the entire Schwarzwald (study A). The Schwarzwald is an ideal study site, as a vast number of small hydrothermal Pb-mineral bearing veins are exposed. These veins typically have a primary ore mineralization which is overprinted by several periods of hydrothermal activity. Hence, these textures do not only record remobilization and structural reactivation processes but also the fluid evolution of the system over hundreds of millions of years. The evolution and the involvement of different fluid types for the Sb-Pb ore deposit type has not been studied in detail so far. Therefore, the first study (chapter 4.1) focused on:

- A detailed textural characterization of individual mineralization stages;
- The combination of textural observations with isotopic, fluid inclusion and geochemical data to refine genetic models for this type of mineralization;
- To corroborate the genetic model with calculated stability diagrams;
- Setting the conclusions into regional and worldwide context.

The main focus of this thesis is on the halogen distribution in the critical zone, where one part deals with the halogen distribution in naturally occurring secondary Pb-minerals (Study B) which were formed due to supergene weathering of primary Pb-deposits (such as those from study A). Therefore, a suitable highly precise bulk method for the simultaneous determination of F, Cl, Br and I was developed. For this study minerals of the pyromorphite mineral group (pyromorphite, mimetite and vanadinite) were investigated. Halogen concentrations in bulk mineral samples but also spatially resolved in zoned and non-zoned crystals were analyzed. Zoned crystals were interpreted to reflect single episodes of fluid flow and weathering and thus this study investigates and distinguishes between the crystallographic and fluid compositional effects on the halogen incorporation for this mineral group. Therefore, the focus of this second study (chapter 4.2) was on:

- Detailed description and comparison of analytical methods to detect the trace halogen elements Br and I and implementation of the combustion ion chromatography method;
- Geochemical bulk sample characterization of pyromorphite-group minerals
- Producing spatially resolved halogen characterization with respect to mineral zoning profiles;

- Characterization of halogen systematics and crystal chemical controls on the incorporation of halogens in pyromorphite-group minerals;
- Detailed evaluation of possible parameters which may influence the formation of pyromorphite-group minerals;
- Halogen ratio comparison between various reservoirs of different water, rock, mineral and soil types.

Whereas study B focused on the halogen distribution in secondary Pb-minerals in the oxidation zone of an ore deposit and detailed investigation of mineral samples, study C investigated the halogen distribution in soil above a formerly mined Pb-deposit and various surface waters. Moreover, this study comprises the investigation of the entire halogen cycle close to the Earth's surface. This is of great interest since only a few studies exist where halogens were correlated between soil samples and soil solution as well as different surface waters from a single location, especially with respect to all halogens including Br and I. Furthermore, the halogen distribution was studied in samples which were collected over two growing seasons at the Feldberg, SW Germany. The aims of this study (chapter 4.3) were as follows:

- Determination of vertical depth profiles of total F, Cl, Br and I concentrations in soil samples taken below a canopy and from an open area;
- Determination of dissolved F_{inorg}, Cl_{inorg}, Br_{inorg} and I_{inorg} concentrations in various ecosystem solutions (throughfall, rainfall, soil solution, adit water, creek water);
- Investigation of vegetation canopy effects on halogen concentrations in the critical zone;
- Evaluation of factors that may facilitate and influence halogen concentration differences between location type or sample type;
- Identification and investigation of soil internal and external processes which govern the halogen distribution in natural surface environments.

The outcome of study C clearly revealed the importance of halogen sorption on interfaces of pedogenic oxides and showed different patterns with respect to halogen distribution in the vertical soil profiles. Since study C solely focused on soil samples which included the entirety of soil size fractions, and halogen data from different size fractions and also information about halogen sorption in soils is generally sparse, study D focused on the following major questions:

- Determination of the proportions of F, Cl, Br and I (organic+ inorganic) that are surface sorbed or incorporated in minerals (clay and pedogenic oxides) in four different soil size fractions (20-63 µm, 2-20 µm, 0.2- < 2 µm and 0.02-0.2 µm);
- Determination of vertical depth profiles of total F, Cl, Br and I concentrations in four different soil size fractions.

3. Choice of study sites and site characteristics

Hydrothermal quartz veins associated with Pb-bearing hydrothermal and supergene mineral phases are found all over Europe, often in the Variscan basement, and were chosen for investigation in study A. Examples of a large variety of former mining districts within these Variscan basement outcrops in Germany are the Harz, Schwarzwald and Erzgebirge (e.g., WALENTA 1957; WAGNER AND COOK 2000; BURISCH et al. 2018; KROLOP et al. 2018). Due to the abundant published and peer-reviewed pre-existing groundwork on these systems, all investigated samples derive from the Schwarzwald. Sample locations for study A and B were distributed throughout the entire Schwarzwald, whereas samples for study C and D only derive from one locality right below the Feldberg peak in the southern Schwarzwald. The approach to collect samples from one locality was necessary in order to investigate the entire halogen cycle with respect to several parameters, such as soil depth, vegetation and time while keeping other disruptive external factors constant. The geology and hydrothermal mineralization of the Schwarzwald are briefly discussed in sub-chapters 1.3 and 3.1. A detailed mineralogical description will not be given in a separate chapter since it is described in detail in the individual study A (chapter 4.1, Appendix I).

The Kammentobel valley ~1360 m above sea level at the north-west flank of the Feldberg was chosen as the locality to investigate the halogen cycle due to the fact that (i) the location had canopy presence and open area side by side, (ii) an accessible horizontal mine adit, (iii) throughfall, rainfall, soil solution and complete soil profiles could be easily gathered right above the ore deposit, (iv) the average outflow of the hydrological path, i.e. all surface fluids, could be collected in the Kammentobel creek and (v) all sample locations are part of a protected forest where no land management is conducted and the samples sites are only separated by several tens of meters. This location offered the opportunity to study the compositional changes of rainwater as it passed through vegetation and about 1 meter of soil before it reached fractured and weathered migmatites, pyromorphite-group minerals formed by supergene alteration of the hydrothermal Pb-deposit, and runoff water collected in the Kammentobel creek. The temperature of this study site ranged annually between -20 and 23°C and the total precipitation was ~1500 mm in 2018 (WETTERKONTOR 2019). The investigated soil developed on a strongly weathered migmatite and can be classified as a Cambisol (IUSS-WORKING-GROUP-WRB 2015). The vertical profile of the Cambisol consists of an organic layer and a mineral topsoil and subsoil. Furthermore, three of the sample locations were situated below a canopy of spruce trees (*Picea abies* (L.) H. Karst), whereas the other three sample locations were located below a by blueberry (*Vaccinium myrtillus* L.) dominated shrub layer.

3.1. Regional geological setting in the Schwarzwald, SW Germany

The Schwarzwald is situated in SW Germany and part of the Central European Variscan Orogeny (KALT et al. 2000). Within the Schwarzwald, several Variscan crystalline basement units are separated by two continental sutures, the Baden-Baden-Zone (BBZ) in the north and the Badenweiler-Lenzkirch-Zone (BLZ) in the south. The basement is dominated by partially migmatized ortho- and paragneisses as well as post-collisional granitic intrusions, which intruded between 335 and 315 Ma (e.g., TODT 1976; ALTHERR et al. 2000; HANN et al. 2003). The crystalline basement was then overlain by a Paleozoic and Mesozoic sedimentary sequence on top of an erosion surface of Permian age (GEYER et al. 2011 and references therein). A starting marine transgression during the Triassic led to the deposition of limestones, shales and carbonates (GEYER et al. 2011). Further carbonates and shales were deposited during the Jurassic, whereas Cretaceous sedimentary depositions are lacking due to erosion in the Schwarzwald (GEYER et al. 2011). The opening of the Upper Rhine Graben, which is part of the European Cenozoic rift system, was induced by the alpine orogenesis in the Paleogene (e.g., ZIEGLER 1992; GEYER et al. 2011). Due to asymmetrical uplift of the rift flanks and erosion processes the sedimentary cover is only exposed in the northern Schwarzwald, whereas in the south the present-day topography represents rocks from up to 2 km below the Permian unconformity (RUPF AND NITSCH 2008; GEYER et al. 2011).

4. Individual studies

4.1. Formation of primary Sb-Pb-deposits and remobilization processes

Title of publication:

Quartz veins with associated Sb-Pb-Ag±Au mineralization in the Schwarzwald, SW Germany: a record of metamorphic cooling, tectonic rifting, and element remobilization processes in the Variscan belt. (Study A)

Primary formed mesothermal antimony (Sb) deposits are distributed worldwide and not only physico-chemical parameters but also the halogen (Cl and F) content in fluids is decisive for the formation. These deposits are comprised of either pure stibnite deposits or the more complex but in turn scientifically more interesting polymetallic Sb-Pb-Ag±Au-W-Sn-As-Zn deposits, also known as orogenic gold deposits (e.g., LENTZ et al. 2002; NEIVA et al. 2008; BALTUKHAEV AND SOLOZHENKIN 2009). These deposits are commonly not only mined for Sb, but can also be important producers of other economically interesting products such as gold. In Europe, numerous ore districts are rich in quartz-veins, linked to the Variscan Orogeny and associated with a Sb-Pb-Ag±Au-type mineralization. Examples of former mining districts can be found amongst others in Germany (Schwarzwald, Rheinisches Schiefergebirge, Harz), France (Vosges mountains, Massif Central), Italy (Sardinia, Lombardy), Spain, Portugal, Austria, Great Britain, Czech Republic and Slovakia (e.g., WALENTA 1957; CLAYTON et al. 1990; ORTEGA et al. 1991; DILL 1993; WAGNER AND COOK 2000). Previous research put a special emphasis on the structural history and fluid evolution of this vein type. The formation of these veins is linked to late-Orogenic, post-compressive brittle tectonic events and thus, they formed during the transition from the Variscan compressive stress regime to post-Variscan strike-slip tectonics (e.g., ARTHAUD AND MATTE 1977; BRIL 1982; WAGNER AND COOK 2000). Furthermore, several precipitation mechanisms for stibnite, the most abundant Sb-bearing mineral, have been proposed, but the literature largely agrees that fluid cooling is the primary precipitation mechanism (WAGNER AND COOK 2000). Fluid cooling can either occur by conductive heat transfer to the host rock or by fluid mixing processes with low temperature fluids (WAGNER AND COOK 2000). However, these vein types are commonly comprised of a complex poly-stage mineral assemblage, which was generally not considered as individual stages that might have formed by different processes or times. The focus of study A was to investigate in detail the evolution of these poly-stage quartz-Sb-Pb-Ag±Au veins over a 300-Ma time span in the Schwarzwald, SW Germany. Therefore, 148 representative samples from 38 localities from the entire Schwarzwald were chosen to be investigated by optical microscopy, electron microprobe analysis and oxygen isotope analysis. Additional samples were analyzed for fluid inclusions by optical microscopy, cathodoluminescence, microthermometry and micro-Raman. The results and interpretation of a detailed petrographic description in combination with

isotopic, fluid inclusion, and geochemical data allowed a refinement of genetic models of this mineralization type. The study concluded that four different successive mineralization stages according to mineral assemblages and textural relations can be distinguished and two stages contain Pb-dominated mineral assemblages: (I) Fe-As(-Sb±Au), (II) Pb-Zn-Cu, (III) Pb-Sb and (IV) Ag-Sb. Due to the similar formation conditions of stages II and III, they will be discussed within the same paragraph.

Stage I: Fe-As (-Sb±Au) mineralization

Fluids with a low salinity below 5 wt% NaCl eq. and very variable temperatures ranging from 100 to 400 °C led to the formation of the first mineralization stage which contained Fe-As sulfides (pyrrhotite, arsenopyrite, pyrite, marcasite) and quartz as gangue mineral. These sulfides contained invisible gold with concentrations up to 3100 ppm in arsenopyrite and trace amounts of Sb. This sequence was then followed by a succession of berthierite and stibnite which further indicated that the fluid in the hydrothermal system contained large amounts of Sb. Invisible gold was remobilized and locally precipitated as discrete grains of electrum at the end of stage I. These fluid compositions with only minor Cl content and low Cl/Br ratios of ~ 90 are very typical for Permian veins in the Schwarzwald (WAGNER AND COOK 2000; BAATARTSOGT et al. 2007; WALTER et al. 2016). The high temperature and large temperature range represents the process of fluid cooling, which is typical for many large Sb deposits worldwide, e.g., in Bolivia or China (DILL et al. 1995; ZHAI et al. 2014). The observed mineral succession is in accordance with the thermodynamic modeling of successive cooling of a low salinity fluid initially in equilibrium with a granitic host rock at a neutral pH (6.55 at 400°C). However, water-rock interactions during the cooling process are required to produce the relative mineral quantities observed. Furthermore, in order to reach pyrite saturation, the fluid must initially have been relatively reduced and sulfur-rich, alternatively, hematite and/or magnetite would have formed.

Stage II & III: Pb-Zn-Cu & Pb-Sb mineralization

The minerals of stage II and III precipitated from a fluid that had remarkably high salinities of 20-27 wt% NaCl eq. and moderate to low temperatures between 50 and 250 °C. The presence of large Cl amounts (Cl/Br ratios of up to 800; WALTER et al. 2016) resulted in very high salinities which is in contrast to low-salinity basement fluids and thus forced mixing between two chemically different fluids. It also enabled metal transport which resulted in mineralogical diversity. The second stage is represented by minor occurrences of Cu-, Pb-, and/or Zn-sulfides, such as tetrahedrite, galena, chalcopyrite and sphalerite. Thus, this mineral succession showed a Pb-, Zn- and Cu-input into the hydrothermal system. Tetrahedrite I was the most abundant mineral in this stage, had an average Ag content of 19 wt% and partially remobilized stibnite. In contrast to stage II, the third stage is abundantly developed in many of

the investigated veins and is characterized by highly variable and complex Pb-Sb mineral assemblages. Commonly, mineral textures were observed, where primary formed stibnite from stage I was replaced during this stage by Pb-Sb-sulfosalts such as zinkenite and füllöppite. Extremely high salinities indicate the involvement of a different fluid reservoir compared to that of stage I. The central European basin was flooded and evaporites deposited during Late Permian to Triassic times (GEYER et al. 2011). Furthermore, intensive brecciation of stage I additionally points to an important tectonic change, resulting in new fluid pathways. This major marine influence led to the mixing of high-salinity and low-salinity mid- and upper-crustal fluids during Jurassic-Cretaceous times. Interestingly, the abundance of stage III Pb-Sb minerals was directly related to the presence of stage I stibnite and the extent of remobilization during an influx of Pb in Jurassic-Cretaceous. In addition, the presence of Ag rich sulfosalts indicates an influx of Ag or remobilization of stage I electrum and stage II tetrahedrite.

Stage IV: Ag-Sb mineralization

In contrast to stage III, the fluids which led to the precipitation of minerals from stage IV had variable salinities between 7.5 and 20 wt% NaCl eq. (Cl/Br ratios up to 150; WALTER et al. 2016) and low temperatures of 50-200 °C. Fluid mixing, which is indicated by this large salinity range, and reaction processes with pre-existing sulfides led to the precipitation of the mineral assemblage in stage IV. The mineral textures of this stage commonly showed replacement reactions of stages II and III minerals. The gradual transition from a Pb-Sb towards an Ag-Sb dominated system was indicated by the initial formation of Pb-Ag-Sb minerals such as diaphorite and freieslebenite, and the late-stage presence of exclusively Ag-Sb minerals such as pyrargyrite, miargyrite, stephanite or allargentum. Tetrahedrite II analyses showed with averagely 32 wt% Ag remarkably higher Ag concentrations compared to tetrahedrite I (19 wt%) from stage II. This shift in fluid composition records a shift in the large scale tectonic setting. The NE-SW striking veins preferably contained a large variety of Ag-rich mineral associations, indicating an orientation preferred reactivation of initially Permian veins due to the Upper Rhine Graben formation during Tertiary.

In summary, this study showed in detail the textural, chemical and fluid compositional evolution of poly-stage quartz-Sb-Pb-Ag±Au veins over a 300-Ma time span in the Schwarzwald. This evolution is characterized by four successive mineralization stages that can be related to distinct mineralization events, fluid sources and precipitation mechanisms. Based on absolute halogen concentrations and ratios, the fluids of the individual stages can be distinguished, as these are indicative of the reservoirs and formation mechanisms. Overall, the study recorded a transition from metamorphic fluids, with minor amounts of halogens in the fluid, to basinal, saline brines, which had extremely high halogen concentrations, over hundreds of millions of

years in a hydrothermal system. It has been illustrated that halogens play an important role in a large variety of different processes throughout the evolvement of a hydrothermal system.

4.2. Halogen (F, Cl, Br, I) distribution in secondary Pb-minerals

Title of publication:

Crystallographic and fluid compositional effects on the halogen (Cl, F, Br, I) incorporation in pyromorphite-group minerals. (Study B)

Galena is a very common primary Pb-bearing ore mineral, associated with a large variety of mineralization types of different ore deposit types. During supergene weathering of galena, pyromorphite-group minerals (PyGM), i.e., pyromorphite, mimetite and vanadinite, can form (PARK JR AND MACDIARMID 1975; KEIM AND MARKL 2015). The particularity of these minerals is the incorporation of high amounts of Pb, As, V and other toxic metals such as Cr, Sb, Bi and U. Due to their extremely low solubility products, toxic and harmful elements are immobilized and the bioavailability reduced (NRIAGU 1973; FLIS et al. 2011; BURMANN et al. 2013). It was previously shown that some PyGM crystals are strongly zoned due to chemical variations in their Ca- and Pb-content, and REE patterns in different zones (MARKL et al. 2014). These variations were linked to chemical variations in the fluids from which the PyGM formed and it was proposed that single fluid pulses may be recorded within the crystal zones (MARKL et al. 2014). Furthermore, the L site in the PyGM formula is mostly occupied by Cl^- or OH^- and rarely by F^- (see chapter 1.3), but experiments showed that the incorporation of Br^- and I^- is thermodynamically stable (WONDRATSCHEK 1963; FLIS et al. 2011). However, systematic halogen distribution with respect to F, Cl, Br and I in bulk PyGM samples and single PYGM zones has not been investigated so far. To gain insights into the halogen distribution in PyGM and their potential as a fluid monitor, 151 samples from 44 localities in the Schwarzwald, SW Germany, have been investigated by combustion ion chromatography, electron microprobe analysis and secondary ion mass spectrometry.

The investigated bulk PyGM samples showed Cl concentrations ranging between 1.9 and 2.5 wt%, whereas the F content generally was < 0.3 wt%. Bulk Br and I concentrations were highly variable, ranging from 0.3 to 20 µg g^{-1} and from < 0.1 to 26 µg g^{-1}, respectively. Furthermore, minerals of the pyromorphite-group showed different halogen incorporation patterns. Pyromorphite samples for instance reached highest I and F levels and low Br concentrations (< 5 µg g^{-1}), whereas mimetite and vanadinite reached the highest Br contents, but the lowest F (generally < 500 µg g^{-1}) and I (< 2 µg g^{-1}) concentrations. These results are quite surprising since arsenic and vanadium have larger ionic radii than phosphorous (SHANNON 1976; FLIS et al. 2010). A larger ionic radius results in larger unit-cell volumes and thus mimetite and

vanadinite should favor the incorporation of I which has a larger radius than Br. However, the results of this study show the opposite: pyromorphite has higher I concentrations than mimetite and vanadinite, whereas the latter have higher Br concentrations. Hedyphane crystals (Ca-rich compared to the “standard” PyGM) have smaller unit-cell dimensions compared to PyGM endmembers and thus it is reasonable that these samples incorporated greater amounts of F. Nevertheless, highest I concentrations were also measured in hedyphane zones and this is a further evidence that the halogen incorporation is not only determined by crystallography. Experiments of FLIS et al. (2011) imply that PyGM crystals reflect the chemical fluid composition of which the crystals precipitated from, since the P/As ratios of the initial and final fluid were identical. This in fact could mean that the fluid composition alternates between P-dominated/I-rich and As-dominated/Br-rich end-members, resulting in I-rich pyromorphite and Br-rich mimetite. This theory is supported by a sample where the core is Br-rich mimetite and the outer rim consists of I-rich pyromorphite, thus indicating a drastic change of the fluid chemistry. Furthermore, As mainly derives from weathering of vein and host rock minerals (BASU AND SCHREIBER 2013), whereas in contrast the primary P source has microbial origin (BURMANN et al. 2013). Different sources for As and P also indicate that the precipitation of PyGM depends on different fluid pathways of different initial fluid sources.

With respect to the investigation of the PyGM zonation our samples were categorized into three zonation types. Type A includes crystals with no macro- and microscopic zonation, type B comprises patchy zoned crystals and type C crystals with a distinctive growth zoning. Samples of all three zonation types showed remarkable variations in their F, Cl, Br and I concentrations independent of major element (Ca- and Pb-content) variations. In general, no systematic halogen variations depending on the zonation were visible, the concentrations rather fluctuated. However, one sample with growth zoning showed decreasing F, Br and I concentrations from core to rim, whereas Cl increased. Since bulk PyGM analyses already indicated that crystallographic reasons do not suffice to explain our observations, an additional process needs to be invoked. A solution is that the growth zones represent different fluid pulses over time (MARKL et al. 2014), which may have interacted to different amounts with halogen sources that could fractionate the halogens. Major halogen sources in natural environments are rainwater, soil and host rocks. The halogen distribution in these different reservoirs will be subject of study C. Hence, the halogen availability in general or changes of physico-chemical parameters such as temperature, pressure and most importantly fluid chemistry are likely to affect the halogen incorporation into PyGM.

In conclusion, this study was able to show that natural PyGM crystals also incorporate considerable amounts of Br and I, in addition to Cl and F. Furthermore, it was shown that crystal-chemical processes may affect the halogen incorporation. However, the exact influence of crystal-chemical controls remains enigmatic and needs an experimental fluid-crystal

halogen partitioning study. The combination of fluid-chemical and eventually to a marginal extent crystallographic processes results in variable halogen incorporation in different types of PyGM and crystal zones. It was shown that the halogen incorporation was mineral specific, thus, halogen ratios may be used as fluid monitors. However, still more research needs to be done to understand the processes in more detail especially regarding the environmental importance of this mineral group.

4.3. Halogen (F, Cl, Br, I) distribution in soil and along the hydrological flow path

Title of publication:

Vegetation canopy effects on total and dissolved Cl, Br, F and I concentrations in soil and their fate along the hydrological flow path. (Study C)

Halogens are not only important for mineralogical or crystallographic reasons in primary (e.g., amphibole and biotite), or secondary minerals (e.g., PyGM, 4.2 study B, Appendix II), but they also play an important role in biological surface processes. It was recently found that the formation of halogenated organic compounds during either microbial decomposition of soil organic matter (AMACHI 2008; SEKI et al. 2012) or by abiotic mechanisms (e.g., abiotic oxidation or halogenation; LERI AND RAVEL 2015) has strong influences on the biogeochemistry of F, Cl, Br and I in forest ecosystems (ÖBERG et al. 2005; CABRAL et al. 2011; LERI AND MYNENI 2012). The origin of halogens and that within the soil column several processes like halogenation, leaching and sorption or desorption take place and were reflected in vertical halogen profiles was already described in detail in chapter 1.2. However, previous studies did not consider F, Cl, Br and I concentrations simultaneously at one location in a variety of samples which covers solid soil samples as well as various ecosystem solutions. The influence of vegetation on the near-surface halogen cycle has generally not been considered, thus, a detailed understanding of the halogen behavior and cycling in surface environments is still lacking. Therefore, study C (Appendix III) aims to provide a large F, Cl, Br and I data set from locations below canopy and under open areas in the Schwarzwald, a temperate climatic region, including soil, soil solution, precipitation, rainwater, adit and creek water samples. In order to investigate halogen distribution patterns and the influence of vegetation under the same site specific conditions, 30 solid soil and 145 liquid samples over two growing periods were collected for this study and analyzed by combustion ion chromatography, ion chromatography, sedigraph analysis and ICP-OES.

Investigated soil samples showed decreasing Cl_{tot} concentrations with increasing soil depth and in general a positive correlation with organic carbon (C_{org}). The vertical pattern illustrates a distinctive Cl accumulation in the organic layers which can be explained by two simultaneous

processes. On the one hand biological chlorination processes of organic matter result in Cl retention (e.g., HJELM et al. 1995; REDON et al. 2011; MONTELIUS et al. 2019). The other process which is reflected in the vertical pattern is the process of nutrient uplift. The investigated soil profiles cover a depth of ~ 60cm and the root zone reaches depths of approximately 40 cm (below canopy) and 50 cm (without canopy), respectively. Important plant nutrients such as N (nitrogen) and P (phosphorus) are obtained by plants from the subsoil via roots (ATTIWILL AND ADAMS 1993; LE DIZÈS AND GONZE 2019). Since Cl is an important micro-nutrient for the ecosystem (KABATA-PENDIAS 2011) an uplift of Cl by plant roots is very likely to occur. The vertical patterns of Br_{tot}, F_{tot} and I_{tot} were contrary to Cl_{tot} concentrations, i.e., increasing with increasing soil depth. Positive correlations to pedogenic oxides illustrated that the retention of Br, F and I was strongly dependent on abiotic processes such as adsorption to iron (Fe) and aluminum (Al) oxides and (oxy)hydroxides by electrostatic interactions. Higher concentrations in the more decomposed layers in the organic layer can be explained by dominating halogenation processes over dehalogenation and a subsequent leaching.

Vegetation canopy effects were visible in throughfall samples with significantly higher dissolved F_{inorg}, Cl_{inorg}, Br_{inorg} and I_{inorg} concentrations compared to rainfall. Furthermore, significantly higher total halogen concentrations were only found for Br_{tot} in the organic layer below canopy. For Cl_{inorg} and I_{inorg} higher dissolved concentrations below canopy were attributed to leaching processes from needles and leaves and wash-off of dry deposition (EATON et al. 1973; PETERS 1991; LOVETT et al. 2005; ROULIER et al. 2019). In general, this study showed that Br and I commonly have similar patterns and are influenced by the same processes. Hence, it can be assumed that higher dissolved Br_{inorg} (throughfall) and Br_{tot} (soil organic layer) concentrations resulted from dry deposition wash-off. Additionally, dissolved F_{inorg} concentrations are influenced by soil dust (BARNARD AND NORDSTROM 1982) and atmospheric input from industrial plants (WANG et al. 2019), which is however, hard to disentangle from natural processes. However, the input of soil dust may have been important at the investigated location, since highest dissolved F_{inorg} concentrations were detected during periods with the lowest rainfall volume. Very dry soils resulted in an increased soil dust production, which led to the increase of dissolved F_{inorg} concentrations and may have also effected dissolved Cl_{inorg}, Br_{inorg} and I_{inorg} concentrations.

Halogen concentrations along the hydrological flow path in soil solutions, adit and creek water hardly showed any differences. Significantly higher dissolved I_{inorg} concentrations in soil solution compared to rainfall concentrations may indicate at least partial equilibration reactions between the soil solution and the solid soil phase. There were no significant differences in dissolved Cl_{inorg}, Br_{inorg} and F_{inorg} concentrations between soil solution and rainfall. Thus, it is assumed that the geochemical equilibrium between the host rock and the soil solution resulted in halogen concentrations similar to those in rainfall. Furthermore, significantly higher dissolved

F_{inorg} concentrations in creek water compared to rainfall, soil solution and adit water were detected, which may be due to the weathering of fluorite-bearing veins. A large number of such veins were described in proximity to the study site and generally in the entire Schwarzwald (e.g., BURISCH et al. 2017). However, the highest dissolved F_{inorg} concentrations analyzed in our study were not exceptionally high, since they lied in the range of other creek and river analyses from Baden-Württemberg (LUBW 2019).

In conclusion, this study showed that halogen-specific processes govern the cycling of F, Cl, Br and I in ecosystems in temperate climatic regions. Furthermore, the results revealed the complexity of biotic and abiotic processes that interact in the critical zone and clearly illustrated the impact of atmospheric input, vegetation and pedogenesis. However, the vertical halogen patterns described in this study were partly contrary to those of previous studies. Hence, the outcome of this study indicates a site-specific halogen geochemistry and is likely only valid for forest ecosystems in temperate regions. In order to get comprehensive knowledge about halogen chemistry, further climatic regions need to be investigated systematically and their differences discussed.

4.4. Halogen (F, Cl, Br, I) sorption in silt and clay fractions in soil

Title of publication:

Halogen (F, Cl, Br, I) sorption in silt and clay fractions of a Cambisol from a temperate forest, SW Germany. (Study D)

Halogen distribution within soil is governed by processes such as halogenation, anion exchange, adsorption or desorption (e.g., GERZABEK et al. 1999; LOGANATHAN et al. 2007; LERI AND RAVEL 2015). In general, it was reported that commonly at interfaces or particle surfaces of for example clay minerals or pedogenic oxides anion adsorption occurs (BOWER AND HATCHER 1967; FUGE 1988; DU et al. 2011). Thereby the specific surface size of each particle is of great importance since with decreasing particle size the surface is increasing and thus the potential surface at which adsorption can take place (SCHEFFER et al. 1998). In the pH range of most soils, pedogenic oxides are positively charged (SCHEFFER et al. 1998) and offer suitable surfaces to adsorb F^-, Cl^-, Br^- or I^-. In contrast, clay mineral surfaces are generally negatively charged and are thus less suitable as anion sorbents. Instead, anion exchange mechanisms play an important role for clay minerals and lead to especially F^- incorporation into the crystal lattice with simultaneous OH^- release (WEERASOORIYA AND WICKRAMARATHNA 1999; CHUBAR et al. 2005). Previous research was particularly focused on F^- incorporation or sorption, whereas the sorption behavior of Cl^-, Br^- and I^- has largely been disregarded. Thus, a detailed understanding of the overall halogen sorption behavior in soils is still lacking.

Therefore, the focus of study D (Appendix IV) is on the determination of the relative amount of sorbed halogens (organic + inorganic) in four particle size fractions (i.e., 20-63 µm (coarse silt), 2-20 µm (fine and medium silt), 0.2- < 2 µm (coarse clay) and 0.02-0.2 µm (medium clay) in the mineral soil. Furthermore, it was also focused on potential vertical patterns of total organic + inorganic halogen (F_{tot}, Cl_{tot}, Br_{tot}, I_{tot}) concentrations. For this, 40 soil samples from four soil size fractions and five soil depths which included total (i.e., structurally bound and sorbed) halogen concentrations were chosen. Total halogen concentrations and the structurally bound halogen proportion after K_2HPO_4 solution treatment were analyzed by combustion ion chromatography (CIC). Sorbed halogen proportions (F_{sorb}, Cl_{sorb}, Br_{sorb}, I_{sorb}) were calculated by subtraction. Clay mineral identification and organic carbon content determination were carried out by X-ray diffraction and CN analyses.

In total, ~ 55 wt% of bulk soil consisted of particles > 63 µm and 40 wt% of coarse silt (20-63 µm; 15 wt%) and fine to medium silt (2-20 µm; 25 wt%) particles. The clay fractions represent by far the smallest weight portion of the investigated bulk soil since 3 wt% consisted of 0.2- < 2 µm and only <1 wt% consisted of 0.02-0.2 µm particles. Investigated soil samples revealed differences in the sorption behavior between F and the other halogens with larger ionic radii (Cl, Br and I) in different soil size fractions. Total F concentrations remained constant with respect to depth within the different particle sizes. On average 17 % of F_{tot} was sorbed to 20-63 µm particles whereas in particle sizes < 20 µm all of F_{tot} was structurally bound. In contrast, Cl_{tot}, Br_{tot} and I_{tot} concentrations were increasing with decreasing particle size. The highest total concentrations and sorbed portions of up to 90 % Cl_{sorb} and 70 % Br_{sorb} and I_{sorb} were found in the smallest 0.02-0.2 µm fraction. Generally, the sorption behavior should increase with decreasing grain size (SPOSITO 1984; SCHEFFER et al. 1998), since the specific surface size of particles is strongly dependent on the particle size (SPOSITO 1984).

Since F has a much smaller radius compared to Cl, Br and I it can be assumed that F is preferentially structurally incorporated into the crystal lattice of for example clay minerals and is thus relatively less prone to sorption. On average 93 % of F over all particle sizes and soil depths was structurally bound and only a minor amount was sorbed to surfaces. This can be explained by the anion substitution between OH^- and F^-, which is, however, strongly pH-dependent. The exchange is most extensive at pH < 4 (CHUBAR et al. 2005), thus, a soil pH of 3-4 (EPP et al. 2020) for the present location offers perfect conditions for extensive anion exchange. Furthermore, no vertical concentration differences of F_{tot} within the mineral soil were found. Commonly, the intensity of weathering in a vertical soil profile decreases with increasing depth (LINSER AND SCHARRER 1966) and thus, it is expected that F-, pedogenic oxide or clay mineral concentrations should show distinctive depth patterns. However, no variations were present and this may be attributed to steady-state or equilibrium conditions between F-release

by weathering, subsequent sorption or structurally incorporation and surface input and subsequent accumulation in upper soil horizons.

Due to much larger ionic radii of Cl, Br and I and their thus resulting rather incompatible substitution for OH^- in clay minerals, they are more prone to sorption processes. This study showed that with on average 32 % of Cl, 25 % of Br and 55 % of I large portions were sorbed. The sorption behavior of Cl^-, Br^- and I^- is strongly governed by pH, since sorption increases with decreasing pH (WEERASOORIYA AND WICKRAMARATHNA 1999). and a soil pH of 3-4 (EPP et al. 2020) therefore provided ideal conditions for halogen sorption to positively charged pedogenic oxides. Despite the larger Cl radius, CHUBAR et al. (2005) reported that Cl^- also competes with OH^- molecules to be incorporated, which makes it likely to be also valid for Br^- and I^-. The incorporation into the crystal lattice of clay minerals would explain why the main proportion of Cl and Br and half of I is not sorbed. For I it was shown that the portions of sorbed and incorporated fractions were equal, whereas Cl and Br were preferentially incorporated. This may be explained by Cl^- and Br^- ions being more compatible within the lattice structure than I^- anions due to I^- ions having the largest ionic radius. No concentration differences of Cl_{tot}, Br_{tot} and I_{tot} occurred with respect to depth within the mineral soil. For Cl, lacking depth variations may indicate steady-state or equilibrium conditions between surface input, sorption processes and nutrient uplift. Furthermore, lacking differences within the mineral soil during soil development may be attributed to large Cl (REDON et al. 2011), Br (CORTIZAS et al. 2016) and I (ROULIER et al. 2018) stocks in the soil, where other biogeochemical enrichment processes may be negligible.

In summary, this study showed that F was mainly structurally bound to clay minerals, whereas large portions of the halogens with larger atom radii (Cl, Br and I) were sorbed to charged surfaces. Besides, it was shown that the amount of sorbed halogens was dependent on the soil particle size, which was linked to large specific surface areas of small particles. However, it was not distinguished between organic and inorganic halogens, which could be subject to further studies.

5. Conclusions

This thesis contributes to a better understanding of the fate of halogens in natural environments. It comprises a detailed investigation of the fluid chemistry and precipitation mechanisms of primary Pb-deposits as well as the halogen distribution within secondary Pb-minerals which were formed due to supergene weathering of primary Pb-deposits. Furthermore, the presented results and conclusions provide a comprehensive knowledge concerning halogen systematics in soils of a temperate forest and along a natural hydrological flow path. Our studies have shown that halogen distribution is governed by a complex coupling of mineralogical, biological, chemical and physical processes.

A transition from metamorphic low salinity fluids (fluids with minor halogen content) to basinal, saline brines (fluids with extremely high halogen concentrations), over hundreds of millions of years in a hydrothermal system was recorded in detail in the Schwarzwald. Primary ore deposits, dominated by Fe-As(-Sb±Au) sulfides (stage I), were formed during Permian by cooling of high temperature, low-salinity metamorphic fluids. Several remobilization processes of the primary mineralization during Jurassic times led to the formation of distinctive Pb-Zn-Cu (stage II) and Pb-Sb (stage III) mineralization. Thereby the focus was on mixing of high-salinity (up to 27 wt% $NaCl+CaCl_2$), mid- and upper-crustal fluids and emphasized the importance of halogens, especially of Cl and F with respect to metal transport and thus indirect enabling of mineral precipitation. Halogens still played an important role during the formation of stage IV Ag-Sb minerals, since, Ag is also mainly transported as Cl-complexes and enormous fluorite abundances have formed during this time.

Supergene weathering of such primary Pb-deposits, especially of the very common mineral galena (PbS) leads to the formation of pyromorphite-group minerals (PyGM). This group mainly comprises the minerals pyromorphite, mimetite and vanadinite. Analyses showed that these minerals incorporate Cl in a weight percent range and also considerable amounts of F, Br and I. It was further shown that halogen corporation was mineral specific, since natural pyromorphite incorporated more I, whereas mimetite and vanadinite had highest Br concentrations. These findings were contrary to expectation since the latter have larger unit cells and I incorporation with a larger ionic radius would be more reasonable. Spatially resolved analyses in single growth zones revealed halogen mass ratio variations independent of major element composition. Hence, the outcome of this study revealed that halogen chemistry of PyGM is primarily not governed by a crystal-chemical control (alone), but rather by fluid composition.

Further investigations showed that halogen-specific processes govern halogen cycling in natural forest ecosystems. Vertical halogen concentration profiles in a soil above a supergene weathering zone revealed the complexity of biotic and abiotic processes that interact in the

critical zone. Thereby especially halogenation and adsorption in particular, as well as nutrient uplift played a central role. Large amounts of Cl were accumulated in the organic layer due to chlorination processes, whereas with increasing soil depth concentrations were decreasing due to nutrient uplift by roots. In contrast, higher concentrations of F, Br and I were found with increasing soil depth because of sorption on pedogenic oxides and incorporation into clay minerals. Our studies further revealed that sorption behavior differed among F, Cl, Br and I. It was shown that most of F was incorporated and structurally bound in clay minerals, most likely by anion exchange with OH^-. Remarkable amounts of Cl, Br and I were sorbed to pedogenic oxides. The highest sorbed halogen portions were found in the medium clay fraction due to the largest specific surface areas. In addition, it was shown that atmospheric halogen input by rainfall, the interaction with vegetation (e.g., dry deposition wash-off), soil and host rock affected the natural fluid composition along the hydrological fluid path.

References

AGUE JJ, BRIMHALL GH (1989) Geochemical modeling of steady state fluid flow and chemical reaction during supergene enrichment of porphyry copper deposits. Econ Geol 84:506-528.

ALTHERR R, HOLL A, HEGNER E, LANGER C, KREUZER H (2000) High-potassium, calc-alkaline I-type plutonism in the European Variscides: northern Vosges (France) and northern Schwarzwald (Germany). Lithos 50:51-73. doi: 10.1016/S0024-4937(99)00052-3.

AMACHI S (2008) Microbial contribution to global iodine cycling: volatilization, accumulation, reduction, oxidation, and sorption of iodine. Microbes and Environments:0811040018-0811040018.

ARTHAUD F, MATTE P (1977) Late Paleozoic strike-slip faulting in southern Europe and northern Africa: Result of a right-lateral shear zone between the Appalachians and the Urals. Geol Soc Am Bull 88:1305-1320. doi: 10.1130/0016-7606(1977)88<1305:LPSFIS>2.0.CO;2.

ATTIWILL PM, ADAMS MA (1993) Nutrient cycling in forests. New phytologist 124:561-582.

BAATARTSOGT B, SCHWINN G, WAGNER T, TAUBALD H, BEITTER T, MARKL G (2007) Contrasting paleofluid systems in the continental basement: a fluid inclusion and stable isotope study of hydrothermal vein mineralization, Schwarzwald district, Germany. Geofluids 7:123-147. doi: 10.1111/j.1468-8123.2007.00169.x.

BALTUKHAEV GI, SOLOZHENKIN PM (2009) Concentration of gold-antimony ores in the Sakha Republic (Yakutia). Russ J Non-Ferr Met 50:199-205. doi: 10.3103/S106782120903002X.

BARNARD WR, NORDSTROM DK (1982) Flouride in precipitation—II. Implications for the geochemical cycling of fluorine. Atmospheric Environment (1967) 16:105-111.

BARNES J, MANNING C, SCAMBELLURI M, SELVERSTONE J (2018) The Behavior of Halogens During Subduction-Zone Processes In: Harlov DE, Aranovich L (eds) The Role of Halogens in Terrestrial and Extraterrestrial Geochemical Processes. pp 545-590.

BASTVIKEN D, THOMSEN F, SVENSSON T, KARLSSON S, SANDÉN P, SHAW G, MATUCHA M, ÖBERG G (2007) Chloride retention in forest soil by microbial uptake and by natural chlorination of organic matter. Geochimica et Cosmochimica Acta 71:3182-3192.

BASU A, SCHREIBER ME (2013) Arsenic release from arsenopyrite weathering: insights from sequential extraction and microscopic studies. J Hazard Mater 262:896-904.

BEHNE W (1953) Untersuchungen zur Geochemie des Chlor und Brom. Geochim Cosmochim Ac 3:186-215.

BEHR H-J, GERLER J (1987) Inclusions of sedimentary brines in post-Variscan mineralizations in the Federal Republic of Germany—a study by neutron activation analysis. Chem Geol 61:65-77. doi: 10.1016/0009-2541(87)90028-3.

BISCHOFF JL, DICKSON FW (1975) Seawater-basalt interaction at 200 C and 500 bars: implications for origin of sea-floor heavy-metal deposits and regulation of seawater chemistry. Earth Planet Sc Lett 25:385-397.

BOWER C, HATCHER J (1967) Adsorption of fluoride by soils and minerals. Soil Science 103:151-154.

BRANDER T (2000) U/HE-chronologische Fallstudien an Eisen-und Manganerzen Department of Geoscience. Ruprecht-Karls University Heidelberg, pp 275.

BRIL H (1982) Fluid inclusions study of Sn− W− Au, Sb− and Pb− Zn mineralizations from the Brioude-Massiac district (French Massif Central). Tscher Miner Petrog 30:1-16. doi: 10.1007/BF01082422.

BURISCH M, MARKS MA, NOWAK M, MARKL G (2016) The effect of temperature and cataclastic deformation on the composition of upper crustal fluids—An experimental approach. Chemical Geology 433:24-35.

BURISCH M, WALTER BF, MARKL G (2017) Silicification of Hydrothermal Gangue Minerals in Pb-zn-cu-fluorite-quartz-baryte Veins. Can Mineral 55:501-514. doi: 10.3749/canmin.1700005

BURISCH M, HARTMANN A, BACH W, KROLOP P, KRAUSE J, GUTZMER J (2018) Genesis of hydrothermal silver-antimony-sulfide veins of the Bräunsdorf sector of the Freiberg District, Germany. Miner Deposita.
BURMANN F, KEIM MF, OELMANN Y, TEIBER H, MARKS MA, MARKL G (2013) The source of phosphate in the oxidation zone of ore deposits: Evidence from oxygen isotope compositions of pyromorphite. Geochimica et Cosmochimica Acta 123:427-439.
CABRAL AR, RADTKE M, MUNNIK F, LEHMANN B, REINHOLZ U, RIESEMEIER H, TUPINAMBÁ M, KWITKO-RIBEIRO R (2011) Iodine in alluvial platinum–palladium nuggets: Evidence for biogenic precious-metal fixation. Chemical Geology 281:125-132.
CHUBAR N, SAMANIDOU V, KOUTS V, GALLIOS G, KANIBOLOTSKY V, STRELKO V, ZHURAVLEV I (2005) Adsorption of fluoride, chloride, bromide, and bromate ions on a novel ion exchanger. Journal of colloid and interface science 291:67-74.
CLAYTON R, SCRIVENER R, STANLEY C (1990) Mineralogical and preliminary fluid inclusion studies of lead-antimony mineralisation in north Cornwall. Proc Ussher 7:258-262.
CORTIZAS AM, VÁZQUEZ CF, KAAL J, BIESTER H, CASAIS MC, RODRÍGUEZ TT, LADO LR (2016) Bromine accumulation in acidic black colluvial soils. Geochimica et Cosmochimica Acta 174:143-155.
DENNEN WH (1960) Principles of mineralogy. Ronald Press Company.
DILL H, WEISER T, BERNHARDT I, KILIBARDA CR (1995) The composite gold-antimony vein deposit at Kharma (Bolivia). Econ Geol 90:51-66. doi: 10.2113/gsecongeo.90.1.51
DILL HG (1993) Die Antimonvorkommen der mitteleuropäischen Alpiden und Varisziden. Zeitschrift der deutschen geologischen Gesellschaft:434-450.
DOWNS A, ADAMS C (1975) Pergamon texts in inorganic chemistry The chemistry of chlorine, bromine, iodine and astatine. Pergamon Press Oxford.
DRUMMOND S, OHMOTO H (1985) Chemical evolution and mineral deposition in boiling hydrothermal systems. Economic Geology 80:126-147.
DU J, WU D, XIAO H, LI P (2011) Adsorption of fluoride on clay minerals and their mechanisms using X-ray photoelectron spectroscopy. Frontiers of Environmental Science & Engineering in China 5:212-226.
DUCE RA, WINCHESTER JW, VAN NAHL TW (1965) Iodine, bromine, and chlorine in the Hawaiian marine atmosphere. Journal of Geophysical Research 70:1775-1799.
EATON JS, LIKENS GE, BORMANN FH (1973) Throughfall and stemflow chemistry in a northern hardwood forest. The Journal of Ecology:495-508.
EPP T, NEIDHARDT H, PAGANO N, MARKS MA, MARKL G, OELMANN Y (2020) Vegetation canopy effects on total and dissolved Cl, Br, F and I concentrations in soil and their fate along the hydrological flow path. Science of The Total Environment 712C:135473.
FLIS J, BORKIEWICZ O, BAJDA T, MANECKI M, KLASA J (2010) Synchrotron-based X-ray diffraction of the lead apatite series Pb10 (PO4) 6Cl2–Pb10 (AsO4) 6Cl2. Journal of synchrotron radiation 17:207-214.
FLIS J, MANECKI M, BAJDA T (2011) Solubility of pyromorphite Pb5 (PO4) 3Cl–mimetite Pb5 (AsO4) 3Cl solid solution series. Geochim Cosmochim Ac 75:1858-1868.
FONTBOTÉ L, KOUZMANOV K, CHIARADIA M, POKROVSKI GS (2017) Sulfide minerals in hydrothermal deposits. Elements 13:97-103.
FÖRTSCH E, WONDRATSCHEK H (1965) Zur Kristallchemie der Minerale der Pyromorphit-Gruppe. Naturwissenschaften 52:182-182.
FRAPE S, FRITZ P, MCNUTT RT (1984) Water-rock interaction and chemistry of groundwaters from the Canadian Shield. Geochim Cosmochim Ac 48:1617-1627. doi: 10.1016/0016-7037(84)90331-4.
FUGE R (1988) Sources of halogens in the environment, influences on human and animal health. Environmental Geochemistry and Health 10:51-61. doi: 10.1007/bf01758592.
FUSSWINKEL T, WAGNER T, WÄLLE M, WENZEL T, HEINRICH CA, MARKL G (2013) Fluid mixing forms basement-hosted Pb-Zn deposits: Insight from metal and halogen geochemistry of individual fluid inclusions. Geology 41:679-682. doi: 10.1130/G34092.1
GALL EA, KÜPPER FC, KLOAREG B (2004) A survey of iodine content in Laminaria digitata. Bot Mar 47:30-37.

GERZABEK MH, MURAMATSU Y, STREBL F, YOSHIDA S (1999) Iodine and bromine contents of some Austrian soils and relations to soil characteristics. Journal of plant nutrition and soil science 162:415-419.
GEYER OF, GWINNER MP, GEYER M, NITSCH E, SIMON T (2011) Geologie von Baden-Württemberg.626.
GÖB S, LOGES A, NOLDE N, BAU M, JACOB DE, MARKL G (2013) Major and trace element compositions (including REE) of mineral, thermal, mine and surface waters in SW Germany and implications for water–rock interaction. Applied Geochemistry 33:127-152. doi: https://doi.org/10.1016/j.apgeochem.2013.02.006.
GREENWOOD N, EARNSHAW A (1984) Chemistry of the Elements. Pergamon press oxford.
HÅLENIUS U, HATERT F, PASERO M, MILLS SJ (2017) New minerals and nomenclature modifications approved in 2017. Mineral Mag 81:1279-1286. doi: 10.1180/minmag.2017.081.072.
HALKA M, NORDSTROM B (2010) Periodic Table of the Elements - Halogens & Noble Gases. Facts on File Inc.
HAMMERLI J, SPANDLER C, OLIVER NHS (2016) Element redistribution and mobility during upper crustal metamorphism of metasedimentary rocks: an example from the eastern Mount Lofty Ranges, South Australia. Contrib Mineral Petrol 171:36. doi: 10.1007/s00410-016-1239-7.
HANN H, CHEN F, ZEDLER H, FRISCH W, LOESCHKE J (2003) The Rand Granite in the southern Schwarzwald and its geodynamic significance in the Variscan belt of SW Germany. Int J Earth Sci 92:821-842. doi: 10.1007/s00531-003-0361-8.
HJELM O, JOHANSSON M-B, ÖBERG-ASOLUND G (1995) Organically bound halogens in coniferous forest soil-Distribution pattern and evidence of in situ production. Chemosphere 30:2353-2364.
HOFMANN A (2003) Sampling mantle heterogeneity through oceanic basalts: isotopes and trace elements. Treatise on geochemistry 2:568.
HOLLAND G, BALLENTINE CJ (2006) Seawater subduction controls the heavy noble gas composition of the mantle. Nature 441:186.
IUSS-WORKING-GROUP-WRB (2015) World reference base for soil resources 2014-International soil classification system for naming soils and creating legends for soil maps. Food and Agriculture Organization of the United Nations, Italy, Rome, pp 203.
IWAMOTO K, SHIRAIWA Y (2012) Characterization of intracellular iodine accumulation by iodine-tolerant microalgae. Procedia Environmental Sciences 15:34-42.
JANICKA U, BAJDA T, MANECKI M (2012) Synthesis and solubility of brompyromorphite Pb5 (PO4) 3Br. Mineralogia Polonica 43:129-135.
JOHANSSON E, SANDÉN P, ÖBERG G (2003) Organic chlorine in deciduous and coniferous forest soils in southern Sweden. Soil Science 168:347-355. doi: 10.1097/01.ss.0000070909.55992.91
KABATA-PENDIAS A (2011) Trace elements in soils and plants. CRC Press.
KALT A, ALTHERR R, HANEL M (2000) The Variscan basement of the Schwarzwald. Eur J Mineral 12:1-43.
KAMENETSKY VS, EGGINS SM (2012) Systematics of metals, metalloids, and volatiles in MORB melts: effects of partial melting, crystal fractionation and degassing (a case study of Macquarie Island glasses). Chem Geol 302:76-86.
KAMPF AR, HOUSLEY RM (2011) Fluorphosphohedyphane, Ca2Pb3 (PO4) 3F, the first apatite supergroup mineral with essential Pb and F. Am Mineral 96:423-429.
KEENE WC, KHALIL MAK, ERICKSON III DJ, MCCULLOCH A, GRAEDEL TE, LOBERT JM, AUCOTT ML, GONG SL, HARPER DB, KLEIMAN G (1999) Composite global emissions of reactive chlorine from anthropogenic and natural sources: Reactive Chlorine Emissions Inventory. Journal of Geophysical Research: Atmospheres 104:8429-8440.
KEIM MF, MARKL G (2015) Weathering of galena: Mineralogical processes, hydrogeochemical fluid path modeling, and estimation of the growth rate of pyromorphite. American Mineralogist 100:1584-1594.

KENDRICK M, HÉMOND C, KAMENETSKY V, DANYUSHEVSKY L, DEVEY CW, RODEMANN T, JACKSON M, PERFIT M (2017) Seawater cycled throughout Earth's mantle in partially serpentinized lithosphere. Nature Geoscience 10:222.

KENDRICK M (2018) Halogens in Seawater, Marine Sediments and the Altered Oceanic Lithosphere In: Harlov DE, Aranovich L (eds) The Role of Halogens in Terrestrial and Extraterrestrial Geochemical Processes. Springer Geochemistry, pp 591-648.

KENDRICK MA, SCAMBELLURI M, HONDA M, PHILLIPS D (2011) High abundances of noble gas and chlorine delivered to the mantle by serpentinite subduction. Nature Geoscience 4:807-812.

KENDRICK MA, BURNARD P (2013) Noble gases and halogens in fluid inclusions: A journey through the Earth's crust The noble gases as geochemical tracers. Springer, pp 319-369.

KENDRICK MA, ARCULUS RJ, DANYUSHEVSKY LV, KAMENETSKY VS, WOODHEAD JD, HONDA M (2014) Subduction-related halogens (Cl, Br and I) and H2O in magmatic glasses from Southwest Pacific Backarc Basins. Earth Planet Sc Lett 400:165-176.

KNIPE R (1993) The Influence of Fault Zone Processes and Diagenesis on Fluid Flow Diagenesis and Basin Development.

KNYAZEV A, CHERNORUKOV N, BULANOV E (2011) Isomorphism and phase diagram of Pb5 (PO4) 3F–Pb5 (PO4) 3Cl system. Thermochim Acta 513:112-118.

KROLOP P, BURISCH M, RICHTER L, FRITZKE B, SEIFERT T (2018) Antimoniferous vein-type mineralization of the Berga Antiform, Eastern-Thuringia, Germany: A fluid inclusion study. Chem Geol. doi: 10.1016/j.chemgeo.2018.02.034.

KUMPIENE J, LAGERKVIST A, MAURICE C (2008) Stabilization of As, Cr, Cu, Pb and Zn in soil using amendments–a review. Waste management 28:215-225.

KÜPPER FC, CARPENTER LJ, LEBLANC C, TOYAMA C, UCHIDA Y, MASKREY BH, ROBINSON J, VERHAEGHE EF, MALIN G, LUTHER III GW (2013) In vivo speciation studies and antioxidant properties of bromine in Laminaria digitata reinforce the significance of iodine accumulation for kelps. J Exp Bot 64:2653-2664.

LÅG J, STEINNES E (1976) Regional distribution of halogens in Norwegian forest soils. Geoderma 16:317-325.

LE DIZÈS S, GONZE M (2019) Behavior of 36Cl in agricultural soil-plant systems: A review of transfer processes and modelling approaches. Journal of environmental radioactivity 196:82-90.

LEBLANC C, COLIN C, COSSE A, DELAGE L, LA BARRE S, MORIN P, FIÉVET B, VOISEUX C, AMBROISE Y, VERHAEGHE E (2006) Iodine transfers in the coastal marine environment: the key role of brown algae and of their vanadium-dependent haloperoxidases. Biochimie 88:1773-1785.

LENTZ DR, THORNE K, YANG X-M (2002) Preliminary analysis of the controls on the various episodes of gold mineralization at the Lake George antimony deposit, New Brunswick. Current research:02-01.

LERI AC, MYNENI SCB (2010) Organochlorine turnover in forest ecosystems: The missing link in the terrestrial chlorine cycle. Global Biogeochemical Cycles 24. doi: 10.1029/2010GB003882.

LERI AC, MYNENI SC (2012) Natural organobromine in terrestrial ecosystems. Geochim Cosmochim Ac 77:1-10.

LERI AC, RAVEL B (2015) Abiotic bromination of soil organic matter. Environmental science & technology 49:13350-13359.

LI Y-H (1991) Distribution patterns of the elements in the ocean: A synthesis. Geochim Cosmochim Ac 55:3223-3240.

LIN H (2010) Earth's Critical Zone and hydropedology: concepts, characteristics, and advances. Hydrology and Earth System Sciences 14:25.

LINSER H, SCHARRER K (1966) Handbuch der Pflanzenernährung und Düngung. Springer-Verlag.

LOGANATHAN P, LIU Q, HEDLEY M, GRAY C (2007) Chemical fractionation of fluorine in soils with a long-term phosphate fertiliser history. Soil Research 45:390-396.

LOVETT GM, LIKENS GE, BUSO DC, DRISCOLL CT, BAILEY SW (2005) The biogeochemistry of chlorine at Hubbard Brook, New Hampshire, USA. Biogeochemistry 72:191-232.
LUBW (2019) Jahreskatalog Fließgewässer 2013 - Wasser Anorganik. http://jdkfg.lubw.baden-wuerttemberg.de/servlet/is/300/ (accessed 27.05.2019)
LÜDERS V (1994) Geochemische Untersuchungen an Gangartmineralen aus dem Bergbaurevier Freiamt-Sexau und dem Badenweiler Quarzriff (Schwarzwald). Abhandlungen des Geologischen Landesamtes Baden-Württemberg 14:173-190.
MARKL G, MARKS MA, HOLZÄPFEL J, WENZEL T (2014) Major, minor, and trace element composition of pyromorphite-group minerals as recorder of supergene weathering processes from the Schwarzwald mining district, SW Germany. Am Mineral 99:1133-1146.
MARKS MA, MARSCHALL HR, SCHÜHLE P, GUTH A, WENZEL T, JACOB DE, BARTH M, MARKL G (2013) Trace element systematics of tourmaline in pegmatitic and hydrothermal systems from the Variscan Schwarzwald (Germany): the importance of major element composition, sector zoning, and fluid or melt composition. Chem Geol 344:73-90. doi: 10.1016/j.chemgeo.2013.02.025.
MCDONOUGH WF, SUN S-S (1995) The composition of the Earth. Chem Geol 120:223-253.
MCLAUGHLIN M, TILLER K, NAIDU R, STEVENS D (1996) Review: the behaviour and environmental impact of contaminants in fertilizers. Soil Research 34:1-54. doi: https://doi.org/10.1071/SR9960001.
METZ R, RICHTER M (1957) Die Blei-Zink-Erzgänge des Schwarzwaldes. Beihefte zum Geologischen Jahrbuch Beiheft 29:277.
MONTELIUS M, THIRY Y, MARANG L, RANGER J, CORNELIS J-T, SVENSSON T, BASTVIKEN D (2015) Experimental evidence of large changes in terrestrial chlorine cycling following altered tree species composition. Environmental science & technology 49:4921-4928.
MONTELIUS M, SVENSSON T, LOURINO-CABANA B, THIRY Y, BASTVIKEN D (2019) Radiotracer evidence that the rhizosphere is a hot-spot for chlorination of soil organic matter. Plant and Soil:1-13.
MURAMATSU Y, WEDEPOHL KH (1998) The distribution of iodine in the earth's crust. Chem Geol 147:201-216.
NEIVA A, ANDRÁŠ P, RAMOS J (2008) Antimony quartz and antimony–gold quartz veins from northern Portugal. Ore Geol Rev 34:533-546. doi: 10.1016/j.oregeorev.2008.03.004.
NRC N (2001) Basic Research Opportunities in Earth Sciences National Academy.
NRIAGU JO (1973) Lead orthophosphates—III. Stabilities of fluoropyromorphite and bromopyromorphite at 25° C. Geochim Cosmochim Ac 37:1735-1743.
ÖBERG G, HOLM M, SANDÉN P, SVENSSON T, PARIKKA M (2005) The Role of Organic-matter-bound Chlorine in the Chlorine Cycle: A Case Study of the Stubbetorp Catchment, Sweden. Biogeochemistry 75:241-269. doi: 10.1007/s10533-004-7259-9.
ÖBERG G, SANDÉN P (2005) Retention of chloride in soil and cycling of organic matter-bound chlorine. Hydrological Processes: An International Journal 19:2123-2136.
ÖBERG G, BASTVIKEN D (2012) Transformation of chloride to organic chlorine in terrestrial environments: variability, extent, and implications. Crit Rev Environ Sci Technol 42:2526-2545.
ORTEGA L, VINDEL E, BENY C (1991) COHN fluid inclusions associated with gold-stibnite mineralization in low-grade metamorphic rocks, Mari Rosa mine, Caceras, Spain. Mineral Mag 55:235-247. doi: 10.1180/minmag.1991.055.379.12.
PARK JR CF, MACDIARMID RA (1975) Ore deposits.
PASERO M, KAMPF AR, FERRARIS C, PEKOV IV, RAKOVAN J, WHITE TJ (2010) Nomenclature of the apatite supergroup minerals. Eur J Mineral 22:163-179.
PETERS NE (1991) Chloride cycling in two forested lake watersheds in the west-central Adirondack Mountains, New York, USA. Water, Air, and Soil Pollution 59:201-215.
PFAFF K, ROMER RL, MARKL G (2009) U-Pb ages of ferberite, chalcedony, agate,'U-mica'and pitchblende: constraints on the mineralization history of the Schwarzwald ore district. Eur J Mineral 21:817-836. doi: 10.1127/0935-1221/2009/0021-1944.
PYLE D, MATHER T (2009) Halogens in igneous processes and their fluxes to the atmosphere and oceans from volcanic activity: a review. Chem Geol 263:110-121.

REDON P-O, ABDELOUAS A, BASTVIKEN D, CECCHINI S, NICOLAS M, THIRY Y (2011) Chloride and Organic Chlorine in Forest Soils: Storage, Residence Times, And Influence of Ecological Conditions. Environmental Science & Technology 45:7202-7208. doi: 10.1021/es2011918.

REDON P-O, JOLIVET C, SABY NP, ABDELOUAS A, THIRY Y (2013) Occurrence of natural organic chlorine in soils for different land uses. Biogeochemistry 114:413-419.

REICH M, VASCONCELOS PM (2015) Geological and economic significance of supergene metal deposits. Elements 11:305-310.

REICH M, BARNES JD, BREECKER DO, BARRA F, MILOJEVIC C, DREW DL (2019) Chlorine isotope fractionation recorded in atacamite during supergene copper oxidation. Chem Geol 525:168-176.

ROULIER M, BUENO M, THIRY Y, COPPIN F, REDON P-O, LE HÉCHO I, PANNIER F (2018) Iodine distribution and cycling in a beech (Fagus sylvatica) temperate forest. Science of the Total Environment 645:431-440.

ROULIER M, COPPIN F, BUENO M, NICOLAS M, THIRY Y, DELLA VEDOVA C, FÉVRIER L, PANNIER F, LE HÉCHO I (2019) Iodine budget in forest soils: Influence of environmental conditions and soil physicochemical properties. Chemosphere.

RUPF I, NITSCH E (2008) Das geologische Landesmodell von Baden-Württemberg: Datengrundlagen, technische Umsetzung und erste geologische Ergebnisse. Landesamt für Geologie, Rohstoffe und Bergbau Baden-Württemberg.

SCHARRER M, KREISSL S, MARKL G (2019) The mineralogical variability of hydrothermal native element-arsenide (five-element) associations and the role of physicochemical and kinetic factors concerning sulfur and arsenic. Ore Geol Rev 113:103025.

SCHECKEL KG, RYAN JA, ALLEN D, LESCANO NV (2005) Determining speciation of Pb in phosphate-amended soils: Method limitations. Science of the Total Environment 350:261-272.

SCHEFFER F, SCHACHTSCHABEL P, BLUME H, HARTGE K, SCHWERTMANN U, BRÜMMER G, RENGER M (1998) Lehrbuch der Bodenkunde/Scheffer/Schachtschabel. Ferdinand Enke Verlag, Stuttgart.

SCHUMACHER ME (2002) Upper Rhine Graben: role of preexisting structures during rift evolution. Tectonics 21:6-1-6-17.

SEKI M, OIKAWA J-I, TAGUCHI T, OHNUKI T, MURAMATSU Y, SAKAMOTO K, AMACHI S (2012) Laccase-catalyzed oxidation of iodide and formation of organically bound iodine in soils. Environmental science & technology 47:390-397.

SEYFRIED JR W, BISCHOFF JL (1981) Experimental seawater-basalt interaction at 300 C, 500 bars, chemical exchange, secondary mineral formation and implications for the transport of heavy metals. Geochim Cosmochim Ac 45:135-147.

SHANNON RD (1976) Revised effective ionic radii and systematic studies of interatomic distances in halides and chalcogenides. Acta crystallographica section A: crystal physics, diffraction, theoretical and general crystallography 32:751-767.

SHERMAN DM, RAGNARSDOTTIR KV, OELKERS EH (2000) Antimony transport in hydrothermal solutions: an EXAFS study of antimony (V) complexation in alkaline sulfide and sulfide–chloride brines at temperatures from 25° C to 300° C at Psat. Chem Geol 167:161-167.

SILLITOE RH (2005) Supergene oxidized and enriched porphyry copper and related deposits. Econ Geol 100:723-768.

SPOSITO G (1984) The surface chemistry of soils. Oxford university press.

STAUDE S, WAGNER T, MARKL G (2007) Mineralogy, mineral compositions and fluid evolution at the Wenzel hydrothermal deposit, Southern Germany: Implications for the formation of Kongsberg-type silver deposits. Can Mineral 45:1147-1176. doi: 10.2113/gscanmin.45.5.1147

STAUDE S, BONS PD, MARKL G (2009) Hydrothermal vein formation by extension-driven dewatering of the middle crust: An example from SW Germany. Earth Planet Sc Lett 286:387-395. doi: 10.1016/j.epsl.2009.07.012.

STEINNES E, FRONTASYEVA MV (2002) Marine gradients of halogens in soil studied by epithermal neutron activation analysis. Journal of Radioanalytical and Nuclear Chemistry 253:173-177. doi: 10.1023/a:1015849525392.

SVERJENSKY DA (1981) The origin of a Mississippi Valley-type deposit in the Viburnum Trend, southeast Missouri. Econ Geol 76:1848-1872.
TAKEDA A, NAKAO A, YAMASAKI S-I, TSUCHIYA N (2018) Distribution and Speciation of Bromine and Iodine in Volcanic Ash Soil Profiles. Soil Science Society of America Journal 82:815-825.
TODT W (1976) Zirkon U/Pb-Alter des Malsburg-Granits vom Südschwarzwald. N Jb Min H 12:532-544.
WAGNER T, COOK N (2000) Late-Variscan antimony mineralisation in the Rheinisches Schiefergebirge, NW Germany: evidence for stibnite precipitation by drastic cooling of high-temperature fluid systems. Miner Deposita 35:206-222. doi: 10.1007/s001260050016.
WALENTA K (1957) Die antimonerzführenden Gänge des Schwarzwaldes. Jahreshefte des Geologischen Landesamtes Baden-Württemberg 2:13-67.
WALTER BF, BURISCH M, MARKL G (2016) Long-term chemical evolution and modification of continental basement brines–a field study from the Schwarzwald, SW Germany. Geofluids 16:604-623. doi: 10.1111/gfl.12167.
WALTER BF, BURISCH M, MARKS MAW, MARKL G (2017) Major element compositions of fluid inclusions from hydrothermal vein-type deposits record eroded sedimentary units in the Schwarzwald district, SW Germany. Miner Deposita 52:1191-1204. doi: 10.1007/s00126-017-0719-7.
WALTER BF, BURISCH M, FUSSWINKEL T, MARKS MAW, STEELE-MACINNIS M, WÄLLE M, APUKHTINA OB, MARKL G (2018) Multi-reservoir fluid mixing processes in rift-related hydrothermal veins, Schwarzwald, SW-Germany. J Geochem Explor 186:158-186. doi: 10.1016/j.gexplo.2017.12.004.
WANG M, YANG J-Y, HE W-Y, LI J-X, ZHU Y-Y, YANG X-E (2019) Vertical distribution of fluorine in farmland soil profiles around phosphorous chemical industry factories. Environmental Science and Pollution Research 26:855-866.
WEBSTER J, BAKER D, AIUPPA A (2018) Halogens in Mafic and Intermediate-Silica Content Magmas In: Harlov DE, Aranovich L (eds) The Role of Halogens in Terrestrial and Extraterrestrial Geochemical Processes. pp 307-430.
WEERASOORIYA R, WICKRAMARATHNA H (1999) Modeling anion adsorption on kaolinite. Journal of colloid and interface science 213:395-399.
WERNER W, FRANZKE HJ (2001) Postvariszische bis neogene Bruchtektonik und Mineralisation im südlichen Zentralschwarzwald. Zeitschrift der deutschen geologischen Gesellschaft:405-437.
WERNER W (2002) Die Erzlagerstätte Schauinsland bei Freiburg im Breisgau: Bergbau, Geologie, Hydrogeologie, Mineralogie, Geochemie, Tektonik und Lagerstättenentstehung. Aedificatio-Verlag.
WETTERKONTOR (2019) Wetterrückblick Feldberg im Schwarzwald (1486 m). https://www.wetterkontor.de/de/wetter/deutschland/rueckblick.asp?id=57&datum=13.06.2019&t=8 (accessed 21.03.2019)
WETZEL A, ALLENBACH R, ALLIA V (2003) Reactivated basement structures affecting the sedimentary facies in a tectonically “quiescent” epicontinental basin: an example from NW Switzerland. Sediment Geol 157:153-172. doi: 10.1016/S0037-0738(02)00230-0.
WHITFIELD M, TURNER D (1979) Water–rock partition coefficients and the composition of seawater and river water. Nature 278:132-137.
WIBERG E (1985) Lehrbuch der anorganischen Chemie. Walter de Gruyter GmbH & Co KG.
WILSON T (1975) Salinity and the major elements of seawater, Chemical Oceanography, 1 JP Riley, G. Skirrow, Academic, San Diego, Calif.
WONDRATSCHEK H (1963) Untersuchungen zur Kristallchemie der Blei-Apatite (Pyromorphite). Neues Jahrbuch für Mineralogie Abhandlungen 99:113-160.
WONG G, BREWER P (1974) Determination and distribution of Iodate in South-Atlantic waters. J Mar Res 32:25-36.
WOOD SA, CRERAR DA, BORCSIK MP (1987) Solubility of the assemblage pyrite-pyrrhotite-magnetite-sphalerite-galena-gold-stibnite-bismuthinite-argen-tite-molybdenite in H 2

O-NaCl-CO 2 solutions from 200 degrees to 350 degrees C degrees. Econ Geol 82:1864-1887. doi: 10.2113/gsecongeo.82.7.1864

WORDEN R (2018) Halogen Elements in Sedimentary Systems and Their Evolution During Diagenesis In: Harlov DE, Aranovich L (eds) The Role of Halogens in Terrestrial and Extraterrestrial Geochemical Processes. pp 185-260.

YARDLEY BW (2005) 100th Anniversary Special Paper: metal concentrations in crustal fluids and their relationship to ore formation. Econ Geol 100:613-632. doi: 10.2113/gsecongeo.100.4.613.

ZHAI W, SUN X, YI J, ZHANG X, MO R, ZHOU F, WEI H, ZENG Q (2014) Geology, geochemistry, and genesis of orogenic gold–antimony mineralization in the Himalayan Orogen, South Tibet, China. Ore Geol Rev 58:68-90.

ZHU C, SVERJENSKY DA (1991) Partitioning of F-Cl-OH between minerals and hydrothermal fluids. Geochim Cosmochim Ac 55:1837-1858.

ZIEGLER PA (1992) European Cenozoic rift system. Tectonophysics 208:91-111. doi: 10.1016/0040-1951(92)90338-7.

Appendix I

Study A

Epp, T., Walter, B. F., Scharrer, M., Lehmann, G., Henze, K., Heimgärtner, C., Bach, W. & Markl, G. (2019). Quartz veins with associated Sb-Pb-Ag±Au mineralization in the Schwarzwald, SW Germany: a record of metamorphic cooling, tectonic rifting, and element remobilization processes in the Variscan belt. Mineralium Deposita, 54(2), 281-306.

Accepted and published
DOI: 10.1007/s00126-018-0855-8
Number of authors: 8
Author position: 1

Mineralium Deposita
https://doi.org/10.1007/s00126-018-0855-8

ARTICLE

Quartz veins with associated Sb-Pb-Ag±Au mineralization in the Schwarzwald, SW Germany: a record of metamorphic cooling, tectonic rifting, and element remobilization processes in the Variscan belt

T. Epp[1] · B. F. Walter[1] · M. Scharrer[1] · G. Lehmann[1] · K. Henze[1] · C. Heimgärtner[1] · W. Bach[2] · G. Markl[1]

Received: 3 May 2018 / Accepted: 1 November 2018

Abstract

A combination of textural observations from 38 Permian Sb-Pb-Ag±Au-bearing quartz veins in the Schwarzwald (SW Germany) with isotopic, fluid inclusion, and geochemical data allows to refine genetic models for this common type of mineralization, to understand the origin of mineralogical diversity and the correlation with large scale tectonic events. Textures record four main mineralization stages: (I) Fe-As(-Sb±Au), (II) Pb-Zn-Cu, (III) Pb-Sb, and (IV) Ag-Sb. Stage I sulfides, dominated by pyrite and arsenopyrite, formed due to cooling of low-salinity metamorphic fluids during the Permian with maximum homogenization temperatures of 400 °C. Invisible gold in arsenopyrite, pyrite, marcasite, and stibnite was remobilized and locally precipitated as electrum at the end of stage I. Minerals of stages II and III comprise a rich diversity of Sb-bearing sulfosalts including, e.g., bournonite, zinkenite, and jamesonite. This assemblage formed during Jurassic times due to mixing of high-salinity, mid- and upper-crustal fluids (up to 27 wt% NaCl+$CaCl_2$) with homogenization temperatures between 50 and 250 °C. Stage III is marked by a rich variety of Pb-Sb sulfosalts. Its local abundance is directly related to the presence of stage I mineralization and its extent of remobilization during a significant influx of Pb in the Jurassic-Cretaceous. The formation of the Upper Rhine Graben during the Tertiary reactivated especially NE-SW-oriented veins. Percolating Ag-rich fluids reacted with earlier stage III Pb-Sb sulfosalts forming Ag-rich minerals (stage IV) such as miargyrite, pyrargyrite, and stephanite. The transition from metamorphic fluids to basinal, saline (e.g., Pb-bearing) brines over hundreds of millions of years as is shown in this study and present in other Variscan occurrences indicates a possibly typical poly-stage characteristic of Sb deposits worldwide, which has, however, not been investigated in detail so far.

Keywords Stibnite · Gold · Remobilization · Fluid cooling · Fluid mixing

Introduction

Shear zone-hosted, mesothermal (Au-)Sb vein deposits are arguably the most important source for Sb. Such Sb deposits occur worldwide and comprise either monotonous stibnite deposits (e.g., Lake George deposit, Canada, Lentz et al. 2002; Sentachan and Sarylakh deposits, Russian Federation, Baltukhaev and Solozhenkin 2009; Schwarz-Schampera 2014) or polymetallic Sb-(Pb-Ag±Au-W-Sn-As-Zn) deposits (e.g., Dúrico-Beirã region, Portugal, Neiva et al. 2008; Bournac deposit, France, Munoz and Shepherd 1987). The quartz vein associated with Sb-Pb-Ag±Au deposit type is common in Europe, where it is strongly associated with the Variscan Orogen. Examples of former (more or less) important European mining districts are Rheinisches Schiefergebirge,

Editorial handling: J. Gutzmer

Electronic supplementary material The online version of this article (https://doi.org/10.1007/s00126-018-0855-8) contains supplementary material, which is available to authorized users.

✉ T. Epp
tatjana.epp@uni-tuebingen.de

[1] Department of Geosciences, Eberhard Karls University Tübingen, Wilhelmstraße 56, 72074 Tübingen, Germany

[2] Department of Geosciences, University of Bremen, Klagenfurter Straße 4, 28359 Bremen, Germany

Published online: 21 November 2018

Harz, Schwarzwald, and Erzgebirge in Germany, Massif Central and Vosges mountains (France), Lombardy, Piemont, and Sardinia (Italy), and some regions in Slovakia, Czech Republic, Spain, Portugal, Austria, and Great Britain (e.g., Walenta 1957; Clayton et al. 1990; Ortega et al. 1991; Munoz et al. 1992; Dill 1993; Wagner and Cook 2000; Cidu et al. 2014; Burisch et al. 2018, this issue).

Previous studies dealt with the structural history and fluid evolution in the context of the Variscan Orogen of Sb(±Au)-quartz veins (Behr et al. 1984; Matte 1991; Schroyen and Muchez 2000; Kroner and Romer 2013; Chicharro et al. 2016). These studies clearly relate these veins to late-Orogenic, post-compressive brittle tectonic events which explains why they are commonly situated within late-Variscan extensional shear zones (Bril 1982; Munoz et al. 1992; Ortega and Vindel 1995; Wagner and Cook 2000). They formed during the transition from the Variscan compressive stress regime to post-Variscan strike slip tectonics (Arthaud and Matte 1977; Malavieille et al. 1990; Doblas et al. 1994; Wagner and Cook 2000). Several models have been proposed for stibnite precipitation in these vein-type deposits of the European Variscan belt and these comprise convective fluid cooling (Bril and Beaufort 1989; Munoz et al. 1992), segregation of H_2O-NaCl-CO_2-CH_4-N_2 fluids (Clayton et al. 1990; Ortega et al. 1991; Ortega and Vindel 1995), fluid boiling (Ortega et al. 1991), and dilution of CO_2-rich metamorphic fluids by near-surface H_2O-NaCl fluids (Bril 1982; Boiron et al. 1990; Couto et al. 1990). It is, however, generally assumed that the precipitation process is dominantly triggered by fluid cooling, either conductively or by fluid mixing with a low temperature fluid (Wagner and Cook 2000). The salinity of the hydrothermal fluid has no apparent influence on the solubility and the precipitation, because, in contrast to Pb and Ag, which are mostly transported as Cl complexes in hydrothermal solutions, the dominant Sb species in reduced hydrothermal fluids presumably is $Sb(OH)_3$ (Wood et al. 1987). However, the common polystadial mineral assemblage is generally not considered when these formation mechanisms were proposed and is therefore investigated more in detail in this study. Furthermore, this study comprehensively investigates the details of ore mineral associations and their evolution over a 300-Ma time span, using 38 localities in the Schwarzwald, a well-known mining district in the Variscan Orogen. Interestingly, the otherwise spatially separated Sb-Ag-sulfide and Sb-sulfide assemblages typical of such veins (Burisch et al. 2018, this issue) are intimately intergrown in the localities investigated in the Schwarzwald. The careful textural analysis of these ores sheds further light on the temporal evolution and major formation mechanisms of four distinct mineralization stages. Stages I and II do not only occur in the Variscan Orogen but worldwide (e.g., Guillemette and Williams-Jones 1993; Dill et al. 1995; Baltukhaev and Solozhenkin 2009). Due to the similarities between this mineralization type in Europe and other worldwide Sb-Au localities, the process of formation investigated in this study is pertinent also to larger, economically significant deposits.

Geological setting

The Schwarzwald in SW Germany (Fig. 1 and ESM Table 1) is part of the Central European Variscan Orogen and dominated by partially migmatized ortho- and paragneisses (Kalt et al. 2000). Variscan crystalline basement units are separated by the Baden-Baden-Zone (BBZ) in the north and the Badenweiler-Lenzkirch-Zone (BLZ) in the south, containing metamorphosed greywackes and conglomerates. The metamorphic rock units were intruded by post-collisional granites between 335 and 315 Ma (e.g., Todt 1976; Altherr et al. 2000; Hann et al. 2003). This crystalline basement was then covered by a Palaeozoic and Mesozoic sedimentary sequence on top of a prominent erosion surface of Permian age (Geyer et al. 2011 and references therein). During the Middle Triassic (Muschelkalk), limestones, shales, and evaporites (carbonates, anhydrite, gypsum and halite; Geyer et al. 2011) were deposited. Clastic and gypsum-bearing sediments followed during the Upper Triassic (Keuper) and further carbonates and shales were deposited during the Jurassic (Geyer et al. 2011). Cretaceous sedimentary rocks are lacking in the region. Since the initiation of rifting in the Upper Rhine Graben and the uplift of the Schwarzwald, Paleogene to Quaternary sediments of up to 4000 m thickness filled the graben structure, including Oligocene halite-sylvite-bearing evaporites, anhydrite, gypsum, and organic-rich claystones (Geyer et al. 2011).

Peaks of hydrothermal activity in the Schwarzwald

In general, most hydrothermal mineralizations in the Schwarzwald are hosted by veins. Most veins are gneiss-hosted, due to pre-existing deep tectonic fault patterns, which, in case of reactivation, offer sufficient pathways for fluid circulation (Knipe 1993; Werner and Franzke 2001). Repeated Permian and Tertiary volcanic activity and the ongoing basement subsidence during the Jurassic due to far-field effects of the opening of the North Atlantic promoted hydrothermal activity and the formation of mineralized veins (e.g., Wetzel et al. 2003; Staude et al. 2007, 2009, 2010a; Walter et al. 2016, 2017, 2018a). Numerous aspects of fluid flow and hydrothermal vein formation in the Schwarzwald are well documented in the published literature: this includes studies on fluid inclusion microthermometry (e.g., Behr and Gerler 1987; Staude et al. 2009; Walter et al. 2015), stable and

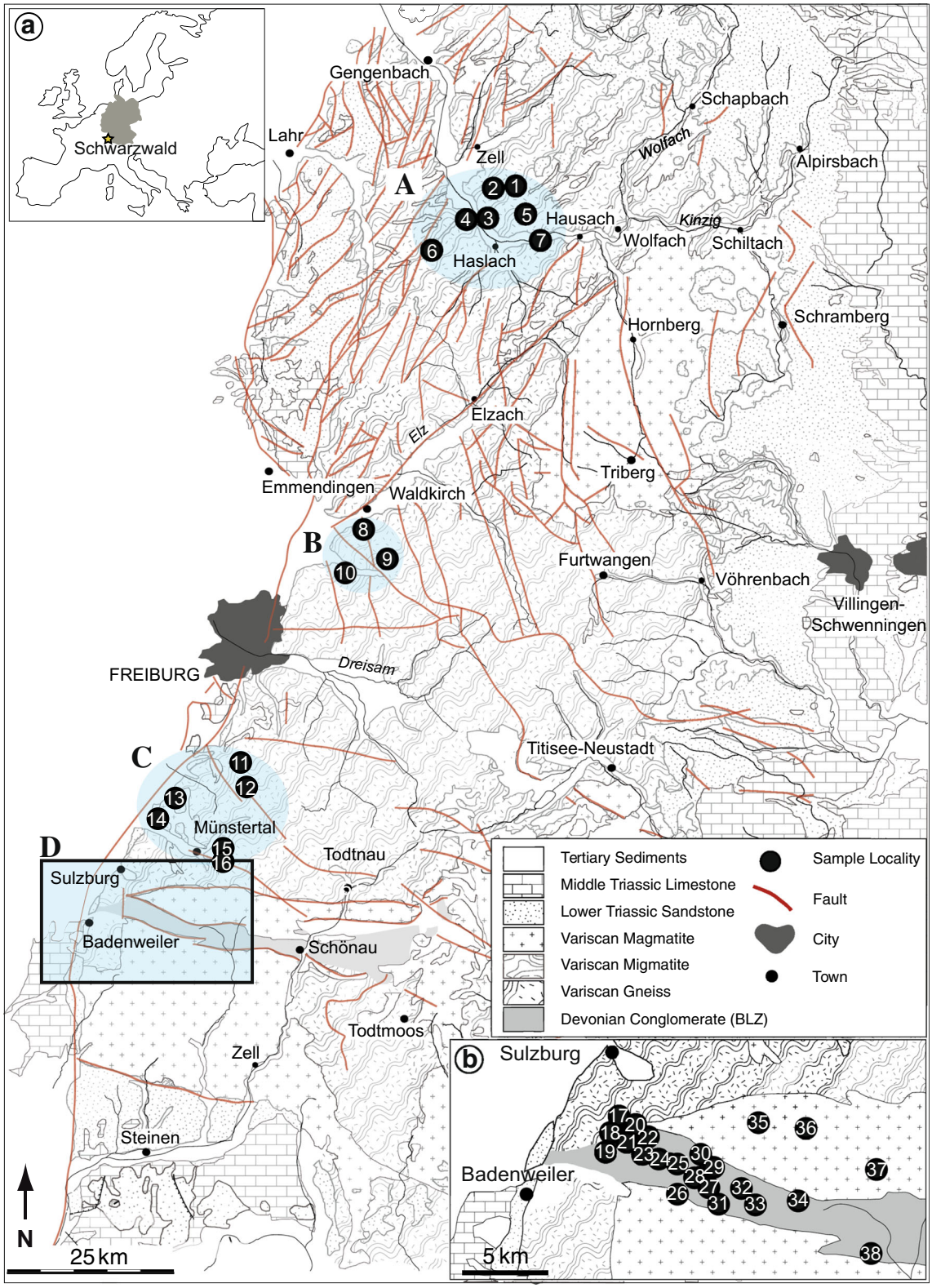

Fig. 1 **a** Geological overview of the Schwarzwald (SW Germany). The blue fields mark regions of quartz veins with associated Sb-Ag-Au mineralization in the Schwarzwald: (A) Kinzigtal, (B) Freiburg, (C) Münstertal, and (D) Badenweiler & Bad Sulzburg. **b** Close-up of area D, the Badenweiler-Lenzkirch-Zone (BLZ). Sample localities 1–38 (for more information refer to ESM Table 1). Map modified after Pfaff et al. (2011)

radiogenic isotopes of O, C, H, S, Sr, Pb, Cu, Fe, and Mg (Staude et al. 2010b; Walter et al. 2015), paleo- and modern fluid models and aquifer data (e.g., Stober and Bucher 1999; Pfaff et al. 2010; Bons et al. 2014; Walter et al. 2016), leaching experiments on basement and cover rocks (Bucher and Stober 2002; Burisch et al. 2016), and regional geological setting (Geyer et al. 2011). This comprehensive knowledge provides a suitable framework to decipher the complex history of vein-type Sb-quartz mineralization.

Hydrothermal veins in the Variscan crystalline basement formed continuously between about 310 Ma and today, but certain peaks in hydrothermal activity exist (e.g., Pfaff et al. 2009; Staude et al. 2009; Walter et al. 2016). Five formation stages are distinguished based on structural, mineralogical, and microthermometric arguments (e.g., Behr and Gerler 1987; Pfaff et al. 2009; Staude et al. 2009; Walter et al. 2016); these are in accordance with observations from other central European districts (e.g., Bril 1982; Chovan et al. 1995; Krolop et al. 2018; Burisch et al. 2018, this issue):

1. Late Carboniferous quartz-tourmaline veins with small amounts of wolframite, scheelite, and cassiterite precipitated from magmatic low-salinity fluids (< 4.5 wt%, up to 550 °C; Marks et al. 2013; Walter et al. 2016).
2. Permian Sb±Ag±Au-bearing quartz veins (277.6 Ma; Walter et al. 2018c, submitted) precipitated from a low-salinity, high-temperature (up to 440 °C) late-Variscan metamorphic basement fluid (Wagner and Cook 2000; Baatartsogt et al. 2007; Staude et al. 2009). This is the group the current contribution is concerned with.
3. Triassic-Jurassic quartz-hematite±barite veins precipitated from medium temperature, high- and low-salinity fluids (Brander 2000; Walter et al. 2016).
4. Jurassic-Cretaceous veins with variable amounts of fluorite, barite, quartz, and carbonates. This complex mineralization type contains either Ag-Bi-Co-Ni-U, Fe-Mn, or Pb-Zn-Cu ores. In contrast to (1)–(3), a deep-seated highly saline brine (20–28 wt% NaCl+$CaCl_2$) was mobilized and precipitation occurred due to binary fluid mixing between deep-seated and shallow brines (e.g., Metz and Richter 1957; Meyer et al. 2000; Werner 2002; Pfaff et al. 2009; Staude et al. 2010a; Walter et al. 2015). Moreover, the formation of fractures in this stage was probably linked to far-field effects from the opening of the North Atlantic (Wetzel et al. 2003; Pfaff et al. 2009; Staude et al. 2009).
5. Post-Cretaceous veins with variable amounts of barite, quartz, fluorite, and carbonates, which were mainly associated with Pb and less commonly Zn and Ag mineralization (Staude et al. 2009), showing large mineralogical and fluid compositional heterogeneities (1–23 wt% NaCl+$CaCl_2$) (Walter et al. 2015, 2016).

Sample description

The following sections give an overview of the local geological setting and also shortly introduce different occurring vein types in the investigated area. Furthermore, the sample locations and a detailed petrographic description were given.

Local geological setting

Antimony-bearing veins in the Schwarzwald exclusively occur in crystalline basement rocks and meta-conglomerates. Currently, the Clara barite-fluorite mine (ESM Table 1) is the only ore deposit exploited in the Schwarzwald, whereas most of our sampling sites were mined during medieval and early modern times (800 AC to 17th century; Dennert 1993). From 17th to the 20th century, minor exploitation took place but ended in the middle of the 20th century (Dennert 1993). Based on field evidence, the veins investigated in this study can be divided into three groups:

1. Veins of the areas A–C (Fig. 1) are a few centimeters to 1 m thick and consist of several massive quartz generations of various crystal sizes with minor amounts of ore minerals. The (outcropping) length of these veins varies between tens and hundreds of meters, and in rare cases (such as the Baberast locality), the mineralized structure can be traced for up to 3 km. The strike orientation is bimodal, either NW-SE or NE-SW, and the dip is near vertical (see ESM Table 1). In direct contact to the veins, the host rock is strongly silicified and host rock clasts are commonly embedded. Bleached zones around the sampled veins are commonly observed in the field and pyrite impregnation of the host rock is typical. Small occurrences of this vein type are located in the vicinity of the Elztal fault in the central Schwarzwald, the Kinzigtal area (area A, Fig. 1), and the area around Freiburg (area B, Fig. 1). Paragneisses, migmatites, and rarely granites are the host rocks in this region (see Fig. 1 and ESM Table 1).
2. The up to 1-m-thick Segen Gottes vein in the Kinzigtal area (area A, Fig. 1) takes a special position, as it comprises various vein generations of different gangue minerals. The (15 cm thick) Sb-bearing quartz veins (identical to group 1, see above) are locally brecciated and the clasts are cemented by successive fluorite-barite-bearing assemblages.
3. The veins of area D (Fig. 1) are part of the longest Sb-bearing mineralized zone in the Schwarzwald, ranging from the Holderpfad in the west to the Kälbelescheuer in the east. The whole set of structures comprises a total length of 5 km. Generally, the veins have a NW-SE-striking orientation and are frequently displaced by Upper Rhine Graben-parallel faults (Markl 2017). The

mineralogy of the veins changes from east to west. In the east, veins with Fe-As-Zn-Cu-bearing assemblages (i.e., arsenopyrite, marcasite, pyrite, sphalerite, chalcopyrite) dominate, whereas in the west, the assemblage is dominated by more Pb-Sb-rich minerals including stibnite, zinkenite, jamesonite, boulangerite, fülöppite, and semseyite. Interestingly, Cu-rich Sb sulfosalts such as chalcostibite and meneghinite and Ag-bearing andorite only occur in the central and western part; bournonite becomes progressively more common towards the east. The minerals contain invisible gold (see below), and one grain of native gold/electrum was found in the central part of the zone. In the same area (particularly in the central and eastern part), a gold-enriched zone (reaching up to 5 ppm in some outcrops) with small native gold-bearing quartz veinlets (together with pyrite/marcasite, galena, sphalerite, arsenopyrite) strikes subparallel to the Sb-bearing quartz veins. Both gold-bearing vein systems are about 200 m apart from each other and can be traced over a few kilometers between Bad Sulzburg and Weiherkopf/Münsterhalden. The conspicuous co-occurrence of the Sb-dominated and the Au-rich mineralization is considered in the present study.

Sample locations and petrographic observations

For this study, 148 representative samples from 38 veins, including both recently sampled and collection specimens, were investigated (Fig. 1 and ESM Table 1). The samples were chosen for their representative character (e.g., textures, mineralogy, structural position in the host rocks, and crystal size for fluid inclusions and isotopes). A specific focus was placed on the eastern Sulzburg Sb-veins in the BLZ (group 3, area D, Fig. 1), hosted by Devonian meta-conglomerates. In this area, the Sb-Au mineralization is found over a large area (about 20 by 5 to 10 km).

Petrographic description

Tangible petrographic attributes of the studied Sb-Pb-Ag±Au-quartz veins are collated below:

Not all investigated veins display the entire paragenetic sequence in samples. Therefore, the detailed petrographic description of the vein mineralogy focuses on veins and samples that show the most complete mineralogical succession to produce a generalized paragenetic scheme (Fig. 2). The detailed mineral assemblage of all investigated localities is reported in ESM Table 1.

In general, the evolution of the veins can, by combining the variable mineral sequence of all veins, be classified into four successive mineralization stages, according to mineral assemblages and textural relations:

Stage I: Fe-As (-Sb±Au) mineralization
Stage II: Pb-Zn-Cu mineralization
Stage III: Pb-Sb mineralization
Stage IV: Ag-Sb mineralization

Stage I was found at all localities, whereas stage II was identified only very locally. Stages III and IV are, in contrast, rather dominant. Quartz, either gray and coarse-grained (quartz I) or white and microcrystalline (quartz II–V, ESM 3a), is the dominant gangue mineral throughout. The ore minerals are intergrown with or grown into voids within the quartz. Locally, lath-shaped pyrrhotite crystals initiate mineralization stage I; these are followed by euhedral Au-bearing arsenopyrite, pyrite, and marcasite (Fig. 3a, b), which form aggregates in quartz I (Fig. 3a, b and ESM 3 1a-c) and often show porous grain surfaces. This association is followed by a succession of berthierite, stibnite (Fig. 3c), and electrum. Electrum (with a maximum diameter of 24 μm) is present as small inclusions in minerals of stage II or around marcasite (Figs. 3b, d and 4d–f). Some samples show that electrum is partially dissolved due to weathering. At the end of this stage, calcite occurs in minor quantities, surrounding stibnite and, at few localities, electrum. Numerous sub-generations of barren, white microcrystalline quartz are recognized.

Stage II is typically initiated by tetrahedrite (I) and galena (I), followed by chalcopyrite and sphalerite (I) (Fig. 3d–f and ESM 3 1d-f). Small electrum grains or stibnite (stage I) are locally found as inclusions in tetrahedrite (I) (Fig. 3d, e). Tetrahedrite I may also be replaced by tetrahedrite II (Fig. 4d, f) and is often very porous. Galena (I) is less abundant in stage II but occurs as anhedral masses (ESM 3 1d) or tiny inclusions in chalcopyrite, sphalerite, or tetrahedrite (freibergite) II. Sphalerite (I) commonly appears as reddish to brownish anhedral crystals (ESM 3 1e). Stage II is predominantly accompanied by fine crystalline quartz.

More variable and complex Sb mineralization marks mineralization stage III. The whole mineral succession was not observed (and is probably not present) at any of the sampling sites. The stage typically commences with the crystallization of bournonite ($PbCuSbS_3$), locally needle-shaped zinkenite ($Pb_9Sb_{22}S_{42}$) which is mostly pseudomorph after stibnite (stage I, Fig. 4a), and jamesonite ($Pb_4FeSb_6S_{14}$). This is followed by the crystallization of andorite ($AgPbSb_3S_6$) and chalcostibite ($CuSbS_2$), which is intergrown with zinkenite and partly replaced by meneghinite ($Pb_{13}CuSb_7S_{24}$). Boulangerite ($Pb_5Sb_4S_{11}$) replaces zinkenite and locally fizélyite ($Pb_{14}Ag_5Sb_{21}S_{48}$) was observed, replacing andorite. Fülöppite ($Pb_3Sb_8S_{15}$) replaces stibnite and is replaced by

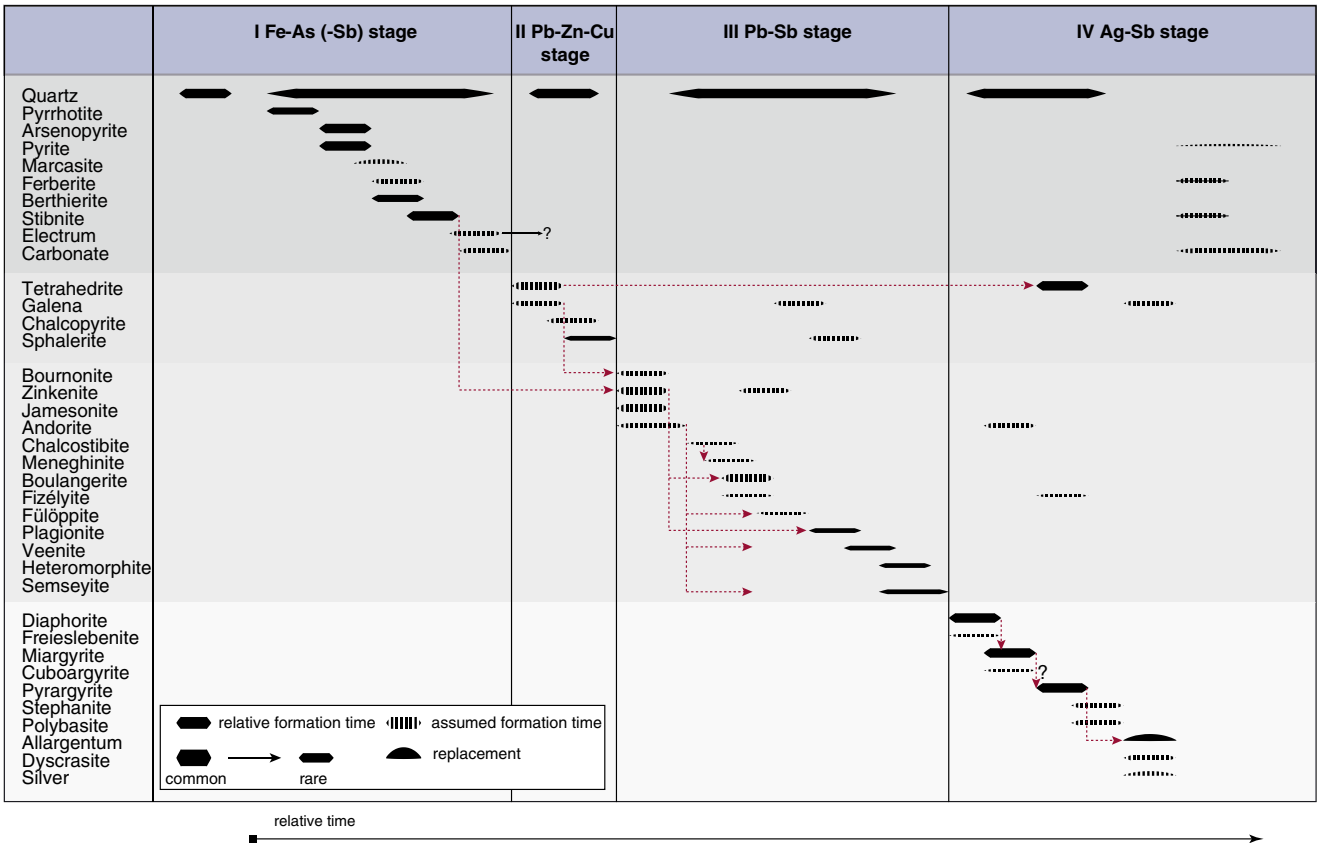

Fig. 2 Paragenetic sequence of all studied Sb-Ag±Au-quartz mineralization in the Schwarzwald with four mineralization stages. Note, not every vein shows the complete sequence. Various gray shades separate different mineralization stages (I to IV). Red dashed arrows indicate replacement reactions

plagionite ($Pb_5Sb_8S_{17}$), which in turn is replaced by veenite ($Pb_2(Sb,As)_2S_5$). Heteromorphite ($Pb_7Sb_8S_{18}$) and semseyite ($Pb_9Sb_8S_{21}$) mark the end of this stage (Fig. 4b). Distinctive replacement reactions between these minerals are common (Figs. 2 and 4a, b). During this stage, quartz is the only gangue mineral.

The silver-dominated assemblage of mineralization stage IV starts with the crystallization of diaphorite ($Pb_2Ag_3Sb_3S_8$) (Fig. 4 d) and freieslebenite ($AgPbSbS_3$). Subsequently, miargyrite ($AgSbS_2$) (ESM 3 2c-e), cuboargyrite ($AgSbS_2$), and pyrargyrite (Ag_3SbS_3) (Fig. 4c, d) form due to variable replacement reactions (i.e., diaphorite ➔ miargyrite, miargyrite ➔ pyrargyrite, tetrahedrite I (stage II) ➔ tetrahedrite/freibergite II (stage IV, Figs. 3f and 4d), pyrargyrite ➔ allargentum, Fig. 4c): pyrargyrite grows around miargyrite, tetrahedrite (II, freibergite) replaces tetrahedrite (I) from stage II and contains inclusions of miargyrite, chalcopyrite, and galena. Furthermore, jamesonite (stage III) grains are enclosed by tetrahedrite II (stage IV). These replacement textures show clearly that Pb-Sb-dominated minerals of stages II and III are replaced by Ag-Sb-rich minerals of stage IV. Stage IV ends with the precipitation of stephanite (Ag_5SbS_4), polybasite ($(Ag,Cu)_{16}Sb_2S_{11}$), allargentum ((Ag,Sb), Fig. 4c), dyscrasite (Ag_3Sb), and native silver (ESM 3 2f). Transparent quartz with pyrite II, berthierite II, and stibnite II is overgrown by a sequence of calcite, ankerite, and less frequently very late quartz during stage IV.

The petrography of the Au-rich impregnations and disseminations near Bad Sulzburg were considered separately, since these form no macroscopically distinct mineralization but occur rather as microscopic veinlets. However, the mineralogy of these veinlets is the same as the stage I mineralization of the Sb-Pb-Ag±Au-quartz veins (described above) and thus are assumed to have formed contemporaneously. Gold grains contain a significant amount of Ag and are, therefore, referred to as electrum. Generally, two associations of electrum with sulfides are observed (Fig. 4e, f; see also Krützfeldt 1985). The first association shows electrum either in pores/free space of weathered pyrite and/or quartz or on altered and silicified host rock minerals (e.g., feldspar, clay minerals, iron (hydro-) oxide mixture, Fig. 4e). This association was found at the Weiherkopf southeast of Bad Sulzburg and is interpreted to be of supergene origin, formed during oxidation of Au-bearing pyrite. Grain sizes of electrum range between 0.2 and 0.6 mm. The second association, found in the Felsengrund southeast of Bad Sulzburg, shows primary, hydrothermally formed electrum within sulfides (especially galena and marcasite) in quartz veinlets (Fig. 4f). Late barite is a

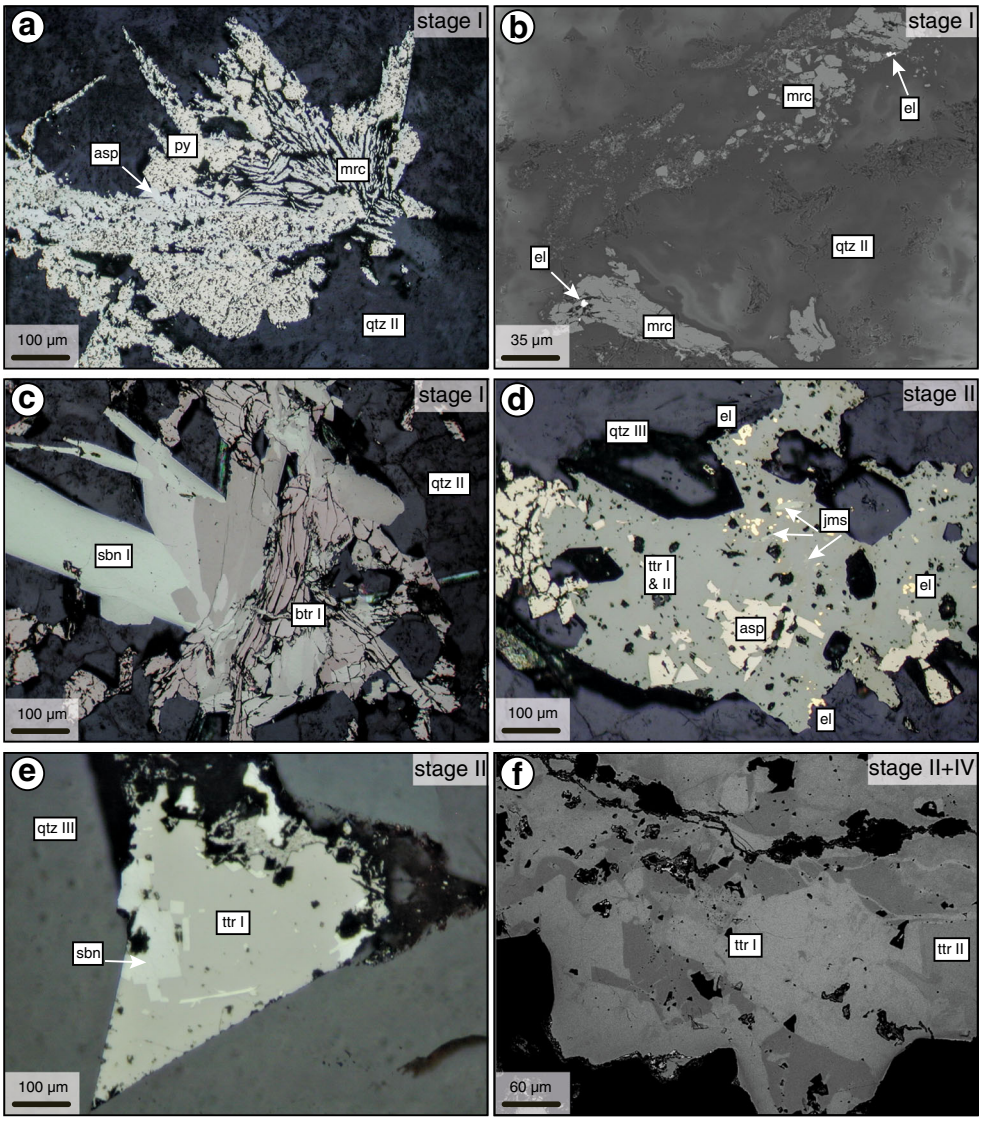

Fig. 3 Photomicrographs illustrating typical relations between ore minerals. RL - reflected light microscopy; BSE - backscattered electron images. **a** RL image in oil illustrating the association of arsenopyrite, pyrite, and marcasite, which replaces pyrrhotite; Artenberg, GL-Ar4. **b** BSE image of marcasite with electrum grains enclosed in quartz II; Segen Gottes, GL-Sg1. **c** RL image in oil berthierite I overgrown by stibnite I in quartz II; Goldengründle, GL-Go1. **d** RL image in oil of quartz III-hosted tetrahedrite I and II with inclusions of arsenopyrite, electrum and jamesonite; Hornbühl, GL-Ho1. **e** RL image in oil of quartz III-hosted tetrahedrite I with numerous stibnite inclusions; Münstergrund, GL-Mü3. **f** BSE image of tetrahedrite I which is replaced by tetrahedrite II (high contrast); Flammeck, TE-FE01E

rare member of this assemblage. Electrum from the other investigated veins in the Schwarzwald is either associated with altered marcasite, which fits with the first association of the Sulzburg veinlets, or occurs as inclusions in sulfides, mainly in tetrahedrite I and II of stage II.

Methods

Electron microprobe analysis

The chemical composition of the ore minerals was determined using a JEOL Superprobe JXA-8900RL at the University of Tübingen. Acceleration voltage of the focused beam was 25 kV at a beam current of 20 nA. Counting times for major elements were 16 s for the element peak and 8 s for each background and for minor elements 30 and 15 s, respectively. A detailed description of the method, detection limits (2σ) and standard deviation are provided in ESM 5.

Fluid inclusion analyses by optical, IR, CL microscopy, and micro-Raman

Relative chronological sequences of fluid inclusions (fluid inclusion assemblages (FIAs)) after Goldstein and Reynolds (1994) were investigated by optical microscopy. A "hot cathode" CL microscope (type HC1–LM) with an acceleration voltage of 14 kV and a beam current density of ~ 9 µA mm^{-2} on the sample surface was applied at the University of Tübingen to retain additional information on the fluid inclusion petrography (Kolchugin et al. 2016).

Microthermometric investigations on quartz were performed using a Linkham (THMS 600) fluid inclusion stage on a Leica DMLP microscope with an optical CCD camera at the University of Tübingen. For the analysis of fluid inclusions in

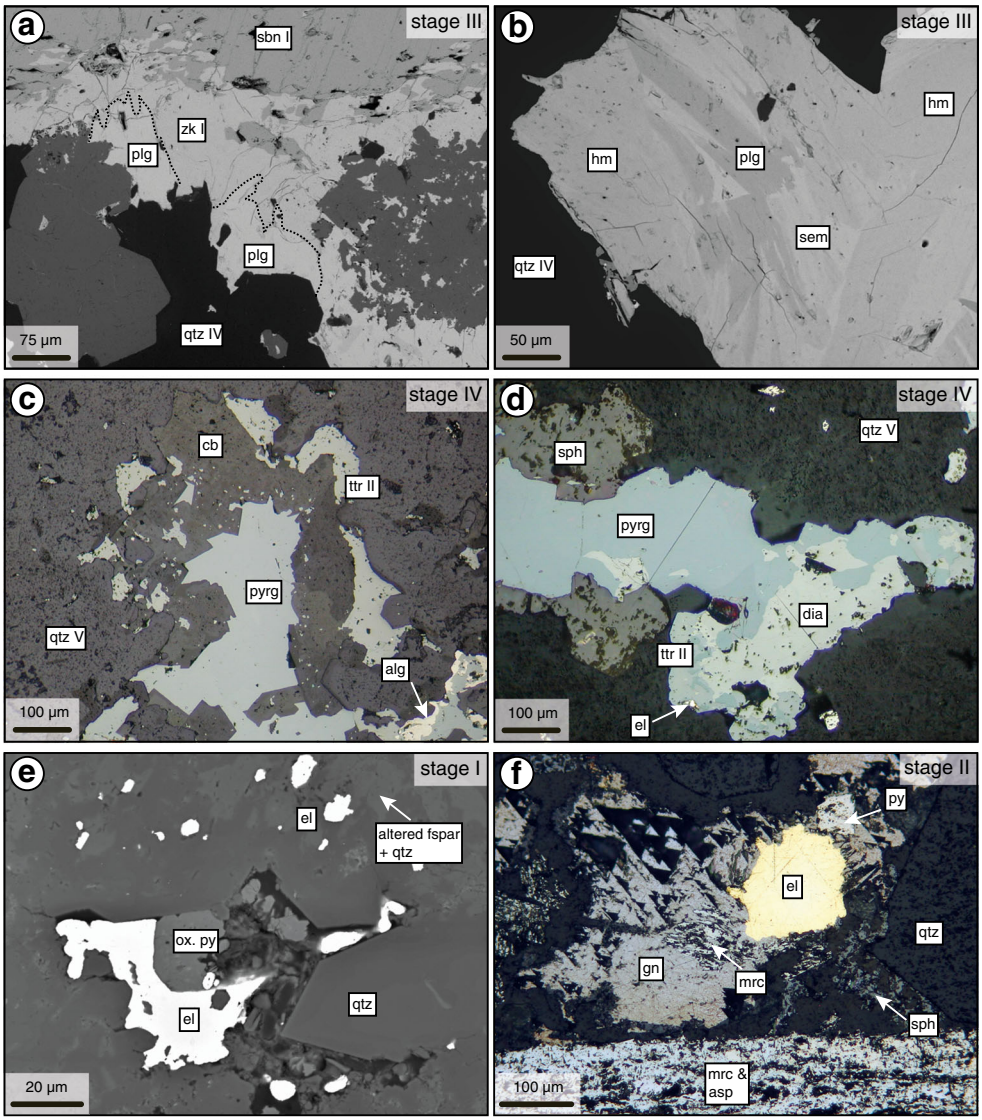

Fig. 4 Photomicrographs illustrating typical relations between ore minerals. RL - reflected light microscopy; BSE - backscattered electron images. **a** BSE image of stibnite replaced by zinkenite I, which is then replaced by plagionite. Black dashed lines show the grain boundaries between zinkenite and plagionite; Ludwig, GL-Lu8. **b** BSE image of plagionite overgrown by co-genetic heteromorphite and semseyite, accompanied by quartz IV; Hornbühl, GL-Ho4. **c** RL image in oil of tetrahedrite (freibergite) II in a quartz V void. Carbonate and pyrargyrite initially grew co-genetically, pyrargyrite precipitated later. Allargentum partly replaces pyrargyrite; Baberast, GL-Ba2. **d** RL image in oil of diaphorite replaced by pyrargyrite and tetrahedrite (freibergite) II with electrum inclusions and overgrown by sphalerite; Barbara, GL-Br2. **e** BSE image of electrum on oxidized pyrite in quartz and altered feldspar; Weiherkopf, CH-70. **f** RL image of a large electrum grain associated with galena and marcasite, pyrite, and sphalerite but mostly overgrown by galena; Felsenloch, CH-54

sphalerite and stibnite, the same setup with an IR camera Retiga 2000R (λ up to 1000 µm) was used at the TU Bergakademie Freiberg. For each inclusion, the ice melting temperature (T_m, ice), the hydrohalite melting temperature (T_m, hh), and the homogenization temperature (T_h) were measured.

For the calculation of salinity in the ternary NaCl-$CaCl_2$-H_2O system, the Excel-based program of Steele-MacInnis et al. (2011) was used. Pressure correction was done using the program HOKIEFLINCS_H2O-NACL (Steele-MacInnis et al. 2012) in combination with estimates on basement and sedimentary overburden based on Geyer et al. (2011 and references therein). A maximum overburden of 1000 m, corresponding to 300 bar, was estimated. For the correction of the homogenization temperature, this maximum pressure results in maximum temperature differences of + 45 °C, the median of all analyses being 15 °C. Further interpretation was done with the raw data to avoid estimation errors. The uncertainties of this approach are discussed by Walter et al. (2015).

Micro-Raman measurements were conducted using a confocal Raman spectrometer Renishaw InVia Reflex at the University of Tübingen. A laser wavelength of 532 nm, with a laser output of 50%, was a numerical aperture of 0.55 and an opening angle of 66.7° was used. With a three-rate accumulation, the measurement time was set to 30 s, a beam diameter of 2 µm, and the slit diaphragm was automatically adjusted and corrected.

Oxygen isotope chemistry

A suite of 50 quartz samples from 30 sites was analyzed for oxygen isotope compositions. Oxygen isotope analyses were performed using a laser extraction procedure that follows the techniques described by Sharp (1990) and Rumble and Hoering (1994) and the $^{18}O/^{16}O$ isotope ratio was measured on a Finnigan MAT-252 gas source mass spectrometer at the University of Tübingen. By combining oxygen isotope

analyses of quartz samples and homogenization temperatures from fluid inclusion studies of primary inclusions, the oxygen isotope composition of the fluid was determined according to the equation of Ligang et al. (1989). ESM 6 reports all minimum and maximum homogenization temperatures, $\delta^{18}O$ quartz, and the calculated $\delta^{18}O$ H_2O values of each sample.

Thermodynamic modelling

For thermodynamic modelling, "The Geochemist's workbench (GWB)" package was used with a tailor-made thermodynamic database for a uniform pressure of 50 MPa and temperatures between 0 and 400 °C. Information about the database is detailed in Burisch et al. (2018, this issue) and in the electronic supplement ESM 4.

Results

In the following section, the results of all applied methods in this study will be presented, within the context of the different mineralization stages described above.

Mineral chemistry

Representative chemical compositions of all analyzed minerals are listed in ESM Table 2. Individual analyses are provided in the ESM 7.

Stage I: Fe-As (-Sb±Au)

Arsenopyrite has a non-stoichiometric composition, which can be explained by varying Sb and As concentrations, whereas the other minerals (marcasite, pyrite, and stibnite) of this stage show almost ideal compositions. Of particular importance are noble metal contents of ore minerals of this stage. Arsenopyrite, marcasite, and pyrite contain invisible gold with maximum values of 3100, 2100, and 710 ppm, respectively (Fig. 5a and ESM Table 2). Some berthierite grains show maximum Au concentrations of 730 ppm. The dominant mineral stibnite contains up to 1800 ppm Au and 1000 ppm Ag. Electrum grains range between 50 and 85 wt% Au (Fig. 5b) and contain up to 2 wt% Pb and 1500 ppm Hg (ESM Table 2). Compositions below the 1:1 line have lower totals and cannot be explained by exchange with other elements such as Cu, Bi, or Hg, overlap corrections or reference material, but by variable porosities. Furthermore, analyses from areas in the central Schwarzwald (i.e., Freiburg, Kinzigtal) show a distinctly higher Ag content of up to 50 wt%, whereas analyses from Bad Sulzburg and Badenweiler have maximum Ag values of 35 wt%.

Stage II: Pb-Zn-Cu

The minerals of this stage show compositions close to their stoichiometric formulae, with the only exception of chalcopyrite, which shows a minor Cu deficit. Tetrahedrite I is the most common mineral in this stage with Cu contents between 15 and 30 wt% (average 23 wt%), whereas the Ag content ranges from 11 to 30 wt% with an average value of 19 wt%. Chalcopyrite incorporates significant amounts of As (up to 3.7 wt%) and Sb (up to 1400 ppm). Galena has Ag concentrations up to 1.2 wt% and Sb up to 2.7 wt%. Important minor elements in sphalerite are Cd and Ag, with maximum amounts of 7700 ppm and 1.7 wt%, respectively. High amounts of Ag have previously been attributed to nano-inclusions of fahlore solid solution (Pfaff et al. 2010).

Stage III: Pb-Sb

Different to the previous two mineralization stages, ore minerals of stage III usually have non-stoichiometric compositions. Highest Ag and Au concentrations were observed in zinkenite with maximum Ag values of 3700 ppm and in jamesonite, with up to 3300 ppm Ag and 1 wt% Au. Andorite and bournonite show exceptionally high Se concentrations of up to 2 and 1.5 wt%, respectively. High Cu concentrations were measured in zinkenite (< 7000 ppm) and jamesonite (< 1 wt%). Besides, andorite and semseyite show the highest Fe content (up to 1600 ppm), whereas only up to 550 ppm were measured in fizélyite, heteromorphite, plagionite, and zinkenite. Highest As concentrations were detected in bournonite (up to 1 wt%), jamesonite (up to 1200 ppm), and zinkenite (up to 1000 ppm).

Stage IV: Ag-Sb

All minerals of this stage contain large amounts of As (up to 4700 ppm), Se (up to 2000 ppm), and Fe (up to 3.3 wt%). Au was detected with maximum amounts of 850 ppm in diaphorite, miargyrite, and pyrargyrite. Tetrahedrite/freibergite II shows Cu concentrations between 12 and 18 wt% (average 15 wt%), whereas the Ag content ranges from 26 to 37 wt% with an average value of 32 wt%. Diaphorite and freieslebenite show a non-ideal Pb site occupancy, with not fully occupied Pb (1.87 a.p.f.u. instead of 2 and 0.61 a.p.f.u. instead of 1, respectively), whereas the Ag and Sb contents are close to ideal. The opposite holds true for pyrargyrite, where the Ag site is not completely filled (2.85 a.p.f.u. instead of 3). Miargyrite and stephanite analyses result in compositions close to their ideal formulae.

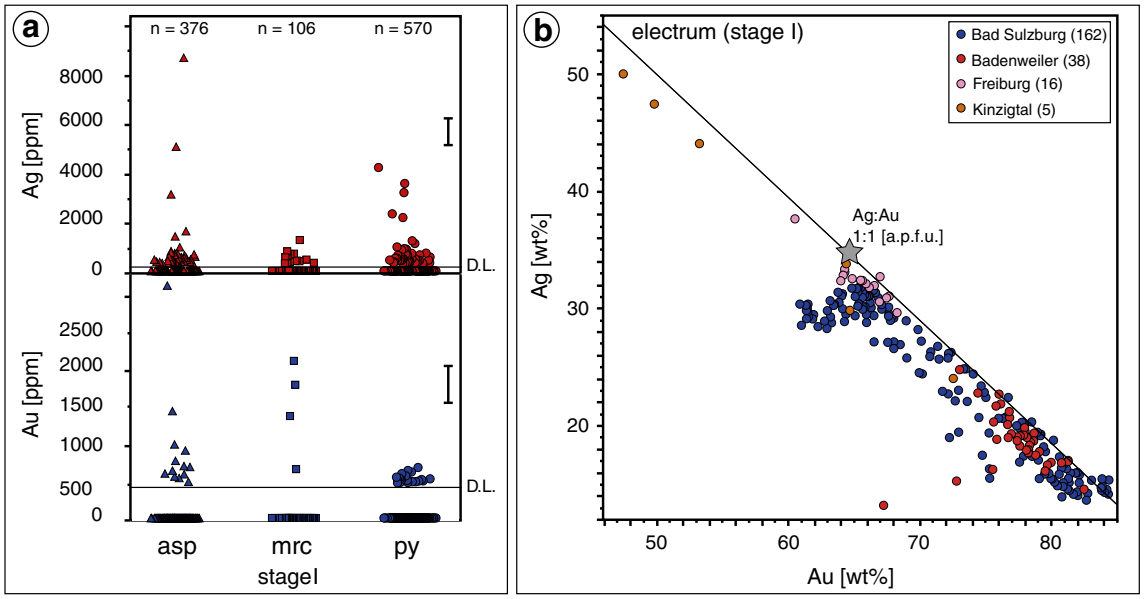

Fig. 5 **a** Ag and Au content in ppm of arsenopyrite, marcasite, and pyrite of all localities of stage I. Black bars show the uncertainty of each measurement, D.L. = detection limit. **b** Ag versus Au (wt%) of all electrum analyses, classified by the areas in the Schwarzwald. Gray star represents the stoichiometric electrum. Variations below the 1:1 line can be explained by lower totals due to porosity

Fluid compositions

Considering the salinity and homogenization temperature of fluid inclusion analyses from both ore and gangue minerals in all stages of the mineralization, three clusters were identified. These are briefly described in the following section. Detailed results are provided in ESM 8. The sum of all presented fluid inclusion analyses records the whole range of fluids involved, as they are composed of fluid inclusions from various quartz generations throughout the entire succession of mineral assemblages (Fig. 6). For temporal interpretation, only primary and pseudo-secondary inclusions were considered and the analyzed secondary inclusions serve only a statistical purpose in fluid composition-homogenization temperature space. Due to the polyphase nature of mineralization (e.g., multistage reaction and overgrowth textures), we were only in rare instances able to directly correlate individual fluid inclusions to ore mineral assemblages (Fig. 6a–d). These include (1) quartz-ore mineral-quartz with a clear temporal succession (Fig. 6c), (2) quartz-ore mineral clusters with a paragenetic association (Fig. 6d), and (3) fluid inclusions in stibnite and sphalerite with a direct age correlation.

Fluid type A: low salinity, high to medium temperature

This fluid type was found in quartz and stibnite from mineralization stage I. Primary, secondary, or pseudo-secondary inclusions of this type are in most cases irregularly shaped; pseudo-secondary ones typically occur in healed cracks in quartz and stibnite. Measured homogenization temperatures (T_h) range from 100 to 400 °C (Fig. 7a), but most analyses show temperatures above 250 °C. Fluids freeze in the range of − 30 to − 45 °C and the first melting can be observed above − 20 °C, providing evidence for a binary NaCl-H_2O system (Steele-MacInnis et al. 2011, Fig. 7b). The final melting temperature of ice is between 0 and 5 °C, resulting in calculated salinities of 0 to 5 wt% (NaCl+$CaCl_2$, Steele-MacInnis et al. 2011). Only H_2O, HCO_3^-, or CO_3^{2-}, but no SO_4^{2-} was detected in micro-Raman analyses.

Fluid type B: high salinity, moderate to low temperature

Fluid type B was recognized in sphalerite from and quartz associated with mineralization stage II and in quartz from stage III. Similar to fluid type A, most primary (Fig. 6f), secondary, or pseudo-secondary inclusions are irregularly shaped (Fig. 6f), but they occur on primary growth zones and well-healed fractures in quartz and sphalerite. Homogenization temperatures vary between 50 and 250 °C into the liquid (Fig. 7a). Above − 50 °C, a first melting is visible, indicating a ternary NaCl-$CaCl_2$-H_2O system (Fig. 7b). Last dissolving phases are ice and hydrohalite. Observations show that the final melting temperature of ice ranges between − 29 and 18.5 °C and of hydrohalite between − 28.5 and − 17.5 °C, which results in calculated salinities of 20 to 26 wt% (NaCl+$CaCl_2$, Steele-MacInnis et al. 2011). The molar Ca/(Ca+Na) ratio ranges between 0.00 and 0.80. In all FIAs, H_2O (Raman bands between 2750 and 3900 nm) was the only Raman-

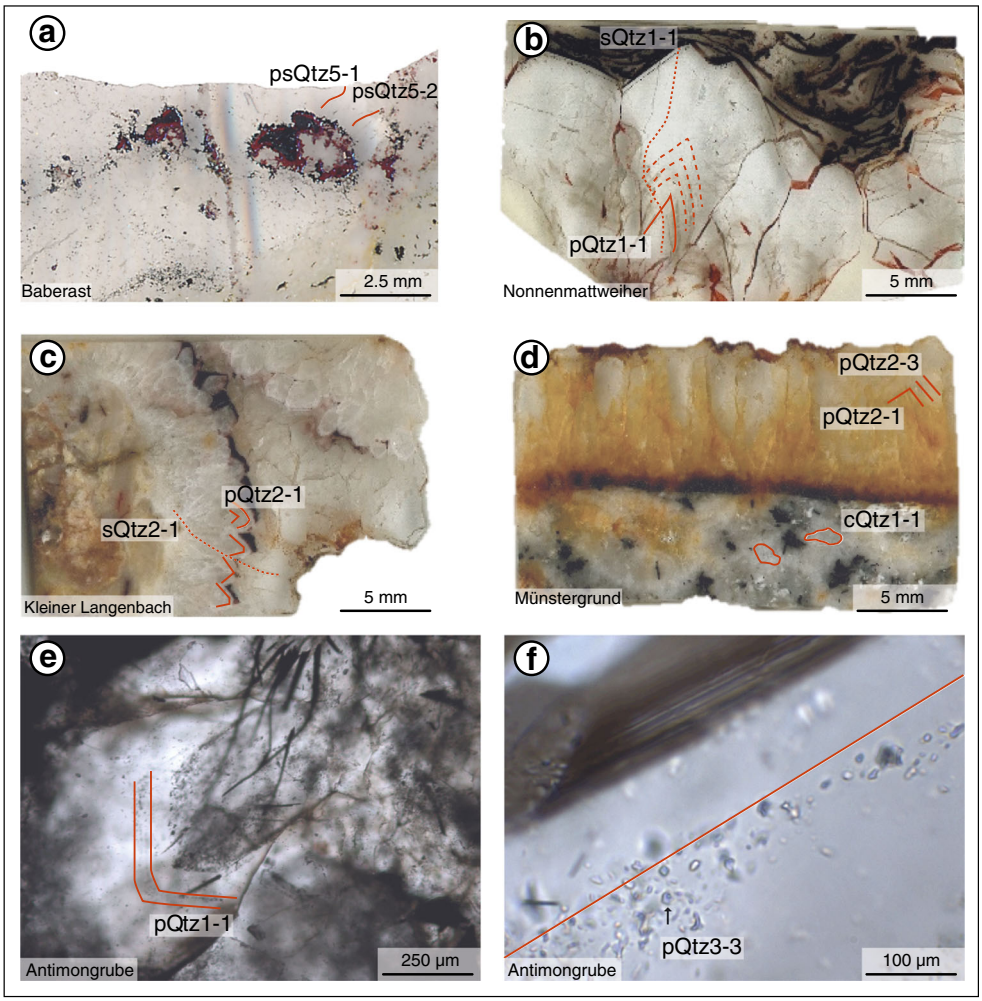

Fig. 6 Photomicrographs illustrating the characteristic attributes of fluid inclusions in different samples and different mineralization stages. **a** Silver mineralization (stage IV) in voids of and intergrown with quartz V (stage IV) and measured pseudo-secondary fluid inclusions in quartz. **b** Various primary fluid inclusions on growth zones in quartz and a secondary inclusion trail, cutting across the whole quartz I crystal, prior to stage I. **c** Several quartz generations, with ore minerals in between two quartz generations (II and III). Analyzed primary and secondary inclusions in quartz II are shown. **d** Clustered fluid inclusions and ore minerals in quartz I overgrown by quartz II with primary inclusions. **e**, **f** Representative microscope images of typical primary fluid inclusion trails in quartz II

active species detected in all analyses. Further, minor NaCl-dependent modifications of the H_2O-bands were recognized (Frezzotti et al. 2012).

Fluid type C: variable salinity, moderate to low temperature

This fluid type was found in inclusions in quartz, associated with stage IV sulfide mineral assemblages. Inclusions of this fluid type have variable sizes and shapes and occur along trails and in clusters. Homogenization temperatures vary between 50 and 200 °C (Fig. 7a). Compared to fluid types A and B, two different clusters of fluid compositions can be distinguished: one with a eutectic temperature of − 21.2 °C and another one with a eutectic temperature of − 52 °C. Final melting temperatures of ice range between − 2.6 and − 18 °C, and hydrohalite melts between − 20.9 and − 25.8 °C. The calculated salinity ranges between 7.5 and 20 wt% ($NaCl+CaCl_2$, Fig. 7a, Steele-MacInnis et al. 2011) and the molar Ca/(Ca+Na) ratio ranges from 0.00 to 0.80. In all FIA, H_2O was the only Raman-active species detected in all analyses with significant NaCl-dependent H_2O-band modifications.

Oxygen isotope data

All oxygen isotope data is reported relative to the SMOW standard. The $\delta^{18}O$ values of quartz vary greatly, quartz (stage I–III) from the Bad Sulzburg area (area D, Fig. 1) showing a range from − 1 to + 18‰, from Ehrenkirchen (area C, Fig. 1) a range from + 12 to + 18‰, and from Münstertal a range from − 3.5 to + 19‰ (area C, Fig. 1). The analyzed range of $\delta^{18}O$ values greatly exceeds the range reported by Baatartsogt et al. (2007) who related $\delta^{18}O$ values of quartz to Variscan (− 12.5 to + 4.4‰) and post-Variscan fluids (− 7.1 to + 2.1‰).

The large dataset of formation temperatures was combined with oxygen isotope data of quartz to calculate $\delta^{18}O$ values of the fluid responsible for vein formation (according to Ligang et al. 1989). For analyses from samples, where no respective fluid inclusion data was available, the $\delta^{18}O$ fluid values were calculated at 50 and 400 °C, representing the minimum and

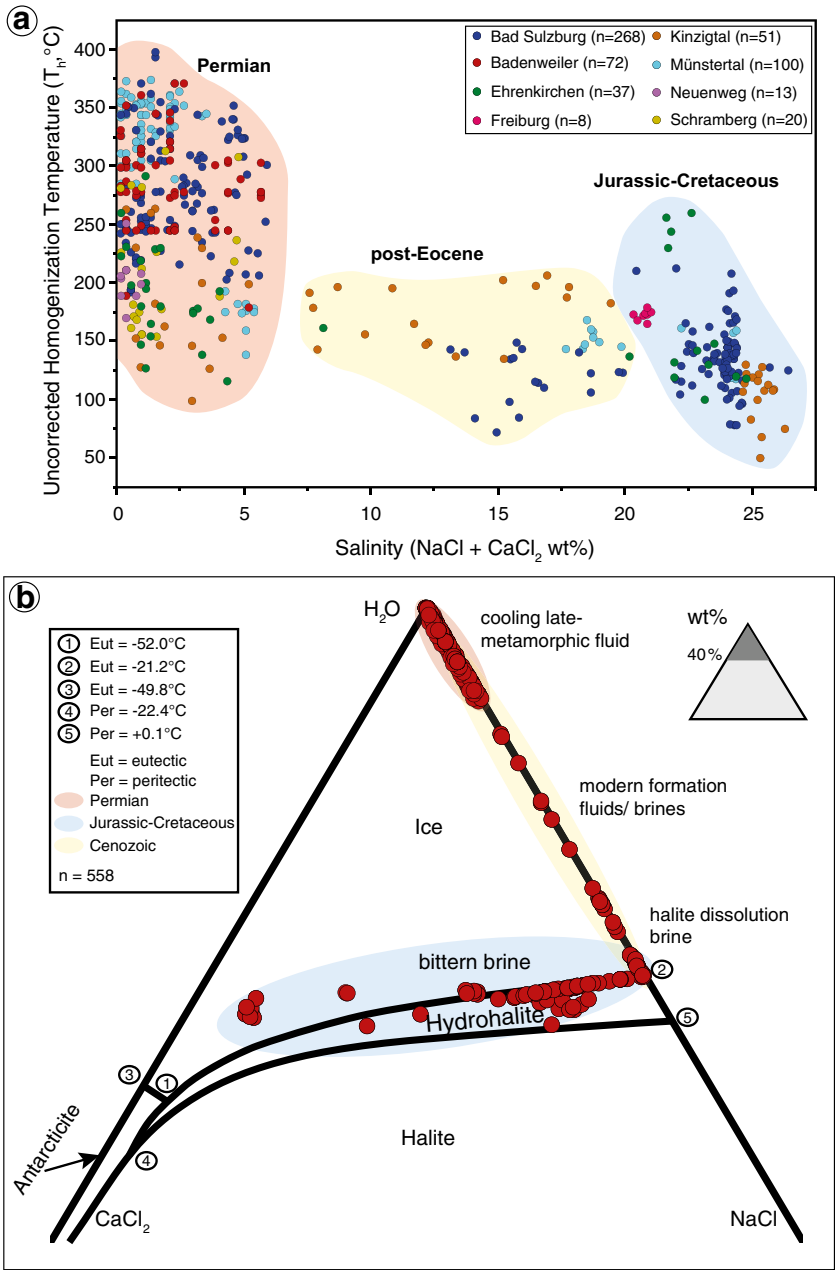

Fig. 7 **a** Homogenization temperature versus calculated fluid salinity (NaCl+$CaCl_2$) in wt%. The different box colors refer to various time periods of mineralization (Walter et al. 2016, 2018a). **b** Phase diagram of the ternary H_2O-$CaCl_2$-NaCl fluid system. Different colors show the same classification as in (**a**)

maximum homogenization temperatures observed in all veins. Unfortunately, the large number of intergrown quartz generations and the commonly lacking textural evidence prevented an exact temporal correlation of a specific quartz generation from one locality to a specific quartz generation from other localities and/or mineralization stages. However, relative trends from initial quartz (I) to successive quartz (II, III) generations are visible within individual localities from which several, temporally distinguished quartz generations were analyzed; also, the overall range of the isotopic ratios serves as a solid base for interpretation. The analyses illustrate that the calculated $\delta^{18}O$ values of fluids associated with Sb-Pb-Ag ±Au veins overlap with magmatic/metamorphic and meteoric fluids, with peaks at ca. − 5‰ and + 6 to + 11‰. Metamorphic fluids typically have $\delta^{18}O$ values of ~ + 3 to + 20‰, magmatic fluids + 5.5 to + 9.5‰, and meteoric water shows variations from − 25 to 0‰ (e.g., Craig 1961; Sheppard 1986; Taylor and Barnes 1997; Kendall and Coplen 2001). The evolutionary trend for a specific locality with several quartz generations indicates an increasing importance of meteoric fluids for successively younger quartz generations. For example, at the Wonnen locality (Münstertal, Area C Fig. 1), the fluid which formed the early quartz I shows a typical magmatic/metamorphic signature (max. +13‰), whereas the subsequent quartz generations (II + III) indicate a meteoric fluid composition (on average − 2.4‰).

Discussion

The discussion section is subdivided into two parts. The first part deals with fluid compositions and age constraints for Sb-Pb-Ag±Au-quartz veins in the Schwarzwald. In the second part, the mineralogical and chemical evolution of the different mineralization stages is discussed in detail, as well as the occurrence of gold and the comparison to other Sb- (Au) occurrences in the Variscan Orogen and worldwide.

Fluid compositions and age constraints

Textural observations correlated to fluid inclusion data, fluid salinities, and oxygen isotopes can be used here to invoke a Permian age for mineralization stage I, whereas stage II and III formed during Jurassic and stage IV during Tertiary times.

With an age of 277.6 Ma (Walter et al. 2018c, submitted), Permian veins are significantly younger than the last magmatic event in the Schwarzwald, which was the intrusion of post-collisional granites between 335 and 315 Ma (e.g., Todt 1976; Altherr et al. 2000; Hann et al. 2003). The rare and local occurrence of ferberite ($FeWO_4$; at the Segen Gottes locality) in the Permian veins is tentatively attributed to the proximity of this locality to the Nordrach pluton from which W-bearing minerals are well-known (Walenta et al. 1970) and which may have been remobilized. Such post-Variscan mobilization processes are common in the Schwarzwald and were described in detail by Werner et al. (1990). Oxygen isotope analyses for quartz from stage I mineralization point to a magmatic/metamorphic fluid signature. Very variable homogenization temperatures (100 to 400 °C, Fig. 7a) and low salinities (0 to 5 wt% NaCl + $CaCl_2$, Fig. 7a) show fluid compositions typical for Permian veins in the Schwarzwald (e.g., Wagner and Cook 2000; Baatartsogt et al. 2007; Walter et al. 2016). The temperature fluctuation is due to fluid cooling and not due to evaluating primary vs. secondary inclusions. This large temperature (cooling) range is similarly observed in many large Sb deposits worldwide, e.g., in Australia, Bolivia, Russian Federation, or China (e.g., Comsti and Taylor 1984; Ashley et al. 1990; Dill et al. 1995; Bortnikov et al. 2010; Zhai et al. 2014). However, individual localities from all over the world generally do not show such a broad temperature range (commonly < 200 °C), which may be linked to factors such as the difference in tectonic setting and/or size of the mineralization (fluids in small fractures in the Schwarzwald may cool down faster than larger volumes of fluids in the large deposits).

The intensive brecciation of stage I minerals and the overgrowth by minerals of stage II indicates significant tectonic processes during the initiation of stage II. In combination with a strong change in fluid composition and formation temperature, this suggests the presence of a significantly different fluid reservoir during stages II and III. During Late Permian to Triassic times, the central European basin was flooded by seawater and evaporites were deposited (e.g., Roscher and Schneider 2006; Geyer et al. 2011). This marine influence is reflected in the fluid composition of the successive stages, which contains increased salinities up to 27 wt% NaCl+$CaCl_2$ (Fig. 7a, b), compared to Permian low-salinity fluids (max. 5 wt%). Furthermore, the recorded fluid composition is in agreement with fluids from other Jurassic-Cretaceous veins that typically show salinities between 20 and 28 wt% (Walter et al. 2016). The presence of significant Pb in the mineralized system is probably related to the high chlorinity of these fluids (as Pb is transported als Cl complexes, Yardley 2005; Wagner et al. 2016), since the sudden increase in Pb is directly correlated with a significant salinity increase, whereas the possible source rocks have remained constant. Moreover, the calculated oxygen isotope values of the fluid show (at some localities) that the younger quartz generations formed from a fluid with increasing influx of meteoric water and/or seawater (Weissert and Erba 2004).

A second significant change in fluid composition is visible for the transition to stage IV, which is also recorded by a change in tectonic regime. Fluid inclusion analyses of quartz directly associated with the Ag-bearing minerals of stage IV show variable salinities ranging between 7.5 and 20 wt% (NaCl+$CaCl_2$). These values are typical of post-Cretaceous fluids in veins of the Schwarzwald district (Walter et al. 2016). This stage and the newly formed Ag-bearing minerals are only locally present, especially in the Central Schwarzwald district, and are generally lacking in the Southern Schwarzwald. Interestingly, stages I to III occur in all veins independent of their strike direction (ESM 3 3), whereas predominantly NE-SW striking veins (i.e., parallel to the Rhine Graben rift) contain a large variety of Ag minerals (ESM 3 3). Thus, there is a correlation between vein orientation and the presence of stage IV. Because it is regarded as unlikely that the tectonic regime changed significantly during a single mineralization event, it is assumed that the Ag mineralization is related to a separate tectonic setting and fluid influx. The orientation of these veins parallel to the Rhine Graben is thus thought to be related to a reactivation of pre-existing Permian veins during the course of the Upper Rhine Graben opening, and hence, a Tertiary age of the Ag-rich stage IV mineralization is deemed very likely.

Mineralogical and chemical evolution

Fe-As(-Sb±Au) stage (stage I)

Initially, this stage is strongly dominated by Fe- and As-bearing minerals, but this transitions to an abundance of Sb-rich sulfides. The initial minerals do, however, contain Sb (as well as Au and Ag) as a minor or trace element. The best example is the As-Sb zoning of arsenopyrite (ESM 3 1b). Antimony was, hence, present in the fluid from the beginning

and this mineral sequence does not record a compositional evolution from an Fe-As- to a Sb-dominated fluid. Rather, the mineral succession records a decrease in temperature (e.g., Wagner and Cook 2000; Krolop et al. 2018; Burisch et al. 2018, this issue).

The fluid inclusions of the first stage (in quartz and in stibnite) record a large temperature range from 400 to 100 °C (Fig. 7a), which further strengthens the argument of fluid cooling. The process of fluid cooling can be thermodynamically modelled by using a fluid of low salinity (5 wt% NaCl) in equilibrium with a granitic host rock (assumed composition, comprised of 5 wt% muscovite, 5 wt% annite, 10 wt% anorthite, 10 wt% albite, 35 wt% quartz, and 35 wt% K-feldspar) at neutral pH (6.55 at 400 °C). Granitic host rocks buffer a fluid at near-neutral conditions (Bucher and Stober 2002; Bucher and Stober 2010; Fig. 8c, d). Starting at 400 °C, the minimum temperature estimate of the source fluid produces a sequence of early pyrite and later stibnite during simple cooling (Fig. 8a, b). However, without additional water-rock interaction during cooling, the quantity

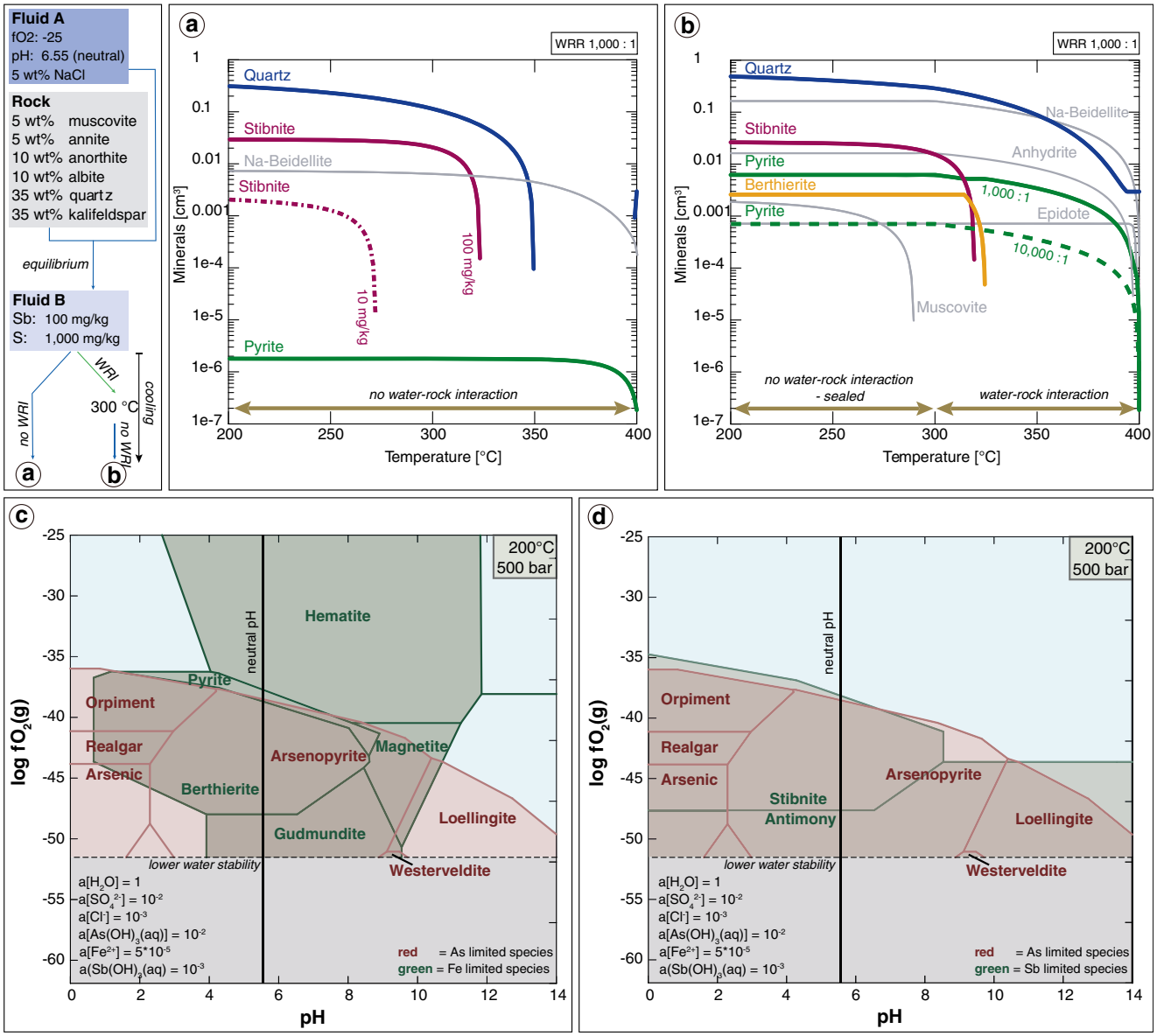

Fig. 8 **a, b** Mineral stability diagram during cooling of a fluid initially in equilibrium with a granitic host rock. WRR = water-rock ratio, WRI = water-rock interaction, gray minerals = not found in samples of this study. **a** No WRI during cooling with Sb concentrations of 100 and 10 mg/kg. **b** WRI during cooling drastically increases the amount of pyrite precipitation. Shown is an example of WRI (1000:1) between 400 and 300 °C and a sealed system from 300 to 200 °C. **c, d** Predominance fO_2-pH diagrams at 200 °C, 500 bar, where the Fe species are shown in **c** and the Sb species in **d**. For a simplified comparison between the predominance field, the As species are shown in both **c** and **d**. Both **c** and **d** represent overlapping predominance fields of the same fluid

of pyrite relative to stibnite and quartz would be too low to match the observed relative phase volumes, since only minor amounts of Fe can be transported at near-neutral conditions. We thus assume that additional Fe was derived near the place of pyrite precipitation from the host rocks. Bleached zones around the veins support this notion. However, in our model, water-rock interaction was only assumed to happen between 400 and 300 °C, as quartz precipitation seals the veins and prevents further reactions. Still, relatively little fluid-rock interaction suffices to explain the observed amounts of pyrite.

The hydrothermal fluid must initially have been relatively reduced and sulfur-rich, otherwise, hematite and/or magnetite would form and deplete the fluid of Fe before pyrite saturation is reached. Graphite- and sulfide-bearing host rocks favor reduced fluids (Kontny et al. 1997) and the Schwarzwald gneisses contain both (e.g., Bucher et al. 2009; Markl et al. 2016; Walter et al. 2018b). Further, the formation of arsenopyrite together with pyrite during the initial fluid stage requires an As/Sb ratio of 10 (Fig. 8c, d). This is at first glance surprising since we are dealing with an Sb-dominated mineralization, but it is thermodynamically essential.

Finally, the mineral berthierite, which based on the observed textures precipitated between pyrite and stibnite, is not thermodynamically stable (data from Seal et al. 1992) in our calculations with a realistic fluid composition (see Fig. 8a–d). It only becomes stable if the stability of berthierite is increased by 2 log$K$ values, which represents twice the estimated uncertainty given by Seal et al. (1992). We have no conclusive explanation of the non-stability of berthierte in our calculations.

Pb-Zn-Cu stage (stage II)

The chemical variability increases during this second stage, where Pb-, Zn-, and Cu-bearing minerals dominate. Tetrahedrite (I) is the only Sb- and Ag-bearing (up to 30 wt% Ag but prevalently < 20 wt%) mineral in this stage. The formation of galena instead of Pb-Sb sulfides (in contrast to stage III) indicates a higher S/Sb activity ratio of the fluid. Mineral textures show that some stibnite of stage I is replaced by tetrahedrite (I) of stage II, indicating a remobilization of stibnite (Fig. 3e). Available aqueous Sb is incorporated in tetrahedrite (I) and, thus, base metal sulfides (i.e., sphalerite, galena, and chalcopyrite) can precipitate. This implies that only minor amounts of stibnite were dissolved and re-precipitated and thus the ore-forming fluid only contained minor Sb, which fits with textural observations. Furthermore, to form tetrahedrite and chalcopyrite in the large quantities observed, increased amounts of Cu in the fluid or more effective precipitation mechanisms need to be invoked. We speculate that rather an increased amount of Cu is probable since no Cu-bearing minerals are present before the occurrence of these minerals and besides, Cu can be more effectively transported in highly saline fluids (Yardley 2005; Wagner et al. 2016), which formed stage II.

Pb-Sb stage (mineralization stage III)

This mineralization stage is characterized by a large variety of chemically very similar minerals. Interestingly, textures show a clear inverse relationship: samples with large modal amounts of stage I-stibnite typically do not show a well-developed stage III and the mineral assemblage ends with the Pb-Zn-Cu stage II; samples with a distinct stage III Pb-Sb mineralization, on the other hand, do not show any or only minor amounts of stage I-stibnite. If it occurs at all, it is present as small relics (stage III minerals intensively replace stibnite, Fig. 4a). Hence, formation of the stage III minerals depends on the existence of an earlier Sb mineralization and remobilization especially of stibnite by Pb±Fe-Ag-bearing fluids (Fig. 9). Locally, these reaction textures are preserved (e.g., stibnite ➔ zinkenite, zinkenite ➔ plagionite, Fig. 2). Thermodynamic calculations show that the Pb-Sb sulfides can precipitate from fluids of variable composition and pH, as long as sufficient Pb is present (Fig. 9). Some reactions (e.g., stibnite ➔ zinkenite) show approximately volume constant textures (Fig. 4a) which indicates a steady Pb increase with simultaneous Sb and S decrease during the evolution of this stage. Although these calculations hold an uncertainty since a constant volume cannot be guaranteed in most cases, it is the only method to investigate the mobility of elements (influx vs. discharge), as the fluid composition (relative elemental content) is unknown. Concluding, an additional Pb influx and replacement of pre-existing stibnite has been essential for ore stage III (Fig. 9).

Apart from Pb, Ag is a conspicuous element in stage III, as shown by the occurrence of the Ag-rich minerals andorite and fizélyite in all investigated occurrences. Ag may have been added by the Pb-rich stage III fluid, or it was remobilized from stage II tetrahedrite and stage I electrum. As there is no textural evidence for tetrahedrite and electrum dissolution, it is plausible that the stage III fluid must have transported some Ag besides Pb.

Ag-Sb stage (stage IV)

Mineral composition and mineral sequence in stage IV record a successive Ag enrichment (Fig. 10): the minerals with the highest Ag contents precipitate at the end of this stage. Textures record abundant replacement processes of stages II and III Pb-Sb minerals by minerals of stage IV (e.g., tetrahedrite I ➔ tetrahedrite II (freibergite), andorite ➔ tetrahedrite II (freibergite), galena ➔ pyrargyrite, andorite ➔ miargyrite, Fig. 2). Stage IV Pb-bearing minerals (i.e., diaphorite and freieslebenite, Fig. 2) only crystallize at the beginning of stage IV. Common reaction textures show that the strongly porous

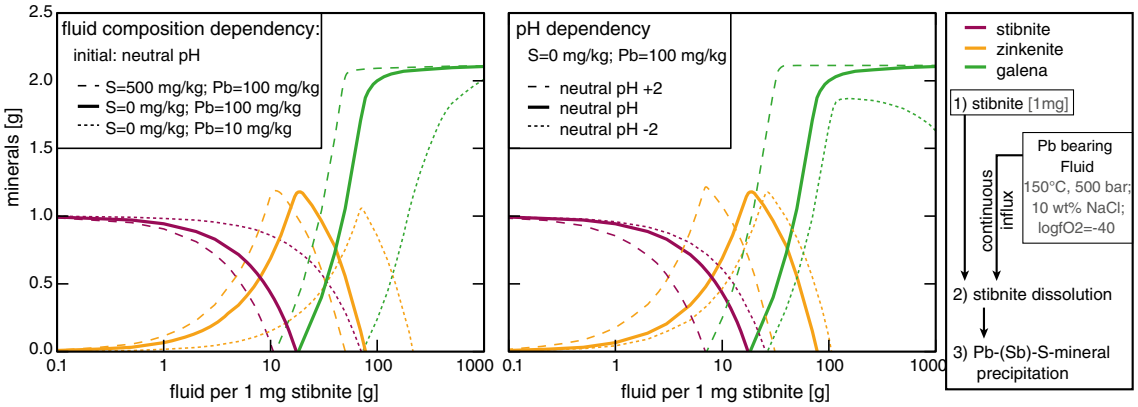

Fig. 9 Mineral stability diagrams at 150 °C (average homogenization temperature) and 500 bar (database condition) showing variable fluid-stibnite ratios during the reaction of a Pb-bearing fluid with pre-existing stibnite. Depicted are the compositional dependency of the fluid and the initial pH dependency of the mineral stability relative to fluid-stibnite ratios. Note that the stability of zinkenite is estimated by the assumption that $\Delta G_f = 0$ for the formation from stibnite and galena

tetrahedrite I is replaced irregularly by tetrahedrite II (freibergite; Fig. 3d, f). Tetrahedrite I of the Pb-Zn-Cu stage II (Figs. 10 and 11) is obviously remobilized and re-precipitated with a Ag-enriched composition (tetrahedrite II (freibergite); Figs. 10 and 11). During this reaction, excessive Cu could not be removed from the system, and hence, local oversaturation leads to the precipitation of chalcopyrite inclusions in tetrahedrite II (freibergite). Moreover, small grains of miargyrite form locally during this process due to the high Ag content of the fluid. Interestingly, there is a correlation of Ag content in tetrahedrite and homogenization temperature of fluid inclusions (Fig. 12): higher homogenization temperatures are

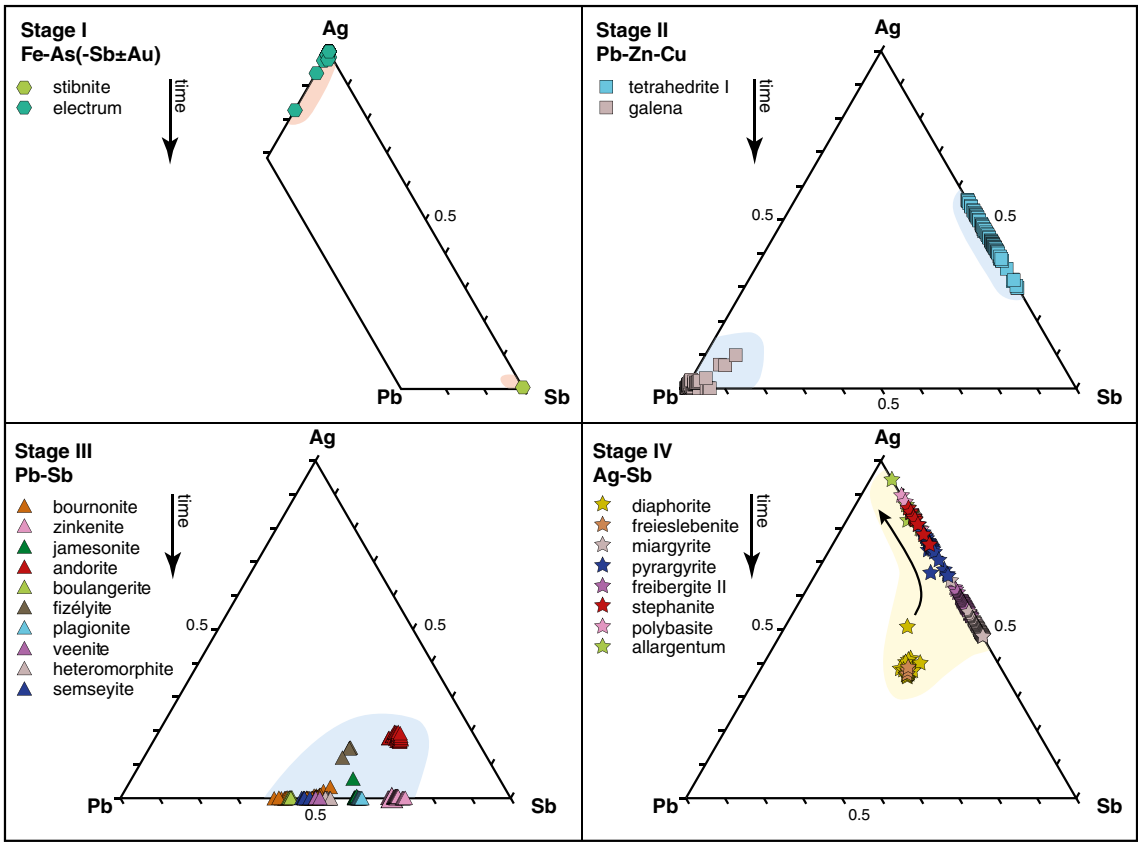

Fig. 10 Composition of all Pb±Ag±Sb-bearing minerals, separated by each mineralization stage and time of crystallization. Red fields show Permian minerals (stage I), blue fields Jurassic-Cretaceous minerals (stage II and III), and the yellow field shows minerals of the Tertiary mineral stage IV. The black arrow indicates a strong Ag enrichment during stage IV, where the youngest minerals show the highest Ag content

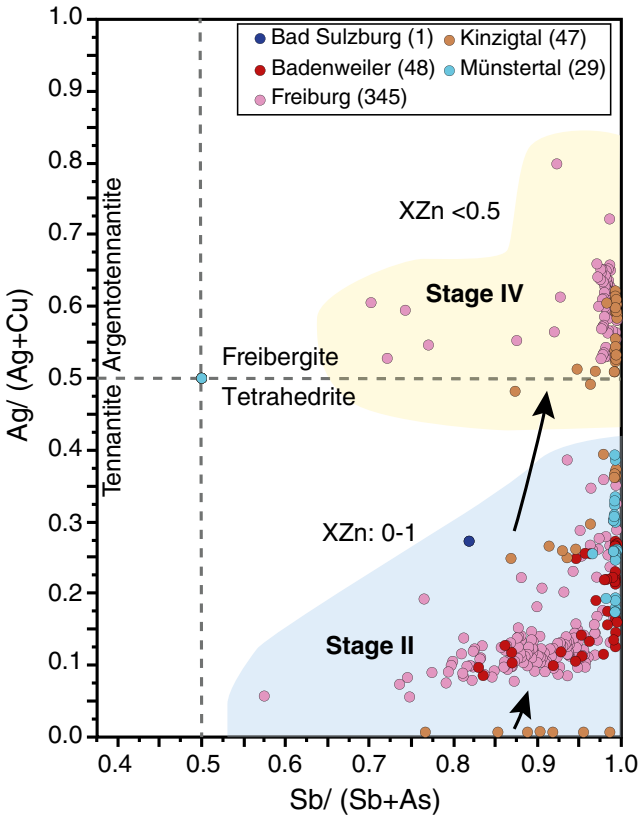

Fig. 11 Ag/(Ag+Cu) versus Sb/(Sb+As) plot of all tetrahedrite analyses, colored according to the different areas sampled. Blue field shows compositions of Jurassic-Cretaceous tetrahedrite I (stage II) and the yellow field those of Tertiary tetrahedrite (freibergite) II (stage IV). Black arrows indicate the evolution of the tetrahedrite composition, oldest at the bottom, youngest at the top

associated with lower Ag content in tetrahedrite, i.e., this is due to a higher Ag content in later stage fluids and not due to crystallographic effects. Precipitation mechanisms for this stage are fluid mixing (indicated by the large spread in salinities even for individual samples) as well as reaction with pre-existing sulfides.

The occurrence of gold

Gold is rather widespread in the studied Sb-quartz vein type mineralization in the Schwarzwald either as invisible gold and/or as native gold/electrum. Invisible gold is present in significant concentrations in minerals of stage I, in pyrite, arsenopyrite, marcasite, and stibnite. Invisible Au concentrations of some samples in this study (up to 3100 ppm) are similar to concentrations commonly observed in large economically significant structurally controlled Au-Sb deposits (~ 100–5000 ppm; e.g., Dill et al. 1995; Ashley et al. 2000; Baltukhaev and Solozhenkin 2009; Kovalev et al. 2011). Generally, changes of physicochemical parameters such as pressure, temperature, Cl concentration, pH, oxygen, or sulfur fugacity provide effective mechanisms for gold precipitation (e.g., Williams-Jones et al. 2009; Zhu et al. 2011).

Due to the intimate correlation between gold and sulfide abundances (i.e., Au as invisible gold in sulfides), one can presume a common precipitation mechanism. Similar to the sulfides, the solubility of gold in the presence of sulfide and chloride complexes (as are present in such hydrothermal systems; Gammons and Williams-Jones 1997; Zhu et al. 2011) decreases with temperature (Seward 1973) indicating that both

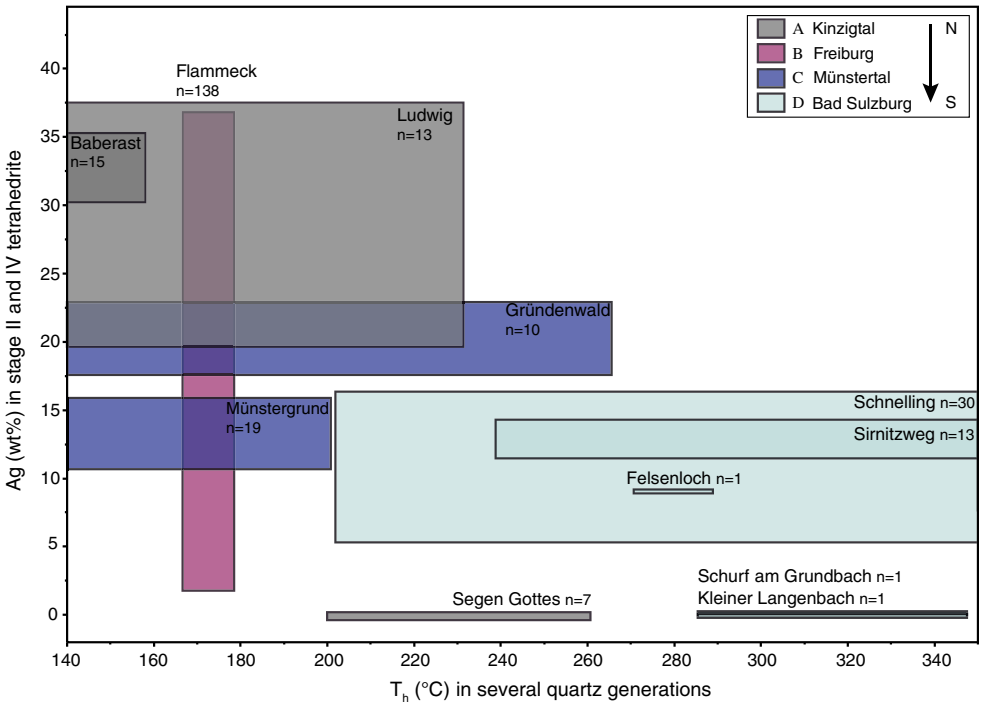

Fig. 12 Ag content (wt%) of tetrahedrite (stage II and IV) versus the homogenization temperature of all four investigated areas in the Schwarzwald. The boxes of each locality represent the temperature range between the minimum and maximum homogenization temperature and the minimum to maximum Ag content

can form by fluid cooling (e.g., Gammons and Williams-Jones 1997; Hagemann and Lüders 2003; Zhu et al. 2011). Furthermore, ongoing sulfide precipitation decreases the sulfide activity and gold-sulfide complexes are de-stabilized (Williams-Jones et al. 2009). Thus, the association between Au and Sb sulfides in quartz veins is typical and has been observed in a large number of deposits (e.g., Distanov et al. 1975; Bril and Beaufort 1989; Clayton et al. 1990; Ortega and Vindel 1995; Obolensky et al. 2007; Zhu et al. 2011).

According to Romer and Kroner (2017), major sources for hydrothermal Au (independent whether it forms discrete grains or is incorporated as invisible gold) in the Variscan basement are Cambrian to Ordovician sedimentary rocks and magmatic arcs; re-distribution in the crust during metamorphism is common in the entire Variscan basement and Au-bearing mineralization is found in many parts of central Europe (e.g., in Germany: Goldkronach, Fichtelgebirge, Pascher 1985, Irber and Lehrberger 1993; Korbach, Rheinisches Schiefergebirge, Lehrberger 1995, Kulick et al. 1997; in France le Bourneix, Laurieras, Saint Yrieix district, Bouchot et al. 1989; in the Czech Republic, Bohemian Massif, Moravek and Pouba 1987, Zachariáš et al. 2014).

Gold also occurs as discrete electrum grains. These are rarely observed in direct association with stage I but occur as small inclusions within minerals of the second, third, and fourth ore stage. Textures show marcasite (stage I) directly associated with electrum (Figs. 3b and 7b), which either formed by direct precipitation during fluid cooling (i.e., primary gold) or, more likely, by remobilization when primary pyrrhotite reacted to pyrite or marcasite. This hypothesis is strengthened by the porous appearance of, e.g., marcasite (Fig. 3b). Some electrum associated with the later stages also could have formed by Au and Ag remobilization of invisible gold during replacement of sulfides from ore stage I during later stages. Since the concentration of invisible gold is extremely low (on average < 0.05 wt% in ore minerals of stage I), the remobilized amount of these ore minerals needed to form electrum is significant. Thus, the probability and abundance of discrete gold grains in individual samples in the Schwarzwald are very low.

Comparison to other occurrences of this mineralization type in the Variscan belt

Sb-(Au)-bearing quartz veins of the type studied here are widespread throughout the Variscan Orogenic belt (ESM 3 4 and Table 1) (e.g., Walenta 1957; Dill 1985; Dill 1986; Gumiel and Arribas 1987; Ortega and Vindel 1995; Dill 1998; Wagner and Cook 2000; Krolop et al. 2018; Burisch et al. 2018, this issue). According to literature, four typical metal associations can be distinguished in these deposits: (1) Fe-As ±Sb-Au, (2) Pb-Zn-Cu±Au, (3) Pb-Sb±Au-Ag, and (4) Ag-Sb which is broadly similar to mineralization stages recognized in this study. However, only the first three metal associations are widespread (e.g., Boiron et al. 1990; Clayton et al. 1990; Munoz et al. 1992; Wagner and Cook 2000; Pochon et al. 2016; Krolop et al. 2018).

The initial stage of mineralization at many deposits is characterized by the mineral succession pyrrhotite, arsenopyrite, pyrite, and late-stage berthierite and stibnite. Only small mineralogical variations are documented, such as the presence of Ag-Sb minerals in the primary ore stage in the Erzgebirge (Burisch et al. 2018, this issue). This indicates a common formation mechanism due to fluid cooling of a, commonly described as a primarily late-metamorphic, Sb-bearing fluid, as has been previously suggested for other localities by, e.g., Wagner and Cook (2000), Neiva et al. (2008), and Krolop et al. (2018). Thus, a similar fluid composition can be invoked in all these Variscan occurrences, indicating a relatively similar fluid regime/source over thousands of kilometers largely independent of host rock. The same holds true for the subsequent stages II and III, suggesting extensive remobilization processes throughout the Variscan belt.

The fourth stage (Ag-Sb), which is abundant in several veins of the Schwarzwald, has only been documented at few other localities in the Variscides (see Table 1 for references), i.e., Urbeis and Charbes (France, No. 6, ESM 3 4), Erzgebirge and Fichtelgebirge (Germany, No. 5 + 8, ESM 3 4), Pribram and Kutná Hora (Czech Republic, No. 9, ESM 3 4), Kremnica (Slovakia, No. 12, ESM 3 4), and the Diógenes mine (Spain, No. 18, ESM 3 4). Local tectonic processes such as the Upper Rhine Graben or the Eger Graben rifting in the course of the Cenozoic tectonic evolution of Europe (Ziegler 1992; Rajchl et al. 2009) may tentatively invoked to explain these late reactivation and remobilization processes.

International context—Sb-Au deposits worldwide

Compared to the small size of structurally controlled Sb-(Au) deposits in Europe, similar deposits in, e.g., China, Canada, Bolivia, Australia, or the Russian Federation are much larger and have great economic significance (e.g., Dill et al. 1995; Kontak et al. 1996; Ashley et al. 2000; Baltukhaev and Solozhenkin 2009). However, independent of deposit size, the mineralogy of the initial stages appears generally similar (e.g., Dill et al. 1995; Ashley et al. 2000; Hagemann and Lüders 2003), and for this reason, similar formation processes and parameters (e.g., fluid chemistry, cooling) may be assumed. Hence, the evolution of stages I through III of the Variscan occurrences is an analogy to many large deposits, the main difference being size and the absence of a distinct late-stage silver-rich assemblage (stage IV) in the large deposits. Our study shows that the characteristic ore succession of the primary mineralization (stage I) can be exclusively explained by fluid cooling. Boiling or fluid mixing, which have been described for some economically significant deposits

Table 1 Overview of characteristic structural, mineralogical, and fluid inclusion data of late-Orogenic Sb-Pb-Ag±Au-quartz mineralization in the European Variscan Orogen

	Country	District	Host rocks	Structural position	Mineralized structures	Mineral assemblage	Th of fluid inclusion types			Formation	Reference
							A	B	C		
1	England	Cornwall	Middle Devonian to Upper Carboniferous volcanite, slates carbonate	Variscan folded sequences, anticlinal zones	Systems of dilational veins, transsecting cleavage and folds	asp[1], py[1], ccp[2], sph[2], gn[3], sbn[3], jms[3], bno[3], bou[3], fhl[3]	250–350 °C	270–290 °C	170–230 °C	Cooling, fluid unmixing	Clayton et al. (1990)
2	Germany	Harz Mountains	Carboniferous, Devonian schist, greywacke			sbn, chalcostibite, bno, zk, plg, bou, jms, sms, dadsonite, heteromorphite, fhl					Dill (1993)
3	Germany	Rheinisches Schiefergebirge	Lower Devonian to Lower Carboniferous slate, sandstone, quartzite, carbonate, greywacke	Variscan major anticlinal zones	Extensional veins, bedding-concordant mineralization	py[1], qtz[1], chlorite[1], sbn[2], zk[2], plg[2], sms[2], sph[2], chalcostibite, bno, jms, btr, bou, fhl, gold (in py)	160–390 °C	110–180 °C		Fluid cooling (boiling)	Dill (1993) Wagner and Cook (2000)
4	Germany	Thüringer Wald	Ordovician to lower Carboniferous slate, greywacke	NE-SW Variscan fault zones		py[1], asp[1], sph[1,4], qtz[1,2,4], sbn[2], zk[3], plg[3], sms[3], bou[3,4], gn[4], ankerite[3,4], siderite[3,4], bno, jms, btr, fhl, gold, antimonides				Fluid cooling, late-stage mixing	Dill (1993) Krolop et al. (2018)
5	Germany	Erzgebirge	Ordovician to Carboniferous phyllite, slate, black shale, volcanite	Variscan anticlinal zones	Dilational veins, cleavage-concordant mineralization	py[1], asp[1], gold[1], sbn[2], qtz[2], sph[3], gn[3], carbonate[3], Pb-Sb-Ag sulfosalts[3], zk, bno, bou, btr, dys, fhl, freibergite					Dill (1993) Wagner and Cook (2000) Burisch et al. (2018)
6	France	Vosges Mountains, Charbes	Gneiss, granite, phyllite, schist			sbn, asp, bou, freieslebenite, fülöppite, dys, pyrg, falor, py, zk, sph, silver, btr, ramdohrite, stibiconite, qtz, cal, dolomite					Wittern and Journée (1997)
6	France	Vosges Mountains, Urbeis	Silurian-Cambrian schist			e.g. sbn, freibergite, asp, btr, cal, ccp, bno, bou, ferberite, gn, pyrg, py, silver, scheelite, sph, stibiconite, fhl, qtz					Meyer and Hohl (1994)
7	Germany	Schwarzwald	Devonian metamorphic conglomerate, Variscan paragneiss and migmatite	Late-Variscan extensional shear zones	Late-orogenic, post-compressive brittle tectonic events	See Fig. 2 for details	100–400 °C	50–250 °C	50–170 °C	Fluid cooling, fluid mixing	Staude et al. (2007, 2010a, 2010b, 2012)) Walter et al. (2016, 2017, 2018a) This study
8	Germany	Fichtelgebirge	Ordovician to Devonian slate, phyllite, diabase, keratophyr			sbn, chalcostibite, zk, plg, sms, bou, jms, menehinite, antimony, Ag-tetrahedrite, gold					Dill (1993)
8	Germany	Oberpfälzer Wald	Ordovician phyllite								Dill (1993)

Table 1 (continued)

	Country	District	Host rocks	Structural position	Mineralized structures	Mineral assemblage	Th of fluid inclusion types			Formation	Reference
							A	B	C		
						chalcostibite, bno, bou, jms, geocronite, antimony, fhl					
9	Czech Republic	Bohemian Massif; Pribram, Kutná Hora	Cambrian to Precambrian slate, granite, sandstone, schist, conglomerate, diabase, gneiss, lamprophyr			sbn, bou, geocronite, bno, sms, jms, btr, pyrg, stephanite, diaphorite, Ag-sulfosalts, aurostibite, antimony, fhl, gold					Dill (1993)
10–13	Slovakia	West-Carpathians, Kremnica	Devonian to Permian, Miocene, migmatite, gneiss, granite, phyllite, schist, andesite			jms, fhl, gold, btr, Ag-Sb sulfosalts, bou, antimony, chalcostibite, zk, dys, cinnabar					Dill (1993)
		West-Carpathians; Dúbrava, Tatra Mountains				scheelite, py[1–3], qtz[1–5], molybdenite[1], asp[2], sph[3], zk[3], dolomite[3–5], fhl[4], bno[4], chalcostibite[4], Pb-Sb-Bi sulfosalts[4], barite[5], cal[5], strontianite[5]	315–355 °C[1]; 305–350 °C[2]	105–170 °C[3]	118–162 °C[4]; 105–158 °C[5]		Chovan et al. (1995)
14-15	France	Massif Armoricain, Massif Central	Upper Precambrian to Silurian shale, sandstone, micaschist, gneiss, granite	Variscan folded and thrusted sequences, major anticlinal zones	Veinlet networks, satellites of extensional shear zones	asp[1],py[1], gold[1], qtz[1–3], cal[1], sph[2], gn[2], ccp[2], sulfosalts[2,3], sbn[3]	280–410 °C	260–390 °C	100–280 °C	Simple cooling, fluid dilution	Bril (1982) Bril and Beaufort (1989) Boiron et al. (1990) Munoz et al. (1992) Pochon et al. (2016)
16	Portugal	Dúrico-Beirao district	Pre-Ordovician to Silurian conglomerate, quartzite, schist	Variscan anticline	N-NE subvertical fractures	asp[1,4], py[1,2,4], gold[1], cassiterite[1], wolframite[1], qtz[1–3], sph[2,3], ccp[2], pyrrhotite[2], fhl[2], jms[3], bou[3], gn[3], carbonate[3,4], btr[4], sbn[4]	290–340 °C	230–320 °C	128–225 °C	Fluid mixing, dilution, and cooling	Couto et al. (1990)
17	Spain	Spanish Hercynian Massif; Mari Rosa	Upper Precambrian greywacke, phyllite, slate	Variscan anticline core	Dilational veins	asp[1], py[1,3], qtz[1,2,3], sbn[2], gold[2], pyrrhotite[3], sph[3], sulfosalts[3], btr	270–390 °C	180–330 °C	150–270 °C	Fluid mixing	Gumiel and Arribas (1987) Ortega et al. (1991) Ortega and Vindel (1995)

Mineralization stages according to the respective reference are shown with superscripts 1–5

asp arsenopyrite, *py* pyrite, *ccp* chalcopyrite, *sph* sphalerite, *gn* galena, *sbn* stibnite, *jms* jamesonite, *bno* bournonite, *bou* boulangerite, *fhl* fahlore, *zk* zinkenite, *plg* plagionite, *sms* semseyite, *btr* berthierite, *qtz* quartz, *pyrg* pyrargyrite, *dys* dyscrasite, *cal* calcite

(e.g., Hillgrove Au-Sb deposit in Australia, Ashley et al. 1990; Ashley et al. 2000; Lake George Sb deposit in Canada, Yang et al. 2004; Woxi deposit in China, Zhu and Peng 2015), may further aid ore formation at some localities, but due to the lack of features such as boiling in fluid inclusions from many localities and a general presence of cooling indicators, further processes are not essential.

Although the vast difference in size between deposits may be attributed to processes such as boiling further aiding precipitation, it is likely that it is predefined by the tectonic setting/absolute fluid volume and is thus structurally controlled. For example, the formation of frequent small scale deposits in Europe may be related to the presence of abundant former micro-continents and predefined small scale fractures (Kalt et al. 2000; Geyer et al. 2011).

Due to the economic insignificance of late-stage sulfosalts in economically important worldwide deposits, their formation is commonly not investigated in sufficient detail. However, all deposits generally show an evolution from an Fe-Sb stage to a Pb-enriched stage (e.g., Kaiman et al. 1980; Ashley et al. 1990; Dill et al. 1995; Bortnikov et al. 2010), where the formation of the commonly occurring Pb- rich sulfosalts (e.g., Hagemann et al. 1994; Chovan et al. 1998; Tomkins et al. 2004) is not linked to the initial cooling process but to remobilization processes of stibnite (e.g. Schwarzwald, this study; Kharma ore deposit in Bolivia, Dill et al. 1995). This could indicate a polystage nature of other deposits around the globe with a typical and common evolutionary process representing a transition from initial cooling of a late-metamorphic fluid system (stage I) to a system dominated by a typical Pb-rich saline basinal brine of initial seawater/meteoric fluid origin (subsequent stages). Hence, this study can be used as an example for future investigations of remobilization processes within hydrothermal Sb deposits worldwide.

Conclusions

Quartz rich Sb-Pb-Ag±Au veins in the Schwarzwald can be seen as representative examples of this ore type with a high mineralogical diversity. They typically show four mineralization stages that can be related to distinct mineralization events,

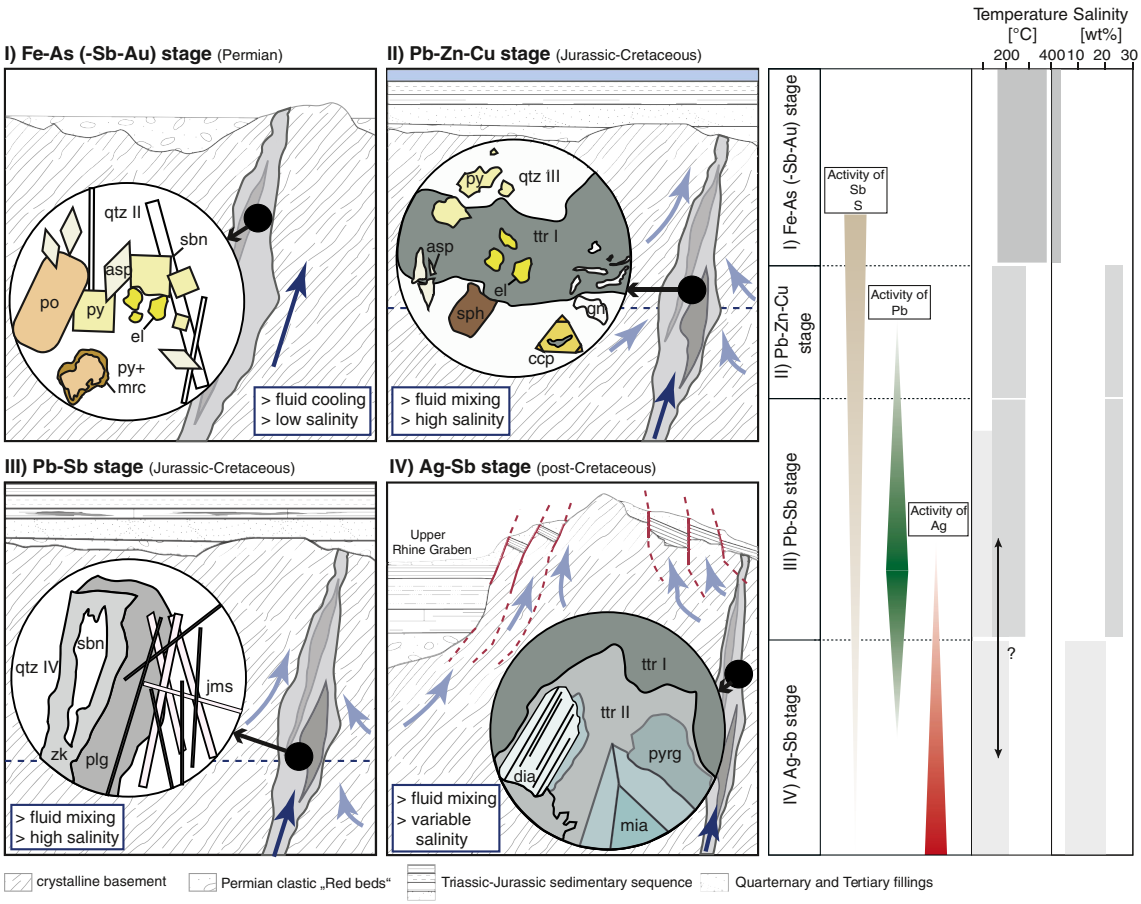

Fig. 13 Summary of all mineralization stages I–IV with representative mineral sketch of each stage, schematically illustrating geological setting, corresponding fluid temperature and salinity, as well as activities of important elements. Po = pyrrhotite, py = pyrite, mrc = marcasite, asp = arsenopyrite, sbn = stibnite, qtz = quartz, sph = sphalerite, ccp = chalcopyrite, ttr = tetrahedrite, gn = galena, zk = zinkenite, plg = plagionite, jms = jamesonite, dia = diaphorite, mia = miargyrite, and pyrg = pyrargyrite. Gray boxes show the ranges of each parameter

metal and fluid source, and precipitation mechanisms: The characteristic mineral sequence of the primary ore stage I is formed by cooling of late-metamorphic (400–100 °C), low-salinity fluids with maximum salinities of 5 wt% (NaCl eq.) (Fig. 13). A remobilization of early minerals which incorporate significant amounts of invisible gold, such as arsenopyrite, pyrite, marcasite, and stibnite, leads to the precipitation of electrum, which is observed at Sb-Au-deposits worldwide. The development and thus the character of later mineralization stages is strongly dependent on the abundance and remobilization of pre-existing Sb minerals. The fluid composition evolved to high-salinity (up to 28 wt% NaCl eq. and < 250 °C) and Pb-rich fluids which remobilized stibnite and formed a complex Pb-Sb mineral assemblage (Fig. 13). This transition from an initially late-metamorphic fluid system to a saline basinal brine fluid system is also evident for many other examples of this deposit type. During the influx of Pb, remobilization of stibnite leads to the formation of various Pb-Sb-bearing sulfosalts, whereas during limited remobilization, galena forms. The last mineralization stage is locally confined to only some localities in the Variscan belt affected by Tertiary tectonic events (e.g., Upper Rhine Graben and Eger Graben). A rift-related hydrothermal fluid with variable salinity and low temperature (7–20 wt%, 150 °C) combined with an influx of Ag into the pre-existing mineralization leads to the replacement of Pb-Sb minerals and formation of a distinct Ag-rich assemblage during this stage.

Acknowledgements We would like to thank Steffen Hagemann and Wolfgang Werner for their constructive comments that improved this manuscript significantly. Bernd Lehmann and Jens Gutzmer are thanked for careful and thoughtful editorial handling of this manuscript. We are grateful to Thomas Wenzel for the assistance with the electron microprobe. Simone Schafflick and Per Jeiseke are thanked for sample preparation. We would also like to thank Bernd Steinhilber and Gabriele Stoschek for isotope measurements and their help with crush leach analyses and technical support. Further thanks go Thomas Seifert for the possibility to analyze fluid inclusions in stibnite and sphalerite at the TU Bergakademie Freiberg and to Matthias Bauer and Lisa Richter for their help and supervision. Olga Apukhtina is thanked for data acquisition at the Münstergrund locality.

References

Altherr R, Holl A, Hegner E, Langer C, Kreuzer H (2000) High-potassium, calc-alkaline I-type plutonism in the European Variscides: northern Vosges (France) and northern Schwarzwald (Germany). Lithos 50:51–73. https://doi.org/10.1016/S0024-4937(99)00052-3

Arthaud F, Matte P (1977) Late Paleozoic strike-slip faulting in southern Europe and northern Africa: result of a right-lateral shear zone between the Appalachians and the Urals. Geol Soc Am Bull 88:1305–1320. https://doi.org/10.1130/0016-7606(1977)88<1305:LPSFIS>2.0.CO;2

Ashley P, Cook N, Hill R (1990) Occurrence and significance of aurostibite in Sb-Au ore from Hillgrove, New-South-Wales, Australia. Neues JB Mineral Monat:537–551

Ashley P, Creagh C, Ryan C (2000) Invisible gold in ore and mineral concentrates from the Hillgrove gold-antimony deposits, NSW, Australia. Mineral Deposita 35:285–301

Baatartsogt B, Schwinn G, Wagner T, Taubald H, Beitter T, Markl G (2007) Contrasting paleofluid systems in the continental basement: a fluid inclusion and stable isotope study of hydrothermal vein mineralization, Schwarzwald district, Germany. Geofluids 7:123–147. https://doi.org/10.1111/j.1468-8123.2007.00169.x

Baltukhaev GI, Solozhenkin PM (2009) Concentration of gold-antimony ores in the Sakha Republic (Yakutia). Russ J Non-Ferr Met+ 50:199–205. https://doi.org/10.3103/S106782120903002X

Behr H-J, Gerler J (1987) Inclusions of sedimentary brines in post-Variscan mineralizations in the Federal Republic of Germany—a study by neutron activation analysis. Chem Geol 61:65–77. https://doi.org/10.1016/0009-2541(87)90028-3

Behr H-J, Engel W, Franke W, Giese P, Weber K (1984) The Variscan belt in Central Europe: main structures, geodynamic implications, open questions. Tectonophysics 109:15–40. https://doi.org/10.1016/0040-1951(84)90168-9

Boiron M, Cathelineau M, Dubessy J, Bastoul A (1990) Fluids in Hercynian Au veins from the French Variscan belt. Mineral Mag 54:231–243

Bons PD, Fusswinkel T, Gomez-Rivas E, Markl G, Wagner T, Walter B (2014) Fluid mixing from below in unconformity-related hydrothermal ore deposits. Geology 42:1035–1038. https://doi.org/10.1130/G35708.1

Bortnikov N, Gamynin G, Vikent'eva O, Prokof'ev VY, Prokop'ev A (2010) The Sarylakh and Sentachan gold-antimony deposits, Sakha-Yakutia: a case of combined mesothermal gold-quartz and epithermal stibnite ores. Geol Ore Deposit+ 52:339–372

Bouchot V, Gros Y, Bonnemaison M (1989) Structural controls on the auriferous shear zones of the Saint Yrieix District, Massif Central, France; evidence from the Le Bourneix and Laurieras gold deposits. Econ Geol 84:1315–1327. https://doi.org/10.2113/gsecongeo.84.5.1315

Brander T (2000) U/HE-chronologische Fallstudien an Eisen-und Manganerzen Department of Geoscience. Ruprecht-Karls University Heidelberg, pp 275.

Bril H (1982) Fluid inclusions study of Sn–W–Au, Sb– and Pb–Zn mineralizations from the Brioude-Massiac district (French Massif Central). Tscher Miner Petrog 30:1–16. https://doi.org/10.1007/BF01082422

Bril H, Beaufort D (1989) Hydrothermal alteration and fluid circulation related to W, Au, and Sb vein mineralization, Haut Allier, Massif Central, France. Econ Geol 84:2237–2251. https://doi.org/10.2113/gsecongeo.84.8.2237

Bucher K, Stober I (2002) Water-rock reaction experiments with Black Forest gneiss and granite Water-rock interaction Springer, pp 61–95.

Bucher K, Stober I (2010) Fluids in the upper continental crust. Geofluids 10:241–253. https://doi.org/10.1007/s00531-008-0328-x.

Bucher K, Zhu Y, Stober I (2009) Groundwater in fractured crystalline rocks, the Clara mine, Black Forest (Germany). Int J Earth Sci 98:1727–1739. https://doi.org/10.1111/j.1468-8123.2010.00279.x.

Burisch M, Marks MA, Nowak M, Markl G (2016) The effect of temperature and cataclastic deformation on the composition of upper crustal fluids—an experimental approach. Chem Geol 433:24–35. https://doi.org/10.1016/j.chemgeo.2016.03.031

Burisch M, Hartmann A, Bach W, Krolop P, Krause J, Gutzmer J (2018, this issue) Genesis of hydrothermal silver-antimony-sulfide veins of the Bräunsdorf sector of the Freiberg District, Germany. Mineral Deposita

Chicharro E, Boiron M-C, López-García JÁ, Barfod DN, Villaseca C (2016) Origin, ore forming fluid evolution and timing of the Logrosán Sn–(W) ore deposits (Central Iberian Zone, Spain). Ore Geol Rev 72:896–913. https://doi.org/10.1016/j.oregeorev.2015.09.020.

Chovan M, Hurai V, Sachan H, Kantor J (1995) Origin of the fluids associated with granodiorite-hosted, Sb-As-Au-W mineralisation at Dúbrava (Nízke Tatry Mts, Western Carpathians). Mineral Deposita 30:48–54. https://doi.org/10.1007/BF00208876

Chovan M, Majzlan J, Kristin J, Ragan M, Siman P (1998) Pb-Sb and Pb-Sb-Bi sulfosalts and associated sulphides from Dúbrava antimony deposit, Nízke Tatry Mts Acta Geologica Universitatis Comenianae.

Cidu R, Biddau R, Dore E, Vacca A, Marini L (2014) Antimony in the soil–water–plant system at the Su Suergiu abandoned mine (Sardinia, Italy): strategies to mitigate contamination. Sci Total Environ 497:319–331. https://doi.org/10.1016/j.scitotenv.2014.07.117.

Clayton R, Scrivener R, Stanley C (1990) Mineralogical and preliminary fluid inclusion studies of lead-antimony mineralisation in north Cornwall. Proc Ussher 7:258–262

Comsti E, Taylor G (1984) Implications of fluid inclusion data on the origin of the Hillgrove gold-antimony deposits. NSW Proceedings of the Australasian Institute of Mining & Metallurgy 289:195–203

Couto H, Roger G, Moëlo Y, Bril H (1990) Le district à antimoine-or Dúrico-Beirão (Portugal): évolution paragénétique et géochimique; implications métallogéniques. Mineral Deposita 25:S69–S81. https://doi.org/10.1007/BF00205252

Craig H (1961) Isotopic variations in meteoric waters. Science 133:1702–1703. https://doi.org/10.1126/science.133.3465.1702

Dennert V (1993) Der Bergbau vom Mittelalter bis heute im Auftrag der Stadt Sulzburg von der Anna Hugo Bloch-Stiftung Red Anneliese Müller and Jost Grosspietsch Bd 1:119–221.

Dill H (1985) Antimoniferous mineralization from the Mid-European Saxothuringian Zone: mineralogy, geology, geochemistry and ensialic origin. Geol Rundsch 74:447–466. https://doi.org/10.1007/BF01821205

Dill H (1986) Die Vererzung am Westrand der Böhmischen Masse. Geologisches Jahrbuch Reihe D 500:73

Dill HG (1993) Die Antimonvorkommen der mitteleuropäischen Alpiden und Varisziden. Z Dtsch Geol Ges:434–450

Dill H (1998) Evolution of Sb mineralisation in modern fold belts: a comparison of the Sb mineralisation in the Central Andes (Bolivia) and the Western Carpathians (Slovakia). Mineral Deposita 33:359–378. https://doi.org/10.1007/s001260050155

Dill H, Weiser T, Bernhardt I, Kilibarda CR (1995) The composite gold-antimony vein deposit at Kharma (Bolivia). Econ Geol 90:51–66. https://doi.org/10.2113/gsecongeo.90.1.51

Distanov E, Stebleva A, Obolenskii A, Kochetkova K, Borisenko A (1975) Origin of the Uderei gold-antimony field in the Yenisei Ridge area. Geol Geofiz 16:19–27

Doblas M, López-Ruiz J, Oyarzun R, Mahecha V, Moya YS, Hoyos M, Cebriá J-M, Capote R, Enrile JH, Lillo J (1994) Extensional tectonics in the Central Iberian Peninsula during the Variscan to Alpine transition. Tectonophysics 238:95–116. https://doi.org/10.1016/0040-1951(94)90051-5.

Frezzotti ML, Tecce F, Casagli A (2012) Raman spectroscopy for fluid inclusion analysis. J Geochem Explor 112:1–20. https://doi.org/10.1016/j.gexplo.2011.09.009.

Gammons C, Williams-Jones A (1997) Chemical mobility of gold in the porphyry-epithermal environment. Econ Geol 92:45–59. https://doi.org/10.2113/gsecongeo.92.1.45

Geyer OF, Gwinner MP, Geyer M, Nitsch E, Simon T (2011) Geologie von Baden-Württemberg. 626.

Goldstein RH, Reynolds TJ (1994) Fluid inclusion microthermometry.

Guillemette N, Williams-Jones A (1993) Genesis of the Sb-W-Au deposits at Ixtahuacan, Guatemala: evidence from fluid inclusions and stable isotopes. Mineral Deposita 28:167–180

Gumiel P, Arribas A (1987) Antimony deposits in the Iberian Peninsula. Econ Geol 82:1453–1463

Hagemann SG, Lüders V (2003) PTX conditions of hydrothermal fluids and precipitation mechanism of stibnite-gold mineralization at the Wiluna lode-gold deposits, Western Australia: conventional and infrared microthermometric constraints. Mineral Deposita 38:936–952. https://doi.org/10.1007/s00126-003-0351-6

Hagemann SG, Gebre-Mariam M, Groves DI (1994) Surface-water influx in shallow-level Archean lode-gold deposits in Western, Australia. Geology 22:1067–1070

Hann H, Chen F, Zedler H, Frisch W, Loeschke J (2003) The Rand Granite in the southern Schwarzwald and its geodynamic significance in the Variscan belt of SW Germany. Int J Earth Sci 92:821–842. https://doi.org/10.1007/s00531-003-0361-8

Irber W, Lehrberger G (1993) Das Gold-Erzrevier von Goldkronach-Brandholz im Fichtelgebirge: Ein modifiziertes Genesemodell. Eur J Mineral 5:225

Kaiman S, Harris D, Dutrizac J (1980) Stibivanite, a new mineral from Lake George antimony deposit, New Brunswick. Can Mineral 18:329–332

Kalt A, Altherr R, Hanel M (2000) The Variscan basement of the Schwarzwald. Eur J Mineral 12:1–43

Kendall C, Coplen TB (2001) Distribution of oxygen-18 and deuterium in river waters across the United States. Hydrol Process 15:1363–1393. https://doi.org/10.1002/hyp.217

Knipe R (1993) The influence of fault zone processes and diagenesis on fluid flow. In: Horbury AD and Robinson AG (ed) Diagenesis and Basin Development, Vol 36, American Association of Petroleum Geologists, pp 135-151

Kolchugin A, Immenhauser A, Walter B, Morozov V (2016) Diagenesis of the palaeo-oil-water transition zone in a Lower Pennsylvanian carbonate reservoir: constraints from cathodoluminescence microscopy, microthermometry, and isotope geochemistry. Mar Pet Geol 72:45–61

Kontak DJ, Horne RJ, Smith PK (1996) Hydrothermal characterization of the West Gore Sb-Au deposit, Meguma Terrane, Nova Scotia, Canada. Econo Geol 91(7):1239–1262. https://doi.org/10.2113/gsecongeo.91.7.1239

Kontny A, Friedrich G, Behr H, Hd W, Horn E, Möller P, Zulauf G (1997) Formation of ore minerals in metamorphic rocks of the German continental deep drilling site (KTB). Journal of Geophysical Research: Solid Earth 102:18323–18336. https://doi.org/10.1029/96JB03395

Kovalev K, Kalinin YA, Naumov E, Kolesnikova M, Korolyuk V (2011) Gold-bearing arsenopyrite in eastern Kazakhstan gold-sulfide deposits. Russ Geol Geophys 52:178–192

Krolop P, Burisch M, Richter L, Fritzke B, Seifert T (2018) Antimoniferous vein-type mineralization of the Berga Antiform, Eastern-Thuringia, Germany: A fluid inclusion study. Chem Geol. https://doi.org/10.1016/j.chemgeo.2018.02.034

Kroner U, Romer R (2013) Two plates—many subduction zones: the Variscan orogeny reconsidered. Gondwana Res 24:298–329. https://doi.org/10.1016/j.gr.2013.03.001

Krützfeldt B (1985) Beobachtungen an Vererzungen in Sedimenten der Zone Badenweiler-Lenzkrich. Der Aufschluss 36:261–265

Kulick J, Meisl S, Theuerjahr A-K (1997) Die Goldlagerstätte des Eisenberges: südwestlich von Korbach. Hessisches Landesamt für Bodenforschung

Lehrberger G (1995) The gold deposits of Europe Prehistoric gold in Europe. Springer, pp 115–144.

Lentz DR, Thorne K, Yang X-M (2002) Preliminary analysis of the controls on the various episodes of gold mineralization at the Lake George antimony deposit, New Brunswick Current research:02–01

Ligang Z, Jingxiu L, Huanbo Z, Zhensheng C (1989) Oxygen isotope fractionation in the quartz-water-salt system. Econ Geol 84:1643–1650. https://doi.org/10.2113/gsecongeo.84.6.1643

Malavieille J, Guihot P, Costa S, Lardeaux J, Gardien V (1990) Collapse of the thickened Variscan crust in the French Massif Central: Mont Pilat extensional shear zone and St. Etienne Late Carboniferous basin. Tectonophysics 177:139–149. https://doi.org/10.1016/0040-1951(90)90278-G

Markl G (2017) Schwarzwald - Lagerstätten und Mineralien aus vier Jahrhunderten. Band 4 - Südlicher Schwarzwald., Bode

Markl G, Burisch M, Neumann U (2016) Natural fracking and the genesis of five-element veins. Mineral Deposita 51:703–712. https://doi.org/10.1007/s00126-016-0662-z

Marks MA, Marschall HR, Schühle P, Guth A, Wenzel T, Jacob DE, Barth M, Markl G (2013) Trace element systematics of tourmaline in pegmatitic and hydrothermal systems from the Variscan Schwarzwald (Germany): the importance of major element composition, sector zoning, and fluid or melt composition. Chem Geol 344:73–90. https://doi.org/10.1016/j.chemgeo.2013.02.025

Matte P (1991) Accretionary history and crustal evolution of the Variscan belt in Western Europe. Tectonophysics 196:309–337. https://doi.org/10.1016/0040-1951(91)90328-P

Metz R, Richter M (1957) Die Blei-Zink-Erzgänge des Schwarzwaldes. Beihefte zum Geologischen Jahrbuch Beiheft 29:277

Meyer J, Hohl J-L (1994) Minerals engineering Reviews in mineralogy and geochemistry. Editions du Rhin

Meyer M, Brockamp O, Clauer N, Renk A, Zuther M (2000) Further evidence for a Jurassic mineralizing event in Central Europe: K–Ar dating of hydrothermal alteration and fluid inclusion systematics in wall rocks of the Käfersteige fluorite vein deposit in the northern Black Forest, Germany. Mineral Deposita 35:754–761. https://doi.org/10.1007/s001260050277

Moravek P, Pouba Z (1987) Precambrian and Phanerozoic history of gold mineralization in the Bohemian Massif. Econ Geol 82:2098–2114. https://doi.org/10.2113/gsecongeo.82.8.2098

Munoz M, Shepherd T (1987) Fluid inclusion study of the bournac polymetallic (Sb-As-Pb-Zn-Fe-Cu...) vein deposit (montagne noire, France). Mineral Deposita 22:11–17

Munoz M, Courjault-Radé P, Tollon F (1992) The massive stibnite veins of the French Palaeozoic basement: a metallogenic marker of Late Variscan brittle extension. Terra Nova 4:171–177. https://doi.org/10.1111/j.1365-3121.1992.tb00468.x

Neiva A, Andráš P, Ramos J (2008) Antimony quartz and antimony–gold quartz veins from northern Portugal. Ore Geol Rev 34:533–546. https://doi.org/10.1016/j.oregeorev.2008.03.004

Obolensky A, Gushchina L, Borisenko A, Borovikov A, Pavlova G (2007) Antimony in hydrothermal processes: solubility, conditions of transfer, and metal-bearing capacity of solutions. Russ Geol Geophys 48:992–1001. https://doi.org/10.1016/j.rgg.2007.11.006

Ortega L, Vindel E (1995) Evolution of ore-forming fluids associated with late Hercynian antimony deposits in central/western Spain; case study of Mari Rosa and El Juncalon. Eur J Mineral 7:655–673 0935–1221/95/0007–0655

Ortega L, Vindel E, Beny C (1991) COHN fluid inclusions associated with gold-stibnite mineralization in low-grade metamorphic rocks, Mari Rosa mine, Caceras, Spain. Mineral Mag 55:235–247. https://doi.org/10.1180/minmag.1991.055.379.12.

Pascher G (1985) Gold aus dem Fichtelgebirge. Ein montanhistorischer und mineralogischer Überblick. Lapis 10:25–42

Pfaff K, Romer RL, Markl G (2009) U-Pb ages of ferberite, chalcedony, agate, 'U-mica'and pitchblende: constraints on the mineralization history of the Schwarzwald ore district. Eur J Mineral 21:817–836. https://doi.org/10.1127/0935-1221/2009/0021-1944

Pfaff K, Hildebrandt LH, Leach DL, Jacob DE, Markl G (2010) Formation of the Wiesloch Mississippi Valley-type Zn-Pb-Ag deposit in the extensional setting of the Upper Rhinegraben, SW Germany. Mineral Deposita 45:647–666. https://doi.org/10.1007/s00126-010-0296-5

Pfaff K, Koenig A, Wenzel T, Ridley I, Hildebrandt LH, Leach DL, Markl G (2011) Trace and minor element variations and sulfur isotopes in crystalline and colloform ZnS: incorporation mechanisms and implications for their genesis. Chem Geol 286:118–134. https://doi.org/10.1016/j.chemgeo.2011.04.018.

Pochon A, Gapais D, Gloaguen E, Gumiaux C, Branquet Y, Cagnard F, Martelet G (2016) Antimony deposits in the Variscan Armorican belt, a link with mafic intrusives? Terra Nova 28:138–145. https://doi.org/10.1111/ter.12201

Rajchl M, Uličný D, Grygar R, Mach K (2009) Evolution of basin architecture in an incipient continental rift: the Cenozoic Most Basin, Eger Graben (Central Europe). Basin Res 21:269–294. https://doi.org/10.1111/j.1365-2117.2008.00393.x

Romer RL, Kroner U (2017) Paleozoic gold in the Appalachians and Variscides. Ore Geol Rev 92:475–505. https://doi.org/10.1016/j.oregeorev.2017.11.021

Roscher M, Schneider JW (2006) Permo-Carboniferous climate: Early Pennsylvanian to Late Permian climate development of Central Europe in a regional and global context. Geol Soc Lond, Spec Publ 265:95–136. https://doi.org/10.1144/GSL.SP.2006.265.01.05

Rumble D, Hoering TC (1994) Analysis for oxygen and sulfur isotope ratios in oxide and sulfide minerals by spot heating with a carbon dioxide laser in a fluorine atmosphere. Acc Chem Res 27:237–241

Schroyen K, Muchez P (2000) Evolution of metamorphic fluids at the Variscan fold-and-thrust belt in eastern Belgium. Sediment Geol 131:163–180. https://doi.org/10.1016/S0037-0738(99)00133-5

Schwarz-Schampera U (2014) Antimony. Critical metals handbook:70–98.

Seal I, Robert R, Robie RA, Barton Jr PB, Hemingway B (1992) Superambient heat capacities of synthetic stibnite, berthierite, and chalcostibite: revised thermodynamic properties and implications for phase equilibria.

Seward TM (1973) Thio complexes of gold and the transport of gold in hydrothermal ore solutions. Geochim Cosmochim Acta 37:379–399. https://doi.org/10.1016/0016-7037(73)90207-X

Sharp ZD (1990) A laser-based microanalytical method for the in situ determination of oxygen isotope ratios of silicates and oxides. Geochim Cosmochim Acta 54:1353–1357. https://doi.org/10.1016/0016-7037(90)90160-M

Sheppard SM (1986) Characterization and isotopic variations in natural waters. Rev Mineral Geochem 16:165–183

Staude S, Wagner T, Markl G (2007) Mineralogy, mineral compositions and fluid evolution at the Wenzel hydrothermal deposit, Southern

Germany: implications for the formation of Kongsberg-type silver deposits. Can Mineral 45:1147–1176. https://doi.org/10.2113/gscanmin.45.5.1147

Staude S, Bons PD, Markl G (2009) Hydrothermal vein formation by extension-driven dewatering of the middle crust: an example from SW Germany. Earth Planet Sci Lett 286:387–395. https://doi.org/10.1016/j.epsl.2009.07.012

Staude S, Dorn A, Pfaff K, Markl G (2010a) Assemblages of Ag–Bi sulfosalts and conditions of their formation: the type locality of schapbachite (Ag0. 4Pb0. 2Bi0. 4S) and neighboring mines in the Schwarzwald ore district, southern Germany. Can Mineral 48:441–466. https://doi.org/10.3749/canmin.48.3.441

Staude S, Mordhorst T, Neumann R, Prebeck W, Markl G (2010b) Compositional variation of the tennantite–tetrahedrite solidsolution series in the Schwarzwald ore district (SW Germany): the role of mineralization processes and fluid source. doi: https://doi.org/10.1180/minmag.2010.074.2.309.

Staude S, Werner W, Mordhorst T, Wemmer K, Jacob DE, Markl G (2012) Multi-stage Ag–Bi–Co–Ni–U and Cu–Bi vein mineralization at Wittichen, Schwarzwald, SW Germany: geological setting, ore mineralogy, and fluid evolution. Mineral Deposita 47:251–276. https://doi.org/10.1007/s00126-011-0365-4

Steele-MacInnis M, Bodnar R, Naden J (2011) Numerical model to determine the composition of H2O–NaCl–CaCl2 fluid inclusions based on microthermometric and microanalytical data. Geochim Cosmochim Acta 75:21–40. https://doi.org/10.1016/j.gca.2010.10.002

Steele-MacInnis M, Lecumberri-Sanchez P, Bodnar RJ (2012) HOKIEFLINCS_H2O-NACL: a Microsoft Excel spreadsheet for interpreting microthermometric data from fluid inclusions based on the PVTX properties of H2O–NaCl. Comput Geosci 49:334–337

Stober I, Bucher K (1999) Deep groundwater in the crystalline basement of the Black Forest region. Appl Geochem 14:237–254. https://doi.org/10.1016/S0883-2927(98)00045-6.

Taylor H, Barnes H (1997) Oxygen and hydrogen isotope relationships in hydrothermal mineral deposits. Geochemistry of hydrothermal ore deposits 3:229–302

Todt W (1976) Zirkon U/Pb-Alter des Malsburg-Granits vom Südschwarzwald. Neues Jb Miner Abh 12:532–544

Tomkins AG, Pattison DR, Zaleski E (2004) The Hemlo gold deposit, Ontario: an example of melting and mobilization of a precious metal-sulfosalt assemblage during amphibolite facies metamorphism and deformation. Econ Geol 99:1063–1084

Wagner T, Cook N (2000) Late-Variscan antimony mineralisation in the Rheinisches Schiefergebirge, NW Germany: evidence for stibnite precipitation by drastic cooling of high-temperature fluid systems. Mineral Deposita 35:206–222. https://doi.org/10.1007/s001260050016

Wagner T, Fusswinkel T, Wälle M, Heinrich CA (2016) Microanalysis of fluid inclusions in crustal hydrothermal systems using laser ablation methods. Elements 12:323–328. https://doi.org/10.2113/gselements.12.5.323

Walenta K (1957) Die antimonerzführenden Gänge des Schwarzwaldes. Jahreshefte des Geologischen Landesamtes Baden-Württemberg 2:13–67

Walenta K, Sawatzki G, Dayal R (1970) Die Wolframerzvorkommen im Gebiet des Nordracher Granitmassivs und seiner Umgebung. Jahresh Geol Landesamt Baden-Wuerttemberg 12:207–226

Walter BF, Immenhauser A, Geske A, Markl G (2015) Exploration of hydrothermal carbonate magnesium isotope signatures as tracers for continental fluid aquifers, Schwarzwald mining district, SW Germany. Chem Geol 400:87–105. https://doi.org/10.1016/j.chemgeo.2015.02.009

Walter BF, Burisch M, Markl G (2016) Long-term chemical evolution and modification of continental basement brines—a field study from the Schwarzwald, SW Germany. Geofluids 16:604–623. https://doi.org/10.1111/gfl.12167

Walter BF, Burisch M, Marks MAW, Markl G (2017) Major element compositions of fluid inclusions from hydrothermal vein-type deposits record eroded sedimentary units in the Schwarzwald district, SW Germany. Mineral Deposita 52:1191–1204. https://doi.org/10.1007/s00126-017-0719-7

Walter BF, Burisch M, Fusswinkel T, Marks MAW, Steele-MacInnis M, Wälle M, Apukhtina OB, Markl G (2018a) Multi-reservoir fluid mixing processes in rift-related hydrothermal veins, Schwarzwald, SW-Germany. J Geochem Explor 186:158–186. https://doi.org/10.1016/j.gexplo.2017.12.004

Walter BF, Kortenbruck P, Zeitvogel C, Wälle M, Mertz-Kraus R, Markl G (submitted 2018b) Chemical evolution of ore-forming brines—basement leaching, metal provenance, and the redox link between barren and ore-bearing hydothermal veins. Chem Geol

Walter BF, Gerdes A, Kleinhanns IC, Dunkl I, von Eynatten H, Kreissl S, Markl G (2018c) The connection between hydrothermal fluids, mineralization, tectonics and magmatism in a continental rift setting: fluorite Sm-Nd and hematite and carbonates U-Pb geochronology from the Rhinegraben in SW Germany. Geochim Cosmochim Acta. https://doi.org/10.1016/j.gca.2018.08.012

Weissert H, Erba E (2004) Volcanism, CO2 and palaeoclimate: a Late Jurassic–Early Cretaceous carbon and oxygen isotope record. J Geol Soc 161:695–702. https://doi.org/10.1144/0016-764903-087

Werner W (2002) Die Erzlagerstätte Schauinsland bei Freiburg im Breisgau: Bergbau, Geologie, Hydrogeologie, Mineralogie, Geochemie, Tektonik und Lagerstättenentstehung. Aedificatio-Verlag.

Werner W, Franzke HJ (2001) Postvariszische bis neogene Bruchtektonik und Mineralisation im südlichen Zentralschwarzwald. Z Dtsch Geol Ges:405–437.

Werner W, Schlaegel-Blaut P, Rieken R (1990) Verbreitung und Ausbildung von Wolfram-Mineralisationen im Kristallin des Schwarzwaldes. Jahreshefte des Geologischen Landesamtes Baden-Württemberg 32:17–61

Wetzel A, Allenbach R, Allia V (2003) Reactivated basement structures affecting the sedimentary facies in a tectonically “quiescent” epicontinental basin: an example from NW Switzerland. Sediment Geol 157:153–172. https://doi.org/10.1016/S0037-0738(02)00230-0

Williams-Jones AE, Bowell RJ, Migdisov AA (2009) Gold in solution. Elements 5:281–287. https://doi.org/10.2113/gselements.5.5.281

Wittern A, Journée J-R (1997) Mineralien finden in den Vogesen: ein Führer zu über 40 Fundstellen. Sven Von Loga, Köln

Wood SA, Crerar DA, Borcsik MP (1987) Solubility of the assemblage pyrite-pyrrhotite-magnetite-sphalerite-galena-gold-stibnite-bismuthinite-argen-tite-molybdenite in H2O-NaCl-CO2 solutions from 200 degrees to 350 degrees C. Econ Geol 82(7):1864–1887. https://doi.org/10.2113/gsecongeo.82.7.1864

Yang X-M, Lentz DR, Chi G, Kyser TK (2004) Fluid–mineral reaction in the Lake George Granodiorite, New Brunswick, Canada: implications for Au–W–Mo–Sb mineralization. Can Mineral 42:1443–1464

Yardley BW (2005) 100th Anniversary Special Paper: metal concentrations in crustal fluids and their relationship to ore formation. Econ Geol 100:613–632. https://doi.org/10.2113/gsecongeo.100.4.613

Zachariáš J, Moravek P, Gadas P, Pertoldova J (2014) The Mokrsko-West gold deposit, Bohemian Massif, Czech Republic: mineralogy, deposit setting and classification. Ore Geol Rev 58:238–263. https://doi.org/10.1016/j.oregeorev.2013.11.005

Zhai W, Sun X, Yi J, Zhang X, Mo R, Zhou F, Wei H, Zeng Q (2014) Geology, geochemistry, and genesis of orogenic gold–antimony mineralization in the Himalayan Orogen, South Tibet, China. Ore Geol Rev 58:68–90

Zhu Y-N, Peng J-T (2015) Infrared microthermometric and noble gas isotope study of fluid inclusions in ore minerals at the Woxi orogenic Au–Sb–W deposit, western Hunan, South China. Ore Geol Rev 65: 55–69

Zhu Y, An F, Tan J (2011) Geochemistry of hydrothermal gold deposits: a review. Geosci Front 2:367–374. https://doi.org/10.1016/j.gsf.2011.05.006

Ziegler PA (1992) European Cenozoic rift system. Tectonophysics 208: 91–111. https://doi.org/10.1016/0040-1951(92)90338-7

Appendix II

Study B

Epp, T., Marks, M. A., Ludwig, T., Kendrick, M. A., Eby, N., Neidhardt, H., Oelmann, Y. & Markl, G. (2019). Crystallographic and fluid compositional effects on the halogen (Cl, F, Br, I) incorporation in pyromorphite-group minerals. American Mineralogist, 104(11), 1673-1688.

Accepted and published
DOI: 10.2138/am-2019-7068
Number of authors: 8
Author position: 1

American Mineralogist, Volume 104, pages 1673–1688, 2019

Crystallographic and fluid compositional effects on the halogen (Cl, F, Br, I) incorporation in pyromorphite-group minerals

Tatjana Epp[1,2,*], Michael A.W. Marks[1], Thomas Ludwig[3], Mark A. Kendrick[4,†], Nelson Eby[5], Harald Neidhardt[2], Yvonne Oelmann[2], and Gregor Markl[1]

[1]Eberhard Karls Universität Tübingen, Fachbereich Geowissenschaften, Wilhelmstraße 56, 72076 Tübingen, Germany
[2]Eberhard Karls Universität Tübingen, Fachbereich Geoökologie, Rümelinstraße 19-23, 72070 Tübingen, Germany
[3]Ruprecht-Karls-Universität Heidelberg, Institut für Geowissenschaften, Im Neuenheimer Feld 234-236, 69120 Heidelberg, Germany
[4]Research School of Earth Sciences, Australian National University, 142 Mills Road, Acton, ACT, 0200, Australia
[5]Department of Environmental, Earth and Atmospheric Sciences, University of Massachusetts, Lowell, Massachusetts 01854, U.S.A.

Abstract

Pyromorphite-group minerals (PyGM), mainly pyromorphite [$Pb_5(PO_4)_3Cl$], mimetite [$Pb_5(AsO_4)_3Cl$], and vanadinite [$Pb_5(VO_4)_3Cl$], are common phases that form by supergene weathering of galena. Their formation is strongly influenced by processes at the Earth's surface and in the soil overlying a lead deposit, and they incorporate high amounts of halogens, mostly Cl and, in some cases, F. The abundance of Br and I in natural PyGM and their potential as process tracers during surface and sub-surface fluid-rock interaction processes has not been investigated in detail due to analytical difficulties. We, therefore, developed methods for the simultaneous determination of Cl, F, Br, and I in PyGM for (1) powdered bulk samples via combustion ion chromatography (CIC) and (2) compositionally zoned crystals by means of secondary ion mass spectrometry (SIMS).

Our study is based on well-characterized samples of pyromorphite (N = 38), mimetite (N = 16), and vanadinite (N = 2) from Schwarzwald (Germany). Natural pyromorphite incorporates more I (up to 26 µg/g) than mimetite (up to 2 µg/g) and vanadinite (up to 1 µg/g), while Br contents are higher in mimetite (up to 20 µg/g) and vanadinite (up to 13 µg/g) compared to pyromorphite (less than 4 µg/g). These results are unexpected, as mimetite and vanadinite have longer As/V-O bonds giving them larger unit cells and larger polyhedral volumes for the Cl site in the $Pb2_6$ octahedron than pyromorphite. Accordingly, pyromorphite was expected to preferentially incorporate Br rather than I, but the opposite is observed. Hence, halogen chemistry of PyGM is probably not governed by a crystal-chemical control (alone) but by fluid composition. However, the exact reasons remain enigmatic. This idea is corroborated by spatially resolved SIMS analyses that show that many pyromorphite-group minerals are strongly zoned with respect to their halogen mass ratios (e.g., Br/Cl, Br/I mass ratios). Furthermore, variations in halogen abundance ratios do not correlate with Ca/Pb, P/As, or P/V ratios and therefore may record alternating and season-dependent environmental parameters including biological activity, vegetation density, physico-chemical soil properties, and rainfall rate. We suggest that the zonation reflects multiple single fluid flow episodes and, hence, records surface processes. However, further experiments concerning the fractionation of halogens between fluid and PyGM are needed before halogen ratios in pyromorphite-group minerals can be used as reliable monitors of fluid-driven processes.

Keywords: Bromine, iodine, combustion ion chromatography, pyromorphite, mimetite, vanadinite

Introduction

More than 1500 localities (www.mindat.org) are known to contain pyromorphite-group minerals (PyGM). The supergene weathering of ore deposits plays a major role in both mobilizing and re-precipitating toxic trace elements such as Pb, As, Cd, and Sb (Siegel 2002; Reich and Vasconcelos 2015). Dissolution of primary minerals and precipitation of secondary mineral phases during oxidation is mainly governed by fluid flow from the surface through the soil and fractured rocks into and through ore deposits (Ruby et al. 1994; Basta and McGowen 2004). The most abundant Pb-bearing ore mineral is galena (PbS). During supergene weathering of galena, pyromorphite-group minerals (PyGM) form in the immediate environment (e.g., Park and MacDiarmid 1975; Ruby et al. 1994; Keim and Markl 2015). Due to their extremely low solubility products (log*K* values in the range of –75 to –86; Nriagu 1973; Flis et al. 2007; Gerke et al. 2009; Bajda 2010), Pb, As, V, and other toxic metals (e.g., Cr, Sb, Bi, U) are immobilized and their bioavailability is thereby reduced when PyGM form (e.g., Flis et al. 2011; Burmann et al. 2013; Markl et al. 2014).

As part of the apatite supergroup, the generalized formula for PyGM is Pb_5A_3L, where A represents PO_4^{3-} (pyromorphite), AsO_4^{3-} (mimetite), or VO_4^{3-} (vanadinite) and L is mostly comprised of Cl^-, F^-, OH^-, Br^-, and/or I^- (e.g., Wondratschek 1963; Knyazev

* E-mail: tatjanaepp@web.de, Orcid 0000-0002-2745-9941
† Present address: School of Earth Sciences, University of Queensland, St Lucia, Queensland 4072, Australia. Orcid 0000-0002-6541-4162

0003-004X/19/0011–1673$05.00/DOI: https://doi.org/10.2138/am-2019-7068

et al. 2011; Markl et al. 2014). Structurally related members of the hedyphane group (hedyphane, phosphohedyphane, and fluoro-phosphohedyphane) have the composition $Ca_2Pb_3A(Cl^-, OH^-, F^-)$, where A is either PO_4^{3-} or AsO_4^{3-} (Pasero et al. 2010). There exists complete miscibility between pyromorphite and mimetite, pyromorphite and phosphohedyphane, and mimetite and hedyphane (e.g., Dennen 1960; Wondratschek 1963; Förtsch and Wondratschek 1965; Flis et al. 2011; Markl et al. 2014). Based on the presently available data on natural samples, the miscibility gap between vanadinite and pyromorphite allows for up to 3 mol% vanadinite component in pyromorphite and up to 39 mol% pyromorphite component in vanadinite (Markl et al. 2014).

The halogen site in PyGM is mostly occupied by Cl^- but can also incorporate significant F^- and OH^- (Markl et al. 2014). However, the only naturally occurring F-dominated end-member is phosphohedyphane (Pasero et al. 2010; Kampf and Housley 2011). Markl et al. (2014) identified the occurrence of naturally existing hydroxylmimetite in which the crystallographic site is dominantly occupied by an OH-end-member. A further natural OH-end-member hydroxylpyromorphite was described (Hålenius et al. 2017). Halogen (F, Cl, Br) end-members have been synthesized (except for I-pyromorphite; Wondratschek 1963; Janicka et al. 2012) and thus appear to be thermodynamically stable at near-surface conditions (Janicka et al. 2012; Wondratschek 1963). However, little is known about the natural abundance of Br and I in these minerals due to their low concentrations in natural fluids (Fuge 1988; Schnetger and Muramatsu 1996) and a lack of suitable analytical techniques.

The variation of halogen contents and halogen ratios (e.g., Br/Cl, F/Cl, Br/I) in a range of minerals including apatite, mica, amphibole, serpentine, and scapolite are used to decipher fluid-involving processes, such as magmatic degassing, metasomatism or hydrothermal processes during fluid-rock interaction and ore formation (e.g., Harlov et al. 2005; Boyce and Hervig 2009; Kendrick and Phillips 2009; John et al. 2011; Marks et al. 2012; Kendrick et al. 2013, 2015; Harlov 2015; Kusebauch et al. 2015a; Teiber et al. 2015; Webster and Piccoli 2015; Burisch et al. 2016; Walter et al. 2018). For apatite in particular it was shown that crystal and fluid chemical processes control halogen incorporation (Kusebauch et al. 2015a). Due to structural similarities between apatite and PyGM, we suggest that halogen contents and ratios in PyGM may also serve as recorders of fluid processes in the near-surface environments. Based on geochemical considerations and estimations of the growth rate of PyGM, compositional zonation in PyGM may even reflect seasonal changes in precipitation and/or changes in the intensity of host rock alteration. This potentially monitors the variable importance of diverse fluid sources and of processes changing the fluids' composition during their growth (Markl et al. 2014; Keim and Markl 2015).

As a first step toward testing the capability of PyGM for monitoring such processes, we present halogen (Cl, F, Br, I) data for a comprehensive set of PyGM from the Schwarzwald mining district in SW Germany. We developed a method for determining bulk halogen contents in PyGM via combustion ion chromatography (CIC), which was cross-calibrated with data from instrumental neutron activity analysis (INAA) and a noble gas technique (NG; Kendrick 2012; Kendrick et al. 2018). Furthermore, secondary ion mass spectrometry (SIMS) was used to resolve small-scale halogen variations in single PyGM crystals.

Materials and methods

Samples and geological background

The samples for this study originate from the Schwarzwald, southwest Germany (Fig. 1), a part of the Central European Variscan fold belt composed of crystalline basement rocks (mainly gneisses and granites), which are overlain by a sequence of terrestrial and marine sedimentary cover rocks (McCann 2008). The Schwarzwald hosts more than 1000 hydrothermal veins (Metz and Richter 1957) with a large variety of mineral assemblages, which have formed continuously between about 310 Ma and today (e.g., Pfaff et al. 2009; Staude et al. 2009; Walter et al. 2016). The hydrothermal veins most important for the present study consist of galena-sphalerite(±chalcopyrite)-bearing assemblages, which are commonly embedded in barite, fluorite, calcite, or quartz.

The PyGM samples investigated in this study are from the entire Schwarzwald region, with many samples from the Kinzigtal area (central Schwarzwald), the Münstertal-Schauinsland-Todtnau region and the area around St. Blasien (southern Schwarzwald). The samples are from 23 different sites (Fig. 1, Table 1), where the hydrothermal veins are hosted either by basement granites, schists, rhyolites, gneisses, and migmatites or quartzitic sandstones of the sedimentary cover. The samples for this study represent a carefully selected subset of the samples that were previously analyzed by Markl et al. (2014) for their major and trace element composition. They comprise a large variety of colors (green, brown, orange, and yellow) and textures (euhedral, prismatic crystals, microcrystalline needles, spherical aggregates, as well as crusts and sinters) and cover a broad range of geological, regional, and compositional variation (Table 1). Based on previous data (Markl et al. 2014), most samples either show P# (= P/P + As + V) < 0.2 (= mimetite, vanadinite) or > 0.8 (= pyromorphite), with only few samples representing intermediate mineral compositions (Fig. 2).

The current oxidative weathering profile of these ore deposits began to develop at 12 Ma and is dominated by supergene minerals younger than 3 Ma (e.g., Hofmann and Eikenberg 1991; Hautmann and Lippolt 2000; Pfaff et al. 2009). The higher areas in the Schwarzwald (including the Feldberg area) were extensively eroded during the last glacial period (Brook et al. 2000; Morel et al. 2003; Ehlers and Gibbard 2004). Therefore, we assume that PyGM from areas that are today >900 m above sea level (localities 10–12, 15; Fig. 1; Table 1) were probably formed in the last 20 000 yr. Some samples are demonstrably younger than 200 yr because they occur as sinters on historic mine walls (localitites 4, 6–7, 12–13, 20–21; Fig. 1, Table 1).

Analytical methods

In total, 41 samples from 23 sites were analyzed with Combustion Ion Chromotography (2 vanadinites, 28 pyromorphites including 1 Pb-phosphohedyphane, and 11 mimetites including 1 mimetite with fluoro-phosphohedyphane zones; Table 1). A subset of 15 of these samples was analyzed by Secondary Ion Mass Spectrometry (10 pyromorphites including 1 Pb-phosphohedyphane, and 5 mimetites including 1 mimetite with fluoro-phosphohedyphane zones).

Combustion ion chromatography (CIC). CIC is an automated combination of combustion digestion (pyrohydrolysis) and ion chromatography. This method was used for the simultaneous determination of halogens (Cl, F, Br, I) at the Universität Tübingen. A 930 Compact IC Flex chromatograph (Metrohm) with chemical suppression and a peristaltic pump for regeneration (100 mmol/L H_2SO_4) connected to a combustion oven and an autosampler for solid samples (MMS 5000; Analytik Jena) was used.

For combustion, a mixture of equal amounts (9.9–10.5 mg) of powdered sample and WO_3 (99.995%; Aldrich 204781) was inserted into a quartz vial that was capped on both sides with quartz wool and placed into a glass vessel. The quartz vials were heated in an extraction line coupled to the IC with a constant flow of Ar (6.0; 100 mL/min) and O_2 (5.0; 300 mL/min) to 1050 °C for 12 min, followed by 10 min of post-combustion and 7 min of cooling. During combustion, a constant water flow (0.2 mL/min) was maintained. The loaded steam was collected in an absorber module containing 10 mL of 500 µg/g H_2O_2 solution. After matrix elimination (using a Metrosep A PCC 2 HC/4.0 column) the solutions were injected into the ion chromatograph. For improved detection of Br and I in the presence of high amounts of Cl, a Metrosep A Supp 5-250/4.0 (kept at 55 °C) and a Metrosep A Supp 4/5/4.0 guard column and an eluent consisting of a mixture of 2 mmol NaOH (suprapure), 1.6 mmol Na_2CO_3 (suprapure), and

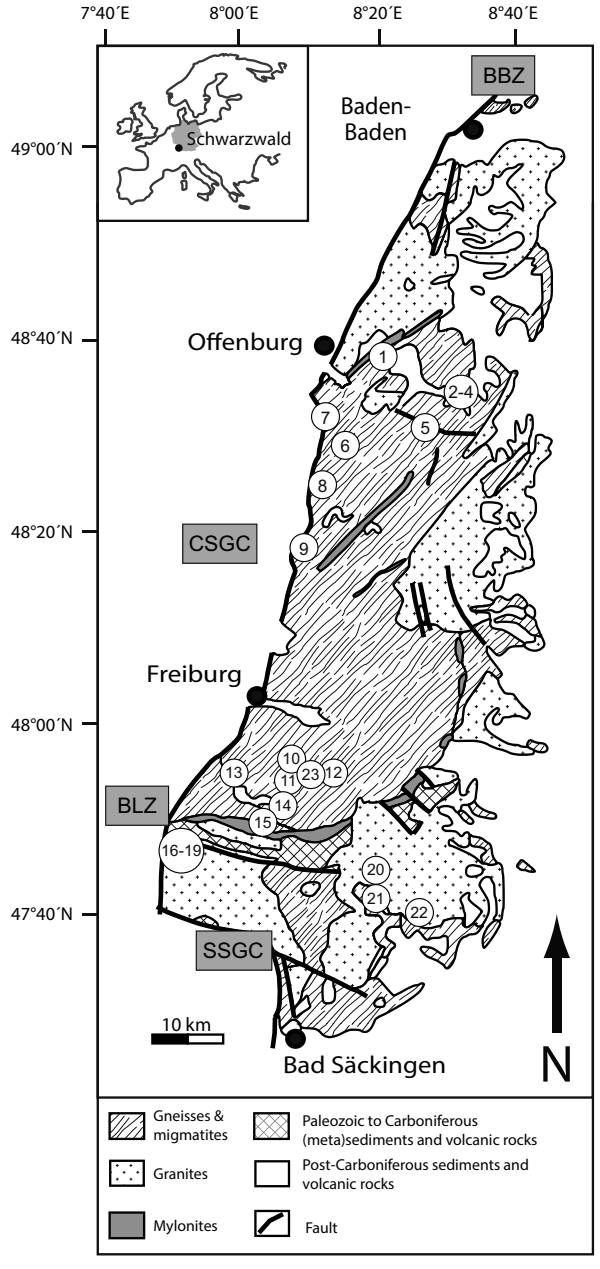

Figure 1. Simplified geological overview of the Schwarzwald (SW Germany). Sample localities 1–23 (for more information refer to Table 1). Abbreviations: BLZ and BBZ = Badenweiler-Lenzkirch and Baden-Baden-Gaggenau Zones; CSGC and SSGC = Central and Southern Schwarzwald Gneiss Complexes. Map modified after Kalt et al. (2000).

5 vol% acetone at a flow rate of 0.7 mL/min was used. This eluent composition was chosen as it minimized the overlap between the Br and Cl signals and optimized the simultaneous detection of low Br concentrations (µg/g level) in the presence of high Cl contents (wt% level). However, a complete separation of the Br and Cl peaks was impossible to achieve and Br was quantified as a shoulder peak on the Cl signal. For the whole analytical procedure, Millipore water (18.2 MΩ·cm) was used.

For the calibration a primary reference solution was prepared by mixing single element-solutions of Cl, F, Br, and I (Roth; 1000 mg/L) and a quadratic 6-point-calibration curve that covered the concentrations investigated was constructed using the Metrohm intelligent Partial Loop Injection Technique (MiPT). Quantification was done using MagIC Net software (Metrohm).

The effective detection limits for powdered samples were about 10–30 µg/g for F and Cl, about 0.1 µg/g for I, and around 0.3 µg/g for Br. Based on the frequent analyses of standard solutions and various reference materials (Table 2), relative uncertainties were generally <10% (1σ level) for F and Cl, and up to ~20% for Br and I, depending on the concentrations.

Instrumental neutron activity analysis (INAA). For cross-calibration with the CIC technique, sample PY-1 was analyzed for Br at University of Massachusetts, Lowell, using Instrumental Neutron Activation Analysis (INAA). Approximately 200 mg of sample was weighed into an acid-cleaned high-purity polyethylene vial. The sample was irradiated in-core for 1 h and the nominal neutron flux was 10^{13} n cm^{-2}s^{-1}. Following a 5 to 7 day decay period, the sample was counted for 10 000 s. The 554 and 777 keV γ-ray energies (Br-82, half-life 35.3 h) were used for the analytical determinations. The 619 keV γ-ray was not used because of potential interference from the 618.3 keV W-187 γ-ray. Peak areas were determined using Canberra Genie software. Further data reduction for decay time, flux, and geometry was done using software developed in-house. The Br concentration was determined by reference to the NIST traceable Dionex Combined Seven Anion Standard II (Thermo-Scientific).

Noble gas (NG). For three samples (JH-053, JH-128, and PY-1), Cl, Br, and I contents were determined from 5–30 mg size sample duplicates by the noble gas method (NG), which enables halogen measurement from irradiation-produced noble gas proxy isotopes ($^{39}Ar_K$, $^{38}Ar_{Cl}$, $^{80}Kr_{Br}$, $^{128}Xe_I$) (e.g., Johnson et al. 2000; Kendrick 2012). The samples were irradiated for 50 h in the Central Facility of the research reactor at the McClellan Nuclear Radiation Center, University of California, Davis, U.S.A., on August 23, 2014 (Irradiation RS#1). The irradiation was monitored with Hb3Gr (1072 Ma; Roddick 1983) and aliquots of 3 scapolite gems used as halogen standards (Kendrick 2012; Kendrick et al. 2013). The samples received a total neutron fluence of 3.7×10^{18} n cm^{-2} with a fast/thermal ratio of 1 (J = 0.0096). Noble gases were extracted from the samples by fusion at 1500 °C in a tantalum resistance furnace and purified over 40 min on a series of Zr-Al getter pumps, which removes active gases such as H_2O, CO_2, and N_2. The purified noble gases were expanded into the MAP-215-50 noble gas mass spectrometer and sequentially analyzed for isotopes of Ar, Kr, and Xe in peak jumping mode over a period of 45 min. This technique enables determination of Br/Cl and I/Cl ratios with analytical precision of 1–2% in a single irradiation. Scapolite standards calibrated relative to experimentally determined neutron capture cross sections have long term reproducibility of ~3–5% (1 s.d.) (Kendrick et al. 2013). However, Cl, Br, and I concentrations are subject to an additional uncertainty related to mass spectrometer sensitivity, giving a total uncertainty (accuracy) of ca. ±10% relative in concentrations (Kendrick et al. 2018).

Electron probe microanalysis. The composition of the samples analyzed by SIMS was determined using a JEOL Superprobe JXA-8900RL at the Fachbereich Geowissenschaften, Universität Tübingen, Germany following the method described in Markl et al. (2014). Acceleration voltage of the defocused beam (15 µm diameter) was 20 kV at a beam current of 20 nA. Counting times for major elements were 16 s for the element peak and 8 s for each background and for minor elements 30 and 15 s, respectively. The following synthetic and natural standards were used for calibration: $Ca_5(PO_4)_3(F,Cl)$ for F*Kα* and Ca*Kα*; $CaMgSi_2O_6$ for Si*Kα*; UO_2 for U*Mα*; and V for V*Kα*. To improve the quality of the analyses, the external standards PY-1 $Pb_5(PO_4)_3Cl$ and MIM-1 $Pb_5(AsO_4)_3Cl$ were used for Pb, P, As, and Cl (see details in Markl et al. 2014). An automatic φρz correction was applied to all analyses. Peak overlaps of Ca by Pb (*Lγ* 1, fourth order) and F by P (*Kα* 1 and 2, third order) were corrected internally. The detailed WDS configuration, including standards, counting times and the resulting average detection limits are given in the electronic supplement[1] ESM 1.

Secondary ion mass spectrometry (SIMS). SIMS analyses were performed using the Heidelberg Ion Probe (Cameca IMS 1280-HR) at the Institute of Earth Sciences, Heidelberg University. Cs^+ ions with a net energy of 23 keV and a beam current of ~2 nA were focused to ~5 µm and rastered over an area of 10 × 10 µm. Negative secondary ions were accelerated to 10 keV with an offset of 50 V to the acceleration voltage. The normal incidence electron gun (NEG) was used to compensate for charge build-up on the samples, which were coated with ~50 nm of gold. The offset of 50 V was also applied to the acceleration voltage of the NEG. The width of the mass spectrometer's energy window was set to 40 eV so that secondary ions with a starting energy of 70 ± 20 eV were transmitted (energy filtering to reduce the impact of molecular interferences). The mass resolving power was set to M/ΔM ≅ 2200. $^{35}Cl^-$ [20 s] was detected with the axial Faraday cup (R = 10^{11}Ω) while all other species (^{19}F [40 s], $^{40}Ca^{37}Cl$ [40 s], ^{81}Br [80 s], and ^{127}I [80 s]) were detected with the axial electron multiplier in counting mode (the times given in square brackets are the total integration

Table 1. Information about the locality, mineralization type, host rock, methods used, crystal shape, and basic mineralogy of all samples investigated

No.	Locality	Samples	Position a.NN (m)	Coordination (UTM)	Host Rock	Mineralization type	Method		
							SIMS	CIC	EPMA
1	Silberbrünnle	JH-078	515	32 U 432271 5365312	gneiss	qtz-ccp-gn-fhl	x		x
2	Clara	JH-087	630	32 U 443346 5359394	gneiss	brt-fl-qtz-gn-fhl-ccp		x	
2	Clara	JH-086	630	32 U 443346 5359394	gneiss	brt-fl-qtz-gn-fhl-ccp		x	
2	Clara	JH-089	630	32 U 443346 5359394	gneiss	brt-fl-qtz-gn-fhl-ccp		x	
3	Friedrich-Christian	JH-094	500	32 U 445999 5359392	gneiss	fl-qtz-gn-ccp		x	
4	Herrensegen	JH-096	500	32 U 446018 5359411	gneiss	fl-qtz-gn-ccp	x		x
4	Herrensegen	JH-092b	500	32 U 446018 5359411	gneiss	fl-qtz-gn-ccp	x		x
4	Herrensegen	JH-092a	500	32 U 446018 5359411	gneiss	fl-qtz-gn-ccp		x	
4	Herrensegen	JH-097a	500	32 U 446018 5359411	gneiss	fl-qtz-gn-ccp		x	
5	Erzengel Gabriel	JH-079	740	32 U 438778 5354736	gneiss	fl-brt-qtz-gn		x	
6	Eichhalde Biberach	JH-101	260	32 U 426794 5354331	gneiss. granite	qtz-sid-fhl-gn-ccp		x	
7	Michael im Weiler	JH-076	370	32 U 423454 5356116	gneiss. granite	brt-qtz-gn-sph-nat.As		x	
7	Michael im Weiler	JH-074	370	32 U 423454 5356116	gneiss. granite	brt-qtz-gn-sph-nat.As		x	
7	Michael im Weiler	JH-077	370	32 U 423454 5356116	gneiss. granite	brt-qtz-gn-sph-nat.As		x	
8	St. Josefi	JH-102	270	32 U 422415 5345980	gneiss	brt-qtz-gn-sph		x	
9	Silberloch	JH-113	460	32 U 419816 5337573	sandstone	brt-qtz-gn(-fhl)		x	
9	Silberloch	JH-112	460	32 U 419816 5337573	sandstone	brt-qtz-gn(-fhl)		x	
10	Gsprenggang	JH-048	1180	32 T 416907 5306385	gneiss. migmatite	qtz-gn-sph		x	
11	Willnau	JH-045	1120	32 T 417456 5304584	migmatite	qtz-brt-gn		x	
12	Kammentobel	JH-122b_Q	1320	32 T 424654 5303177	migmatite	sid/goe-gn	x		x
12	Kammentobel	JH-122b_L	1320	32 T 424654 5303177	migmatite	sid/goe-gn	x		x
12	Kammentobel	JH-119	1320	32 T 424654 5303177	migmatite	sid/goe-gn	x	x	x
12	Kammentobel	JH-118	1320	32 T 424654 5303177	migmatite	sid/goe-gn	x	x	x
12	Kammentobel	JH-117	1320	32 T 424654 5303177	migmatite	sid/goe-gn	x	x	x
12	Kammentobel	JH-122	1320	32 T 424654 5303177	migmatite	sid/goe-gn		x	
12	Kammentobel	JH-121	1320	32 T 424654 5303177	migmatite	sid/goe-gn		x	
12	Kammentobel	JH-120	1320	32 T 424654 5303177	migmatite	sid/goe-gn		x	
13	Klöpfe	JH-127a	700	32 T 409466 5303259	migmatite	qtz-brt-gn	x		x
14	Anton Wieden	JH-058	820	32 T 417227 5299318	gneiss. granite	fl-brt-qtz-gn-sph(-ccp)		x	
15	Pfingstsegen (Aitern)	JH-066	960	32 T 414854 5296459	schist	fl-brt-qtz-gn		x	
16	Karlstollen	JH-036	660	32 T 401019 5294106	schist	qtz-brt-gn		x	
17	Hausbaden	JH-017	610	32 T 400777 5293817	granite	qtz-brt-fl-gn(-sph-ccp)	x	x	x
17	Hausbaden	JH-022	610	32 T 400777 5293817	granite	qtz-brt-fl-gn(-sph-ccp)		x	
17	Hausbaden	JH-020	610	32 T 400777 5293817	granite	qtz-brt-fl-gn(-sph-ccp)		x	
18	Altemannfels	JH-128	610	32 T 400795 5293679	gneiss. sandstone	qtz-brt-gn	x		x
18	Altemannfels	JH-128b	610	32 T 400795 5293679	gneiss. sandstone	qtz-brt-gn	x		x
18	Altemannfels	JH-128e	610	32 T 400795 5293679	gneiss. sandstone	qtz-brt-gn		x	
19	Wilhelminen- stollen	JH-028	620	32 T 400771 5293509	granite	qtz-brt-gn		x	
19	Wilhelminen- stollen	JH-025	620	32 T 400771 5293509	granite	qtz-brt-gn		x	
21	Neuhoffnung	JH-129b	740	32 T 434064 5285952	gneiss. granite	fl-brt-qtz-dol-gn-sph-ccp	x		x
21	Neuhoffnung	JH-129a	740	32 T 434064 5285952	gneiss. granite	fl-brt-qtz-dol-gn-sph-ccp		x	
21	Neuhoffnung	JH-011	740	32 T 434064 5285952	gneiss. granite	fl-brt-qtz-dol-gn-sph-ccp		x	
21	Neuhoffnung	JH-001	740	32 T 434064 5285952	gneiss. granite	fl-brt-qtz-dol-gn-sph-ccp		x	
21	Neuhoffnung	JH-007a	740	32 T 434064 5285952	gneiss. granite	fl-brt-qtz-dol-gn-sph-ccp		x	
21	Neuhoffnung	JH-013	740	32 T 434064 5285952	gneiss. granite	fl-brt-qtz-dol-gn-sph-ccp		x	
21	Neuhoffnung	JH-002	740	32 T 434064 5285952	gneiss. granite	fl-brt-qtz-dol-gn-sph-ccp		x	
21	Neuhoffnung	JH-016	740	32 T 434064 5285952	gneiss. granite	fl-brt-qtz-dol-gn-sph-ccp		x	
20	Gottes Ehre. Urberg	JH-054	790	32 T 434060 5286155	gneiss. granite	fl-brt-qtz-dol-gn-sph-ccp		x	
20	Gottes Ehre. Urberg	JH-005	790	32 T 434060 5286155	gneiss. granite	fl-brt-qtz-dol-gn-sph-ccp		x	
22	Segalen	JH-114	700	32 T 439729 5283604	rhyolite	fl-brt-qtz-gn	x		x
23	Osterzeitstollen	JH-053	1040	32 T 417712 5306115	gneiss. granite		x	x	

(Table extends on next page)

times). Prior to each analysis, the sample was sputtered for 90 s with a raster size of 15 µm and the analysis started after a sputter time of ~190 s. There were two significant molecular interferences: $^{31}P^{16}O_2^{18}O$ and $^{44}Ca^{37}Cl$ on ^{81}Br. The first was fully resolved while the latter would have required a very high MRP (mass resolving power) of ~15 900 and was not resolved. To correct for the contribution of $^{44}Ca^{37}Cl$ on the ^{81}Br peak the $^{40}Ca^{37}Cl$ intensity was extrapolated to $^{44}Ca^{37}Cl$ and subtracted (Marks et al. 2012). This resulted in relative corrections of 0 to –13%.

The samples showed a strong increase of the halogen ion count rates during sputtering, as shown in Figure 3a for sample PY-1. The increase of the count rates is very similar for all halogens, which results in reasonably constant ratios (Fig. 3b). For comparison, results using the same analytical setup are shown for an obsidian glass (Pichavant et al. 1987) in Figures 3c and 3d. This glass (and other glasses) did not show this increase of halogen count rates. Because the count rates of all halogens increase simultaneously, Cl (major element in all samples investigated) was chosen as a reference element. P was taken into consideration but showed a completely different behavior over sputter time.

Halogen reference materials or standards for SIMS are in short supply (e.g., Marks et al. 2017; Kendrick et al. 2018) and is even worse for exotic minerals like PyGMs: there are no reference materials with a remotely similar matrix. For further detailed studies on such materials, it is desirable to produce matrix-matched synthetic reference materials with known concentrations of the halogens. The ion yields (RIY) of F, Br, and I relative to Cl were therefore determined on samples JH-053, JH-128, and PY-1 using data from the other analytical methods. The results are presented in the electronic supplement[1] 2. The mean value of the RIYs on these three reference samples was used to quantify the halogens in the unknown samples. It is currently not clear whether the high variation in the RIYs is caused by matrix effects, by the inhomogeneity of the reference samples, or other unknown factors. The accuracy of the SIMS data is therefore semi-quantitative at best. This should however not affect the data on relative halogen incorporation within one sample, which was the goal of the SIMS analyses.

Results

Consistency of the data set

Three samples (PY-1, JH-053, and JH-128) have been analyzed by EPMA (Markl et al. 2014 and this study), NG (this study) and INAA (only PY-1, this study) for testing the

TABLE 1. —*EXTENDED*

No.	zoned	Shape	#Ca	#P	Color	Mineral
1	x	crystalline	0.13	0.95	green	pym
2		crystalline	0.04	1.00	green	pym
2		crystalline	0.01	0.92	yellow- orange	pym
2		crystalline	0.00	0.02	orange	mim
3		crystalline	0.01	1.00	green	pym
4	x	spherical	0.16	0.98	green	pym
4	x	crystalline	0.10	0.99	green	pym
4		crust	0.03	1.00	green	pym
4		crystalline	0.00	1.00	green	pym
5		crystalline	0.00	0.98	green	pym
6		crust	0.19	1.00	green	pym- p.hed
7		crystalline	0.00	0.15	orange	mim
7		crust	0.00	0.82	orange	pym
7		crystalline	0.00	0.00	yellow	mim
8		crystalline	0.00	0.52	green	mim
9		crystalline	0.07	0.95	green	pym
9		crystalline	0.02	0.93	yellow	pym
10		spherical	0.02	1.00	green	pym
11		crystalline	0.00	1.00	green	pym
12		crystalline	0.00	1.00	green	pym
12		crystalline	0.00	1.00	green	pym
12		crystalline	0.00	1.00	yellow- green	pym
12	x	crust	0.04	1.00	yellow- green	pym
12		crust	0.00	1.00	yellow- brown	pym
12		crystalline	0.00	1.00	green	pym
12	x	crystalline	0.03	1.00	yellow- green	pym
12		crust	0.00	1.00	green	pym
13	x	crust	0.19	0.99	green- gray	pym- Pb p.hed
14		crystalline	0.01	0.04	yellow	mim
15		crystalline	0.01	0.92	green	pym
16		spherical	0.05	0.05	orange	mim
17	x	spherical	0.01–0.40	0.05–0.99	orange	mim- p.hed
17		spherical	0.05	0.19	yellow	mim
17		crystalline	0.14	1.00	green	pym
18		spherical			orange	mim
18	x	spherical	0.11	0.11	orange	mim
18		spherical	0.10	0.09	orange	mim
19		crystalline	0.07	0.99	yellow- green	pym
19		crystalline	0.10	0.89	orange	pym
21	x	spherical	0.11	0.59	green- gray	mim
21		spherical	0.03	0.43	orange	mim
21		crust	0.01	0.95	orange	pym
21		spherical	0.11	0.97	green	pym
21		crystalline	0.00	0.99	green	pym
21		crystalline	0.03	1.00	green	pym
21		crystalline	0.04	0.99	yellow-green	pym
21		crystalline	0.02	0.96	yellow	pym
20		crystalline	0.00	0.04	red-brown	van
20		spherical	0.01	0.01	yellow	mim
22	x	crust	0.08	0.24	yellow	mim
23		crystalline	0.00	0.07	brown	van

accuracy of the CIC method. The mean Cl concentrations based on CIC and EPMA data for PY-1, JH-053, and JH-128 show a maximum relative difference of 3%, demonstrating the consistency between these two methods (Fig. 4; Table 2). For most samples investigated during this study, Cl contents determined by EPMA and CIC overlap within uncertainty (Fig. 4). Note that the relatively large range of EPMA data for some of the samples indicates strong compositional zonation, which is not mirrored in the CIC data, which derive from much larger bulk sample amounts. A few samples show higher EPMA than CIC-derived Cl concentrations (Fig. 4), which can, however, not be traced back to especially strong zonation in these samples. Accordingly, the reason for this observation remains unclear. The CIC determinations agreed within a 90% confidence interval with the electron microprobe results. In comparison, NG-derived Cl data are 2–5% higher than the CIC data (Table 2). The Br contents obtained by the NG method for PY-1, JH-128, and JH-053 are 20–30 rel% higher than those obtained by CIC and 17 rel% lower than those obtained by INAA (PY-1 only) (Table 2). This scatter is partly a function of the different standardization protocols (see methods) but may also indicate that the separation of the Br from the dominating Cl peak during ion chromatography was not perfect (see above). Note, however, that CIC results for other reference materials such as granite and basalt are within the reported literature values (Table 2).

Iodine concentrations obtained by the NG and CIC methods are within 24 rel% of one another for JH53 and consistent for sample JH128 in which I was below the CIC detection limit. However, the I concentration obtained by the NG method for sample PY-1 is about twice the one obtained by CIC (Table 2).

The SIMS data indicate that small-scale heterogeneities in Br and I concentrations are present in many of the investigated samples. Therefore, sample heterogeneity may contribute to the different results obtained from the different techniques. The sample masses of ~10 mg for CIC and 5–30 mg for the NG method overlap and sample duplicates analyzed by the NG

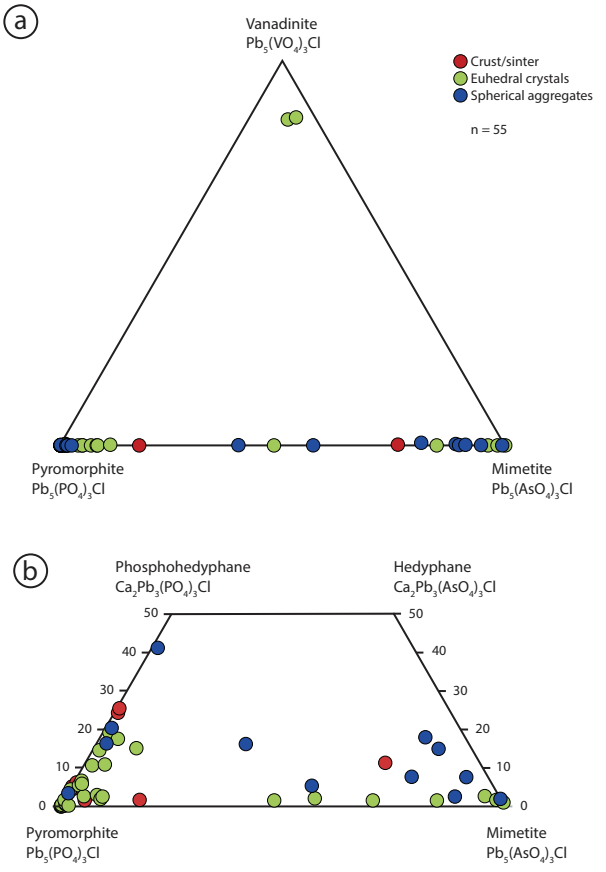

FIGURE 2. Ternary diagram showing the sample classification of the pyromorphite-group minerals, n = number of analyzed samples. (**a**) All analyses of this study plotted in the ternary diagram pyromorphite-vanadinite-mimetite. The color-coding refers to the three distinguished crystal shapes. (**b**) The same analyses plotted in the trapezoid pyromorphite-phosphohedyphane-mimetite-hedyphane.

Table 2. Internal reference material of samples JH-053, JH-128, and PY-1 characterized by different methods

Sample	Mineral/sample type	Method	Cl (wt%)		Br (µg/g)				I (µg/g)			
			mean	1 σ	mean	min	max	1 σ	mean	min	max	1 σ
JH 053	vanadinite	NG	2.68	0.1	19.3			0.3	0.72			0.01
		EPMA	2.34	0.07								
		CIC	2.37	0.07	13.13			0.8	0.86			0.3
		SIMS			26.86	23.99	34.27	3.35	0.58	0.35	0.80	0.17
JH 128	mimetite	NG	2.82	0.1	6.46			0.1	0.065			0.002
		EPMA	2.45	0.19								
		CIC	2.43	0.057	4.53			0.32	b.d.l.			b.d.l.
		SIMS			8.11	7.65	8.62	0.40	0.10	0.08	0.17	0.04
PY-1	pyromorphite	NG	2.8	0.1	2.15			0.03	3.2			0.1
		EPMA	2.54	0.19								
		INAA			2.3			0.12				
		CIC	2.46	0.06	1.63			0.15	1.34			0.1
		SIMS			0.82	0.66	1.02	0.13	3.09	1.70	3.83	0.84

method were reproduced at the 3% level for Cl, 0.3–9% for Br and 1–21% for I, with the greatest heterogeneity indicated for the duplicate pair including the smallest sample aliquot (Table 2). Further work to cross-calibrate these techniques is desirable. However, given the demonstrable heterogeneity of the sample material (and the orders of magnitude variation in halogen abundances in natural materials), these results provide confidence that the CIC results reported below are meaningful.

Bulk halogen (Cl, F, Br, I) contents

The EPMA and CIC data indicate that the samples contain between 1.9 and 2.5 wt% Cl and generally <0.3 wt% F (Table 3). An exceptionally high F content of 1 wt% was determined in sample JH-001, where fluorite occurs as a gangue mineral. Although pyromorphite (JH-101) and mimetite (JH-017) contain fluoro-phosphohedyphane zones, they do not have exceptionally high bulk F contents, as these zones are only up to 100 µm thick and are therefore too small to influence the bulk data. Bulk Br contents are highly variable and range from 0.3 to 20 µg/g, as do I contents, which vary from <0.1 to 26 µg/g (Table 3).

The contents of F, Br, and I correlate strongly with the major element composition (Fig. 5): pyromorphite samples (P# > 0.6) reach high levels of F and show only low Br contents (<5 µg/g). In contrast, mimetite (P# < 0.4) and vanadinite reach the highest Br contents but contain only little F (generally <500 µg/g) and I (<2 µg/g). Mimetite with phosphohedyphane zones shows the same systematics as mimetite, and pyromorphite with phosphohedyphane zones the same as pyromorphite (Fig. 5).

Spatially resolved halogen data

The samples analyzed by SIMS and EPMA do not show large variations on the A site, with P# [P/(P+As+V)] in pyromorphites ranging from 0.98 to 1 and between 0.0 to 0.2 in mimetites. The visible zonation in BSE images (Figs. 6 and 7) is mainly due to variations in Pb and Ca (Supplemental[1] Table S1).

Type-A samples do not show any obvious zonation patterns in BSE images. The example shown in Figure 6a has a constant Pb# of 1.00 and shows increasing Br/I from core (0.4) to rim (5.0), due to increasing Br contents. A similar trend is visible in the F/Cl ratio (0.001 to 0.004), because Cl slightly decreases

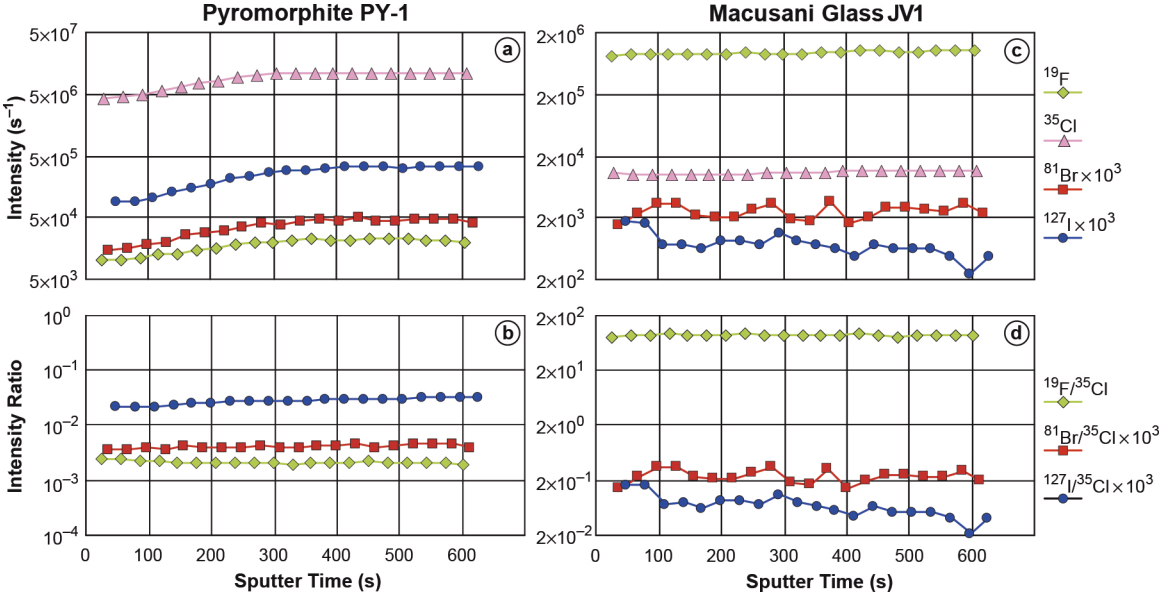

Figure 3. Halogen count rates and ratios using SIMS with (**a** and **b**) a pyromorphite sample and (**c** and **d**) with obsidian glass. Note the strong increase of count rates on the pyromorphite that is not present on the glass. However, the ratios on the pyromorphite are reasonably constant.

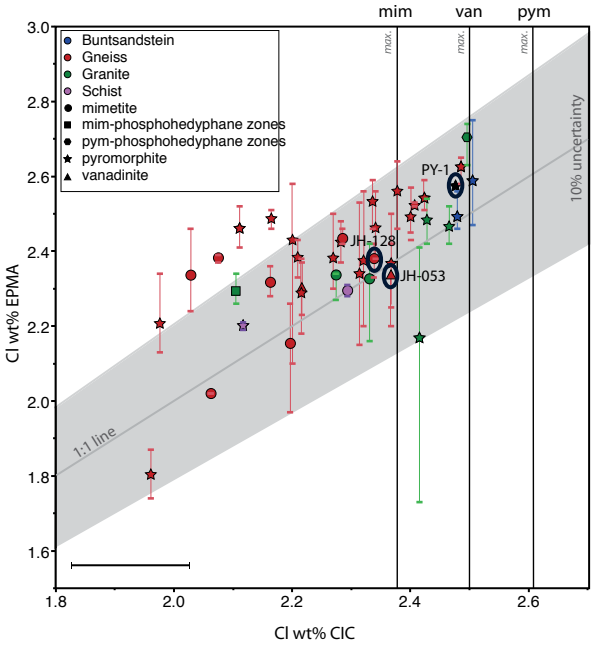

Figure 4. Method comparison between the electron microprobe analyses and the combustion ion chromatography with respect to the Cl content (in wt%). The Cl content of all CIC analyses and the appropriate Cl content determined with the EPMA. Black circles show the three standard materials; JH-128 = mimetite, JH-053 = vanadinite, PY-1 = pyromorphite. Black vertical lines show the maximum Cl-content that can be theoretically incorporated into the three end-members. The color-coding refers to different host rocks and the shapes to different minerals. Vertical bars show the minimum and maximum detected Cl content with the EPMA, and each symbol represents the mean value. Vertical black bar = 1σ uncertainty EPMA, horizontal black bar = 1σ uncertainty CIC.

toward the rim, whereas F increases (Fig. 6a).

Type B samples (Fig. 6b) show dark and relatively Ca-rich areas (Ca# 0.2–0.25) and brighter, relatively Ca-poor areas (Ca# 0.01). In the example shown, the brightest area has the lowest F/Cl (0.01), but the highest Br/I ratio (0.11) due to relatively low F (200 µg/g) and I (15 µg/g) contents. In the remaining parts of this sample, non-systematic variations of all four halogens occur, with remarkably high I contents (up to 35 µg/g) relative to Br (1–2 µg/g) (Fig. 6b).

Type C samples show clear halogen variations from internal (relatively old) to external (relatively younger) zones (Figs. 6c, 7a, and 7b). In pyromorphite JH-118, F (from 400 to 17 µg/g), Br (from 2.3 to 0.6 µg/g), and I (from 2 to 0.08 µg/g) contents decrease from core to rim, resulting in increasing Br/I but decreasing F/Cl and Br/Cl ratios in the same direction (Fig. 6c). In pyromorphite JH-078, no systematic halogen variations from core to rim are evident and Br/Cl, Br/I, and F/Cl ratios scatter in an unsystematic way (Fig. 7a). Halogen variations in mimetite JH-114 (Fig. 7b) are less compared to pyromorphites JH-118 (Fig. 6c) and JH-078 (Fig. 7a), whereas F, Br, and I contents are relatively constant in most of the sample. A later overgrowth shows higher F and I but lower Br contents. This results in distinctly higher F/Cl and lower Br/I and Br/Cl ratios.

Discussion

Based on our results using different analytical techniques, we are able to distinguish different types of halogen incorporation (1) into different PyGMs in general, and (2) into specific zones of individual crystals.

Crystal chemical controls on the incorporation of F, Br, and I in pyromorphite-group minerals

The experimental study of Wondratschek (1963) showed that the incorporation of Cl, F, and Br into PyGM is thermodynamically stable. In his study, Cl-, F-, and Br-PyGM end-members were synthesized, but the synthesis of the I-pyromorphite end-member was not successful (Wondratschek 1963). In natural PyGM, Cl is by far the most abundant halogen (we found a minimum concentration of 1.9 wt% in our samples), probably because Cl is the dominant halogen in basically all natural fluids (Cicerone 1981; Neal et al. 2010; Göb et al. 2013). Flis et al. (2011) synthesized several solid solution compositions of the pyromorphite-mimetite series with variable P/As ratios. The P/A ratios of initial fluid and final solid composition were identical, which implies that no fractionation of P and As occurs between fluid and solid phases. In other words, PyGM P/As ratios reflect the P/As ratio of the fluid they crystallized from. In the following, we assume that this is also true for the halogens, but we stress that this is just an assumption. We believe that this assumption is reasonable, as the halogens (except for Cl) are trace elements in natural fluids and, hence, Henry's law applies. Hence, we suggest that the relation of halogen content and major element composition of the analyzed PyGM sheds light on the relative preferred incorporation of the different halogens into the different PyGMs, although the actual abundance of the halogens in the PyGM-forming fluid is unknown.

The halogen site of a Ca-poor PyGM is preferentially occupied by Cl relative to F, because compositions close to Pb_5A_3L have larger unit-cell dimensions than compositions such as $Ca_2Pb_3A_3L$, and because larger unit-cell dimensions favor the incorporation of the halogen with the larger ionic radius (Markl et al. 2014; Pasero et al. 2010). This explains why hedyphane samples (Ca-rich compared to the "standard" PyGM), which have smaller unit-cell dimensions, incorporate greater amounts of F than, e.g., pyromorphite or mimetite. This is supported by the occurrence of phosphohedyphane (Ca-rich), which is the only naturally occurring F-dominated end-member (Pasero et al. 2010; Kampf and Housley 2011). It is also illustrated by sample JH-127 in which the highest F content correlates with the highest Ca# (Fig. 6b).

On the other hand, the highest I content (the halogen with the largest ionic radius) was also detected in hedyphane zones (Supplemental[1] Table S1), which implies that halogen incorporation is not only dependent on the occupation of the Pb-Ca site in the PyGM crystal. Furthermore, we observed that the degree of Br and I substitution correlates with the P/(P+As) ratio of the PyGMs (Fig. 5 and 8): higher P/(P+As) ratios favor substitution by I. The explanation for the observed data is, however, difficult, and simple crystallographic arguments do not suffice. Arsenic (As^{5+}) has an effective ionic radius of 0.335 Å and vanadium (V^{5+}) of 0.355 Å, whereas phosphorous (P^{5+}) has an ionic radius

TABLE 3. All combustion ion chromatography analyses and important EPMA data

	EPMA								CIC							
	apfu															
Sample	P	As	V	Pb	Ca	Cl (wt%)			Cl (wt%)	Br (µg/g)	F (µg/g)	I (µg/g)	Cl/Br ratio σ (%)	F/Cl ratio σ (%)	Br/I ratio σ (%)	
						mean	min	max								
JH-001	2.9	0.1	0.0	4.5	0.6	2.46	2.41	2.52	2.11 ± 0.06	0.60 ± 0.35	9668.60 ± 4177.81	4.61 ± 0.46	35184.67 0.58	0.46 0.43	0.13 0.59	
JH-002	2.9	0.0	0.0	4.9	0.2	2.38	2.30	2.50	2.27 ± 0.07	1.30 ± 0.17	1010.37 ± 257.67	2.56 ± 0.10	17456.51 0.14	0.04 0.26	0.51 0.14	
JH-005	0.0	2.9	0.0	5.1	0.0	2.02	2.02	2.02	2.06 ± 0.05	10.33 ± 2.08	90.73 ± 14.88	0.00 ± 0.00	1995.62 0.20	0.00 0.17	0.00 0.00	
JH-007a	2.9	0.0	0.0	5.1	0.0	2.29	2.18	2.38	2.22 ± 0.05	1.40 ± 0.53	877.70 ± 208.82	5.28 ± 0.18	15825.40 0.38	0.04 0.24	0.27 0.38	
JH-011	2.7	0.1	0.0	5.3	0.0	1.81	1.74	1.87	1.94 ± 0.04	4.23 ± 0.84	2815.70 ± 884.70	0.97 ± 0.35	4574.91 0.20	0.15 0.37	4.37 0.21	
JH-013	2.9	0.0	0.0	4.9	0.1	2.63	2.58	2.65	2.49 ± 0.08	0.85 ± 0.21	666.10 ± 164.63	25.70 ± 0.52	29243.80 0.25	0.03 0.25	0.03 0.25	
JH-016	2.8	0.1	0.0	5.0	0.1	2.49	2.45	2.53	2.40 ± 0.06	0.97 ± 0.15	613.07 ± 137.12	0.85 ± 0.07	24831.48 0.16	0.03 0.23	1.14 0.18	
JH-017	0.3	2.6	0.0	5.0	0.1	2.29	2.26	2.34	2.11 ± 0.05	3.97 ± 0.23	2197.37 ± 788.82	2.28 ± 0.34	5316.19 0.06	0.10 0.36	1.74 0.16	
JH-020	3.0	0.0	0.0	4.4	0.7	2.17	1.73	2.41	2.42 ± 0.07	0.73 ± 0.47	1112.70 ± 331.76	13.28 ± 0.21	32937.18 0.65	0.05 0.30	0.06 0.64	
JH-022	0.6	2.4	0.0	4.8	0.2	2.34	2.27	2.34	2.27 ± 0.05	4.53 ± 0.29	207.93 ± 25.85	0.41 ± 0.00	5015.78 0.07	0.01 0.13	11.14 0.00	
JH-025	2.6	0.3	0.0	4.6	0.5	2.47	2.42	2.52	2.47 ± 0.07	1.07 ± 0.23	385.17 ± 72.33	6.31 ± 0.27	23114.41 0.22	0.02 0.19	0.17 0.22	
JH-028b	2.9	0.0	0.0	4.7	0.4	2.49	2.42	2.54	2.43 ± 0.07	0.35 ± 0.35	76.23 ± 3.56	0.31 ± 0.00	69370.86 1.01	0.00 0.05	1.14 0.00	
JH-036	0.2	2.8	0.0	4.8	0.2	2.30	2.28	2.31	2.29 ± 0.06	5.20 ± 0.17	171.47 ± 19.06	0.50 ± 0.14	4410.15 0.04	0.01 0.11	10.36 0.29	
JH-045	2.9	0.0	0.0	5.1	0.0	2.52	2.52	2.53	2.41 ± 0.07	0.83 ± 0.29	79.60 ± 2.35	0.67 ± 0.07	28887.12 0.35	0.00 0.04	1.25 0.36	
JH-048	2.9	0.0	0.0	5.0	0.1	2.43	2.10	2.58	2.20 ± 0.06	1.00 ± 0.28	165.90 ± 12.90	0.19 ± 0.00	22005.67 0.28	0.01 0.08	5.26 0.00	
JH-053	0.2	0.2	2.3	5.3	0.0	2.34	2.20	2.42	2.37 ± 0.08	13.13 ± 0.76	34.90 ± 9.71	0.86 ± 0.38	1802.53 0.07	0.00 0.28	15.31 0.44	
JH-054	0.1	0.3	2.3	5.3	0.0	2.31	2.23	2.37	2.22 ± 0.06	11.77 ± 1.47	5926.77 ± 2512.50	0.00 ± 0.00	1883.60 0.13	0.27 0.42	0.00 0.00	
JH-058	0.1	2.9	0.0	5.0	0.0	2.32	2.16	2.42	2.33 ± 1.14	14.00 ± 0.66	183.70 ± 16.20	0.00 ± 0.00	1664.24 0.74	0.01 0.74	0.00 0.00	
JH-066	2.6	0.2	0.0	5.1	0.1	2.20	2.19	2.21	2.12 ± 0.05	1.03 ± 0.76	1250.23 ± 379.91	0.46 ± 0.00	20486.94 0.74	0.06 0.30	2.24 0.00	
JH-074	2.3	0.5	0.0	5.2	0.0	2.49	2.46	2.51	2.16 ± 0.06	2.33 ± 0.55	36.17 ± 4.44	3.20 ± 0.21	9277.27 0.24	0.00 0.13	0.73 0.25	
JH-076	0.5	2.5	0.0	5.1	0.0	2.34	2.24	2.46	2.03 ± 0.05	12.43 ± 0.76	51.80 ± 8.52	0.00 ± 0.00	1631.12 0.07	0.00 0.17	0.00 0.00	
JH-077	0.0	3.0	0.0	5.1	0.0	2.32	2.28	2.36	2.16 ± 0.07	20.23 ± 1.45	52.30 ± 9.75	0.00 ± 0.00	1068.89 0.08	0.00 0.19	0.00 0.00	
JH-079	2.8	0.0	0.0	5.1	0.0	2.46	2.38	2.56	2.34 ± 0.07	1.87 ± 0.21	3151.43 ± 1223.35	3.86 ± 0.06	12541.52 0.12	0.13 0.39	0.48 0.11	
JH-086	2.7	0.2	0.0	5.0	0.1	2.54	2.51	2.59	2.42 ± 0.07	0.90 ± 0.52	394.63 ± 83.39	0.70 ± 0.15	26930.56 0.58	0.02 0.21	1.28 0.61	
JH-087	2.9	0.0	0.0	4.9	0.2	2.56	2.46	2.64	2.38 ± 0.07	1.10 ± 0.36	5851.77 ± 2442.42	3.14 ± 0.14	21617.00 0.33	0.25 0.42	0.35 0.33	
JH-089	0.1	3.0	0.0	5.0	0.0	2.43	2.42	2.46	2.28 ± 0.04	1.20 ± 0.98	403.43 ± 33.64	0.95 ± 0.00	19040.89 0.82	0.02 0.09	1.26 0.00	
JH-092a	2.8	0.0	0.0	5.0	0.2	2.49	2.43	2.57	2.40 ± 0.07	1.17 ± 0.23	59.53 ± 2.41	0.61 ± 0.03	20580.17 0.20	0.00 0.05	1.90 0.20	
JH-094	2.8	0.0	0.0	5.1	0.0	2.54	2.46	2.59	2.34 ± 0.09	1.03 ± 0.21	366.13 ± 47.74	2.40 ± 0.43	22642.23 0.20	0.02 0.14	0.43 0.27	
JH-097a	2.9	0.0	0.0	5.2	0.0	2.37	2.25	2.50	2.37 ± 0.08	1.40 ± 0.26	73.57 ± 1.70	0.80 ± 0.00	16910.79 0.19	0.00 0.04	1.76 0.19	
JH-101	2.9	0.0	0.0	4.2	1.0	2.70	2.63	2.74	2.50 ± 0.08	0.73 ± 0.47	143.07 ± 13.37	1.22 ± 0.07	34088.59 0.65	0.01 0.10	0.60 0.65	
JH-102	1.5	1.4	0.0	5.1	0.0	2.38	2.37	2.39	2.07 ± 0.06	10.83 ± 0.55	105.27 ± 6.68	1.49 ± 0.15	1915.05 0.06	0.01 0.07	7.28 0.12	
JH-112	2.7	0.2	0.0	5.0	0.1	2.49	2.46	2.56	2.48 ± 0.07	1.40 ± 0.56	47.00 ± 4.00	9.34 ± 0.98	17709.93 0.40	0.00 0.09	0.15 0.41	
JH-113	2.7	0.1	0.0	4.8	0.4	2.59	2.47	2.75	2.51 ± 0.07	1.73 ± 0.31	51.37 ± 3.49	10.08 ± 0.26	14453.56 0.18	0.00 0.07	0.17 0.18	
JH-117	2.8	0.0	0.0	5.2	0.0	2.21	2.13	2.34	1.97 ± 0.04	1.00 ± 0.10	239.90 ± 23.45	2.87 ± 0.06	19745.40 0.05	0.01 0.12	0.35 0.05	
JH-118	2.9	0.0	0.0	5.0	0.2	2.38	2.20	2.56	2.32 ± 0.06	0.53 ± 0.45	189.30 ± 18.42	1.13 ± 0.27	43513.31 0.85	0.01 0.10	0.47 0.88	
JH-119	2.9	0.0	0.0	5.2	0.0	2.39	2.33	2.43	2.21 ± 0.06	1.17 ± 0.23	129.43 ± 9.13	2.62 ± 0.17	18937.26 0.20	0.01 0.08	0.44 0.21	
JH-120									2.42 ± 0.07	0.93 ± 0.38	111.43 ± 6.73	1.75 ± 0.39	25933.61 0.41	0.00 0.07	0.53 0.46	
JH-121	2.9	0.0	0.0	5.0	0.2	2.34	2.15	2.53	2.31 ± 0.06	0.90 ± 0.26	112.57 ± 7.55	2.53 ± 0.13	25709.33 0.30	0.00 0.07	0.36 0.30	
JH-122	2.8	0.0	0.0	5.2	0.0	2.43	2.37	2.48	2.28 ± 0.06	1.03 ± 0.15	86.33 ± 2.76	0.12 ± 0.00	22087.39 0.15	0.00 0.04	8.33 0.00	
JH-128e	0.3	2.7	0.0	4.6	0.5	2.38	2.33	2.42	2.34 ± 0.06	4.37 ± 0.21	133.27 ± 9.87	0.00 ± 0.00	5354.43 0.05	0.01 0.08	0.00 0.00	
JH-129a	1.3	1.7	0.0	4.9	0.2	2.15	1.97	2.26	2.20 ± 0.06	4.97 ± 0.47	346.90 ± 62.57	0.89 ± 0.39	4422.26 0.10	0.02 0.18	5.58 0.44	

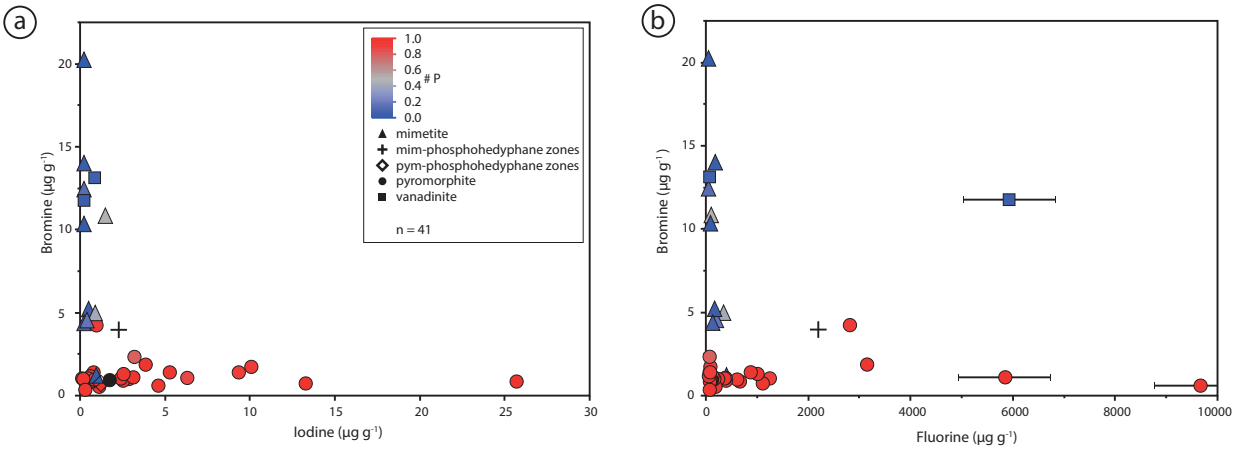

FIGURE 5. (**a**) Bromine vs. iodine and (**b**) bromine vs. fluorine content, respectively, of all CIC analyses. The symbols refer to different minerals, the color-coding to the appropriate P# = P/(P+As+V). Error bars are smaller than the symbol size, with the exception of three samples, where the bars were shown accordingly. N = number of analyzed samples.

of only 0.17 Å (Shannon 1976; Flis et al. 2010). Thus, mimetite and vanadinite have similar and larger unit-cell volumes than pyromorphite, correlating with significantly longer B-O (B = As, V, P) bond lengths that increase linearly with cell volume (e.g., Shannon 1976; Dai and Hughes 1989; Okudera 2013). Furthermore, the polyhedral volume of the Cl site in the $Pb2_6$ octahedron is smaller in pyromorphite (40.1 $Å^3$) compared to mimetite (41.9 $Å^3$) and vanadinite (42.0 $Å^3$) (Okudera 2013). Hence, Br (which has a smaller ionic radius than I) should be preferentially incorporated (relative) in pyromorphite and I preferentially incorporated in mimetite and vanadinite. However, the opposite is observed: pyromorphite has higher I concentrations (Fig. 9).

If, crystallography does not explain the observed incorporation patterns, they could be a function of the composition of the fluid from which the PyGMs crystallize. In this case, we would have to assume that fluid composition alternates (see e.g., Fig. 7b) between P-dominated/I-rich and As-dominated/Br-rich end-members. Based on the experiments of Flis et al. (2011) that imply that the PyGM mirrors the composition of the coexisting fluid the resulting minerals would be I-rich pyromorphite and Br-rich mimetite. This is the case in sample JH 114 (Fig. 7b), where the core is Br-rich mimetite, whereas the outer rim is I-rich pyromorphite. This sample clearly records a drastic change of the fluid chemistry with time. Arsenic in the fluid mainly derives from weathering of vein and host rock minerals (Basu and Schreiber 2013), whereas the primary P source has microbial origin, i.e., plant litter from topsoil horizons (Burmann et al. 2013). This distinction would imply that different fluid pathways of different initial fluid sources would lead to either pyromorphite or mimetite precipitation. The positive correlation of pyromorphite with I and of mimetite with Br indicates that not only P and As have different sources, but also I and Br are derived from different reservoirs. This is surprising, as both halogens are believed to be "biophilic" (Fuge 1988), and we have no explanation so far for this observation. However, not only the initial source but also the amount of available As or P at the time of PyGM formation determines which PyGM precipitates.

Possible parameters influencing the formation of pyromorphite-group minerals

Minor variations of the major element composition in single PyGM crystals can be explained by relatively constant boundary conditions during their formation. It seems unlikely to us that factors such as weathering of the host rock or fluid pathways

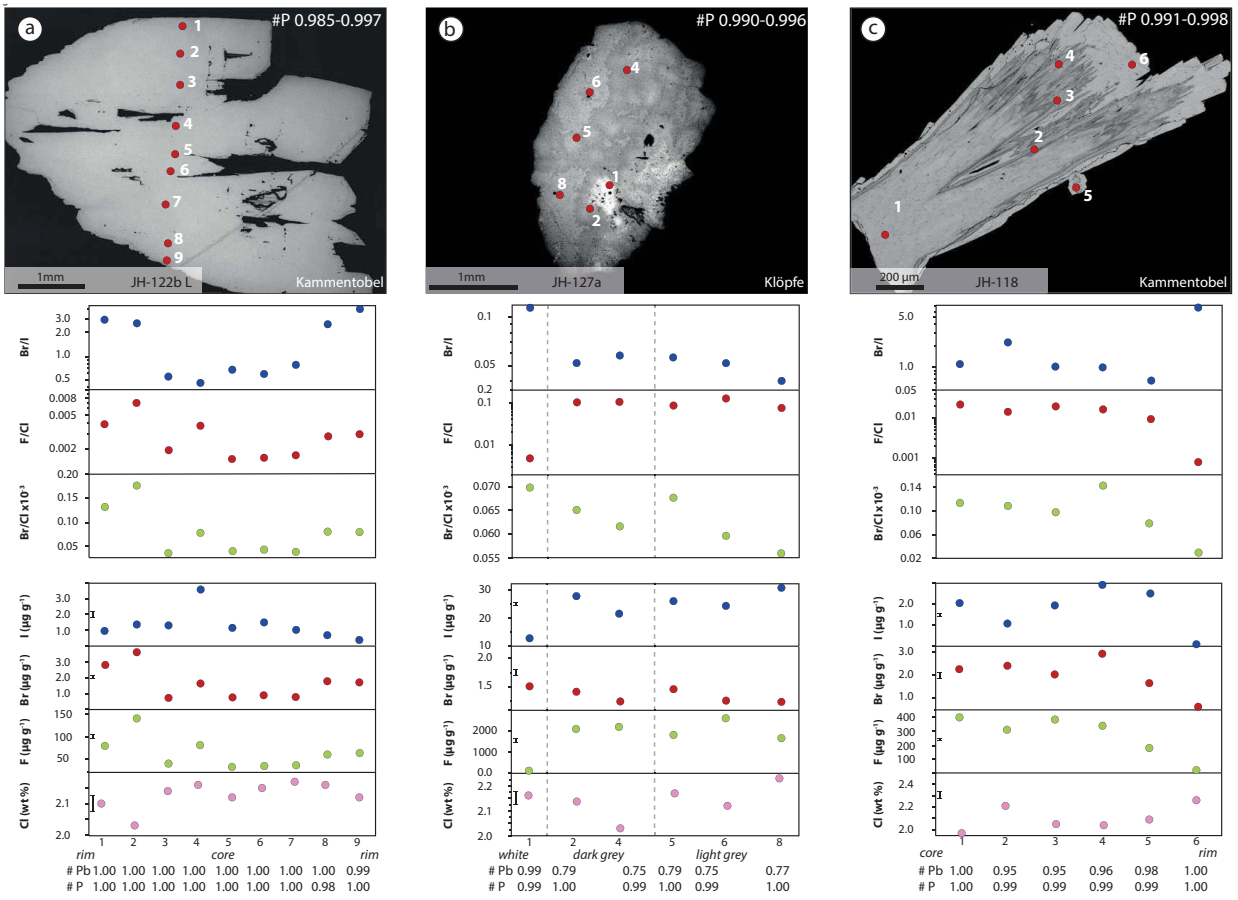

Figure 6. BSE images of (**a**) a macro- and microscopic non-zoned crystal, (**b**) a patchy zoned crystal, and (**c**) a crystal with growth zoning combined with spatially resolved SIMS halogen data. Halogen ratios and absolute element concentrations are shown. Black vertical bars show average 1σ uncertainties of all measurements. Variations in grayscale in the BSE images are due to variations in Pb content.

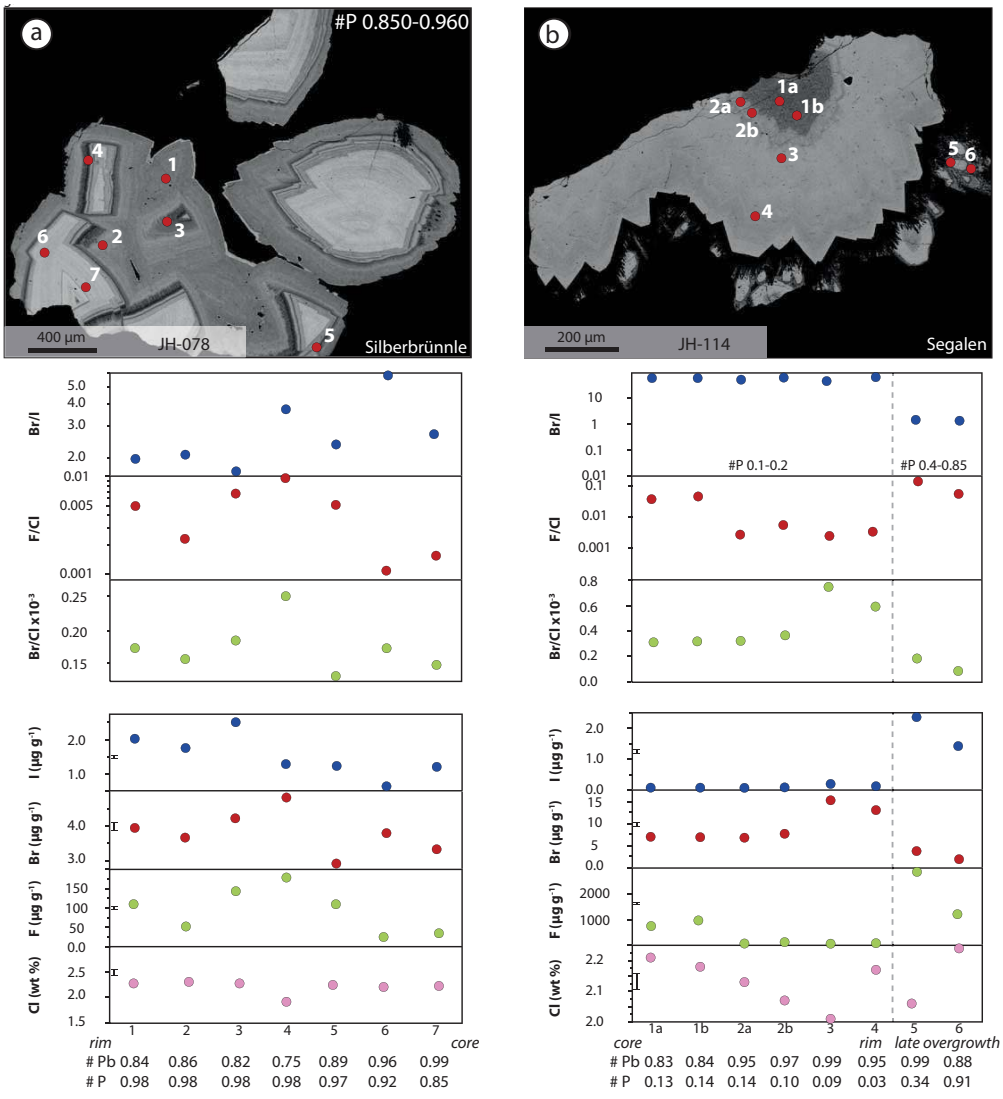

FIGURE 7. BSE images of crystals with a distinct growth zoning (a+b) combined with spatially resolved SIMS halogen data. Halogen ratios and absolute element concentrations are shown. Black vertical bars show average 1σ uncertainties of all measurements. Variations in grayscale in the BSE images are due to variations in Pb content.

change abruptly on such relatively short timescales.

However, trace elements are more prone to small scale processes in the environment and compositional zonation provides details about the crystal's formation environment and the evolution of the environmental parameters. This is comparable to zoned crystals in magmatic, metamorphic, and hydrothermal systems (Harlov et al. 2005; Boyce and Hervig 2009; Webster and Piccoli 2015).

The composition of a mineral in equilibrium with a fluid is determined by external physico-chemical parameters such as temperature, pressure, and fluid composition. Due to the shallow formation depth of the PyGM, temperature, and pressure can be assumed to be relatively constant for individual crystals and thus, the fractionation factor for individual elements between fluid and mineral should be relatively constant throughout the crystallization of individual mineral aggregates. For instance, it is well known that the temperature in shallow underground workings at dozens to a hundred meters' depth is basically constant and is identical to the annual mean temperature at the surface. The effect of temperature may only be important when different localities are compared. For example the mean annual temperature in the Rhine valley is close to 20 °C while the highest Schwarzwald peaks have a mean annual temperature of 5 °C.

We suggest that the halogen variations within single PyGM crystals and aggregates reflect the compositional evolution of the fluid from which they precipitated. The composition of fluids from which secondary/supergene mineral phases are formed within the oxidation zone of ore deposits is initially governed by the composition of the precipitation. However, halogen input by rainfall is not a major contributor to halogen concentrations in the soil or vegetation (Lovett et al. 2005), but the amount of water that is available to leach rocks has an influence on the

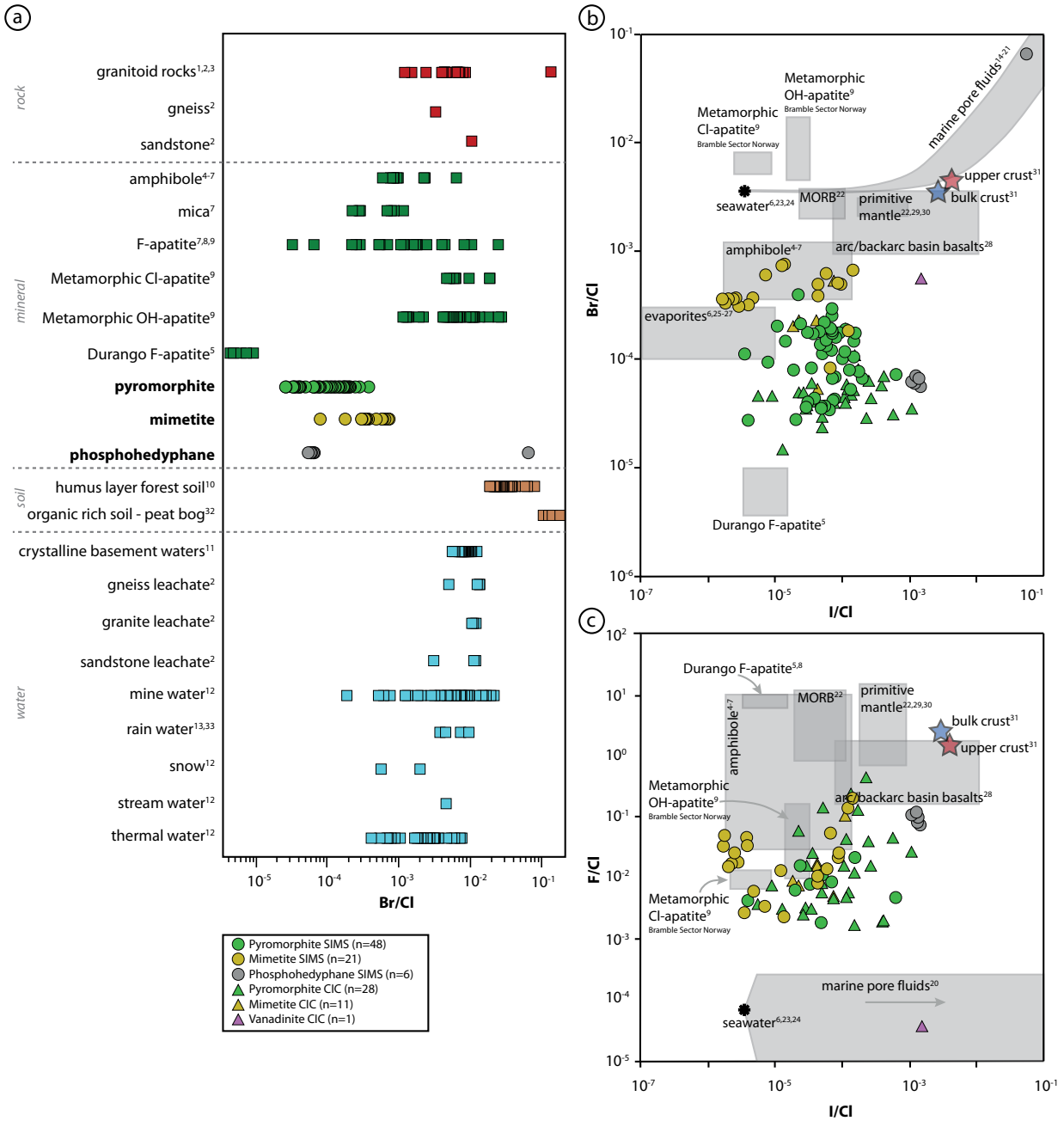

Figure 8. The halogen systematics in different reservoirs (**a**) Br/Cl ratios of several rock, mineral, soil, and water types. Bold minerals = data of this study. Pyromorphite, mimetite, and phosphohedyphane ratios plot between Durango F-apatite and metamorphic Cl- and OH-apatite and lie below water and soil analyses. (**b**) Br/Cl plotted against I/Cl shows that mimetite data partly overlaps with the amphibole field, whereas pyromorphite plots between the Durango F-apatite field and the amphibole field. (**c**) F/Cl plotted against I/Cl shows that the data of this study plots between sedimentary pore fluids and apatite and amphibole analyses. Gray fields indicate several reservoirs, based on literature data, analyzed with different analytical techniques. NG = noble gas, IC = ion chromatography, SIMS = secondary ion mass spectrometry, ICP-MS = inductively coupled plasma–mass spectrometry, TXRF = total reflection X-ray fluorescence spectroscopy. [1]Wang et al. (2018); [2]Burisch et al. (2016); [3]Behne (1953); [4]Kusebauch et al. (2015a), IC, ICP-MS; [5]Kendrick (2012), NG; [6]Kendrick and Burnard (2013); [7]Teiber et al. (2014), EPMA, TXRF; [8]Marks et al. (2012), SIMS; [9]Kusebauch et al. (2015b), SIMS; [10]Låg and Steinnes (1976); [11]Seelig and Bucher (2010); [12]Göb et al. (2013), samples from Germany; [13]Neal et al. (2010), samples from the U.K.; [14]Kendrick et al. (2011); [15]Fehn et al. (2000); [16]Fehn et al. (2007); [17]Fehn et al. (2007); [18]Muramatsu et al. (2001); [19]Muramatsu et al. (2007); [20]Gieskes and Mahn (2007); [21]Tomaru et al. (2009); [22]Kendrick et al. (2017); [23]McCaffrey et al. (1987); [24]Fuge and Johnson (1986); [25]Herrmann (1980); [26]Siemann and Schramm (2000); [27]Böhlke and Irwin (1992); [28]Kendrick et al. (2014) and references therein; [29]Palme and O'Neill (2003); [30]Lyubetskaya and Korenaga (2007); [31]Rudnick and Shan (2003); [32]Biester et al. (2006); [33]Biester et al. (2004).

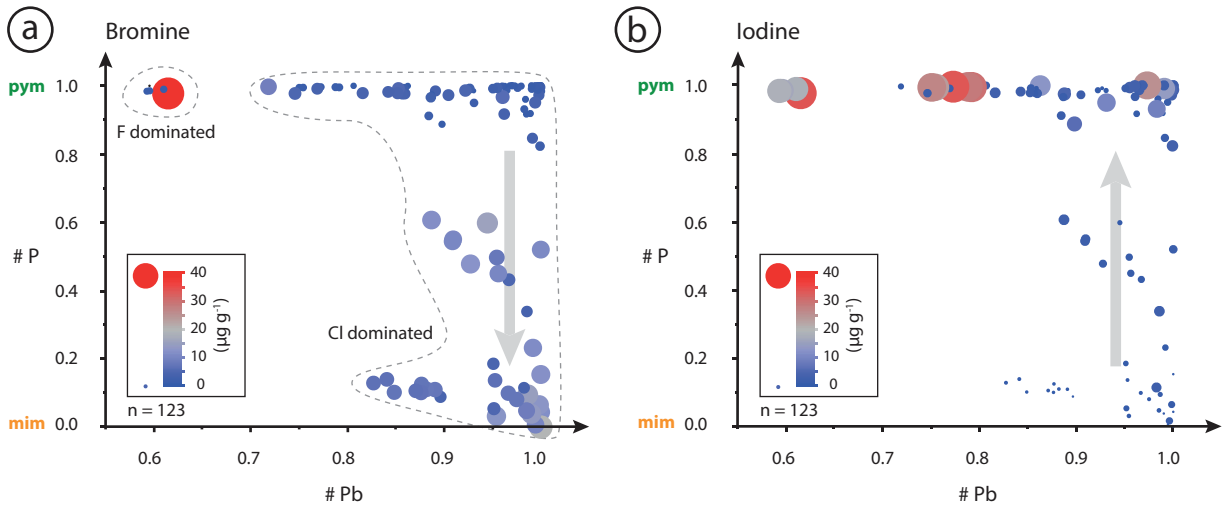

Figure 9. Bromine (**a**) and iodine (**b**) incorporation in PyGM, data based on all CIC and SIMS analyses. Abbreviations: pym = pyromorphite, mim = mimetite; P# = P/(P+As+V); Pb# = Pb/(Pb+As). Small blue symbols refer to minor element content and transition to large red symbols to higher element content. Dashed lines mark samples with either F or Cl as dominating halogen. (**a**) Increasing Br content with decreasing P# and slightly increasing Pb#. (**b**) Increasing I content with increasing P# and slightly decreasing Pb#.

process of chemical weathering of minerals (Carroll 2012). If the principle of lower fluid/rock ratios resulting in lower release rate, but higher halogen concentrations in the fluid (Huang et al. 1986; Burisch et al. 2016) is applied to halogen release by weathering of minerals, higher rainfall rates lead to a decrease in halogen concentrations of the fluid, i.e., the soil solution, which in turn results in variable halogen content among distinct growth zones of PyGM.

Halogens as a tracer: Halogen variations independent of major element composition

Pyromorphite and mimetite crystals can be strongly zoned with respect to their halogen contents (Figs. 6a–6c, 7a, and 7b). Because zoning can be found in crystals with a constant major element composition (P# and Ca#), exclusively crystallographic reasons can be excluded, and an additional process needs to be invoked. Individual growth zones in PyGM have been interpreted to represent single episodes of fluid flow and related weathering reactions (e.g., Markl et al. 2014), and it has been shown that there are still active processes of PyGM crystallization on the walls of some underground workings and in medieval dumps (Burmann et al. 2013). Thus, small variations in the environmental conditions during PyGM formation, such as availability of halogens or other physico-chemical parameters, can affect halogen incorporation.

Potential halogen sources for PyGM formation include soil, rock, and rainwater. The halogen contents in these environmental components are known in very different detail and vary greatly (Fig. 8, Table 4). In general, on Earth F and Cl have similar abundance (Kabata-Pendias 2011), but Cl is the dominant halogen in different types of waters, rocks, and soils (similar as in PyGM) although some rock types like, e.g., evolved leucogranites contain more F than Cl (Table 4).

The highest Cl concentrations in surface waters are observed in seawater (18 800 mg/L) and geothermal waters (1070 mg/L; Table 4). Rain and creek water contain Cl concentrations between 0.07 and 8.16 mg/L. In soils (depending on soil type and sampling depth), Cl concentrations are highly variable, with maximum Cl concentrations (up to 1200 mg/kg) in the humus layer of a forest soil (Table 4). Whole-rock analyses from various igneous, metamorphic, and sedimentary rock types show variable Cl concentrations but are similar to the range observed in the soils (Table 4).

Comprehensive data sets that include Cl, F, Br, and I content for the different geochemical reservoirs are sparse (Table 4). However, different reservoirs can be distinguished according to their Br/Cl, I/Cl, and F/Cl ratio (Figs. 8a–8c). The range of halogen ratios in PyGM compared to other known rocks, minerals, and fluids show that the Br/Cl ratios are notably lower in PyGM (Figs. 8a–8c), suggesting that Br is preferentially excluded from PyGM formation relative to Cl. The low Br/Cl ratios of PyGM partly overlap with those of F-apatite and to some extend with mica, mine, and thermal waters (Fig. 8a). Considering Br/Cl vs. I/Cl ratios mimetite data fall in the amphibole field (Fig. 8b), whereas pyromorphites, phosphoheyphanes, and vandadinites do not overlap with any of the known data. One phosphohedyphane outlier lies within the marine pore fluids reservoir due to extremely high Br and I concentrations (Fig. 8b), reflecting a possible organic contamination. When comparing F/Cl and I/Cl ratios, PyGM ratios partly overlap with amphibole, Cl-apatite and OH-apatite (Fig. 8c). However, F/Cl ratios of PyGM are distinctly lower compared to the other reservoirs, showing that the main distinctive feature are not I/Cl ratios but Br/Cl and F/Cl ratios (Figs. 8a–8c). Vanadinite has a F/Cl ratio comparable to seawater but an orders of magnitude higher I/Cl ratio (Fig. 8c).

The variations in halogen concentrations within and between the different geochemical reservoirs are attributed to a combination of complex abiotic and biotic processes. For example, the initial halogen composition of rainwater is altered during seepage through the organic layer on top of the mineral soil, underlying

mineral soil horizons and the host rock. Because (sub-)surface fluids are involved in the precipitation of PyGM, the halogen cycle in combination with the H_2O cycle has to be considered to understand variations in halogen availability during mineral formation.

The composition and seasonality of local rainfall are subordinately relevant due to its low halogen content; more important is its influence on the intensity of host rock alteration. The halogen composition of rainwater has been shown to fluctuate (Yuita et al. 2006). Absolute I concentrations in rain vary, depending on seasonal changes in rainfall frequency and intensity. Furthermore, rainwater in continental sites has lower halogen concentrations than coastal sites (Fuge 1988). Higher Br/Cl and I/Cl ratios were reported for inland areas (Fuge 1988; Neal et al. 2010) due to the relative enrichment of Br and I. After precipitation, the initial halogen content in the rainwater can be altered by vegetation, as plants commonly take up growth-relevant elements through the roots and thus increase the Cl concentrations in plant tissue and in throughfall relative to directly incident rainfall (Lovett et al. 2005; Oelmann et al. 2007). The impact of vegetation on throughfall is, however, negligible compared to other processes, because the Cl in the soil solution is primarily derived from weathering and not from rainfall (Lovett et al. 2005; Svensson et al. 2012). Halogens (Cl and Br) were regarded in the past as conservative tracers in fluid-involving processes in soils and upper crustal rocks (Öberg and Sandén 2005). There is increasing evidence that halides serve as important nutrients and are therefore actively being cycled by plants and microorganisms (Leri and Myneni 2012; Öberg and Bastviken 2012). Furthermore, evapotranspiration has an influence on downward water fluxes (Oelmann et al. 2007), because increased evapotranspiration leads to a limited transport of water in soil (Johansson et al. 2003 and references therein). Thus, it is likely that the effect of evaporation has an impact on halogen incorporation. Vegetation density and vegetation type may also influence halogen input into the soil to various extent (e.g., Låg and Steinnes 1976).

TABLE 4. Halogen data compilation in water, soil, rocks and vegetation, b.d.l. = below the detection limit

Sample type	Region	Absolute concentration (mg/kg, L^{-1})				Reference
		Cl	F	Br	I	
		Water				
Rain water	Tübingen; DE	0.121	0.0121	b.d.l.		Göb et al. (2013)
Rain water	Hafren forest, U.K.	4.49		0.0172	0.013	Neal et al. (2010)
Rain water	New Hampshire, U.S.A.	4.35–8.16				Lovett et al. (1996)
Rain water	Chile	0.5		0.0039	0.00048	Biester et al. (2006)
Cloud water	Hafren forest, U.K.	47.8		0.156	0.00848	Neal et al. (2010)
Throughfall	Slavkov forest; CZ	0.029–0.041				Krám et al. (1997)
Throughfall (under sugar maple)	Hardwood forest, U.S.A.	1.29–2.35				Eaton et al. (1973)
Throughfall (under yellow birch)	Hardwood forest, U.S.A.	0.93–0.95				Eaton et al. (1973)
Throughfall (under beech)	Hardwood forest, U.S.A.	0.75–1.25				Eaton et al. (1973)
Creek water	Feldberg; DE	0.393	0.0233	b.d.l.		Göb et al. (2013)
Creek water	Oberwolfach; DE	1.44	0.58	0.00675		Göb et al. (2013)
Stream water	Slavkov forest, CZ	0.069–0.0665				Krám et al. (1997)
Mine water	Feldberg; DE	0.744	0.0488	0.00454		Göb et al. (2013)
Thermal water	Leuze, Stuttgart; DE	1070	1.21	1.96		Göb et al. (2013)
Sea water		18800	1.3	67	0.06	(Wong and Brewer 1974; Wilson 1975; Whitfield and Turner 1979; Fuge 1988; Li 1991)
		Soil				
Agricultural soils	France	19–100 (med.:50)				Redon et al. (2013)
Grassland soils	France	13–1248 (med.:54)				Redon et al. (2013)
Forest soils	France	34–340 (med.:90)				Redon et al. (2013)
Forest soils	Japan			68–130	20–23	Yuita et al. (1978)
Humus layer forest soils	Norway	300–1200		5–100	3–20	Låg and Steinnes (1976)
Organic rich soil – peat bog	Chile	350–1200		40–200	10–20	Biester et al. (2004, 2006)
A horizon soil forest	Tsukuba, Japan				70	Yuita et al. (2006)
B horizon soil forest	Tsukuba, Japan				40–55	Yuita et al. (2006)
		Rock leachates				
Gneiss leachates	Schwarzwald, DE	0.1–2.4	0.002–0.75	b.d.l.-0.035		Burisch et al. (2016)
Granite, leachates	Schwarzwald, DE	0.29–13.8	0.016–1.78	b.d.l.-0.144		Burisch et al. (2016)
Sandstone, leachates	Schwarzwald, DE	0.12–2.68	0.012–0.027	b.d.l.-0.035		Burisch et al. (2016)
		Rock				
A-type granite	U.S.A., Canada	45–400	400–12200			Eby (1990)
Granite	Germany	70–300		<1–9.5		Behne (1953)
Granite	Schwarzwald, DE	240	980	1.5		Burisch et al. (2016)
Gabbro	Harzburg, DE	20		<1		Behne (1953)
Basalt	Göttingen, DE	30–120		<1–2.2		Behne (1953)
Keuper clay	Friedland a.d. Leine, DE	370		4.4		Behne (1953)
Gneiss		140–1000		0.007–0.055		Johns and Huang (1967); Muramatsu and Wedepohl (1998)
Gneiss	Schwarzwald, DE	120	600	0.4		Burisch et al. (2016)
Amphibolites	China,	100–400	659	0.020–0.026		Johns and Huang (1967); Gao et al. (1998); Muramatsu and Wedepohl (1998)
Sandstone	China	68–180	482–489			Gao et al. (1998)
Sandstone	Schwarzwald, DE	47	68	0.5		Burisch et al. (2016)
		Vegetation				
Wood	New Hampshire, U.S.A.	9–185				Lovett et al. (2005)
Bark	New Hampshire, U.S.A.	37–170				Lovett et al. (2005)
Foliage (temperate-zone forest)	New Hampshire, U.S.A.	9–2500				Lovett et al. (2005)

A major halogen source for groundwater or soil water is rock weathering by leaching and dissolution of minerals, which strongly depends on the fluid/rock ratio (Carroll 2012). For example, feldspar dissolution experiments of Huang et al. (1986) revealed that elements are more rapidly released at higher fluid/rock ratios. However, even though a lower fluid/rock ratio may result in a lower release rate, it also results in higher halogen concentrations in the final fluid (Huang et al. 1986; Burisch et al. 2016), because lower fluid/rock ratios favor an increased retention time at the water-rock interface (Oliva et al. 2003). Microbial activity also influences the process of weathering and thus elemental release (Oliva et al. 2003; Wu et al. 2008), where the heterotrophic bacterial metabolism is pH dependent. For example, a lower pH (e.g., due to nitrification processes) results in accelerated Ca release from minor phases in granite (Oliva et al. 2003; Wu et al. 2008). Consequently, variations in pH may also influence the release of halogens during biogeochemical weathering. However, soil-vegetation interactions are very complex. For example, the environmental pH of the soil depends on, among others, host rock, type of vegetation, microbial activity, chemical processes within the soil, and rainfall amount (Jenny 1941). Furthermore, vegetation and biological activity are also essential in defining the degree of weathering of the host rock (Park et al. 1990; Oades 1993; Seybold et al. 1999). Not only the vegetation but also the thickness of the soil cover affects the weathering process, where a thin soil cover favors chemical weathering and the release of halogens into the fluid (Oliva et al. 2003). At the same time, weathering results in the formation of secondary minerals in the soil such as pedogenic oxides (Fe- and Al-oxides and hydroxides) and clay minerals. These minerals are able to adsorb halides, thereby potentially further altering the halogen composition in the fluid (Nodvin et al. 1986; Loganathan et al. 2007). $FeOOH{\cdot}nH_2O$ strongly incorporates halogens into its structure, e.g., up to wt% Cl and some parts per million of I.

Implications

Halogen concentrations in PyGM crystals from different localities, of various bulk compositions, and between specific zones in single crystals are controlled by changes in the physicochemical conditions during their formation (e.g., composition of the fluid, temperature variations). Furthermore, crystal-chemical effects may have an influence, but their exact effect is not completely understood. Fluid-chemical and possibly crystallographic effects can lead to variable halogen incorporation in different types of PyGM (pyromorphite, mimetite, vanadinite). Thus, halogen ratios of different PyGM may be used as fluid monitors, because it was shown that the halogens are preferentially incorporated into specific PyGM. Further studies, aimed at each respective process, are needed to understand and correlate the zonation to individual processes. We therefore suggest interdisciplinary studies that not only take into account abiotic aspects of mineral growth but also potential biological influences on the weathering (and formation) of PyGM in near-surface environments. Furthermore, experimental work on mineral-fluid partitioning behavior for the different halogens with respect to mineral type is essential for further understanding halogen incorporation into PyGM. The environmental importance of this mineral group due to incorporation and removal of toxic elements from the environment requires a more detailed investigation. Moreover, PyGM are of further interest as they incorporate significant amounts of Cl, thus depriving the fluid of Cl, which is an important complexing agent for many toxic elements. This, in turn, implies that the mobility of these toxic elements is reduced, not only by direct incorporation into PyGM but also by removal of Cl from the fluid and thus decreasing their mobility.

Acknowledgments

We are grateful to Thomas Wenzel for his invaluable help with the electron microprobe. Simone Schafflick is thanked for the sample preparation. Further thanks go to Bernd Steinhilber, who helped to develop the ideal method for the analyses. Axel Schmitt is thanked for providing the Macusani glass sample. Furthermore, we thank the Editor Don Baker, the Associate Editor Andrew Madden, and two anonymous reviewers for their constructive feedback that improved this manuscript significantly.

Funding

This research was funded by the German Research Foundation (DFG) Grant No. MA 2135/23-1 and OE 516/8-1. M.A. Kendrick was supported by an Australian Research Council Future Fellowship (FT13 0100141).

References cited

Bajda, T. (2010) Solubility of mimetite $Pb_5(AsO_4)_3Cl$ at 5–55 °C. Environmental Chemistry, 7(3), 268–278.

Basta, N., and McGowen, S. (2004) Evaluation of chemical immobilization treatments for reducing heavy metal transport in a smelter-contaminated soil. Environmental Pollution, 127(1), 73–82.

Basu, A., and Schreiber, M.E. (2013) Arsenic release from arsenopyrite weathering: insights from sequential extraction and microscopic studies. Journal of Hazardous Materials, 262, 896–904.

Behne, W. (1953) Untersuchungen zur Geochemie des Chlor und Brom. Geochimica et Cosmochimica Acta, 3(4), 186–215.

Biester, H., Keppler, F., Putschnew, A., Martinez-Cortizas, A., and Petri, M. (2004) Halogen retention, organohalogens, and the role of organic matter decomposition on halogen enrichment in two Chilean peat bos. Environmental Science & Technology, 38(7), 1984–1991.

Biester, H., Hemmerich, S., and Petri, M. (2006) Halogens in porewater of peat bogs—the role of peat decomposition and dissolved organic matter. Biogeosciences Discussions, 2(5), 1457–1486.

Böhlke, J.K., and Irwin, J.J. (1992) Brine history indicated by argon, krypton, chlorine, bromine, and iodine analyses of fluid inclusions from the Mississippi Valley type lead-fluorite-barite deposits at Hansonburg, New Mexico. Earth and Planetary Science Letters, 110(1), 51–66.

Boyce, J.W., and Hervig, R.L. (2009) Apatite as a monitor of late-stage magmatic processes at Volcán Irazú, Costa Rica. Contributions to Mineralogy and Petrology, 157(2), 135.

Brook, E.J., Harder, S., Severinghaus, J., Steig, E.J., and Sucher, C.M. (2000) On the origin and timing of rapid changes in atmospheric methane during the last glacial period. Global Biogeochemical Cycles, 14(2), 559–572.

Burisch, M., Marks, M.A., Nowak, M., and Markl, G. (2016) The effect of temperature and cataclastic deformation on the composition of upper crustal fluids—An experimental approach. Chemical Geology, 433, 24–35.

Burmann, F., Keim, M.F., Oelmann, Y., Teiber, H., Marks, M.A., and Markl, G. (2013) The source of phosphate in the oxidation zone of ore deposits: Evidence from oxygen isotope compositions of pyromorphite. Geochimica et Cosmochimica Acta, 123, 427–439.

Carroll, D. (2012) Rock Weathering. Springer Science & Business Media.

Cicerone, R.J. (1981) Halogens in the atmosphere. Reviews of Geophysics, 19(1), 123–139.

Dai, Y., and Hughes, J.M. (1989) Crystal structure refinements of vanadinite and pyromorphite. Canadian Mineralogist, 27(2), 189–192.

Dennen, W.H. (1960) Principles of Mineralogy. Ronald Press Company.

Eaton, J.S., Likens, G.E., and Bormann, F.H. (1973) Throughfall and stemflow chemistry in a northern hardwood forest. The Journal of Ecology, 495–508.

Eby, G.N. (1990) The A-type granitoids: a review of their occurrence and chemical characteristics and speculations on their petrogenesis. Lithos, 26(1-2), 115–134.

Ehlers, J., and Gibbard, P.L. (2004) Quaternary glaciations-extent and chronology: Part I: Europe. Elsevier.

Fehn, U., Snyder, G., and Egeberg, P.K. (2000) Dating of Pore Waters with ^{129}I: Relevance for the Origin of Marine Gas Hydrates. Science, 289, 2332–2335.

Fehn, U., Snyder, G.T., and Muramatsu, Y. (2007) Iodine as a tracer of organic material: ^{129}I results from gas hydrate systems and fore arc fluids. Journal of Geochemical Exploration, 95(1), 66–80.

Flis, J., Manecki, M., and Bajda, T. (2007) Solubility of pyromorphite-mimetite

solid solutions at 5-65 °C: Variability of thermodynamic stability of minerals from pyromorphite-mimetite series at 5-65 °C. Geochimica et Cosmochimica Acta, 71, p. A285–A285.
Flis, J., Borkiewicz, O., Bajda, T., Manecki, M., and Klasa, J. (2010) Synchrotron-based X-ray diffraction of the lead apatite series $Pb_{10}(PO_4)6C_{l2}$–$Pb_{10}(AsO_4)_6Cl_2$. Journal of Synchrotron Radiation, 17(2), 207–214.
Flis, J., Manecki, M., and Badja, T. (2011) Solubility of pyromorphite $Pb_5(PO_4)_3Cl$–mimetite $Pb_5(AsO_4)_3Cl$ solid solution series. Geochimica et Cosmochimica Acta, 75(7), 1858–1868.
Förtsch, E., and Wondratschek, H. (1965) Zur Kristallchemie der Minerale der Pyromorphit-Gruppe. Naturwissenschaften, 52(8), 182.
Fuge, R. (1988) Sources of halogens in the environment, influences on human and animal health. Environmental Geochemistry and Health, 10(2), 51–61.
Fuge, R., and Johnson, C.C. (1986) The geochemistry of iodine—a review. Environmental Geochemistry and Health, 8(2), 31–54.
Gao, S., Luo, T.-C., Zhang, B.-R., Zhang, H.-F., Han, Y.-w., Zhao, Z.-D., and Hu, Y.-K. (1998) Chemical composition of the continental crust as revealed by studies in East China. Geochimica et Cosmochimica Acta, 62(11), 1959–1975.
Gerke, T.L., Scheckel, K.G., and Schock, M.R. (2009) Identification and distribution of vanadinite ($Pb_5(V^{5+}O_4)_3Cl$) in lead pipe corrosion by-products. Environmental Science & Technology, 43(12), 4412–4418.
Gieskes, J.M., and Mahn, C. (2007) Halide systematics in interstitial waters of ocean drilling sediment cores. Applied Geochemistry, 22(3), 515–533.
Göb, S., Loges, A., Nolde, N., Bau, M., Jacob, D.E., and Markl, G. (2013) Major and trace element compositions (including REE) of mineral, thermal, mine and surface waters in SW Germany and implications for water–rock interaction. Applied Geochemistry, 33, 127–152.
Hålenius, U., Hatert, F., Pasero, M., and Mills, S.J. (2017) New minerals and nomenclature modifications approved in 2017. Mineralogical Magazine, 81(5), 1279–1286.
Harlov, D.E. (2015) Apatite: A fingerprint for metasomatic processes. Elements, 11(3), 171–176.
Harlov, D.E., Wirth, R., and Förster, H.-J. (2005) An experimental study of dissolution–reprecipitation in fluorapatite: fluid infiltration and the formation of monazite. Contributions to Mineralogy and Petrology, 150(3), 268–286.
Hautmann, S., and Lippolt, H. (2000) 40Ar/39Ar dating of central European K–Mn oxides—a chronological framework of supergene alteration processes during the Neogene. Chemical Geology, 170(1-4), 37–80.
Herrmann, A.G. (1980) Bromide distribution between halite and NaCl-saturated seawater. Chemical Geology, 28, 171–177.
Hofmann, B., and Eikenberg, J. (1991) The Krunkelbach uranium deposit, Schwarzwald, Germany; correlation of radiometric ages (U-Pb, U-Xe-Kr, K-Ar, ^{230}Th-^{234}U). Economic Geology, 86(5), 1031–1049.
Huang, W., Bishop, A., and Brown, R. (1986) The effect of fluid/rock ratio on feldspar dissolution and illite formation under reservoir conditions. Clay Minerals, 21(4), 585–601.
Janicka, U., Bajda, T., and Manecki, M. (2012) Synthesis and solubility of brompyromorphite $Pb_5(PO_4)_3Br$. Mineralogia Polonica, 43(1-2), 129–135.
Jenny, H. (1941) Factors of Soil Formation. McGraw□Hill, New York.
Johansson, E., Sandén, P., and Öberg, G. (2003) Organic chlorine in deciduous and coniferous forest soils in southern Sweden. Soil Science, 168(5), 347–355.
John, T., Scambelluri, M., Frische, M., Barnes, J.D., and Bach, W. (2011) Dehydration of subducting serpentinite: implications for halogen mobility in subduction zones and the deep halogen cycle. Earth and Planetary Science Letters, 308(1-2), 65–76.
Johns, W., and Huang, W. (1967) Distribution of chlorine in terrestrial rocks. Geochimica et Cosmochimica Acta, 31(1), 35–49.
Johnson, L., Burgess, R., Turner, G., Milledge, H., and Harris, J. (2000) Noble gas and halogen geochemistry of mantle fluids: comparison of African and Canadian diamonds. Geochimica et Cosmochimica Acta, 64(4), 717–732.
Kabata-Pendias, A. (2011) Trace Elements in Soils and Plants. CRC Press, 534 p.
Kalt, A., Altherr, R., and Hanel, M. (2000) The Variscan basement of the Schwarzwald. European Journal of Mineralogy, 12, 1–43.
Kampf, A.R., and Housley, R.M. (2011) Fluorphosphohedyphane, $Ca_2Pb_3(PO_4)_3F$, the first apatite supergroup mineral with essential Pb and F. American Mineralogist, 96, 423–429.
Keim, M.F., and Markl, G. (2015) Weathering of galena: Mineralogical processes, hydrogeochemical fluid path modeling, and estimation of the growth rate of pyromorphite. American Mineralogist, 100, 1584–1594.
Kendrick, M.A. (2012) High precision Cl, Br and I determinations in mineral standards using the noble gas method. Chemical Geology, 292, 116–126.
Kendrick, M.A., and Burnard, P. (2013) Noble gases and halogens in fluid inclusions: A journey through the Earth's crust. The Noble Gases as Geochemical Tracers. P. Burnard, p. 319–369. Springer-Verlag, Berlin.
Kendrick, M., and Phillips, D. (2009) New constraints on the release of noble gases during in vacuo crushing and application to scapolite Br–Cl–I and ^{40}Ar/^{39}Ar age determinations. Geochimica et Cosmochimica Acta, 73(19), 5673–5692.
Kendrick, M., Phillips, D., Wallace, M., and Miller, J.M. (2011) Halogens and noble gases in sedimentary formation waters and Zn–Pb deposits: A case study from the Lennard Shelf, Australia. Applied Geochemistry, 26(12), 2089–2100.
Kendrick, M.A., Kamenetsky, V.S., Phillips, D., and Honda, M. (2012) Halogen systematics (Cl, Br, I) in mid-ocean ridge basalts: a Macquarie Island case study. Geochimica et Cosmochimica Acta, 81, 82–93.
Kendrick, M.A., Arculus, R., Burnard, P., and Honda, M. (2013) Quantifying brine assimilation by submarine magmas: Examples from the Galápagos Spreading Centre and Lau Basin. Geochimica et Cosmochimica Acta, 123, 150–165.
Kendrick, M.A., Jackson, M.G., Kent, A.J.R., Hauri, E.H., Wallace, P.J., and Woodhead, J. (2014) Contrasting behaviours of CO_2, S, H_2O and halogens (F, Cl, Br, and I) in enriched-mantle melts from Pitcairn and Society seamounts. Chemical Geology, 370, 69–81.
Kendrick, M.A., Honda, M., and Vanko, D.A. (2015) Halogens and noble gases in Mathematician Ridge meta-gabbros, NE Pacific: implications for oceanic hydrothermal root zones and global volatile cycles. Contributions to Mineralogy and Petrology, 170(5-6), 43.
Kendrick, M.A., Hémond, C., Kamenetsky, V.S., Danyushevsky, L., Devey, C.W., Rodemann, T., and Perfit, M.R. (2017) Seawater cycled throughout Earth's mantle in partially serpentinized lithosphere. Nature Geoscience, 10(3), 222.
Kendrick, M.A., D'Andres, J., Holden, P., and Ireland, T. (2018) Halogens (F, Cl, Br, I) in Thirteen USGS, GSJ and NIST International Rock and Glass Reference Materials. Geostandards and Geoanalytical Research.
Knyazev, A., Chernorukov, N., and Bulanov, E. (2011) Phase diagram of apatite system $Ca_{10}(PO_4)_6Cl_2$–$Pb_{10}(PO_4)_6Cl_2$. Thermochimica Acta, 526(1-2), 72–77.
Krám, P., Hruška, J., Wenner, B.S., Discoll, C.T., and Johnson, C.E. (1997) The biogeochemistry of basic cations in two forest catchments with contrasting lithology in the Czech Republic. Biogeochemistry, 37(2), 173–202.
Kusebauch, C., John, T., Barnes, J.D., Klügel, A., and Austrheim, H.O. (2015a) Halogen element and stable chlorine isotope fractionation caused by fluid–rock interaction (Bamble Sector, SE Norway). Journal of Petrology, 56(2), 299–324.
Kusebauch, C., John, T., Whitehouse, M.J., and Engvik, A.K. (2015b) Apatite as probe for the halogen composition of metamorphic fluids (Bamble Sector, SE Norway). Contributions to Mineralogy and Petrology, 170(4), 34.
Låg, J., and Steinnes, E. (1976) Regional distribution of halogens in Norwegian forest soils. Geoderma, 16(4), 317–325.
Leri, A.C., and Myneni, S.C. (2012) Natural organobromine in terrestrial ecosystems. Geochimica et Cosmochimica Acta, 77, 1–10.
Loganathan, P., Liu, Q., Hedley, M.J., and Gray, C.W. (2007) Chemical fractionation of fluorine in soils with a long-term phosphate fertiliser history. Soil Research, 45, 390–396. doi: https://doi.org/10.1071/SR07030.
Lovett, G.M., Likens, G.E., Buso, D.C., Driscoll, C.T., and Bailey, S.W. (2005) The biogeochemistry of chlorine at Hubbard Brook, New Hampshire, USA. Biogeochemistry, 72(2), 191–232.
Lyubetskaya, T., and Korenaga, J. (2007) Chemical composition of Earth's primitive mantle and its variance: 1. Method and results. Journal of Geophysical Research: Solid Earth, 112(B3).
Markl, G., Marks, M.A., Holzäpfel, J., and Wenzel, T. (2014) Major, minor, and trace element composition of pyromorphite-group minerals as recorder of supergene weathering processes from the Schwarzwald mining district, SW Germany. American Mineralogist, 99, 1133–1146.
Marks, M.A., Wenzel, T., Whitehouse, M.J., Loose, M., Zack, T., Barth, M., Worgard, L., Krasz, V., Eby, G.N., and Stosnach, H. (2012) The volatile inventory (F, Cl, Br, S, C) of magmatic apatite: An integrated analytical approach. Chemical Geology, 291, 241–255.
Marks, M.A., Kendrick, M.A., Eby, G.N., Zack, T., and Wenzel, T. (2017) The F, Cl, Br and I Contents of Reference Glasses BHVO-2G, BIR-1G, BCR-2G, GSD-1G, GSE-1G, NIST SRM 610 and NIST SRM 612. Geostandards and Geoanalytical Research, 41(1), 107–122.
McCaffrey, M., Lazar, B., and Holland, H. (1987) The evaporation path of seawater and the coprecipitation of Br^- and K^+ with halite. Journal of Sedimentary Research, 57(5), 928–937.
McCann, T. (Ed.). (2008) The Geology of Central Europe: Mesozioc and cenozoic. Geological Society of London.
Metz, R., and Richter, M. (1957) Die Blei-Zink-Erzgänge des Schwarzwaldes. Beihefte zum Geologischen Jahrbuch, Beiheft, 29, 277.
Morel, P., Von Blanckenburg, F., Schaller, M., Kubik, P.W., and Hinderer, M. (2003) Lithology, landscape dissection and glaciation controls on catchment erosion as determined by cosmogenic nuclides in river sediment (the Wutach Gorge, Black Forest). Terra Nova, 15(6), 398–404.
Muramatsu, Y., and Wedepohl, K.H. (1998) The distribution of iodine in the Earth's crust. Chemical Geology, 147(3-4), 201–216.
Muramatsu, Y., Fehn, U., and Yoshida, S. (2001) Recycling of iodine in fore-arc areas: evidence from the iodine brines in Chiba, Japan. Earth and Planetary Science Letters, 192(4), 583–593.
Muramatsu, Y., Doi, T., Tomaru, H., Fehn, U., Takeuchi, R., and Matsumoto, R. (2007) Halogen concentrations in pore waters and sediments of the Nankai Trough, Japan: Implications for the origin of gas hydrates. Applied Geochemistry, 22(3), 534–556.
Neal, C., Robinson, M., Reynolds, B., Neal, M., Rowland, P., Grant, S., Norris, D., Williams, B., Sleep, D., and Lawlor, A. (2010) Hydrology and water quality of

the headwaters of the River Severn: Stream acidity recovery and interactions with plantation forestry under an improving pollution climate. Science of the Total Environment, 408(21), 5035–5051.
Nodvin, S.C., Driscoll, C.T., and Likens, G.E. (1986) Simple partitioning of anions and dissolved organic carbon in a forest soil. Soil Science, 142, 27–35.
Nriagu, J.O. (1973) Lead orthophosphates-III. Stabilities of fluoropyromorphite and bromopyromorphite at 25° C. Geochimica et Cosmochimica Acta, 37(7), 1735–1743.
Oades, J.M. (1993) The role of biology in the formation, stabilization and degradation of soil structure. In Soil Structure/Soil Biota Interrelationships (pp. 377–400). Elsevier.
Öberg, G., and Bastviken, D. (2012) Transformation of chloride to organic chlorine in terrestrial environments: variability, extent, and implications. Critical Reviews in Environmental Science and Technology, 42(23), 2526–2545.
Öberg, G., and Sandén, P. (2005) Retention of chloride in soil and cycling of organic matter-bound chlorine. Hydrological Processes: An International Journal, 19(11), 2123–2136.
Oelmann, Y., Kreutziger, Y., Temperton, V.M., Buchmann, N., Roscher, C., Schumacher, J., Schulze, E.-D., Weisser, W.W., and Wilcke, W. (2007) Nitrogen and phosphorus budgets in experimental grasslands of variable diversity. Journal of Environmental Quality, 36(2), 396–407.
Okudera, H. (2013) Relationships among channel topology and atomic displacements in the structures of $Pb_5(BO_4)_3Cl$ with B= P (pyromorphite), V (vanadinite), and As (mimetite). American Mineralogist, 98, 1573–1579.
Oliva, P., Viers, J., and Dupré, B. (2003) Chemical weathering in granitic environments. Chemical Geology, 202, 225–256.
Palme, H., and O'Neill, H.St.C. (2003) Cosmochemical estimates of mantle composition. Treatise on Geochemistry, 2, 568.
Park, C.F. Jr., and MacDiarmid, R.A. (1975) Ore Deposits. Freeman.
Park, K.S., Sims, R.C., Dupont, R.R., Doucette, W.J., and Matthews, J.E. (1990) Fate of PAH compounds in two soil types: influence of volatilization, abiotic loss and biological activity. Environmental Toxicology and Chemistry: An International Journal, 9(2), 187–195.
Pasero, M., Kampf, A.R., Ferraris, C., Pekov, I.V., Rakovan, J., and White, T.J. (2010) Nomenclature of the apatite supergroup minerals. European Journal of Mineralogy, 22(2), 163–179.
Pfaff, K., Romer, R.L., and Markl, G. (2009) U-Pb ages of ferberite, chalcedony, agate,'U-mica'and pitchblende: constraints on the mineralization history of the Schwarzwald ore district. European Journal of Mineralogy, 21(4), 817–836.
Pichavant, M., Herrera, J.V., Boulmier, S., Joron, J.L., Juteau, M., Marin, L., Sheppard, S.M.F., Treuil, M., and Vernet, M. (1987) The Macusani glasses, SE Peru: evidence of chemical fractionation in peraluminous magmas. In B.O. Mysen, Ed., Magmatic Processes: Physicochemical Principles, p. 359–373. The Geochemical Society, Washington, D.C.
Redon, P.-O., Jolivet, C., Saby, N.P., Abdelouas, A., and Thiry, Y. (2013) Occurrence of natural organic chlorine in soils for different land uses. Biogeochemistry, 114(1-3), 413–419.
Reich, M., and Vasconcelos, P.M. (2015) Geological and economic significance of supergene metal deposits. Elements, 11(5), 305–310.
Roddick, J. (1983) High precision intercalibration of ^{40}Ar-^{39}Ar standards. Geochimica et Cosmochimica Acta, 47(5), 887–898.
Ruby, M.V., Davis, A., and Nicholson, A. (1994) In situ formation of lead phosphates in soils as a method to immobilize lead. Environmental Science & Technology, 28(4), 646–654.
Rudnick, R.L., and Shan, G. (2003) Composition of the continental crust. Treatise on Geochemistry, 3, 659.
Schnetger, B., and Muramatsu, Y. (1996) Determination of halogens, with special reference to iodine, in geological and biological samples using pyrohydrolysis for preparation and inductively coupled plasma mass spectrometry and ion chromatography for measurement. Analyst, 121(11), 1627–1631.
Seelig, U., and Bucher, K. (2010) Halogens in water from the crystalline basement of the Gotthard rail base tunnel (central Alps). Geochimica et Cosmochimica Acta, 74(9), 2581–2595.
Seybold, C.A., Herrick, J.E., and Brejda, J.J. (1999) Soil resilience: a fundamental component of soil quality. Soil Science, 164, 224–234.
Shannon, R.D. (1976) Revised effective ionic radii and systematic studies of interatomic distances in halides and chalcogenides. Acta Crystallographica, A32, 751–767.
Siegel, F.R. (2002) Environmental Geochemistry of Potentially Toxic Metals. Springer.
Siemann, M.G., and Schramm, M. (2000) Thermodynamic modelling of the Br partition between aqueous solutions and halite. Geochimica et Cosmochimica Acta, 64(10), 1681–1693.
Staude, S., Bons, P.D., and Markl, G. (2009) Hydrothermal vein formation by extension-driven dewatering of the middle crust: An example from SW Germany. Earth and Planetary Science Letters, 286(3-4), 387–395.
Svensson, T., Lovett, G.M., and Likens, G.E. (2012) Is chloride a conservative ion in forest ecosystems? Biogeochemistry, 107, 125–134. doi: 10.1007/s10533-010-9538-y.
Teiber, H., Marks, M.A., Wenzel, T., Siebel, W., Altherr, R., and Markl, G. (2014) The distribution of halogens (F, Cl, Br) in granitoid rocks. Chemical Geology, 374, 92–109.
Teiber, H., Scharrer, M., Marks, M.A., Arzamastsev, A.A., Wenzel, T., and Markl, G. (2015) Equilibrium partitioning and subsequent re-distribution of halogens among apatite–biotite–amphibole assemblages from mantle-derived plutonic rocks: Complexities revealed. Lithos, 220, 221–237.
Tomaru, H., Fehn, U., Lu, Z., Takeuchi, R., Inagaki, F., Imachi, H., Kotani, R., Matsumoto, R., and Aoike, K. (2009) Dating of dissolved iodine in pore waters from the gas hydrate occurrence offshore Shimokita Peninsula, Japan: ^{129}I results from the D/V *Chikyu* Shakedown Cruise. Resource Geology, 59(4), 359–373.
Walter, B.F., Burisch, M., Fusswinkel, T., Marks, M.A.W., Steele-MacInnis, M., Wälle, M., Apukhtina, O.B., and Markl, G. (2018) Multi-reservoir fluid mixing processes in rift-related hydrothermal veins, Schwarzwald, SW-Germany. Journal of Geochemical Exploration, 186, 158–186.
Walter, B.F., Burisch, M., and Markl, G. (2016) Long-term chemical evolution and modification of continental basement brines—a field study from the Schwarzwald, SW Germany. Geofluids, 16(3), 604–623.
Wang, L.-X., Ma, C.-Q., Zhang, C., Zhu, Y.-X., and Marks, M.A. (2018) Halogen geochemistry of I- and A-type granites from Jiuhuashan region (South China): Insights into the elevated fluorine in A-type granite. Chemical Geology, 478, 164–182.
Webster, J.D., and Piccoli, P.M. (2015) Magmatic apatite: A powerful, yet deceptive, mineral. Elements, 11(3), 177–182.
Whitfield, M., and Turner, D. (1979) Water–rock partition coefficients and the composition of seawater and river water. Nature, 278, 132–137.
Wilson, T. (1975) Salinity and the major elements of seawater, Chemical Oceanography, 1 JP Riley, G. Skirrow Academic Press, San Diego, Calif.
Wondratschek, H. (1963) Untersuchungen zur Kristallchemie der Blei-Apatite (Pyromorphite). Neues Jahrbuch für Mineralogie Abhandlungen, 99, 113–160.
Wong, G., and Brewer, P. (1974) Determination and distribution of iodate in South-Atlantic waters. Journal of Marine Research, 32(1), 25–36.
Wu, W., Xu, S., Yang, J., and Yin, H. (2008) Silicate weathering and CO_2 consumption deduced from the seven Chinese rivers originating in the Qinghai-Tibet Plateau. Chemical Geology, 249(3-4), 307–320.
Yuita, K., Shibuya, M., and Nozaki, T. (1978) The accumulation of bromine and iodine in Japanese soils. Abstract 11th Soil Science Congress Edmonton, Alberta, 260.
Yuita, K., Kihou, N., Ichihasi, H., Yabusaki, S., Fujiwara, H., Kurishima, K., and Noda, T. (2006) Behavior of iodine in a forest plot, an upland field and a paddy field in the upland area of Tsukuba, Japan: Seasonal variations in iodine concentration in precipitation and soil water and estimation of the annual iodine accumulative amount in soil horizons. Soil Science and Plant Nutrition, 52(1), 122–132.

Manuscript received March 28, 2019
Manuscript accepted July 26, 2019
Manuscript handled by Andrew Elwood Madden

Endnote:

[1]Deposit item AM-19-117068, Supplemental Material. Deposit items are free to all readers and found on the MSA website, via the specific issue's Table of Contents (go to http://www.minsocam.org/MSA/AmMin/TOC/2019/Nov2019_data/Nov2019_data.html).

Appendix III

Study C

Epp, T., Neidhardt, H., Pagano, N., Marks, M. AW., Markl, G. & Oelmann, Y. (2020). Vegetation canopy effects on total and dissolved Cl, Br, F and I concentrations in soil and their fate along the hydrological flow path. Science of the Total Environment, 712, 135473.

Accepted and published
DOI: 10.1016/j.scitotenv.2019.135473
Number of authors: 6
Author position: 1

Science of the Total Environment 712 (2020) 135473

Contents lists available at ScienceDirect

Science of the Total Environment

journal homepage: www.elsevier.com/locate/scitotenv

Vegetation canopy effects on total and dissolved Cl, Br, F and I concentrations in soil and their fate along the hydrological flow path

Tatjana Epp [a,b,*], Harald Neidhardt [b], Norina Pagano [b], Michael A.W. Marks [a], Gregor Markl [a], Yvonne Oelmann [b]

[a] Geoscience, University of Tübingen, Wilhelmstraße 56, 72074 Tübingen, Germany
[b] Geoecology, University of Tübingen, Rümelinstraße 19-23, 72070 Tübingen, Germany

HIGHLIGHTS

- Cl concentrations in soil decreased with increasing soil depth.
- Br, F and I concentrations in soil increased with increasing soil depth.
- Biological and geochemical processes caused Cl vs. Br, F and I depth patterns.
- Halogen concentrations were higher in throughfall as compared to rainfall.

GRAPHICAL ABSTRACT

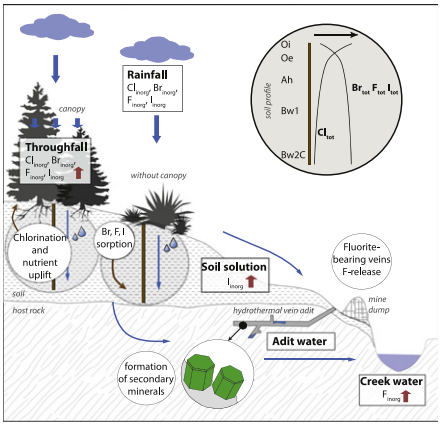

ARTICLE INFO

Article history:
Received 28 August 2019
Received in revised form 6 November 2019
Accepted 9 November 2019
Available online 22 November 2019

Editor: Paulo Pereira

Keywords:
Halogen cycle
Soil profiles
Iodine
Bromine
Surface waters
Vegetation influence

ABSTRACT

Although halogens are omnipresent in the environment, detailed understanding of processes involving chlorine (Cl), bromine (Br), fluorine (F) and iodine (I) in the terrestrial halogen cycle is still sparse. Our objectives were to (i) assess vertical depth profiles of total and water-extractable inorganic halogen concentrations (Cl_{tot}, Br_{tot}, F_{tot}, I_{tot}) in solid soil, (ii) test the effect of a tree canopy, and (iii) follow the fate of dissolved inorganic halogens along the hydrological flow path. More than 200 soil samples and ecosystem solutions (rainwater, soil solution, adit and creek water) collected in the Schwarzwald, SW Germany, were analyzed by combustion ion chromatography and ion chromatography for total and inorganic halogen concentrations.

We found decreasing Cl_{tot} concentrations with increasing soil depth which were indicative of biological chlorination of organic matter and nutrient uplift, both associated with Cl accumulation in upper soil horizons. Vertical patterns of total Br, F and I were contrary to Cl_{tot} concentrations and were related significantly (positively) to pedogenic oxides, revealing their dependence on abiotic processes. The presence of a canopy at our study site resulted in significantly higher halogen concentrations in throughfall compared to rainfall and higher Br_{tot} concentrations in the organic layer. We attribute this difference to leaching from leaves and needles and washoff of dry deposition. There were hardly any differences in halogen concentrations along the hydrological flow path except for significantly higher inorganic I concentrations in soil solution compared to rainfall due to equilibrium reactions between the soil solution and the solid soil phase. Highest inorganic F concentrations of up to

* Corresponding author at: Geoscience, University of Tübingen, Wilhelmstraße 56, 72074 Tübingen, Germany.
E-mail addresses: tatjana.epp@uni-tuebingen.de (T. Epp), harald.neidhardt@uni-tuebingen.de (H. Neidhardt), norina.pagano@uni-tuebingen.de (N. Pagano), marks@uni-tuebingen.de (M.A.W. Marks), markl@uni-tuebingen.de (G. Markl), yvonne.oelmann@uni-tuebingen.de (Y. Oelmann).

https://doi.org/10.1016/j.scitotenv.2019.135473

0.2 mg L^{-1} were detected in creek water samples and may originate from the weathering of fluorite-bearing veins. Our study indicates halogen-specific processes underlying Cl, Br, I and F cycling in ecosystems.

1. Introduction

Halogens chlorine (Cl), bromine (Br), fluorine (F) and iodine (I) are ubiquitous in the environment, but only Cl represents an important micro-nutrient for both, plants and microorganisms (e.g., Yuita, 1983; Fuge, 1988; Marschner, 1995; Kabata-Pendias, 2011). In terrestrial ecosystems, halogens are mainly present as aqueous anions (halides) and complexes. These are bound to organic substances and mineral surfaces, are part of mineral structures, or form volatile gases (Soper and Weckström, 2006; Matucha et al., 2010; Epp et al., 2019). Accordingly, halogens occur as organic (Cl_{org}, Br_{org}, F_{org}, I_{org}) and inorganic (Cl_{inorg}, Br_{inorg}, F_{inorg}, I_{inorg}) species. A proportion of both can be water-extractable from solid phases or present in ecosystem solutions in dissolved form. Bulk analyses of ecosystem samples commonly comprise a mixture of inorganic and organic halogen species. The heavier halogens Cl, Br and I dissolved in water were commonly regarded as inert tracers for water flow through soils and host rock (e.g., Conway, 1942; Schlesinger, 1997). In recent decades, this paradigm has been challenged because halogens were shown to be involved in a number of retention processes (Bastviken et al., 2007; Vodyanitskii and Makarov, 2017). For example, the formation of halogenated organic compounds during either microbial decomposition (Amachi, 2008; Seki et al., 2012) of soil organic matter (SOM) or by abiotic mechanisms such as abiotic oxidation or halogenation (Leri and Ravel, 2015) has recently been identified as a key process in the biogeochemistry of Cl, Br and I in forest ecosystems (Öberg et al., 2005; Cabral et al., 2011; Leri and Myneni, 2012). Accordingly, atmospheric halogen input in dissolved form accumulates in the organic layer of forests through halogenation. This is in line with results reported for Cl (Bastviken et al., 2007; Montelius et al., 2016). Bromination was even favored over chlorination during decomposition of litter in a temperate coniferous forest ecosystem (Leri and Myneni, 2012). Accordingly, Takeda et al. (2018) found a vertical depth pattern in volcanic ash soil, namely a decrease in total Br concentrations with increasing soil depth similar to that reported above for Cl. The same applied to I as well (Takeda et al., 2018). For F_{tot} constant concentrations with depth in agricultural regions and decreasing F_{tot} concentrations in industrial areas were described for soils in the Southwest of China (Wang et al., 2019). It is tempting to regard these vertical depth patterns of total halogen concentrations described in the literature caused by halogenation as universally valid.

However, opposite patterns were reported as well in Spain and France, e.g., an increase in Br_{tot} and I_{tot} concentrations with increasing soil depth (Cortizas et al., 2016; Roulier et al., 2019). These authors argue that a combination of the level of bromination linked to the age of SOM and the stabilization of brominated organic compounds by complexation with aluminum (Al; in deeper soil layers) could serve as an explanation. Not only complexation but also adsorption to positively charged surfaces of secondary minerals formed during pedogenesis ("pedogenic oxides": iron (Fe) and aluminum (Al) oxides and (oxy)hydroxides) contribute to the retention of negatively charged ions in soil solution. In line, adsorption of dissolved I_{inorg} and F_{inorg} onto pedogenic oxides in soil was reported (Gerzabek et al., 1999; Loganathan et al., 2007). However, most previous studies did not investigate Cl, Br, F and I at the same time, instead the halogens were studied individually at different site conditions. Thus, different vertical depth patterns between halogens might be caused by different site conditions. Alternatively, vertical depth patterns that differ between halogens could be a result of different underlying processes (Cl: chlorination; Br, I, F: sorption to pedogenic oxides) rather than of site-specific conditions. The joint analysis of all halogens (Cl, Br, F and I) at the same sites could help to judge the potentially halogen-specific importance of processes underlying vertical depth patterns of total halogen concentrations in soil.

Not only soil internal processes but also external halogen input may influence vertical patterns of halogen concentrations in soil. Locations far away from the coast commonly receive small amounts of atmospheric deposition of halogens (Låg and Steinnes, 1976; Steinnes and Frontasyeva, 2002; Johansson et al., 2003b; Montelius et al., 2015). However, rainfall may get enriched in halogens when passing through a vegetation canopy (throughfall). Accordingly, higher dissolved Cl and I concentrations in throughfall as compared to rainfall were observed and explained by dissolution of dry deposition on tissue surfaces and by leaching from organic compounds in the canopy (Lovett et al., 2005; Montelius et al., 2015; Takeda et al., 2016; Roulier et al., 2019). Locations in the presence or absence of a canopy should thus be characterized by different halogen inputs, which should be reflected in the vertical depth pattern in soils.

Moreover, rainfall and throughfall percolate through the soil and the underlying host rock, where complex release and transformation processes take place (e.g., Lovett et al., 2005). Furthermore, Lovett et al. (2005) reported that dissolved Cl_{inorg} concentrations were higher in soil solution as compared to rainfall because of Cl release from the organic soil layer. Decreasing dissolved Cl_{inorg} concentrations with depth were explained by subsequent adsorption or uptake by plants in the subsoil. For I, the order was dependent on the sorption capacity of the soil: dissolved I_{inorg} iodide concentrations in rainfall < in soil solution in case of low sorption capacity (Roulier et al., 2019), iodide concentrations in rainfall > soil solution > stream water in the case of a high sorption capacity as in Andosols (Takeda et al., 2016).

Here, we focus on the entire halogen cycle, i.e., rainfall water that percolates through the vegetation, soil horizons and/or weathered rock, subsequently interacts with a former ore deposit and finally discharges as creek runoff. Furthermore, our study considers Cl, Br, F and I distribution at a locality below canopy and at a locality without canopy. This enables us to compare directly the halogen distribution patterns under the same site specific conditions.

We studied a Cambisol developed on gneissic host rock located in a spruce (*Picea abies* (L.) H. Karst.) forest. Such sites are characterized by a thick organic layer on top of the mineral soil, an input of organic matter into the topsoil horizons and formation of secondary pedogenic oxides in the subsoil.

We hypothesized that

(i) Cl_{tot} concentrations will decrease with increasing soil depth and this will be linked to SOM concentrations. Bromination, fluorination and iodination during SOM decomposition will be evident by increased total Br, F and I concentrations in more decomposed as compared to less decomposed organic layers. The overall pattern will be an increase of total Br, F and I concentrations down to the mineral soil.
(ii) Increased halogen input in the presence of a canopy will increase halogen concentrations along the vertical depth profile as compared to locations where a canopy is not present.
(iii) Halogen concentrations in rainfall will be lower than in soil solution and this difference will depend on the halogen-specific affinity to adsorption in soil (greater for Cl). Halogen concentrations in adit water and creek water will be higher than in soil solution.

2. Methods

2.1. Study site

We selected the Kammentobel valley which is located in the forest "Napf" in the St. Wilhelm valley, right below the Feldberg mountain peak in the Schwarzwald, southwest Germany, as our study site (Fig. 1). The study site is situated at ~1360 m a.s.l. (approximately 500 km to the nearest ocean) and in 2018 the annual temperature ranged between 23 and −20 °C, total precipitation was ~1500 mm (Deutscher-Wetterdienst, 2019; WetterKontor, 2019). In general, the climate at the Feldberg is temperate. The soil developed on strongly weathered gneisses from the Schwarzwald low mountain range and can be classified as Cambisol according to IUSS-Working-Group-WRB (2015). A vertical soil profile is typically characterized by an organic layer and a mineral topsoil and subsoil. Three sample locations were situated below the canopy of spruce trees (*Picea abies* (L.) H.Karst.; C 1–3) and another three below a shrub layer dominated by blueberry (*Vaccinium myrtillus* L.) without trees (OC 1–3). The forest itself and the open area are part of a protected forest where no land management is conducted. In the vicinity there are meadows which are used as pastures. The individual localities (three below a canopy and three without a canopy) are only a few 10 m away from each other which enabled the investigation of the canopy impact without having differences in location properties. Since, the locations are so close to each other it is unlikely that there are significant rainfall volume or compositional changes between canopy and without canopy. In the following, triplicates are summarized and labelled as C (below canopy) and OC (without canopy), respectively.

2.2. Sampling strategy

A large variety of different samples was collected and thus, each individual sampling strategy will be briefly explained in the following. Six soil profiles were taken once at the beginning of the project (maximum depth: 0.57 m) in the protected forest area where there is no land use.

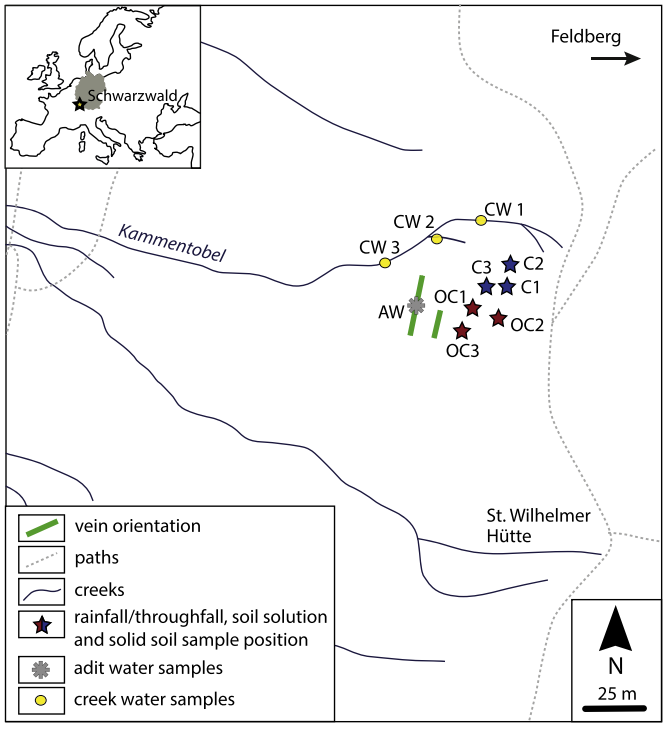

Fig. 1. Simplified overview of all sample locations and types from the Feldberg, southwest Germany. C = with canopy; OC = without canopy; AW = adit water; CW = creek water.

The maximum depth of the soil profiles marks the transition to the parental host rock. Soil profiles comprised the organic layer (Oi, Oe; Table 1), the topsoil (Ah; Table 1) and the subsoil (Bw1, Bw2C; Table 1) and analyzed samples were selected from each soil horizon, as summarized in Table 1. Halogen concentrations were determined from both organic layers (Oi, Oe), as well as from the topsoil (Ah) and the two subsoil horizons (Bw1 and Bw2C). The soil samples were collected systematically along the profile so that all characteristic soil horizons could have been considered for analyses. Accordingly, 30 soil samples were analyzed for total (Cl_{tot}, Br_{tot}, $F_{tot,}$ I_{tot}) and water-extractable halogen concentrations (water-extractable Cl_{inorg}, Br_{inorg}, F_{inorg} and I_{inorg}).

Ecosystem solution samples (i.e., rainfall, throughfall, soil solution, adit water and creek water) were collected regularly over two growing seasons (2017 and 2018). Due to snow cover during winter and strict nature preservation measures in spring and early summer, the sampling period was restricted to May/July/August/October in 2017 and August/September/October in 2018. There was a long-lasting dry period in summer 2018: In the period August to October 2017, 360 mm total rainfall was recorded, whereas in the same period in 2018 it was 163 mm (Deutscher-Wetterdienst, 2019; WetterKontor, 2019). Therefore, due to water shortage, monthly sampling of ecosystem solutions was not always possible.

Rainfall, throughfall and soil solutions were collected at the same locations as the soil samples (Fig. 1). Rainfall (OC) and throughfall (C) samples were collected in triplicates by means of a PE funnel (diameter of 0.12 m) connected to a PE sampling bottle which were installed at 1 m above the surface in the open area in October 2016. In September 2016, we installed suction cups (plastic suction cups 32 mm without shaft, 4313.32/00, ecoTech, Bonn, Germany) at different depths (0.15, 0.35 and 0.55 m) in triplicates at each location. After an equilibration period of 7 months, we started to collect soil solution. At each location one tensiometer (mechanical tensiometer, 4221, ecoTech, Bonn, Germany) was installed. The vacuum applied to the suction cups was adjusted to the soil matric potential measured by means of the tensiometer in order to capture the proportion of soil solution that percolates through the soil. Due to the dry period, adit water (Fig. 1) could be collected twice only (05/24/2017, 08/09/2017) and represents water accumulations on the mine floor. Creek water was sampled at three different locations (Fig. 1). Ecosystem solution samples were transported in a refrigerator and subsequently frozen until analysis. In total, 145 liquid samples (21 rainfall, 21 throughfall, 44 soil solution, 8 adit water, 21 creek water) were analyzed in this study.

2.3. Halogen analyses

Sieved (2 mm) soil samples were dried at 40 °C for five days, to avoid loss of halogens to the gaseous phase. To determine the amount of water-soluble halogens, dried soil (5 g) was extracted with 30 ml Millipore water for 1 h on a vertical shaker. The extractions were filtered in the ion chromatograph, which contains an internal filter of 0.2 μm pore size. An aliquot of the extraction solution was analyzed for the water-soluble inorganic halogen contents by ion chromatography (IC).

Total halogen concentrations (Cl_{tot}, $Br_{tot,}$ F_{tot} and I_{tot}) in homogenized (milled by planetary ball mill) solid soil samples (triplicates for each depth and location) were determined via combustion ion chromatography (CIC) at the University of Tübingen. To this end, a 930 Compact IC Flex chromatograph (Metrohm, Filderstadt, Germany) with chemical suppression and a peristaltic pump for regeneration (100 mmol L^{-1} H_2SO_4) connected to an autosampler for solid samples (MMS 5000; Analytik Jena), which was additionally connected to a combustion oven, was used. The eluent used for the CIC measurements was a mixture consisting of 2 mmol NaOH (suprapure), 1.6 mmol Na_2CO_3 (suprapure) and 5 vol% acetone. The entire analytical method is described in detail in Epp et al. (2019). For the CIC the limit of detection was 0.2 mg kg^{-1} for Cl, 0.02 mg kg^{-1} for Br and I and 0.8 mg kg^{-1} for

Table 1
Soil properties of soil profiles. Horizons were classified according to IUSS-Working-Group-WRB, 2015. C = with canopy; OC = without canopy; C_{org} = organic carbon; $_{ox}$ = poorly crystalline; $_{d}$ = crystalline.

Location	Depth	Horizon	pH	C_{org} (g kg^{-1})	Oxalate-extractable pedogenic oxides			Dithionite-extractable pedogenic oxides		
					Al_{ox} (mg kg^{-1})	Fe_{ox} (mg kg^{-1})	Mn_{ox} (mg kg^{-1})	Al_{d} (mg kg^{-1})	Fe_{d} (mg kg^{-1})	Mn_{d} (mg kg^{-1})
C1	0–3.5 cm	Oi		410						
C1	3.5–7.0 cm	Oe		170						
C1	7.0–18.0 cm	Ah	3.7	70	2700	4100	75	9400	30,600	500
C1	32.0–37.0 cm	Bw1	4.3	40	3300	4000	130	12,200	36,500	700
C1	52.0–57.0 cm	Bw2C	4.4	20	3600	4100	170	11,300	36,800	800
C2	0–2.0 cm	Oi		2100						
C2	2.0–5.0 cm	Oe		110						
C2	5.0–15.0 cm	Ah	3.7	50	2650	4100	80	10,000	36,500	410
C2	30.0–35.0 cm	Bw1	4.2	30	2700	4000	220	12,000	37,200	800
C2	50.0–55.0 cm	Bw2C	4.3	20	3800	4000	200	12,100	36,800	1120
C3	0.0–2.5 cm	Oi		360						
C3	2.5–6.0 cm	Oe		170						
C3	6.0–17.0 cm	Ah	3.8	60	2100	3500	210	9300	33,200	1700
C3	31.0–36.0 cm	Bw1	4.3	25	3000	3800	300	11,100	35,400	1400
C3	51.0–56.0 cm	Bw2C	4.5	20	3200	3300	300	11,100	33,700	1300
OC1	0–1.5 cm	Oi		200						
OC1	1.5–4.5 cm	Oe		120						
OC1	4.5–13.5 cm	Ah	3.7	50	2100	4200	200	8300	38,100	650
OC1	29.5–34.5 cm	Bw1	4.3	30	2900	3600	300	10,900	43,500	1300
OC1	49.5–54.5 cm	Bw2C	4.5	20	3000	3200	300	10,900	38,000	1400
OC2	0–2.5 cm	Oi		4200						
OC2	2.5–6.0 cm	Oe		180						
OC2	6.0–20.0 cm	Ah	3.7	60	2300	3700	340	8200	44,000	900
OC2	30.0–36.0 cm	Bw1	4.2	30	2400	3500	200	9800	54,400	1100
OC2	51.0–56.0 cm	Bw2C	4.4	20	3300	3300	2600	11,9000	43,300	1100
OC3	0–2.0 cm	Oi		100						
OC3	2.0–6.0 cm	Oe		130						
OC3	6.0–15.0 cm	Ah	3.8	60	2700	3800	110	13,400	40,000	650
OC3	31.0–36.0 cm	Bw1	4.1	40	3500	4100	230	12,200	34,200	1000
OC3	51.0–56.0 cm	Bw2C	4.4	30	3300	3400	300	13,400	37,400	1800

F for solid samples of 10 mg. Based on standard solutions (single element solutions of Cl, Br F and I; Roth; 1000 mgL^{-1}) and various reference materials (SO_3, GSN), the long term reproducibility (1σ) for solid samples of the measurements was within a 10% margin for Cl, Br and I and 20% for F. Liquid samples (water-extractable Cl_{inorg}, Br_{inorg}, F_{inorg} and I_{inorg}; dissolved Cl_{inorg}, Br_{inorg}, F_{inorg} and I_{inorg} in ecosystem solutions) were determined via ion chromatography (IC) using an autosampler for liquid samples (858 Professional Sample Processor, Metrohm). Limits of detection (calculated according to DIN 32645) of the IC were 0.01 mg L^{-1} for Cl and 0.001 mg L^{-1} for Br, F and I for all liquid samples. For liquid samples the precisions of repeated measurement were 5% for Cl, Br and I and 15% for F.

2.4. Complementary analyses

We used dried (40 °C) and sieved (<2 mm) sample material for all complementary analyses (except for total carbon (C_{tot}) concentrations). The soil pH was determined from an extraction of 5 g soil with a 0.01 M $CaCl_2$ solution and a pH meter (pH 340, WTW GmbH) according to DIN EN 15933 (2012-11-00). C_{tot} contents were analyzed from homogenized samples (dried at 105 °C; ground with a planetary ball mill) with an Elemental Analyzer (Vario EL III, Elementar Analysensysteme GmbH). Due to the absence of $CaCO_3$ in the acidic mineral soil (pH < 4.5), C_{tot} is considered as total organic C (C_{org}, Table 1). Poorly crystalline pedogenic oxides (Fe_{ox}, Al_{ox} and manganese oxide (Mn_{ox}), Table 1) were measured as ammonium-oxalate extractable compounds (Schwertmann, 1964). The sum of poorly crystalline and crystalline pedogenic oxides (Fe_{d}, Al_{d} and Mn_{d}, Table 1) were determined with the dithionite-citrate method as described in Burt (2004). Iron, Al and Mn concentrations in extraction solutions were analyzed by ICP-OES (Optima 5300 DV, PerkinElmer, Baesweiler, Germany). Texture (sand, silt, clay) was analyzed after organic matter destruction and sodium pyrophosphate treatment with a combination of wet sieving and sedigraph analysis (SediGraph III Particle Size Analyzer, micromeritics).

2.5. Statistical analyses

All statistical analyses were conducted using IBM® SPSS® Statistics Version 25. The Shapiro-Wilk test was applied to test for normal distribution and homogeneity of variances was assessed by using the Levene test. Variables with $p > 0.05$ were considered as normally distributed and all variables respected these parameters. A repeated measures ANOVA for solid soil samples with location as between-subject factor and depth as within-subject factor was used to disentangle the effects of location and depth on halogen concentrations in soil. Halogen distribution between various liquid sample types were tested using a one-way ANOVA with Games-Howell as post hoc test. In order to detect significant variations in halogen concentration at each depth between C and OC in soil water a Kruskal-Wallis test was conducted. Non-parametric tests were applied when the variance analysis requirements were not fulfilled and the data was not normally distributed. The differences in the organic layer between C and OC was tested by a one-way ANOVA. Because evaporation – a process we did not intend to consider – might influence halogen concentrations particularly in rainfall and throughfall, we calculated Spearman rank correlations of halogen concentrations on rainfall volume for the given sampling intervals. Spearman rank correlations were also conducted to detect possible correlations between halogen concentrations and various soil parameters. In general, for $p < 0.05$ differences and correlations were considered as statistically significant. Linear regressions were calculated for correlations between total halogen concentrations and pedogenic oxides.

3. Results

3.1. Rainfall and throughfall

The concentrations of dissolved Cl_{inorg}, Br_{inorg} and F_{inorg} in rainfall differed significantly between sampling intervals (Fig. 2; significant effect of time in repeated measures ANOVA, $0.001 < p < 0.05$). Correlations between concentrations of halogens and volume were significant for Br_{inorg} in throughfall ($r = -0.964$, $p < 0.001$, Fig. A3) and F_{inorg} in rainfall ($r = -0.757$, $p = 0.049$, Fig. A3). Averaged halogen concentrations across all sampling periods were significantly higher in throughfall as compared to rainfall (Cl: 5.28 ± 1.78 mg L^{-1} versus 0.32 ± 0.09 mg L^{-1}; Br: 0.006 ± 0.001 mg L^{-1} vs. 0.002 ± 0.000 mg L^{-1}, $p < 0.001$; F: 0.019 ± 0.004 mg L^{-1} vs. 0.003 ± 0.000 mg L^{-1}; Fig. 2). The effect of the canopy expressed as the ratio between concentrations in throughfall:concentrations in rainfall decreased in the order Cl (16) > F (6) > Br (3). Only a few samples (14 out of 42 samples) contained detectable amounts of I_{inorg} (>0.001 mg L^{-1}) and thus, did not allow for further statistical analyses.

3.2. Solid soil phase

In general, the largest shift in total halogen concentrations was visible between the organic layer and the mineral soil (Fig. 3). Cl_{tot} concentrations in soil samples decreased with depth from 300 to 60 mg kg^{-1} (Fig. 3; significant depth effect in repeated measures ANOVA, $p = 0.01$). The same was true for water-extractable Cl_{inorg} concentrations: In the subsoil about 5% was water-extractable Cl_{inorg}, whereas in the topsoil up to 20% was extractable ($p = 0.002$, Fig. A1). Water-extractable Cl_{inorg} concentrations ranged from 0.8 to 50 mg kg^{-1}, representing on average a proportion of 9% of the Cl_{tot} concentration (Fig. 3, Fig. A1). Water-extractable Cl_{inorg} concentrations were correlated significantly with Cl_{tot} concentrations (Table A1). Both, Cl_{tot} concentrations and water-extractable Cl_{inorg} concentrations were correlated significantly with C_{org} concentrations ($r = 0.92$ and 0.81, respectively, $p < 0.001$, Table A1), considering all investigated horizons (Oi, Oe, Ah, Bw1, Bw2C). Cl_{tot} was not significantly correlated with the clay content ($r = 0.50$, $p = 0.39$) but with the pedogenic oxides Al_{ox} ($r = -0.51$, $p = 0.03$, Table A1) and Mn_{ox} ($r = -0.64$, $p < 0.001$, Table A1).

Total concentrations of the other halogens increased with depth (Fig. 3; Br_{tot} from 8 to 40 mg kg^{-1}, F_{tot} from 100 to 450 mg kg^{-1} and I_{tot} from 2 to 10 mg kg^{-1}; significant depth effect in repeated measures ANOVA, p reached from <0.001 to 0.005). The largest variations were observed considering the organic soil horizons (Oi, Oe) only, Br_{tot} ($p < 0.001$), F_{tot} ($p = 0.007$) and I_{tot} ($p = 0.001$). The pattern of water-extractable Br_{inorg} throughout all horizons did not change with depth (Fig. A1; $p = 0.39$), whereas water-extractable F_{inorg} concentrations significantly decreased (Fig. A1; $p = 0.001$). On average, 0.7% were water-extractable Br_{inorg}, 0.4% F_{inorg} and 0% I_{inorg} (concentrations below limit of detection), respectively (Fig. A1). The contribution of water-extractable Br_{inorg} and F_{inorg} concentrations to Br_{tot} and F_{tot} concentrations decreased with depth ($p > 0.05$). Furthermore, Br_{tot}, F_{tot} and I_{tot} were negatively correlated with C_{org} concentrations ($-0.75 < r < -0.80$, $p < 0.001$). There were significant correlations between Br_{tot}, I_{tot} and Al_{ox} (Fig. 4a, Table A1), Br_{tot}, I_{tot} and Al_d (Fig. 4b, Table A1) and between F_{tot} and Fe_d concentrations (Fig. 4c, Table A1). Concomitantly, pedogenic oxide concentrations (Al_{ox}, Mn_{ox} and Mn_d) correlated negatively with C_{org} concentrations ($-0.47 < r < -0.69$, $p < 0.05$, Table A1). There was no significant correlation between the proportion of clay and Br_{tot} ($r = 0.10$, $p = 0.87$), F_{tot} ($r = -0.70$, $p = 0.19$) or I_{tot} concentrations ($r = -0.30$, $p = 0.62$).

The organic layer thickness did not vary between C and OC locations. Taking into account the organic layers and mineral soil, we found no effect of location (open area versus below the canopy) on any of the total halogen concentrations of any soil horizon ($p > 0.05$). If the organic layer was considered separately, we found a significant location effect for Br_{tot} concentrations (higher Br_{tot} concentrations below canopy; $p = 0.03$) in the Oi horizon, but no significant location effect for Cl_{tot}, F_{tot} or I_{tot} concentrations ($p > 0.1$).

3.3. Soil solution

There was no relation between sampling month and dissolved inorganic halogen concentrations (no seasonality). Thus, samples from different sampling intervals were averaged which also facilitates the comparison with data for the solid soil phase. Concentrations of dissolved Cl_{inorg} and Br_{inorg} in soil solution decreased with increasing depth from 13.8 to 0.61 mg L^{-1} and from 0.007 to 0.001 mg L^{-1}, respectively (Fig. A2). However, high variability among replicates resulted in non-significant trends. Similarly, there were no distinctive vertical patterns of F_{inorg} and I_{inorg} concentrations in soil solutions visible. Concentrations fluctuated between 0.006 and 0.016 mg L^{-1} for F_{inorg} and between 0.012 and 0.024 mg L^{-1} for I_{inorg} (Fig. A2) in the three horizons of the mineral soil (Ah, Bw1, Bw2C). Accordingly, we did not find a correlation of dissolved inorganic halogen concentrations in soil solution neither to water-extractable inorganic nor to total halogen concentrations in the soil solid phase ($-0.44 < r < 0.35$; $0.07 < p < 0.93$).

3.4. Adit water and creek water

Due to the sparse amount of adit waters the available data set was limited. Nevertheless, water was collected twice and dissolved Cl_{inorg} in adit water ranged from 0.040 to 0.057 mg L^{-1}, Br_{inorg} from 0.003 to 0.008 mg L^{-1} and F_{inorg} from 0.015 to 0.037 mg L^{-1} (Fig. 5). The halogen concentrations (dissolved Cl_{inorg}, Br_{inorg} and F_{inorg}) in creek water were relatively constant as indicated by no significant effect of the sampling interval ($p > 0.11$). Dissolved I_{inorg} concentrations in creek water always were below the detection limit (<0.001 mg L^{-1}).

4. Discussion

4.1. Vertical distribution of halogens in the soil and the role of soil organic matter

We found a significant decrease in Cl_{tot} concentrations in the soil solid phase with increasing depth (Fig. 3). Furthermore, Cl_{tot} concentrations were positively correlated with the C_{org} concentrations. This is in line with our first hypothesis and confirms that although Cl is considered as a very mobile element in soil (e.g., Rhykerd and Overdahl, 1972; Fuge et al., 1986; Bodek, 1988; Johansson et al., 2003a; Lovett et al., 2005 and references therein), there was a pronounced accumulation of Cl in the organic layer (soil horizons Oi and Oe). This distribution pattern points at chlorination as underlying fixation process (Hjelm et al., 1995 and references therein; Öberg and Grøn, 1998; Leri and Myneni, 2010; Redon et al., 2011; Le Dizès and Gonze, 2019). Montelius et al. (2019) found that soil with plants depicted a higher chlorination capacity than bulk soil without plants. In order to elaborate if higher Cl_{tot} concentrations at our locations below canopy were the result of enhanced chlorination of SOM in the rhizosphere, we would need further data like information about the soil humidity, temperature etc. A complementary explanation for the observed vertical profiles could be related to nutrient uplift by the vegetation. The root zone at the investigated locations reaches a depth of approximately 40 cm below canopy and 50 cm without canopy. Nutrients, such as N or P, are acquired by plants from the subsoil via roots and are subsequently returned to the topsoil by litterfall (Attiwill and Adams, 1993; Le Dizès and Gonze, 2019). Because Cl represents a micro-nutrient for the ecosystem (Kabata-Pendias, 2011) the process of nutrient uplift may also apply for Cl. Lower water-extractable Cl_{inorg} concentrations in the subsoil as compared to the topsoil (Fig. A1) further supported the assumed Cl uplift namely the increased exploitation of water-extractable Cl_{inorg} by

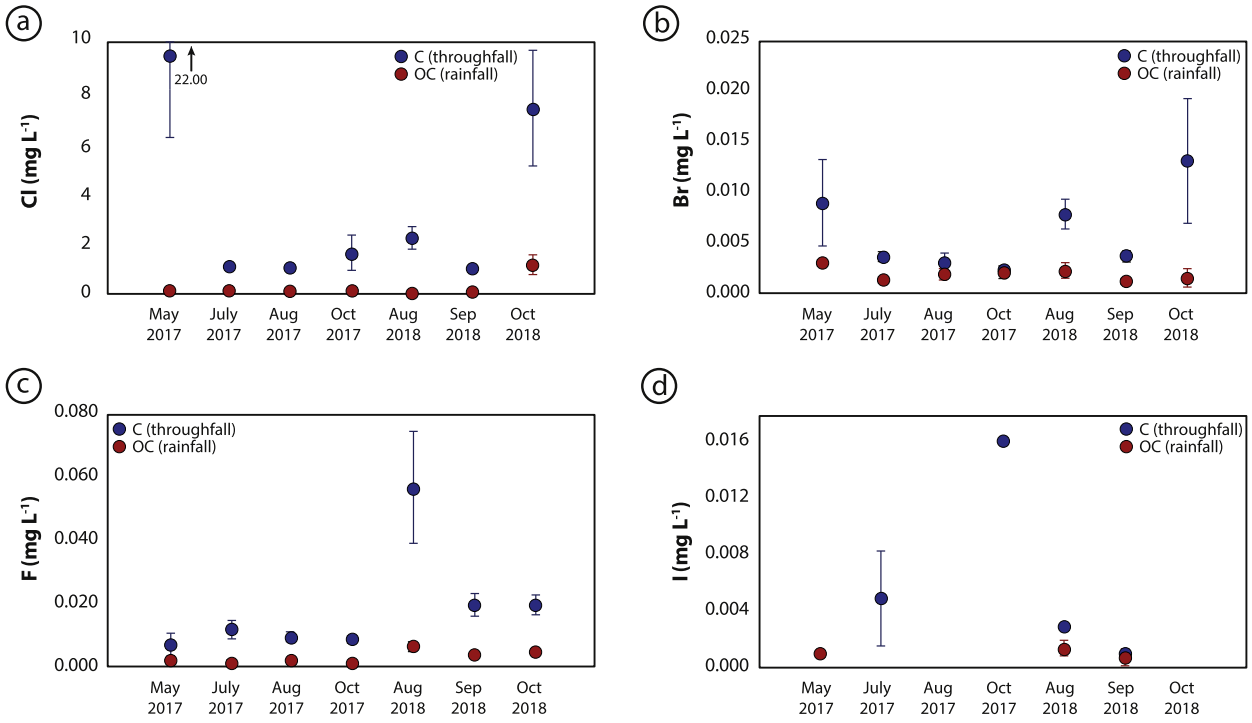

Fig. 2. (a)–(d) Halogen concentrations (mg L^{-1}) in throughfall and rainfall samples during sampling intervals of two growing seasons. Blue = C (throughfall), red = OC (rainfall). The error bars show the standard deviation. C: n = 21, OC: n = 21.

plants in subsoil compared to topsoil. However, the uplift of Cl is difficult to identify and disentangle from other biogeochemical processes such as fixation of halogens in C_{org} via halogenation. Furthermore, Cl_{inorg} is released from soil parent materials at first, which is however, overprinted by uplift and enrichment on the surface soil due to biological processes. Stable isotope approaches have provided new insights for water and nutrient uplift in forested ecosystems (Uhlig et al., 2017) which should be tested for Cl in future research. In general, Cl_{tot} concentrations are expected to be higher in more decomposed organic layers (Cl_{tot} Oi < Cl_{tot} Oe) because Cl_{inorg} is incorporated into organic matter resulting in an absolute enrichment (Myneni 2002; Cortizas et al., 2016). Furthermore, Cl is enriched relative to C_{org} caused by mass loss

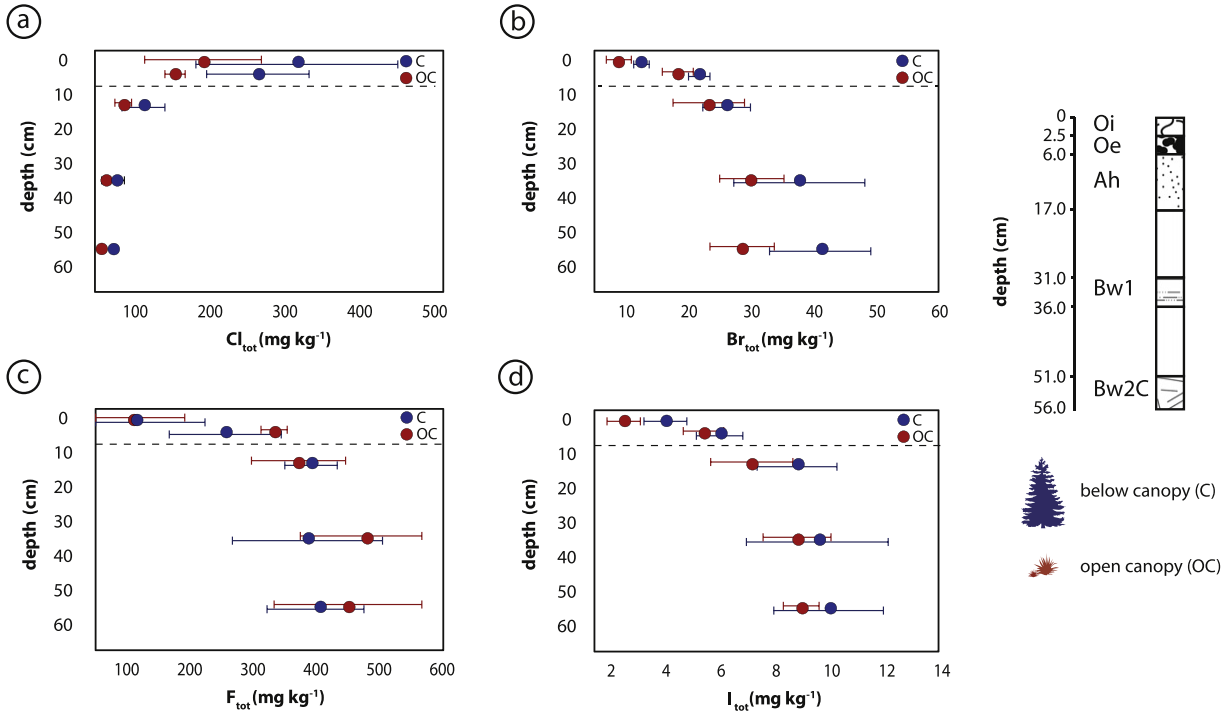

Fig. 3. (a)–(d) Vertical depth patterns of halogen concentrations (mg kg^{-1}) in solid soil samples. Schematic soil profile (in cm) with corresponding soil horizons according to IUSS-Working-Group-WRB (2015). Blue = C (throughfall), red = OC (rainfall). For the thicknesses on the y axis averaged values were taken over all profiles. The error bars show the standard deviation, C: n = 15, OC: n = 15.

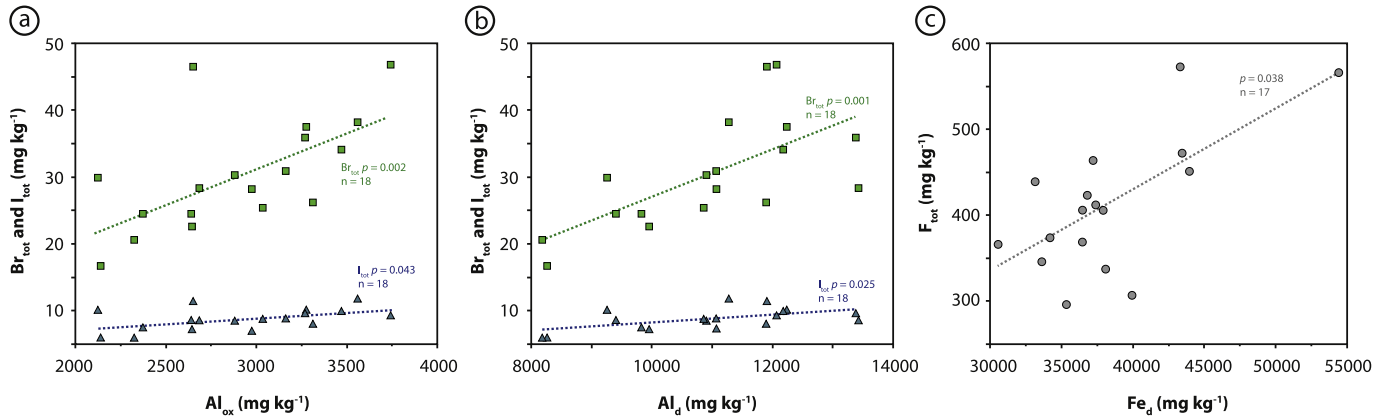

Fig. 4. (a) Br_{tot} and I_{tot} vs Al_{ox} (poorly crystalline Al oxides), (b) Br_{tot} and I_{tot} vs Al_d (sum of poorly crystalline and crystalline Al oxides), (c) F_{tot} vs Fe_d (sum of poorly crystalline and crystalline Fe oxides).

due to heterotrophic respiration of CO_2. However, organic layers did not differ with respect to Cl_{tot} concentrations (Fig. 3). Therefore, not only halogenation, but also dehalogenation (transformation of Cl_{inorg} to Cl_{org}) and subsequent leaching of dissolved Cl_{inorg} (or loss due to volatilization) apparently plays an important role in the organic layers (Montelius et al., 2016). In sum, we could show that dissolved Cl_{inorg} interacts with the solid soil phase and this interaction is likely linked to the cycling of C_{org}.

Contrary to Cl_{tot}, concentrations of Br_{tot}, F_{tot} and I_{tot} were significantly lower in the organic layer as compared to the underlying mineral soil. The observed trend in F_{tot} is in line with the low affinity of F to organic matter (Kabata-Pendias, 2011). However, similar to Cl, Br and I are

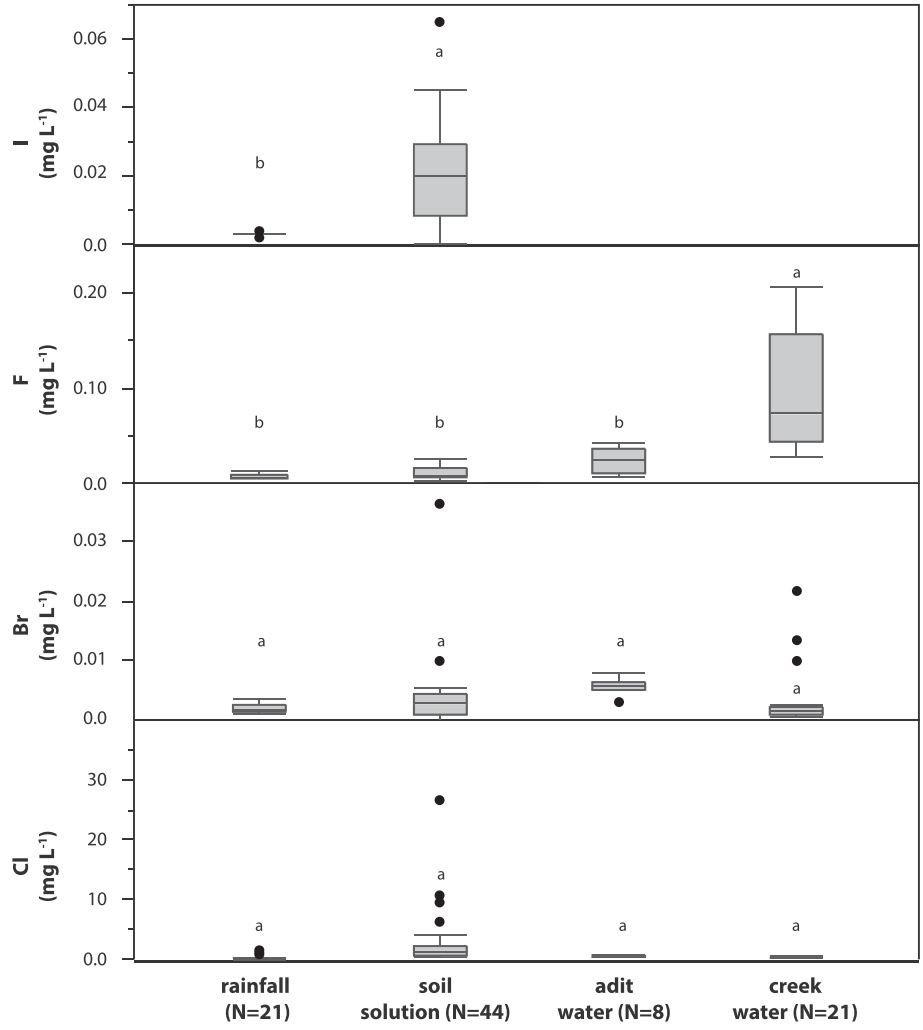

Fig. 5. Box plots displaying the interquartile range and outliers around the median halogen concentration for each liquid sample type. For Cl, Br and F all analyses from all sample types were above the detection limit. For I, 16 out of 21 rainfall samples were above the detection limit and for soil water 30 out of 44. No I concentrations were shown for adit and creek water, since all analyses were below the detection limit. Different letters indicate significant differences ($p < 0.05$).

supposed to be closely associated with the occurrence of organic matter (Yamada, 1968; Fuge, 1988; Keppler et al., 2003; Kabata-Pendias, 2011; Leri and Myneni, 2012; Takeda et al., 2018). Br_{tot}, F_{tot} and I_{tot} concentrations were negatively correlated with C_{org} which itself was negatively correlated with pedogenic oxides. We interpret this as a non-causal link between two co-occurring processes during pedogenesis (accumulation of organic matter in the uppermost part of the profile and formation of secondary minerals in the subsoil). Nevertheless, higher concentrations of Br_{tot}, I_{tot} and F_{tot} in the more decomposed layers are in line with our first hypothesis and imply that halogenation processes dominate over dehalogenation and subsequent leaching in the organic layer in the case of Br, F and I.

In mineral soil, F_{tot} and I_{tot} concentrations did not differ among soil depths (Fig. 3). This might be related to the low solubility of F-bearing minerals like apatite (Migdisov and Williams-Jones, 2014) as compared to Cl-bearing hydroxysilicates (such as biotite and amphibole) in soil. The low solubility of F is further supported by the order of Cl > Br > F regarding the proportion of water-extractable to total halogen concentrations. Fluorine in soil is commonly considered as strongly adsorbed to clay mineral surfaces (Weinstein and Davison, 2004), but can be also incorporated into the crystal lattice of clays and hydroxysilicates by replacing OH^- (Fuge, 1988; Liu et al., 2014). However, we did not find a significant correlation between clay contents and F_{tot} concentrations ($p > 0.1$), thus not corroborating the general high affinity to clays (Piotrowska and Wiacek, 1975). Furthermore, pedogenic oxides contribute to the clay fraction in soil and might explain the retention of dissolved F_{inorg} in mineral soil via electrostatic interactions between their positively charged surfaces and dissolved F_{inorg}. In line, we observed a positive correlation of F_{tot} concentrations to pedogenic oxides. We consider the weathering of F-bearing minerals like biotite and the subsequent adsorption to pedogenic oxides as the primary cause for the constant F_{tot} concentrations across the mineral soil. The same processes likely cause the vertical patterns of Br and I in soil i.e., weathering via high solubility in the topsoil due to a low pH and subsequent adsorption processes. The former is in line with the weathering of gneiss, as gneiss is known to incorporate Br (Burisch et al., 2016; no data exists for I). Furthermore, Br_{tot} and I_{tot} showed a positive correlation to pedogenic oxides, corroborating the importance of adsorption processes for these halogens as well. In addition, not only sorption to pedogenic oxides but also the formation of secondary minerals could explain the observed accumulation of Br_{tot}, F_{tot} and I_{tot} in subsoils. The similar depth distribution pattern of Br, F and I and the opposed trends with regard to Cl is further strengthened by the fact that Br, I and F do not represent essential nutrients (Kabata-Pendias, 2011) and are thus not uplifted by roots from the subsoil. Our results highlight that Cl cycling differed from Br, F and I cycling in soil at our study site. In our temperate coniferous forest, Cl cycling was dominated by biological processes whereas Br, F and I cycling was controlled by abiotic processes (e.g., formation of pedogenic oxides, changes in pH etc.).

4.2. The impact of a canopy on the hydrological pathway and soil profiles

A generally increased halogen input in the presence of a canopy (throughfall) was observed for dissolved Cl_{inorg}, Br_{inorg}, F_{inorg} and I_{inorg} (Fig. 2), which is in agreement with our second hypothesis. Evaporation processes may influence the halogen concentrations, depending on the sample locations. Although evaporation processes are likely to take place in collectors without canopy due to direct solar exposition, still the halogen concentrations in throughfall samples were always higher. Thus, evaporation processes were not further considered. A higher Cl_{inorg} throughfall input can be explained by the wash-off of dry deposited dissolved Cl, or the leaching of Cl from foliage (Eaton et al., 1973; Peters, 1991; Lovett et al., 2005). Furthermore, Cl_{org} compounds originating from the organic compounds in the canopy might be also leached which, however, was not considered since only Cl_{inorg} was measured in throughfall and rainfall. Furthermore, higher dissolved I_{inorg} fluxes compared to rainfall fluxes were also attributed to leaching from needles and leaves (Roulier et al., 2019). Since our previous results (discussed in Section 4.1) showed that Br and I are commonly influenced by the same processes and reflect similar patterns, it can be assumed that dry deposition wash-off also affects dissolved Br_{inorg} concentrations in throughfall. In addition, dissolved Cl_{inorg}, Br_{inorg} and I_{inorg} concentrations in throughfall mainly derive from natural sources (e.g., sea water; Fuge, 1988), whereas, dissolved F_{inorg} concentrations are mainly influenced by atmospheric dry deposition from industrial plants (Wang et al., 2019). However, the possible influence of atmospheric inputs from industrial plants from the Upper Rhine Graben is difficult to estimate in our study because halogen concentrations are not routinely assessed in federal monitoring programs. Furthermore, dust deposition of soil material on the spruce needles can also increase dissolved F_{inorg} concentrations in throughfall as reported by Barnard and Nordstrom (1982). This process may also, to some degree, effect the halogen budget of Cl_{inorg}, Br_{inorg} and I_{inorg}. During the sampling intervals with the highest dissolved F_{inorg} concentrations the rainfall volume was by far the lowest, resulting in very dry soils and thus an increased dust production and increased F_{inorg} concentrations. Therefore, dust deposition of soil material seems to be a plausible explanation.

In line with our second hypothesis, Cl_{tot} and water-extractable Cl_{inorg} concentrations in soil showed a more pronounced (higher concentration differences between the organic layer and lower mineral soils) vertical depth profile in the presence of a canopy than did Br, I and F concentrations. The more pronounced profile of Cl is probably linked to the importance of chlorination processes since chlorination dominates over dechlorination (the other halogens showed the opposite) and this is a very important enrichment process for Cl (Bastviken et al., 2007; Montelius et al., 2016). Although significant differences between rainfall and throughfall occurred, a significant impact of the canopy was only visible in the organic layer for Br_{tot} (Fig. 3b). This could indicate that bromination plays a more important role than fluorination.

In addition, the mineral soil horizons did not reflect different halogen deposition related to the presence of a canopy because halogen input fluxes might be negligible as compared to halogen stocks in soil. For the calculation of the halogen stocks each horizon thickness was accounted with the mean total halogen concentrations, the appropriate concentrations were summed up by taking the total depth into consideration and then multiplied with the soil density. Based on a bulk density of 1300 kg m^{-3} and a soil depth of 0.60 m, the soil was the main halogen stock for Br, F and I (Br: 271,035 g ha^{-1}, F: 3,717,455 g ha^{-1}, I: 78,600 g ha^{-1}) in our study. However, this was not as strongly observed for Cl (772,750 g ha^{-1}). Furthermore, I-stocks are in line with 72,000 ± 7000 g ha^{-1} reported by Roulier et al. (2018). Indeed, annual input fluxes via throughfall represented a minor fraction of the total halogen stocks in soil (Br: 110 g ha^{-1} $year^{-1}$, F: 340 g ha^{-1} $year^{-1}$ F, I: mostly below the detection limit), but for Cl the fluxes are larger than the reservoir (Cl: 96,000 g ha^{-1} $year^{-1}$).

In sum, wash-off of dry deposition and leaching increased dissolved inorganic halogen concentrations in throughfall but this increase did only slightly (Cl) or not (Br, F and I) translate into canopy effects on total halogen concentrations in soil due to the small input as compared to halogen stocks in soil.

4.3. The fate of halogens in the aqueous phase along the hydrological pathway

We found significantly higher dissolved I_{inorg} concentrations in soil solution as compared to rainfall (Fig. 5) and this partly confirms our third hypothesis. The I_{inorg} input via rainfall was negligible, since almost all concentrations were below the detection limit. Thus, our observations indicate a further source of I_{inorg} and enrichment processes during the passage of rainfall through the soil. In general, the soil solution is in equilibrium with the solid soil phase, i.e., an equilibrium between adsorbed and dissolved I and between mineral and dissolved phases.

Therefore, higher dissolved I_{inorg} concentrations in the soil solution point to equilibrium conditions with the solid phase (lacking in rainfall). Apart from this, no significant differences in dissolved Cl_{inorg}, Br_{inorg} and F_{inorg} concentrations between ecosystem solutions were visible (Fig. 5). This is in contrast to our third hypothesis stating differences in dissolved Cl_{inorg} concentrations. A lacking difference might be related to the fact that dissolved Cl_{inorg} generally does not show a strong binding affinity for soil components (Leri and Myneni, 2010). By contrast, the affinity to adsorption in soil is highest for dissolved F_{inorg} with respect to the other halides (Chubar et al., 2005). Thus, one would expect lower dissolved F_{inorg} concentrations in soil solution due to the accumulation in relatively immobile forms (Loganathan et al., 2007). Since no significant differences between rainfall and soil solution for dissolved C_{linorg}, Br_{inorg} and F_{inorg} occurred, our results indicate that geochemical equilibrium reactions between the host rock and the soil solution resulted in halogen concentrations comparable to those in rainfall.

Furthermore, the other dissolved halide concentrations (Cl_{inorg}, Br_{inorg}, I_{inorg}) in adit and creek water did not show significantly higher concentrations than in soil solution. The only exception was higher dissolved F_{inorg} concentrations in creek water compared to soil solution. Distinctly higher F_{inorg} concentrations in creek water can be explained by leaching processes of dump material which contains crushed host rock material (rich in biotite and clay minerals) and can be found adjacent to the creek at the investigated location. Along the sampled Kammentobel creek several large dumps from mining activities in medieval times provide sufficient host rock material that could serve as F_{inorg} source through weathering. A more plausible explanation is the weathering of possible fluorite-bearing veins which were described for an area in close proximity to the study site. However, the highest F_{inorg} concentrations of our study lie in the range of other creek and river analyses from (Baden-Württemberg LUBW, 2019) and are thus not exceptionally high. In conclusion, halogen concentrations did not differ among ecosystem solutions. In conjunction with the explanation of vertical depth profiles of halogens in the solid soil, similar concentrations among ecosystem solutions indicate balanced release (weathering, dehalogenation) and retention (halogenation, adsorption, precipitation) processes rather than an inert behavior that was previously assumed.

5. Conclusions

We found that Cl_{tot} concentrations decreased with increasing depth and were linked to C_{org} concentrations. Chlorination processes and nutrient uplift by root uptake likely accumulated Cl in the topsoil. The other halogens (Br_{tot}, F_{tot} and I_{tot}) showed opposed vertical trends and a negative correlation with C_{org}. Thus, pH-related weathering and a high solubility in combination with adsorption processes to pedogenic oxides were geochemical processes controlling the cycling of Br_{tot}, F_{tot} and I_{tot}. Furthermore, our results show that the presence of a canopy had a major influence on throughfall halogen composition due to the wash-off of dry deposition and leaching from foliage. Within the soil profile only Br_{tot} in the organic Oi horizon was significantly influenced by the canopy, indicating the importance of bromination. The lacking difference between the location with and without canopy in the vertical soil profile is attributed to the additional halogen input by throughfall, which by far is exceeded by weathering and sorption processes in soil. Higher dissolved I_{inorg} concentrations in soil solution compared to rainfall (rainfall concentrations below the detection limit) were found due to the equilibration between soil solution and the solid soil phase. No differences between dissolved Cl_{inorg}, Br_{inorg} and F_{inorg} concentrations in soil solution and rainfall further strengthens the argument that halogen concentrations in soil solution are similar to the rainfall composition due to equilibrium reactions between the host rock and the soil. Significantly higher dissolved F_{inorg} concentrations in creek water possibly result from weathered fluorite-bearing veins.

In conclusion, our results revealed the complexity of processes which control the halogen cycling close to the surface and illustrate the impact of atmospheric input, vegetation and pedogenesis. In order to decipher the relative importance of processes involved in the halogen cycle such as uplift, halogenation/dehalogenation, weathering/adsorption we encourage the use of isotope approaches. Since our results partly deviate from those of other studies, the importance of biological and abiotic processes for the halogens might be site specific and thus, requires more detailed studies on various sites.

Supplementary data to this article can be found online at https://doi.org/10.1016/j.scitotenv.2019.135473.

Declaration of competing interest

The authors declare that they have no known competing financial interests or personal relationships that could have appeared to influence the work reported in this paper.

Acknowledgements

We would like to thank Joel Jambreck for the collection of the soil samples and Manuel Fritsch for support with the soil analyses. We further thank Bernd Steinhilber and Gabriele Stoschek for anion measurements in liquid samples. Furthermore, we thank the Editor Paulo Pereira and three anonymous reviewers for their constructive feedback that improved this manuscript significantly. This study was funded by the German Research Foundation (DFG) [grant numbers Oe516/8-1, Ma2135/20-1].

References

Amachi, S., 2008. Microbial contribution to global iodine cycling: volatilization, accumulation, reduction, oxidation, and sorption of iodine. Microbes Environ. 23 (4), 269–276.
Attiwill, P.M., Adams, M.A., 1993. Nutrient cycling in forests. New Phytol. 124, 561–582.
Barnard, W.R., Nordstrom, D.K., 1982. Flouride in precipitation—II. Implications for the geochemical cycling of fluorine. Atmospheric Environment (1967) 16, 105–111.
Bastviken, D., Thomsen, F., Svensson, T., Karlsson, S., Sandén, P., Shaw, G., Matucha, M., Öberg, G., 2007. Chloride retention in forest soil by microbial uptake and by natural chlorination of organic matter. Geochim. Cosmochim. Acta 71, 3182–3192.
Bodek, I., 1988. Environmental Inorganic Chemistry: Properties, Processes, and Estimation Methods. Pergamon.
Burisch, M., Marks, M.A., Nowak, M., Markl, G., 2016. The effect of temperature and cataclastic deformation on the composition of upper crustal fluids—an experimental approach. Chem. Geol. 433, 24–35.
Burt, R., 2004. Soil Survey Laboratory Methods Manual. Soil Survey Investigations Report No. 42, Version 4.0. Natural Resources Conservation Service, US Department of Agriculture, Washington, DC.
Cabral, A.R., Radtke, M., Munnik, F., Lehmann, B., Reinholz, U., Riesemeier, H., Tupinambá, M., Kwitko-Ribeiro, R., 2011. Iodine in alluvial platinum–palladium nuggets: evidence for biogenic precious-metal fixation. Chem. Geol. 281, 125–132.
Chubar, N., Samanidou, V., Kouts, V., Gallios, G., Kanibolotsky, V., Strelko, V., Zhuravlev, I., 2005. Adsorption of fluoride, chloride, bromide, and bromate ions on a novel ion exchanger. J. Colloid Interface Sci. 291, 67–74.
Conway, E.J., 1942. The chemical evolution of the ocean proceedings of the Royal Irish Academy section B: biological, geological, and chemical science. JSTOR 161–212.
Cortizas, A.M., Vázquez, C.F., Kaal, J., Biester, H., Casais, M.C., Rodríguez, T.T., Lado, L.R., 2016. Bromine accumulation in acidic black colluvial soils. Geochim. Cosmochim. Acta 174, 143–155.
Deutscher-Wetterdienst, 2019. Klimadaten Deutschland - Monats- und Tageswerte (Archiv). https://www.dwd.de/DE/leistungen/klimadatendeutschland/klarchivtagmonat.html (accessed 21.03.2019).
Eaton, J.S., Likens, G.E., Bormann, F.H., 1973. Throughfall and stemflow chemistry in a northern hardwood forest. The Journal of Ecology 495–508.
Epp, T., Marks, M.A., Ludwig, T., Kendrick, M.A., Eby, N., Neidhardt, H., Oelmann, Y., Markl, G., 2019. Crystallographic and fluid compositional effects on the halogen (cl, F, Br, I) incorporation in pyromorphite-group minerals. Am. Mineral. 104, 1673–1688. https://doi.org/10.2138/am-2019-7068.
Fuge, R., 1988. Sources of halogens in the environment, influences on human and animal health. Environ. Geochem. Health 10, 51–61. https://doi.org/10.1007/bf01758592.
Fuge, R., Andrews, M., Johnson, C., 1986. Chlorine and iodine, potential pathfinder elements in exploration geochemistry. Appl. Geochem. 1, 111–116.
Gerzabek, M.H., Muramatsu, Y., Strebl, F., Yoshida, S., 1999. Iodine and bromine contents of some Austrian soils and relations to soil characteristics. J. Plant Nutr. Soil Sci. 162, 415–419.
Hjelm, O., Johansson, M.-B., Öberg-Asolund, G., 1995. Organically bound halogens in coniferous forest soil-distribution pattern and evidence of in situ production. Chemosphere 30, 2353–2364.

IUSS-Working-Group-WRB, 2015. World Reference Base for Soil Resources 2014- International Soil Classification System for Naming Soils and Creating Legends for Soil Maps. Food and Agriculture Organization of the United Nations, Italy, Rome, p. 203.
Johansson, E., Sandén, P., Öberg, G., 2003a. Spatial patterns of organic chlorine and chloride in Swedish forest soil. Chemosphere 52, 391–397.
Johansson, E., Sandén, P., Öberg, G., 2003b. Organic chlorine in deciduous and coniferous forest soils in southern Sweden. Soil Sci. 168, 347–355. https://doi.org/10.1097/01.ss.0000070909.55992.91.
Kabata-Pendias, A., 2011. Trace Elements in Soils and Plants. CRC Press.
Keppler, F., Biester, H., Putschew, A., Silk, P.J., Schöler, H.F., Müller, G., 2003. Organoiodine formation during humification in peatlands. Environ. Chem. Lett. 1, 219–223. https://doi.org/10.1007/s10311-003-0044-5.
Låg, J., Steinnes, E., 1976. Regional distribution of halogens in Norwegian forest soils. Geoderma 16, 317–325.
Le Dizès, S., Gonze, M., 2019. Behavior of 36Cl in agricultural soil-plant systems: a review of transfer processes and modelling approaches. J. Environ. Radioact. 196, 82–90.
Leri, A.C., Myneni, S.C.B., 2010. Organochlorine turnover in forest ecosystems: the missing link in the terrestrial chlorine cycle. Glob. Biogeochem. Cycles 24. https://doi.org/10.1029/2010GB003882.
Leri, A.C., Myneni, S.C.B., 2012. Natural organobromine in terrestrial ecosystems. Geochim. Cosmochim. Acta 77, 1–10. https://doi.org/10.1016/j.gca.2011.11.012.
Leri, A.C., Ravel, B., 2015. Abiotic bromination of soil organic matter. Environ. Sci. Technol. 49, 13350–13359.
Liu, X., Wang, B., Zheng, B., 2014. Geochemical process of fluorine in soil. Chin. J. Geochem. 33, 277–279.
Loganathan, P., Liu, Q., Hedley, M.J., Gray, C.W., 2007. Chemical fractionation of fluorine in soils with a long-term phosphate fertiliser history. Soil Research 45, 390–396. https://doi.org/10.1071/SR07030.
Lovett, G.M., Likens, G.E., Buso, D.C., Driscoll, C.T., Bailey, S.W., 2005. The biogeochemistry of chlorine at Hubbard Brook, New Hampshire, USA. Biogeochemistry 72, 191–232.
LUBW, 2019. Jahreskatalog Fließgewässer 2013 - Wasser Anorganik. http://jdkfg.lubw.baden-wuerttemberg.de/servlet/is/300/ (accessed 27.05.2019).
Marschner, H., 1995. Mineral Nutrition of Higher Plants. 2nd edn. Academic Pres.
Matucha, M., Clarke, N., Lachmanová, Z., Forczek, S.T., Fuksová, K., Gryndler, M., 2010. Biogeochemical cycles of chlorine in the coniferous forest ecosystem: practical implications. Plant Soil Environ. 56, 357.
Migdisov, A.A., Williams-Jones, A., 2014. Hydrothermal transport and deposition of the rare earth elements by fluorine-bearing aqueous liquids. Mineral. Deposita 49, 987–997.
Montelius, M., Thiry, Y., Marang, L., Ranger, J., Cornelis, J.-T., Svensson, T., Bastviken, D., 2015. Experimental evidence of large changes in terrestrial chlorine cycling following altered tree species composition. Environ. Sci. Technol. 49, 4921–4928.
Montelius, M., Svensson, T., Lourino-Cabana, B., Thiry, Y., Bastviken, D., 2016. Chlorination and dechlorination rates in a forest soil—a combined modelling and experimental approach. Sci. Total Environ. 554, 203–210.
Montelius, M., Svensson, T., Lourino-Cabana, B., Thiry, Y., Bastviken, D., 2019. Radiotracer evidence that the rhizosphere is a hot-spot for chlorination of soil organic matter. Plant Soil 1–13.
Myneni, S.C., 2002. Formation of stable chlorinated hydrocarbons in weathering plant material. Science 295, 1039–1041.
Öberg, G., Grøn, C., 1998. Sources of organic halogens in spruce forest soil. Environ. Sci. Technol. 32, 1573–1579. https://doi.org/10.1021/es9708225.
Öberg, G., Holm, M., Sandén, P., Svensson, T., Parikka, M., 2005. The role of organic-matter-bound chlorine in the chlorine cycle: a case study of the Stubbetorp Catchment, Sweden. Biogeochemistry 75, 241–269. https://doi.org/10.1007/s10533-004-7259-9.
Peters, N.E., 1991. Chloride cycling in two forested lake watersheds in the west-central Adirondack Mountains, New York, USA. Water Air Soil Pollut. 59, 201–215.
Piotrowska, M., Wiacek, K., 1975. Fluorine Content in some Polish Soils. Rocz Nauk Roln. p. 101a 93.
Redon, P.-O., Abdelouas, A., Bastviken, D., Cecchini, S., Nicolas, M., Thiry, Y., 2011. Chloride and organic chlorine in forest soils: storage, residence times, and influence of ecological conditions. Environ. Sci. Technol. 45, 7202–7208. https://doi.org/10.1021/es2011918.
Rhykerd, C.L., Overdahl, C.J., 1972. In: Hanson, C.H. (Ed.), Nutrition and Fertilizer Use. Alfalfa Science and Technology, pp. 437–468.
Roulier, M., Bueno, M., Thiry, Y., Coppin, F., Redon, P.-O., Le Hécho, I., Pannier, F., 2018. Iodine distribution and cycling in a beech (Fagus sylvatica) temperate forest. Sci. Total Environ. 645, 431–440.
Roulier, M., Coppin, F., Bueno, M., Nicolas, M., Thiry, Y., Della Vedova, C., Février, L., Pannier, F., Le Hécho, I., 2019. Iodine budget in forest soils: influence of environmental conditions and soil physicochemical properties. Chemosphere 224, 20–28.
Schlesinger, W., 1997. Biogeochemistry: An Analysis of Global Change. Academic Press, San Diego. Biogeochemistry: An Analysis of Global Change. 2nd ed. Academic Press, San Diego.
Schwertmann, U., 1964. Differenzierung der Eisenoxide des Bodens durch Extraktion mit Ammoniumoxalat-Lösung. Zeitschrift für Pflanzenernährung, Düngung, Bodenkunde 105, 194–202.
Seki, M., Oikawa, J., Taguchi, T., Ohnuki, T., Muramatsu, Y., Sakamoto, K., Amachi, S., 2012. Laccase-catalyzed oxidation of iodide and formation of organically bound iodine in soils. Environ. Sci. Technol. 47, 390–397.
Soper, A.K., Weckström, K., 2006. Ion solvation and water structure in potassium halide aqueous solutions. Biophys. Chem. 124, 180–191.
Steinnes, E., Frontasyeva, M.V., 2002. Marine gradients of halogens in soil studied by epithermal neutron activation analysis. J. Radioanal. Nucl. Chem. 253, 173–177. https://doi.org/10.1023/a:1015849525392.
Takeda, A., Tsukada, H., Takaku, Y., Satta, N., Baba, M., Shibata, T., Hasegawa, H., Unno, Y., HISAMATSU, S., 2016. Determination of iodide, iodate and total iodine in natural water samples by HPLC with amperometric and spectrophotometric detection, and off-line UV irradiation. Anal. Sci. 32, 839–845.
Takeda, A., Nakao, A., Yamasaki, S., Tsuchiya, N., 2018. Distribution and speciation of bromine and iodine in volcanic ash soil profiles. Soil Sci. Soc. Am. J. 82, 815–825.
Uhlig, D., Schuessler, J.A., Bouchez, J., Dixon, J.L., von Blackenburg, F., 2017. Quantifying nutrient uptake as driver of rock weathering in forest ecosystems by magnesium stable isotopes. Biogeosciences 14, 3111–3128.
Vodyanitskii, Y.N., Makarov, M., 2017. Organochlorine compounds and the biogeochemical cycle of chlorine in soils: a review. Eurasian Soil Science 50, 1025–1032.
Wang, M., J-y, Y., He, W., Li, J., Y-y, Z., X-e, Y., 2019. Vertical distribution of fluorine in farmland soil profiles around phosphorous chemical industry factories. Environ. Sci. Pollut. Res. 26, 855–866.
Weinstein, L.H., Davison, A., 2004. Fluorides in the Environment: Effects on Plants and Animals. CABI.
WetterKontor, 2019. Wetterrückblick Feldberg im Schwarzwald (1486 m). https://www.wetterkontor.de/de/wetter/deutschland/rueckblick.asp?id=57&datum=13.06.2019&t=8 (accessed 21.03.2019).
Yamada, Y., 1968. Occurrence of bromine in plants and soil. Talanta 15, 1135–1141. https://doi.org/10.1016/0039-9140(68)80036-0.
Yuita, K., 1983. Iodine, bromine and chlorine contents in soils and plants of Japan AU. Soil Science and Plant Nutrition 29, 403–428. https://doi.org/10.1080/00380768.1983.10434645.

Appendix IV

Study D

Epp, T., Marks, M. AW., Neidhardt, H., Oelmann, Y. & Markl, G. (submitted). Halogen (F, Cl, Br, I) sorption in silt and clay fractions of a Cambisol from a temperate forest, SW Germany.

Manuscript submitted

Number of authors: 5

Author position: 1

Wordcount: 7890

Halogen (F, Cl, Br, I) sorption in silt and clay fractions of a Cambisol from a temperate forest

Tatjana Epp[1,2]*, Michael A.W. Marks[1], Harald Neidhardt[2], Yvonne Oelmann[2], Gregor Markl[1]

[1] Geoscience, University of Tübingen, Wilhelmstraße 56, 72074 Tübingen, Germany; tatjana.epp@uni-tuebingen.de, michael.marks@uni-tuebingen.de, markl@uni-tuebingen.de

[2] Geoecology, University of Tübingen, Rümelinstraße 19-23, 72070 Tübingen, Germany; harald.neidhardt@uni-tuebingen.de, yvonne.oelmann@uni-tuebingen.de

*Corresponding author: Tatjana Epp, tatjana.epp@uni-tuebingen.de

Abstract

In spite of considerable efforts on understanding the role of halogens in soil biogeochemistry, information about sorption of fluorine (F), chlorine (Cl), bromine (Br) and iodine (I) and concentration data for different soil size fractions is still sparse. For surface sorption processes the surface area and therefore the particle size is highly relevant. The objectives of this study were to determine the proportions of F, Cl, Br and I (organic + inorganic) that are surface sorbed or incorporated in the structure of clay minerals and pedogenic oxides for different soil horizons in a temperate forest ecosystem (in SW Germany). Because the surface sorption largely depends on the (specific) surface area, we determined halogen concentrations in different soil size fractions (i.e., coarse silt with 20-63 µm, medium and fine silt with 2-20 µm, coarse clay with 0.2- < 2 µm and medium clay with 0.02-0.2 µm). Total halogen concentrations and the

structurally bound halogen proportion after K_2HPO_4 solution treatment were analyzed by combustion ion chromatography (CIC). Sorbed halogen proportions were calculated by subtracting the structurally bound proportion from the total concentrations.

While F was mainly structurally bound in the crystal lattice and by specific sorption to clay minerals, the halogens with larger atom radii (Cl, Br and I) were predominantly unspecifically sorbed. Around 70 % of Br and I and 90 % of Cl were sorbed in the medium clay fraction (0.02-0.2 µm) in mineral subsoil while > 95 % of F was structurally bound, most likely in clay minerals by exchange reactions between OH^- and F^- in the crystal lattice but also as specific sorption mechanism. The proportion of sorbed Cl, Br and I was highest in the medium clay fraction (the finest fraction we studied), although this fraction only contributed about 1 wt% to the bulk soil. This is probably related to the highest sorption capacity of small particles due to their large specific surface area. Vertical depth profiles of halogens in the individual soil size fractions matched with the bulk soil vertical patterns. Lacking vertical concentration differences of F_{tot}, Br_{tot} and I_{tot} in the mineral soil during soil development might be due to steady state or equilibrium conditions between weathering, sorption processes and surface input. In contrast, the vertical depth pattern of Cl_{tot} tended to decrease, reflecting the process of Cl accumulation in the topsoil and nutrient uplift. Our study provides new data on the different biogeochemical sorption behavior of the various halogens in soils of forest ecosystems which seem to be halogen-specific, with the amount of sorbed halogens further dependent on soil particle sizes. The understanding of halogen sorption behavior might have implications for retention processes of pollutants in landfills or radioactive waste disposal.

Key words: Sorption processes, particle size fractions, Cambisol, fluorine, chlorine bromine, iodine

Introduction

The halogens, fluorine (F), chlorine (Cl), bromine (Br) and iodine (I) are important elements in natural ecosystems and their understanding is necessary for a variety of organic and inorganic reactions in soils, the critical zone and in the Earth's crust in general (e.e., Fuge 1988; Bastviken et al. 2007; Redon et al. 2011; Öberg and Bastviken 2012; Kendrick and Burnard 2013). While Cl is an essential micro-nutrient for plants and micro-organisms (Raven 2017), F, Br and I are no essential micro-nutrients but appear to be involved in a large variety of organic processes (e.g., Yuita 1983; Fuge 1988; Marschner 1995; Kabata-Pendias 2011), and act as important ligands in inorganic processes like metal transport (Lecumberri-Sanchez and Bodnar 2018). In large concentrations halogens can have harmful effects on living organisms (Chubar et al. 2005). Processes within soils (such as halogenation; e.g., Asplund and Grimvall 1991; Montelius et al. 2015; Montelius et al. 2016) and external halogen input (such as dry deposition wash-off and canopy leaching; e.g., Lovett et al. 2005; Roulier et al. 2019) strongly influence the halogen distribution and availability in soils. The Cl distribution for example, is strongly governed by chlorination processes in the organic layer which result in an accumulation of Cl_{tot} in the organic layer and decreasing Cl_{tot} concentrations with increasing soil depth (e.g., Bastviken et al. 2007; Montelius et al. 2016; Epp et al. 2020). In contrast, F_{tot}, Br_{tot} and I_{tot} concentrations increase with increasing soil depth (Epp et al. 2020), which may be linked to sorption on for example positively charged surfaces of pedogenic oxides (iron (Fe), manganese (Mn) and aluminum (Al) oxides and (oxy) hydroxides) that form during pedogenesis (Gerzabek et al. 1999; Loganathan et al. 2007; Cortizas et al. 2016; Roulier et al. 2019). Further explanations for these depth profiles could be weathering and subsequent leaching (Davison and Weinstein 2006; Liu et al. 2014 and references therein; Fuge 2019) or the combination of the level of for example bromination linked to the age of SOM and stabilization of brominated organic substances by complexation with Al (Cortizas et al. 2016).

Modification of host rock material and primary mineral weathering and formation of secondary minerals such as clay minerals are governed by progressive soil formation (Chadwick and Chorover 2001; Cornelis et al. 2014). In general, soils consist of highly variable particle size mixtures with gaseous and liquid interstitial phases. Numerous reactions such as sorption and desorption processes take place at interfaces of water and charged surfaces of the solid soil phase, for instance clay minerals or pedogenic oxides (Scheffer et al. 1998; Schoonheydt and Johnston 2006). These sorption processes are strongly dependent on the size and type of the particle surfaces, where the specific surface size increases with decreasing particle size. With respect to silicate phases, allophane ($Al_2O_3*(SiO_2)_{1.7}*(H_2O)_{2.8}$) and imogolite ($Al_2SiO_3(OH)_4$) have the largest specific surfaces ranging between 700 and 1100 $m^2\ g^{-1}$ (Parfitt 1989; Scheffer et al. 1998 and references therein). With specific surfaces between 600 and 800 $m^2\ g^{-1}$ smectite and vermiculite have the largest specific surfaces among clay minerals. In comparison, specific surface areas of pedogenic oxides, like goethite and hematite range between 50 and 150 $m^2\ g^{-1}$, whereas ferrihydrite has by far the largest surface of 300 to 400 $m^2\ g^{-1}$ (Parfitt 1989; Scheffer et al. 1998 and references therein). Due to their large specific surface area, clay minerals and also pedogenic oxides are particularly effective sorbents for a large variety of ions. While clay minerals are generally negatively charged in the pH range of most soils, pedogenic oxides are rather positively charged and, thus, can sorb anions (Scheffer et al. 1998) such as F^-, Cl^-, Br^- or I^-. In general, the sorption of F^-, Cl^-, Br^- and I^- on pedogenic oxides or clay minerals increases with decreasing pH (Weerasooriya and Wickramarathna 1999; Goldberg and Kabengi 2010). Decreasing sorption behavior is linked with increasing solution ionic strength of the background electrolyte and no adsorption was reported at pH 8.8, the point of zero net proton charge (Weerasooriya and Wickramarathna 1999). With regard to sorption of ions, two general processes can be distinguished: (1) inner-sphere adsorption, where ligand exchange takes place, hence the ion and the ligands which form complexes are in direct contact , and (2) outer-sphere adsorption, where hydrated ions are weakly bound to mineral surfaces by electrostatic

interactions, i.e., where water molecules are interconnected between ions and the ligands (e.g., Sposito 1989; Scheffer et al. 1998; Strawn and Sparks 1999). According to theoretical models fluoride was described to form inner-sphere complexes with pedogenic oxides, while Cl^- rather forms outer-sphere complexes (Scheffer et al. 1998; Eskandarpour et al. 2008). Only a few studies dealt with Br^- adsorption of natural soils with complex matrices (Li et al. 1995; Goldberg and Kabengi 2010) or oxides (Petkovic et al. 1994; Chubar et al. 2005) and clay minerals (Weerasooriya and Wickramarathna 1999) with less complex matrices. These studies found that Br^- is typically adsorbed on Fe and Al oxides but shows a relatively weak adsorption behavior on kaolinite by outer-sphere complexation (Weerasooriya and Wickramarathna 1999; Goldberg and Kabengi 2010). In natural soils Br^- was found to be adsorbed on soils at pH below 7 and that adsorption may be attributed to clay minerals or exchange reactions between Br^- and negatively charged organic compounds (Li et al. 1995; Goldberg and Kabengi 2010). Furthermore, sorption experiments of Kaplan et al. (2000) with a large variety of natural model substances revealed that most of I^- in natural arid sediments was weakly adsorbed on illite and minor amounts of I^- were adsorbed by surface complexation with soft metals such as mercury or silver which were included in the illite structure as trace impurities, which could easily be desorbed. A weak I^- adsorption on kaolinite was also explained by outer-sphere complexation mechanisms (Weerasooriya and Wickramarathna 1999). In contrast, only minor amounts or no I^- sorption could be observed on individually sampled and investigated calcite, chlorite, goethite, montmorillonite, quartz or vermiculite model substances (Kaplan et al. 2000).

Previous studies almost exclusively investigated halogen sorption on natural model substances such as mineral separates or synthesized Fe- and Al oxides. Sorption processes in natural soil samples were rarely considered and a distinction between sorbed (unspecifically) and structurally bound halogens (i.e., halogens in the crystal lattice and specifically sorbed) within soil depth has not been investigated yet. Especially the sorption behavior of all halogens has

not been investigated in previous studies so far. Hence, information on the relative amount of halogens sorbed to clay minerals, pedogenic oxides or organic compounds and the role of different particle sizes and thus potential grain size effects has been lacking. The objectives of this study were to determine the relative amount of sorbed halogens (organic + inorganic) (1) for each halogen and to investigate if the sorption behavior of F, Cl, Br and I is similar, and (2) in four particle size fractions (i.e., 20-63 µm (coarse silt), 2-20 µm (fine and medium silt), 0.2 - < 2 µm (coarse clay) and 0.02 – 0.2 µm (medium clay) in the mineral soil. Our analytical approach enables us to distinguish structurally bound (organic + inorganic) F, Cl, Br and I from sorbed (organic + inorganic) halogens in three soil horizons in mineral top- and subsoil. Furthermore, we paid attention to potential vertical patterns of F_{tot}, Cl_{tot}, Br_{tot} and I_{tot} concentrations (organic + inorganic) of three soil horizons in the different soil size fractions. The distinction between organic and inorganic halogens is not topic of this study, this could be subject to further studies. We investigated a Cambisol developed on gneissic host rock located in a spruce forest (*Picea abies* (L.) H. Karst). Typically, this soil type consists of an organic layer on top of the mineral soil, a mineral topsoil and mineral subsoil (Fig. 1).

Material and Methods

Study area

The investigated soil samples derive from the Kammentobel valley, close to the Feldberg peak in the Schwarzwald, SW Germany. The annual temperature in 2018 ranged between 23 and -20 °C and total precipitation was ~1500 mm (Deutscher-Wetterdienst 2019; WetterKontor 2019). The samples of this study represent a carefully selected subset of soil samples that were previously analyzed by Epp et al. (2020) regarding their bulk halogen (F, Cl, Br and I) composition and pedogenic oxide content (see chapter 2.3). The vegetation comprises spruce trees (*Picea abies* (L.) H. Karst) and blueberry (*Vaccinium myrtillus* L.). The investigated soil can be classified as Cambisol according to IUSS-Working-Group-WRB (2015) and developed

on strongly weathered gneisses (migmatites) from the Schwarzwald low mountain range. The investigated soil profile comprises a depth of 57 cm and soil horizon Bw2C in the subsoil can be found until a depth of ~ 70cm, then the transition to the host rock is reached. In total, triplicate samples from each soil horizon i.e., mineral topsoil (Ah) and subsoil (Bw1, Bw2C) were selected. Further details on the study site are given in Epp et al. (2020). The vertical halogen distribution in the four investigated particle sizes will be presented as a preliminary data set and is included in this study as there have not been many studies on this topic so far.

Sample preparation

The soil material used in this study was first sieved (< 2 mm) and dried at 40 °C for five days in order to minimize loss of halogens to the gaseous phase. For further investigation, respective samples from each location were combined to form composite samples. The sieved soil samples (< 2 mm) were then mixed with Millipore water (18.2 MΩ*cm) and subsequently passed through 500, 250, 125, 63 and 20 µm stainless steel sieves to capture the remaining solid material for further size-specific particle separation.

The fraction < 20 µm was transferred into a 1 L Atterberg cylinder with a drop height of 25 cm and suspended with Millipore water. This procedure was applied to separate the clay fractions < 2 µm from the remaining medium and fine silt fraction (2-20µm) according to Stokes' law (Stokes 1901) as described by Atterberg (1912). Note that the clay fractions do not exclusively consist of clay minerals, but also contain to a certain extent pedogenic oxides. The sediment was shaken in the cylinder and left to stand for 22 hours. During this period heavier silt and sand sized particles (> 2 µm) sedimented, whereas clay-sized particles (< 2 µm) remained in suspension and could be separated from the remainder. Subsequently, the cylinder was refilled with Millipore water and the procedure was repeated until the supernatant liquid was no longer muddy. Depending on the soil horizon, this procedure took up to 10 runs for the mineral top- and subsoil.

The obtained clay fractions < 2 µm were then separated by vacuum filtration (Welch Ilmvac^{TM}) using 0.8 µm cellulose nitrate membrane filters with a diameter of 10 cm (neoLab®). In order to separate the coarse clay (0.2- < 2 µm) from the medium clay (0.02-0.2 µm) fraction, all samples were cooled-centrifuged with a ROTANTA 460RS, using a 5624 rotor. The separation was conducted according to Tributh and Lagaly (1986) and the following frame conditions were applied: 100 ml plastic centrifuge tubes with a diameter of 4 cm, r_0 = 10.3 cm, r = 12.3 cm and the sediment was mixed with 80 ml Millipore water. As a first step, the fine clay fraction (d = 0.02 µm) was separated by 4400 rotations per minute (RPM min^{-1}) for t = 6 h 22 min. Subsequently, the first 2 cm were sampled by pipetting and the tubes were refilled with Millipore water to 80 ml. In total, three runs were implemented, but it turned out that the fine clay fraction (< 0.02 µm) was too fine to get reliably completely separated or used for further investigations. Since the fine clay fraction was partly removed and not further considered, it is only referred to the medium clay fraction as the finest fraction. In order to separate the medium clay fraction (d = 0.2 µm) from the coarse clay fraction, the samples were centrifuged at 2000 RPM min^{-1} for t = 21 min. In total 57 runs were required to separate the fine and medium from the coarse clay fraction.

Note that during the whole procedure we did not use H_2O_2 to eliminate organic particles or any dispersing agents (such as HCl) as pre-treatment in order to minimize potential contamination with halogens. Therefore, the determined halogen concentrations of the samples represent the sum of organic and inorganic halogen components. By using Millipore water during all grain size separation steps, water-soluble (and loosely bound/exchangeable) halogens were removed. In the bulk soil, water-extractable halogen proportions ranged from 0.4 % (F^-) to 9 % (Cl^-) as reported in Epp et al. (2020). Total halogen concentrations (F_{tot}, Cl_{tot}, Br_{tot}, I_{tot}; i.e., organic + inorganic halogens) of all three soil horizons (Ah, Bw1, Bw2C) based on CIC measurements represent both structurally bound halogens and halogens sorbed to particle surfaces.

Possible organic contamination during sample treatment can be excluded, since total organic carbon (C_{org}) content of soil fractions was 40 % lower than total C_{org} of bulk soil. The different particle size fractions contained various C_{org} amounts. The bulk C_{org} concentration in soil horizon Bw1 (after taking the relative amount compared to bulk soil into consideration) contained in the coarse silt fraction 6 g kg^{-1}, in the medium and fine silt fraction 10 g kg^{-1}, in the coarse clay fraction 1 g kg^{-1} and in the medium clay fraction < 1 g kg^{-1}.

Desorption experiments

To remove strongly sorbed halogens on soil particles, the already grain size separated samples were mixed with a solution of 350 mg K_2HPO_4 (≥ 99%, Roth) in 10 mL Millipore water for which the pH was adjusted to 3-4 by adding 140 µL HNO_3 (65 %, suprapure, Merck). It is generally known that phosphate is highly exchangeable with other anions (Manning and Goldberg 1996). Kaolinite and illite generally have a specific surface area of 10 - 100 m^2 g^{-1}, whereas clay minerals and pedogenic oxides in extreme cases reach values up to 1000 m^2 g^{-1} (Parfitt 1989; Santamarina et al. 2002 and references therein). These values are most likely only representative for the smaller grain size fractions and thus represent maximum specific surface areas. To assure excess of phosphate, we assumed a total specific surface area of 1000 m^2 g^{-1} and used an initial phosphate content of 2.5 µmol m^{-2} (Torrent et al. 1990). Each analyzed sample varied with respect to total mass used and the total surface area of our samples reached up to 150 m^2. For this maximum surface 0.4 mmol would have sufficed, thus we have used a 2 mmol phosphate to provide more than adequate surface coverage. The samples were left in the solution for three days and were occasionally shaken. The silt fractions were then separated from the K_2HPO_4 solution by vacuum filtration, briefly washed with Millipore water and subsequently dried at room temperature. The clay fractions were centrifuged and supernatant solutions pipetted. The same procedure was repeated with Millipore water and solid samples were dried at room temperature. After phosphate treatment of samples from Ah, Bw1 and Bw2C

224 horizons from below canopy (C) only contained structurally bound halogens (F_{inc}, Cl_{inc}, Br_{inc},
225 I_{inc}), since sorbed halogens (F_{sorb}, Cl_{sorb}, Br_{sorb}, I_{sorb}) were desorbed. Halogen analyses in liquid
226 samples represent the dissolved inorganic F (F_{inorg}) and Cl (Cl_{inorg}) concentration.

227 **Halogen analyses**

228 After size fractionation, all samples were manually mortared and homogenized before analysis
229 of total halogen concentrations by combustion ion chromatography (CIC). The same applies to
230 subsamples that have been additionally treated with K_2HPO_4 to remove the surface sorbed
231 halogens and to solely assess the fraction of structurally bound halogens. For the CIC analyses,
232 an autosampler for solid samples (MMS 5000; Analytik Jena) connected to a combustion oven
233 and to a 930 Compact IC Flex chromatograph (Metrohm, Germany) with chemical suppression
234 and a peristaltic pump for regeneration (100 mmol L^{-1} H_2SO_4) was used. Separation of analytes
235 was achieved with a Metrosep A Supp 5 – 250/4.0 column (Metrohm) using an eluent consisting
236 of 8 mmol L^{-1} Na_2CO_3 (suprapure, Merck ®). The limits of detection were: 0.8 mg kg^{-1} for F,
237 0.2 mg kg^{-1} for Cl and 0.02 mg kg^{-1} for Br and I (calculated according to DIN 32645). Based
238 on the analysis of standard solutions (single element solutions of F, Cl, Br and I; Roth; 1000
239 mg L^{-1}) and various reference materials (SO3, GSN), the long-term reproducibility (1σ) was
240 within a 20 % margin for F and 10 % for Cl, Br and I. Sorbed halogen concentrations were
241 calculated by subtraction of structurally bound halogen concentrations from total halogen
242 concentrations. Note that structurally bound concentrations comprise bound in the crystal lattice
243 as well as specifically sorbed. A detailed description of the analytical method can be found in
244 Epp et al. (2019).

245 Liquid samples of the residual K_2HPO_4 extraction solution were analyzed for F_{inorg} and Cl_{inorg}
246 using an autosampler for liquid samples (858 Professional Sample Processor, Metrohm). Limits
247 of detection were for F 0.2 mg L^{-1} and for Cl 0.5 mg L^{-1} (calculated according to DIN 32645),

while Br_{inorg} and I_{inorg} concentrations were below the detection limit as the samples have been diluted by a factor of 1000 to avoid column overload by phosphate.

Complementary analyses

We used dried (40 °C) and sieved (<2 mm) bulk sample material for the analyses of pedogenic oxides. The analyses of poorly crystalline pedogenic oxides (Fe_{ox} and Al_{ox}) and the sum of poorly crystalline and crystalline pedogenic oxides (Fe_d and Al_d) have already been reported in Epp et al. (2020). Hence, further methodical aspects can be found in this previous study. Coarse clay and medium clay fractions of soil horizons Ah, Bw1 and Bw2C were analyzed by means of X-ray diffraction (XRD). The XRD analyses were conducted on texture samples on a glass slide with preferred orientation using a Bruker D8 Advance at the University of Tübingen. Total carbon (C_{tot}) concentrations were analyzed from homogenized samples with an Elemental Analyzer (Vario EL III, Elementar Analysensystem GmbH). Due to very minor amounts of $CaCO_3$ (< 1 %) in the acidic mineral soil (pH < 4.5), C_{tot} is considered to be adequate to total organic C (C_{org}).

Data analyses

IBM® SPSS® Statistics Version 25 was used for all statistical evaluation. Spearman rank correlations were conducted to detect possible correlations between halogen concentrations and various soil parameters. Generally, for $p < 0.05$, differences and correlations were considered as statistically significant. The Shapiro-Wilk test was applied to test for normal distribution and the Levene test was assessed for checking the homogeneity of variances. If homogeneity of variance was not given, the Welch test was used and the Games-Howell as post-hoc test. Halogen concentrations of F_{sorb}, Cl_{sorb}, Br_{sorb} and I_{sorb} between different particle sizes were compared using the one-way ANOVA to determine possible relations of halogen concentrations and grain size.

Results

On average 40 wt% of bulk soil consisted of coarse silt (20-63 µm; 15 wt%) and fine to medium silt (2-20 µm; 25 wt%) particles. The clay fractions represented by far the smallest weight portion of the investigated bulk soil, with 3 wt% of 0.2- < 2 µm and <1 wt% of 0.02- 0.2 µm particles, only. Based on XRD analyses, coarse and medium clay samples were composed of vermiculite, illite, kaolinite and gibbsite, i.e., did not contain any swellable clay minerals. The organic carbon content in the different particle sizes ranged between 2.5 and 10 % (Tab. 1) and was on average 15 % lower in samples after phosphate treatment (Fig. 2a). In the following, total halogen concentrations and the proportions of sorbed halogens will be shown separately for each halogen in the four different particle size fractions.

Fluorine sorption in various particle sizes

In the coarse silt fraction (20-63 µm), F_{inc} concentrations were slightly higher than F_{tot} concentrations in soil horizons Ah and Bw2C. In soil horizon Bw1 F_{inc} concentration was only half as high as F_{tot}, thus 50 % of F was structurally bound (Fig. 3) in this horizon, whereas in Ah and Bw2C F was entirely structurally bound. Dissolved F_{inorg} concentrations in the supernatant phosphate solution were decreasing with soil depth from 3 to 1.8 mg L^{-1} (Fig. A1). Similar was observed in the medium and fine silt fraction (2-20 µm), since F_{inc} concentration was also higher than F_{tot} concentration, all of F was structurally bound in the Ah horizon. Soil horizon Bw1 showed that 90 % of F_{tot} was F_{inc}, whereas in soil horizon Bw2C 100 % of F was structurally bound and nothing of F was sorbed (Fig. 3). Dissolved F_{inorg} decreased with depth from 3.5 to 1.4 mg L^{-1} (Fig. A1). The amount of incorporated F in the coarse clay fraction (0-2-<2 µm) was in the same order of magnitude as for the silt fractions. In soil horizon Ah 93 % of F_{tot} and in soil horizons Bw1 and Bw2C all of F_{tot} was structurally bound (Fig. 3). Dissolved F_{inorg} in the supernatant phosphate solution decreased with depth from 2.7 to 1.7 mg L^{-1} (Fig. A1). Concentrations of F_{inc} were constant with depth in the medium clay fraction (0.02-0.2 µm),

297 ranging between 650 and 680 mg kg^{-1}. Comparable to the other size fractions, 96 to 100 % of
298 F was structurally bound, and thus, only up to 4 % sorbed (Fig. 3). The supernatant phosphate
299 solution showed decreasing dissolved F_{inorg} from 3.0 to 1.8 mg L^{-1} with depth (Fig. A1). In
300 general, F_{tot} concentrations (ranging in total between 500 and 800 mg kg^{-1}) and the proportions
301 of F_{inc} and F_{sorb}, respectively, were relatively constant throughout the four investigated particle
302 sizes and showed that most F was structurally bound. Comparing the few proportions of F_{sorb}
303 between the particle sizes, mean values of 17 % F_{sorb} showed that by far most of F was sorbed
304 to particles in the coarse silt fraction. A slight decrease from 9 to 4 % F_{sorb} related to the size
305 was observed from the medium and fine silt to the medium clay fraction. However, F_{sorb}
306 concentrations did not differ significantly between the particle sizes ($p > 0.05$). Furthermore,
307 F_{tot} concentrations were negatively correlated with particle size ($r = -0.536$, $p = 0.002$). Molar
308 ratios showed by far higher F_{tot} concentrations in each particle size fraction compared to Cl_{tot},
309 Br_{tot} and I_{tot}. In the coarse silt fraction the ratios were as follows: F/Cl = 8, F/Br = 70, F/I =390,
310 in the medium and fine silt fraction: F/Cl = 10, F/Br = 50, F/I = 200, in the coarse clay fraction:
311 F/Cl = 10, F/Br = 45, F/I = 250 and in the medium clay fraction: F/Cl = 1, F/Br = 15 and F/I =
312 100. Vertical F_{tot} concentration depth profiles of all four particle sizes were strongly
313 overlapping with concentrations ranging between 500 and 1200 mg kg^{-1}. Within the mineral
314 soil F_{tot} concentrations were relatively constant (Fig. 4).

315 **Chlorine sorption in various particle sizes**

316 In the coarse silt fraction Cl_{inc} concentrations tended to decrease with increasing depth from
317 150 to 90 mg kg^{-1} (Tab. 1) and showed on average a Cl proportion of 20 % (Fig. 3) which was
318 sorbed relative to total Cl concentration. Dissolved Cl_{inorg} in the supernatant phosphate solution
319 increased from 1.5 to 2.7 mg L^{-1} (Fig. A1) with increasing soil depth. Similar observations were
320 made in the medium to fine silt fraction, where a trend of decreasing Cl_{inc} concentrations from
321 120 to 90 mg kg^{-1} was observed (Tab. 1). Throughout the three soil horizons also on average

20 % was Cl_{sorb} relative to Cl_{tot} concentrations. No vertical variations occurred in dissolved Cl_{inorg} in the supernatant phosphate solution with average concentrations of 1.5 mg L^{-1} (Fig. A1). Concentrations of Cl_{inc} also tended to decrease slightly in the coarse clay fraction with depth from 130 to 110 mg kg^{-1} (Tab. 1). In soil horizons Ah and Bw2C 25 to 30 % of Cl_{tot} concentrations were Cl_{sorb}, but it was only 5 % Cl_{sorb} in Bw1 (Fig. 3). Concentrations of dissolved Cl_{inorg} in the supernatant phosphate solution varied between 0.4 and 0.9 mg L^{-1} with no clear vertical trend (Fig. A1). In contrast, in the medium clay fraction Cl_{tot} concentrations were by far higher compared to the other particle sizes and ranged between 600 and 1800 mg kg^{-1} (Tab. 1). Furthermore, 80 to 90% of Cl_{tot} in the medium and fine clay fraction was sorbed (Fig. 3), which is on average 65 % more than in the coarser grain size fractions. A large difference was visible in dissolved Cl_{inorg} concentrations in the supernatant phosphate solution between mineral topsoil (0.7 mg L^{-1}) and subsoil (4.5 mg L^{-1}, Fig. A1). Comparing Cl_{sorb} concentrations of all particle sizes, concentrations were significantly higher in the medium clay fraction (p = 0.007- 0.008). In addition, Cl_{tot} concentrations were negatively correlated with particle size (r = -0.405, p = 0.021). Vertical Cl_{tot} concentration profiles tended to show a slight decrease in all four particle sizes with increasing soil depth (Fig. 4). In the coarse silt, medium and fine silt and coarse clay fractions Cl_{tot} concentrations ranged between 100 and 180 mg kg^{-1}. In strong contrast were Cl_{tot} concentrations in the medium clay fraction which reached values up to 2500 mg kg^{-1} (Fig. 4).

Bromine sorption in various particle sizes

Structurally bound Br concentrations tended to show a slight decrease with depth from 40 to 25 mg kg^{-1} in the coarse silt fraction. On average, only 10% of Br_{tot} concentrations were sorbed. In the medium and fine silt fraction Br_{tot} concentrations were increasing from mineral topsoil (40 mg kg^{-1}) to mineral subsoil (70 mg kg^{-1}). In soil horizon Ah 97 % of Br_{tot} was structurally bound and hence, only 3 % sorbed, whereas in the mineral subsoil 30 % of Br_{tot} was sorbed (Fig. 3).

Relatively similar observations were made in the coarse clay fraction. Total Br concentrations also tended to increase with depth from 40 to 80 mg kg^{-1} (Tab. 1) and on average a Br proportion of 20 % which was sorbed relative to Br_{tot} concentrations was observed. Compared to the coarse silt fraction, there was an increase in the Br proportion which was sorbed. Total Br concentrations were by far higher in the medium clay fraction with concentrations between 150 and 170 mg kg^{-1} (Tab. 1). In the Bw1 horizon 60 % of Br_{tot} was sorbed and in Bw2C even 70 %. In the smallest particle size fraction by far the highest amount of Br was sorbed compared to the three other particle sizes (Fig. 3). Comparing Br_{sorb} concentrations of all particle sizes, concentrations were significantly higher in the medium clay fraction ($p < 0.001$). Furthermore, Br_{tot} concentrations were negatively correlated with particle size ($r = -0.863$, $p < 0.001$). Vertical Br_{tot} concentration profiles tended to show an increase with depth in all four particle sizes (Fig. 4). The concentrations seemed to increase with decreasing particle size, since the vertical profiles were not overlapping but shifted to higher concentrations with decreasing particle size. Total Br concentrations ranged in the coarse silt, medium and fine silt fraction and in the coarse clay fraction between 20 and 80 mg kg^{-1} and in the medium clay fraction from 140 to 220 mg kg^{-1}.

Iodine sorption in various particle sizes

In the coarse silt fraction I_{inc} concentrations tended to decrease from 7 to 2 mg kg^{-1} with increasing depth (Tab. 1). Only a I portion of 5 % which was sorbed relative to I_{tot} concentrations was observed in the Ah horizon, whereas it was between 60 and 70 % in soil horizons Bw1 and Bw2C (Fig. 3). In the medium silt fractions I_{inc} concentrations were unsystematically fluctuating between 5 and 9 mg kg^{-1} and our analyses showed that on average 60 % of I_{tot} was sorbed. Similar observations were made in the coarse clay fractions where I_{inc} concentrations ranged between 8 and 13 mg kg^{-1} and on average 50 % of I_{tot} was sorbed. Structurally bound I concentrations ranged between 12 and 18 mg kg^{-1} in the medium clay

fraction and thus tend to be slightly higher compared to the other three particle sizes. On average 70 % of I_{tot} was sorbed in the smallest particle size. In general, the proportion of I which was adsorbed ranged between 50 and 70 % in the four investigated particle sized with the highest proportion adsorbed in the smallest particle size fraction. Comparing I_{sorb} concentrations of all particle sizes, concentrations were significantly higher in the medium clay fraction ($p < 0.001$). Furthermore, I_{tot} concentrations were negatively correlated with particle size ($r = -0.820$, $p < 0.001$). Vertical I_{tot} concentration profiles tended to show an increase with depth in all four particle sizes (Fig. 4). The concentrations seemed to increase with decreasing particle size, since the vertical profiles were not overlapping but shifted to higher concentrations with decreasing particle size. Total I concentrations ranged in the coarse silt, the medium and fine silt fraction and in the coarse clay fraction from 6 to 26 mg kg^{-1} and in the medium clay fraction from 25 to 60 mg kg^{-1}.

Comparison of F, Cl, Br and I sorption behavior

There were notable differences comparing the halogen concentrations and the amount of sorbed and structurally bound proportions between F, Cl, Br and I, independent of the particle size. Total F concentrations were by far higher than Cl_{tot}, Br_{tot} and I_{tot}, which was already expressed as molar ratios in chapter 3.1. Between Cl, Br and I the concentration differences were not that large, as the molar ratio of Cl/Br was on average 8 and of Cl/I it was on average 50, which are in fact both almost six times lower compared to the molar F ratios. Furthermore, especially the sorption behavior of F was different compared to Cl, Br and I. On average over all particle sizes and soil horizons 93 % of F_{tot} was structurally bound, whereas our results showed that on average large proportions of Cl (32 %), Br (25 %) and I (55 %) were sorbed.

Discussion

Various halogen (F, Cl, Br, I) sorption behavior

We observed that most of F^- (on average 93 %) was structurally bound and only a minor amount weakly sorbed to surfaces. In general, F has a much smaller radius compared to Cl, Br and I (Latscha et al. 2011) and thus we assume that F is less prone to be unspecifically sorbed to surfaces and rather structurally incorporated into the crystal lattice of for example clay minerals or specifically sorbed. The study of Weerasooriya and Wickramarathna (1999) reported for kaolinite that changes in ionic strength only had a minor effect on the adsorption of F^-, which indicated an inner-sphere complexation. Furthermore, an anion substitution mechanism between OH^- and F^- was revealed by an increasing pH with F^- concentration in the kaolinite system (Weerasooriya and Wickramarathna 1999). An increasing pH from 3.7 to 4.4 with increasing soil depth was also found for our location (Fig. 2b). This anion substitution mechanism has been generally observed for F in clay minerals and is strongly pH-dependent (Romo and Roy 1957; Bower and Hatcher 1967; Fuge 1988; Du et al. 2011). It was found that in acidic solutions at pH 3-4 exchange of OH^- by F^- was twice as high as in neutral or alkaline solutions (Chubar et al. 2005). Lower pH results in less OH^- ion availability which could possibly compete with F^- for specifically sorption (Chubar et al. 2005). The determined soil pH of 3-4 in Epp et al. (2020) for the present location (Fig. 2b) offers therefore perfect conditions for an extensive anion exchange. Total fluorine concentrations in all soil size fractions (except for Cl in the medium clay fraction) were by far higher than Br, I and also Cl (Tab. 1). This becomes even clearer by taking the halogen ratios in the different particle fractions into account. These illustrate that F was 10 times higher than Cl in the coarse silt, medium and fine silt and coarse clay fraction and showed a molar ratio of 1 in the medium clay fraction. The molar concentration ratios of F were even higher for Br with on average 45 times and I with on average 230 times. Our XRD analyses revealed that coarse and medium clay fractions mainly consisted of vermiculite, illite, kaolinite and gibbsite. This indicates that clay minerals play an important role in the composition of our investigated samples and can explain high F_{tot} concentrations,

421 which were likely achieved by anion substitution in the crystal lattice and specific sorption of
422 these clay minerals.

423 Our analyses showed that with on average 32 % of Cl, 25 % of Br and 55 % of I large portions
424 were sorbed. Compared to F, Cl, Br and I have much larger ionic radii (Latscha et al. 2011) and
425 hence, we suppose that they are in contrast more prone to be unspecifically sorbed on surfaces
426 than to be structurally bound. Further differences were described for Cl, Br and I with regard to
427 the formation of complexation types. In contrast to F^-, Cl^- Br^- and I^- were shown to be strongly
428 affected by changes in ionic strength in kaolinite and thus, indicated outer-sphere complexation
429 (Weerasooriya and Wickramarathna 1999). Outer-sphere complexation is characterized by a
430 weak sorption to mineral surfaces by electrostatic interactions (e.g., Sposito 1989; Scheffer et
431 al. 1998; Strawn and Sparks 1999). Furthermore, the presence of Cl^-, Br^- and I^- did not lead to
432 a pH change in the kaolinite system (Weerasooriya and Wickramarathna 1999). Hence, anion
433 substitution is not likely to be a valid mechanism for Cl^-, Br^- and I^-, but is important for F^- and
434 could explain the contrasting sorption behavior observed in this study. In the pH range of
435 common soils, pedogenic oxides mostly have positively charged surfaces (Scheffer et al. 1998
436 and references therein) and thus serve as sorbing agents for halogens. This was confirmed for
437 example by positive correlations between total Br and total I concentrations and pedogenic
438 oxides as already described in Epp et al. (2020). In general, adsorption of halogens increases
439 with decreasing pH (Weerasooriya and Wickramarathna 1999). Soil pH of the investigated
440 sample location ranged between 3 and 4 (Epp et al. 2020) and thus provided ideal conditions
441 for halogen sorption to pedogenic oxides (Fig. 2b). Chubar et al. (2005) reported for Cl^- to
442 compete also with OH^- to be incorporated and to be sorbed best at pH 3-4. If this exchange may
443 be true for Cl despite a large ionic radius, it makes it likely to be also valid for Br^- and I^-. The
444 incorporation into the crystal lattice of clay minerals would explain why the main proportion of
445 Cl and Br and half of I is not sorbed. For I we have shown that the portions which were sorbed

and incorporated were equal, whereas Cl and Br were still preferentially incorporated. A larger sorption extent for I than for Cl and Br might be due to the large ionic radius of I, since the radius of I is 1.6 times that of F (Latscha et al. 2011). A further argument would be an abundant supply of Cl^- and Br^- which occupy possible sites in the lattice before they could be occupied by rather unsuitable I^- anions. Our results highlight that most of F (on average 93 %) was structurally bound into crystal lattices of minerals – likely of clay minerals, whereas on average over all soil horizons 32 % of Cl, 25 % of Br and 55 % of I were sorbed to surfaces of pedogenic oxides.

Halogen (F, Cl, Br, I) sorption on different particles sizes

We found remarkable differences in the sorption behavior between F and the other halogens (Cl, Br and I) with respect to the soil size fractions, as they show a contrary trend (Fig. 3). On average 17 %, corresponding to F_{sorb} concentrations of 60 mg kg^{-1}, of F_{tot} was sorbed to 20-63 µm particles. In the other three particle size fractions, F_{sorb} decreased so that all of F_{tot} was structurally bound (Tab. 1). Nevertheless, the amount of F_{sorb} did not vary significantly between the particle sizes. In contrast, Cl_{tot}, Br_{tot} and I_{tot} concentrations increased with decreasing particle size and were by far highest in the smallest soil fraction (0.02-0.2 µm) with about 70 % of Br_{sorb} and I_{sorb} and up to 90 % Cl_{sorb} in the mineral subsoil (Fig. 3). This is in line with significantly higher Cl_{sorb}, Br_{sorb} and I_{sorb} concentrations in the fraction with the smallest particles. In general, sorption behavior should increase with decreasing grain size (Sposito 1984; Scheffer et al. 1998), since the specific surface size of particles is strongly dependent on the particle size (Sposito 1984). Thus, our results for Cl, Br and I are in line with the generally expected halogen sorption behavior. The small particle size fraction is commonly considered as the „clay mineral fraction" implying mostly structurally bound halogens; our results show that sorption to clay and/or pedogenic oxides play a role as well.

Vertical distribution of halogens in different soil size fractions

The vertical depth patterns for F, Cl, Br and I in soil size fractions < 63 µm (this study), were very similar to those of bulk soil sample profiles described in Epp et al. (2020), which included particle sizes up to 2 mm (Fig. 4). Bulk soil data was always in the lower concentration range compared to halogen concentrations analyzed in the present study (Fig. 4). This can be explained by absence or negligible amounts of clay minerals (Hosking et al. 1957) or pedogenic oxides in soil size fractions > 63 µm, resulting in lower total halogen concentrations.

Vertical F_{tot} profiles of all investigated soil size fractions tended to show no vertical patterns with depth within the top- and subsoil (Fig. 4). Overall, all vertical F_{tot} profiles were strongly overlapping, thus no clear concentration differences between the individual soil fractions (Fig. 4). High F concentrations in soil are due to weathering of F-rich minerals in the host rock (Totsche et al. 2000; Zhang et al. 2010 and references therein). The host rock of the study site contains F-bearing minerals such as biotite, and if F is released by weathering it can be subsequently incorporated into secondary clay minerals or adsorbed onto pedogenic oxides. Commonly, the intensity of weathering in a vertical soil profile decreases with increasing depth (Linser and Scharrer 1966) and thus, it is expected that F, pedogenic oxide or clay mineral concentrations should show distinctive depth patterns. However, concentrations of pedogenic oxides and clay minerals did not vary within the top- and subsoil (Fig. 2 c & d) and point to the absence of an intensity of weathering depth profile. Very low Fe_{ox}/Fe_d ratios between 0.06 and 0.1 of the soil column (Epp et al. 2020) indicated that scarcely any iron from silicate weathering is supplied. Formerly present biotite from the host rock may already be dissolved. Hence, no vertical concentration differences of F_{tot} within the mineral soil may be attributed to steady state or equilibrium conditions between F-release by weathering, subsequent adsorption or structurally incorporation and surface input and subsequent accumulation in upper soil horizons. Besides, lacking differences between the soil horizons during soil development could

have been caused by a low solubility and slow reaction kinetics of clay minerals (Meyer and Howard 1983).

Within the top- and subsoil Cl_{tot} was also relatively constant. Since the organic particles were not explicitly removed during sample preparation, it is very likely that the investigated samples still contained organic compounds which either incorporated or adsorbed halogens. The vertical depth patterns of Cl point to an accumulation of Cl in the Ah horizon and probably nutrient uplift in the subsoil, hence, the same processes like in the bulk soil were visible (see details in Epp et al. 2020). Chlorination in the organic layer is the underlying fixation process which results in an accumulation of Cl in the organic layer and in the Ah horizon (Hjelm et al. 1995 and references therein; Öberg and Grøn 1998; Redon et al. 2011). Lacking depth variations may indicate steady state or equilibrium conditions between surface input, sorption processes and nutrient uplift. Large Cl stocks in soil (e.g., Redon et al. 2011) could probably also have led to lacking differences in the horizons during soil development.

With regard to sorption processes, in the case of Br higher adsorption to soil particles in subsoil horizons (deeper than 50 cm) was described by Li et al. (1995) and was attributed to exchange reactions between Br and negatively charged organic compounds. The same study reported adsorption of Br to be rather negligible in the topsoil (upper 50 cm). These results are in contrast to our findings since, sorption of Br in the topsoil was not negligible, and we found on average 11 % of Br to be sorbed to pedogenic oxides or organic compounds. Such contrasting findings can be explained by different soil types and concomitant soil properties. In the study of Li et al. (1995) a Spodosol was investigated which is typically characterized by a low pH, moist and acidic conditions which results in redistribution of organic matter and Fe- and Al oxides from mineral topsoil into the mineral subsoil (Yli-Halla et al. 2006; Chesworth et al. 2008). In contrast, our investigated Cambisol showed organic soil horizons (Oi and Oe) on top and in the different particle size fractions a C_{org} content of up to 10 % in the mineral top- and subsoil (Ah,

520 Bw1 and Bw2C) clearly indicate the presence and the potential importance of organic
521 compounds. The discrepancy with our data can be explained by different soil properties. The
522 presence of the Bw1 soil horizon in our investigated Cambisol contains pedogenic oxides where
523 Br_{inorg} sorption is vital, also in depths > 50 cm.

524 Although the medium clay fraction only contributes 1 wt% to bulk soil, F_{tot} concentrations in
525 this fraction were the same as in the other investigated fractions. In addition, around 50 wt% of
526 Br_{tot} and I_{tot} and even 70 wt% of Cl_{tot} were analyzed in the medium clay fraction. Similar or
527 even much higher concentrations in samples that contribute only marginally to the total sample
528 weight in relation to their weight further indicate the importance of halogen incorporation and
529 adsorption processes in soils. In sum, our results showed that lacking halogen variations with
530 depth might be due to equilibrium conditions between weathering, sorption processes and
531 surface input. Besides, large halogen pools might inhibit concentration differences during soil
532 development.

533 **Implications**

534 The obtained data along with our previously published study allowed us to portray the sorption
535 behavior of F, Cl, Br and I in a vertical soil profile from a temperate forest in four different soil
536 size fractions. Our study showed that almost all F was structurally incorporated into the crystal
537 lattice of, or specifically sorbed to e.g., clay minerals, independent of particle size. This can be
538 attributed to substitution mechanisms between OH^- and F^-. Opposing behavior was found for
539 the other halogens where in the subsoil 90 % of Cl and up to 70 % of Br and I was unspecifically
540 sorbed to soil particles such as pedogenic oxides. For Cl, Br and I it was shown that the amount
541 of halogen sorption was strongly dependent on particle size. By far highest Cl_{tot}, Br_{tot} and I_{tot}
542 concentrations were detected in the smallest fraction (medium clay 0.02-0.2 µm).

543 Further understanding of sorption behavior on clay minerals may have implications for
544 retention of organic and inorganic pollutants. Landfill sludges can contain for example Cl-

bearing organic and inorganic pollutants. Material used in such landfills contain large amounts of clay minerals which enhance the sorption of organic compounds. Furthermore, the radionuclides ^{36}Cl and ^{129}I have a long half-life and their disposal and its effects are of current importance. Thus, understanding the sorption behavior of halogens on for instance clay minerals is crucial for retention processes of pollutants in landfills or potentially for radioactive waste disposal. Steady state or equilibrium conditions between weathering, sorption processes and surface input probably caused lacking distinctive vertical concentration differences of F_{tot}, Cl_{tot}, Br_{tot} and I_{tot} in the mineral soil during soil development. Other biogeochemical processes might be negligible compared to the large halogen stocks in the soil which may inhibit visible concentration differences. The fact that the bulk soil only consisted of 1 wt% medium clay and still this fraction contained most of Cl, Br and I emphasized the importance of halogen sorption to clay minerals and/ or pedogenic oxides. In conclusion, our results revealed the importance of sorption processes for Cl, Br and I and incorporation processes for F which control the vertical halogen distribution in a Cambisol of a temperate forest.

Acknowledgements

We are grateful to Frieder Lauxmann for his help with the XRD analyses. Further thank goes to Lukas Schmid for his support with the centrifugation during the elaborate preparation process. Annelie Papsdorf and Sabine Flaiz is thanked for the CN analyses. Furthermore, we are very grateful to Christian Mikutta, Stefan Dultz and Peter Kühn for very constructive discussions. This study was funded by the German Research Foundation (DFG) [grant numbers Ma2135/20-1, Oe516/8-1].

References

568 Asplund G, Grimvall A (1991) Organohalogens in nature. Environmental science & technology
569 25:1346-1350.
570 Atterberg A (1912) Die mechanische Bodenanalyse. Internationale Mitteilungen für
571 Bodenkunde:312-342.
572 Bastviken D, Thomsen F, Svensson T, Karlsson S, Sandén P, Shaw G, Matucha M, Öberg G
573 (2007) Chloride retention in forest soil by microbial uptake and by natural chlorination
574 of organic matter. Geochimica et Cosmochimica Acta 71:3182-3192.
575 Bower C, Hatcher J (1967) Adsorption of fluoride by soils and minerals. Soil Science 103:151-
576 154.
577 Chadwick OA, Chorover J (2001) The chemistry of pedogenic thresholds. Geoderma 100:321-
578 353.
579 Chesworth W, Camps Arbestain M, Macías F (2008) Calcareous Soils In Encyclopedia of Soil
580 Science; Chesworth, W., Ed. Springer: Dordrecht, Netherlands.
581 Chubar N, Samanidou V, Kouts V, Gallios G, Kanibolotsky V, Strelko V, Zhuravlev I (2005)
582 Adsorption of fluoride, chloride, bromide, and bromate ions on a novel ion exchanger.
583 Journal of colloid and interface science 291:67-74.
584 Cornelis J-T, Weis D, Lavkulich L, Vermeire M-L, Delvaux B, Barling J (2014) Silicon isotopes
585 record dissolution and re-precipitation of pedogenic clay minerals in a podzolic soil
586 chronosequence. Geoderma 235:19-29.
587 Cortizas AM, Vázquez CF, Kaal J, Biester H, Casais MC, Rodríguez TT, Lado LR (2016)
588 Bromine accumulation in acidic black colluvial soils. Geochimica et Cosmochimica Acta
589 174:143-155.
590 Davison AW, Weinstein LH (2006) Some problems relating to fluorides in the environment:
591 effects on plants and animals. Advances in Fluorine Science 1:251-298.
592 Deutscher-Wetterdienst (2019) Klimadaten Deutschland - Monats- und Tageswerte (Archiv).
593 Du J, Wu D, Xiao H, Li P (2011) Adsorption of fluoride on clay minerals and their mechanisms
594 using X-ray photoelectron spectroscopy. Frontiers of Environmental Science &
595 Engineering in China 5:212-226.

596 Epp T, Marks MA, Ludwig T, Kendrick MA, Eby N, Neidhardt H, Oelmann Y, Markl G (2019)
597 Crystallographic and fluid compositional effects on the halogen (Cl, F, Br, I)
598 incorporation in pyromorphite-group minerals. American Mineralogist 104:1673-1688.
599 doi: https://doi.org/10.2138/am-2019-7068.
600 Epp T, Neidhardt H, Pagano N, Marks MA, Markl G, Oelmann Y (2020) Vegetation canopy
601 effects on total and dissolved Cl, Br, F and I concentrations in soil and their fate along
602 the hydrological flow path. Science of The Total Environment 712C:135473.
603 Eskandarpour A, Onyango MS, Ochieng A, Asai S (2008) Removal of fluoride ions from
604 aqueous solution at low pH using schwertmannite. Journal of Hazardous Materials
605 152:571-579.
606 Fuge R (1988) Sources of halogens in the environment, influences on human and animal
607 health. Environmental Geochemistry and Health 10:51-61. doi: 10.1007/bf01758592.
608 Fuge R (2019) Fluorine in the environment, a review of its sources and geochemistry. Applied
609 geochemistry 100:393-406.
610 Gerzabek MH, Muramatsu Y, Strebl F, Yoshida S (1999) Iodine and bromine contents of some
611 Austrian soils and relations to soil characteristics. Journal of plant nutrition and soil
612 science 162:415-419.
613 Goldberg S, Kabengi NJ (2010) Bromide Adsorption by Reference Minerals and Soils. Vadose
614 Zone Journal 9:780-786.
615 Hjelm O, Johansson M-B, Öberg-Asolund G (1995) Organically bound halogens in coniferous
616 forest soil-Distribution pattern and evidence of in situ production. Chemosphere
617 30:2353-2364.
618 Hosking J, Neilson ME, Carthew A (1957) A study of clay mineralogy and particle size.
619 Australian Journal of Agricultural Research 8:45-74.
620 IUSS-Working-Group-WRB (2015) World reference base for soil resources 2014- International
621 soil classification system for naming soils and creating legends for soil maps. Food and
622 Agriculture Organization of the United Nations, Italy, Rome, pp 203.
623 Kabata-Pendias A (2011) Trace elements in soils and plants. CRC Press.

624 Kaplan DI, Serne RJ, Parker KE, Kutnyakov IV (2000) Iodide sorption to subsurface sediments
625 and illitic minerals. Environmental Science & Technology 34:399-405.
626 Kendrick MA, Burnard P (2013) Noble gases and halogens in fluid inclusions: A journey
627 through the Earth's crust The noble gases as geochemical tracers. Springer, pp 319-
628 369.
629 Latscha HP, Klein HA, Mutz M (2011) Allgemeine Chemie: Chemie-Basiswissen I. Springer-
630 Verlag.
631 Lecumberri-Sanchez P, Bodnar R (2018) Halogen Geochemistry of Ore Deposits:
632 Contributions Towards Understanding Sources and Processes In: Harlov DE,
633 Aranovich L (eds) The Role of Halogens in Terrestrial and Extraterrestrial Geochemical
634 Processes. Springer Geochemistry, pp 261-305.
635 Li Y, Alva A, Calvert D, Banks D (1995) Adsorption and transport of nitrate and bromide in a
636 spodosol. Soil science 160:400-404.
637 Linser H, Scharrer K (1966) Handbuch der Pflanzenernährung und Düngung. Springer-Verlag.
638 Liu X, Wang B, Zheng B (2014) Geochemical process of fluorine in soil. Chinese Journal of
639 Geochemistry 33:277-279.
640 Loganathan P, Liu Q, Hedley MJ, Gray CW (2007) Chemical fractionation of fluorine in soils
641 with a long-term phosphate fertiliser history. Soil Research 45:390-396. doi:
642 https://doi.org/10.1071/SR07030.
643 Lovett GM, Likens GE, Buso DC, Driscoll CT, Bailey SW (2005) The biogeochemistry of
644 chlorine at Hubbard Brook, New Hampshire, USA. Biogeochemistry 72:191-232. doi:
645 10.1007/s10533-004-0357-x.
646 Manning BA, Goldberg S (1996) Modeling competitive adsorption of arsenate with phosphate
647 and molybdate on oxide minerals. Soil Science Society of America Journal 60:121-131.
648 Marschner H (1995) Mineral nutrition of higher plants. 2nd. Edn Academic Pres.
649 Meyer D, Howard J (1983) Evaluation of clays and clay minerals for application to repository
650 sealing. D'Appolonia Consulting Engineers.

651 Montelius M, Thiry Y, Marang L, Ranger J, Cornelis J-T, Svensson T, Bastviken D (2015)
652 Experimental evidence of large changes in terrestrial chlorine cycling following altered
653 tree species composition. Environmental science & technology 49:4921-4928.
654 Montelius M, Svensson T, Lourino-Cabana B, Thiry Y, Bastviken D (2016) Chlorination and
655 dechlorination rates in a forest soil—a combined modelling and experimental approach.
656 Science of the total Environment 554:203-210.
657 Öberg G, Grøn C (1998) Sources of Organic Halogens in Spruce Forest Soil. Environmental
658 Science & Technology 32:1573-1579. doi: 10.1021/es9708225.
659 Öberg G, Bastviken D (2012) Transformation of chloride to organic chlorine in terrestrial
660 environments: variability, extent, and implications. Crit Rev Environ Sci Technol
661 42:2526-2545.
662 Parfitt R (1989) Phosphate reactions with natural allophane, ferrihydrite and goethite. Journal
663 of Soil Science 40:359-369.
664 Petkovic MD, Milonjic SK, Dondur VT (1994) Determination of Surface lonization and
665 Complexation Constants at Colloidal Aluminum Oxide/Electrolyte Interface. Separation
666 science and technology 29:627-638.
667 Redon P-O, Abdelouas A, Bastviken D, Cecchini S, Nicolas M, Thiry Y (2011) Chloride and
668 Organic Chlorine in Forest Soils: Storage, Residence Times, And Influence of
669 Ecological Conditions. Environmental Science & Technology 45:7202-7208. doi:
670 10.1021/es2011918.
671 Romo L, Roy R (1957) Studies of the Substitution of OH–by F–in Various Hydroxylic Minerals.
672 American Mineralogist: Journal of Earth and Planetary Materials 42:165-177.
673 Roulier M, Coppin F, Bueno M, Nicolas M, Thiry Y, Della Vedova C, Février L, Pannier F, Le
674 Hécho I (2019) Iodine budget in forest soils: Influence of environmental conditions and
675 soil physicochemical properties. Chemosphere.
676 Santamarina J, Klein K, Wang Y, Prencke E (2002) Specific surface: determination and
677 relevance. Canadian Geotechnical Journal 39:233-241.

678 Scheffer F, Schachtschabel P, Blume H, Hartge K, Schwertmann U, Brümmer G, Renger M
679 (1998) Lehrbuch der Bodenkunde/Scheffer/Schachtschabel. Ferdinand Enke Verlag,
680 Stuttgart.
681 Schoonheydt RA, Johnston CT (2006) Surface and interface chemistry of clay minerals
682 Developments in clay science. pp 87-113.
683 Sposito G (1984) The surface chemistry of soils. Oxford university press.
684 Sposito G (1989) The Chemistry of Soils. Oxford University Press, New York.
685 Stokes SGG (1901) Mathematical and physical papers. University Press, Cambridge.
686 Strawn DG, Sparks DL (1999) The use of XAFS to distinguish between inner-and outer-sphere
687 lead adsorption complexes on montmorillonite. Journal of Colloid and Interface Science
688 216:257-269.
689 Torrent J, Barron V, Schwertmann U (1990) Phosphate adsorption and desorption by goethites
690 differing in crystal morphology. Soil Science Society of America Journal 54:1007-1012.
691 Totsche KU, Wilcke W, Körber M, Kobza J, Zech W (2000) Evaluation of fluoride-induced metal
692 mobilization in soil columns. Journal of environmental quality 29:454-459.
693 Tributh H, Lagaly G (1986) Aufbereitung und Identifizierung von Boden-und Lagerstättentonen.
694 II Korngrößenanalyse und Gewinnung von Tonsubfraktionen. GIT-Fachzeitschrift für
695 das Laboratorium 30:771-776.
696 Weerasooriya R, Wickramarathna H (1999) Modeling anion adsorption on kaolinite. Journal of
697 colloid and interface science 213:395-399.
698 WetterKontor (2019) Wetterrückblick Feldberg im Schwarzwald (1486 m). WetterKontor.
699 Yli-Halla M, Mokma DL, Wilding LP (2006) Formation of a cultivated Spodosol in east-central
700 Finland. Agricultural and Food Science 15:12-22.
701 Yuita K (1983) Iodine, bromine and chlorine contents in soils and plants of Japan AU. Soil
702 Science and Plant Nutrition 29:403-428. doi: 10.1080/00380768.1983.10434645.
703 Zhang C, Li Z, Gu M, Deng C, Liu M, Li L (2010) Spatial and vertical distribution and pollution
704 assessment of soil fluorine in a lead-zinc mining area in the Karst region of Guangxi,
705 China. Plant, Soil and Environment 56:282-287.

Figures

Figure 1. (a) Simplified overview of all soil sample locations from the Feldberg, southwest Germany, including depiction of the typical forest at the investigated site. C = with canopy, OC = without canopy, **(b)** Schematic vertical soil profile of the investigated Cambisol and the corresponding soil horizons.

Figure 2. (a) Amount of C_{org} in % of different particle sizes and soil depth, **(b)** pH data for each soil depth, pH = $CaCl_2$, **(c)** amount of coarse, medium and fine clay fractions in % (in relation to bulk soil composition) for each soil depth, **(d)** content of pedogenic oxides in mg kg^{-1} for each soil depth. Al_{ox}, Fe_{ox} = poorly crystalline Al and Fe oxides, Al_d and Fe_d = sum of poorly crystalline and crystalline Al and Fe oxides. **(b) – (d)** data from Epp et al. (2020).

Figure 3. (a)-(d) four different soil size fractions (20-63 µm, 2-20 µm, 0.2-<2 µm and 0.02-2 µm) versus adsorbed (%) halogen amount in mineral topsoil (Ah) and subsoil (Bw1 and Bw2C). Grey bars illustrate the entire range of halogens in percentage. Black dot marks mean values over all horizons in each particle size.

Figure 4. (a)-(d) Vertical depth patterns of total halogen concentrations (incorporated and adsorbed + inorganic and organic; mg kg^{-1}) in four different soil size fractions. Dark blue = bulk soil data from Epp et al. (2020), n = 18, light blue = halogen concentration in soil size fraction 20-63 µm, n = 6; pink = halogen concentration in soil size fraction 2-20 µm, n = 6; grey = halogen concentration in soil size fraction 0.2-<2 µm, n = 6 and green = halogen concentration in soil size fraction 0.02-0.2 µm, n = 6. For the horizon thicknesses on the y axis average values were taken over all profiles for each soil horizon. The error bars show the standard deviation.

Appendix

Figure A1. (a) and **(b)** Dissolved inorganic F and Cl concentrations in the supernatant phosphate solution in each soil size fraction and each soil horizon after the desorption treatment of the soil samples in mg L^{-1}. Residual solution of all soil size fractions of each soil horizon were analyzed by ion chromatography.

Figure A2. (a)-(d) Adsorbed halogen concentrations of all soil size fractions versus Al_{ox}, Fe_{ox} (poorly crystalline Al and Fe oxides) and vs Al_d and Fe_d (sum of poorly crystalline and crystalline Al and Fe oxides).

Tab. 1 Halogen concentrations in mineral topsoil and subsoil of different soil size fractions. Horizons were classified according to IUSS Working Group-WRB (2015). Total = halogen concentration adsorbed + incorporated (= inorganic + organic), inc. = halogen concentration incorporated, ads. = halogen concentration adsorbed, "-" = no further sample material available.

		Br					Cl					F					I					C_{org}	
Horizon (each n =1)	**Soil size fraction**	**total (mg kg^{-1})**	**inc. (mg kg^{-1})**	**% inc.**	**ads. (mg kg^{-1})**	**% ads.**	**total (mg kg^{-1})**	**inc. (mg kg^{-1})**	**% inc.**	**ads. (mg kg^{-1})**	**% ads.**	**total (mg kg^{-1})**	**inc. (mg kg^{-1})**	**% inc.**	**ads. (mg kg^{-1})**	**% ads.**	**total (mg kg^{-1})**	**Inc. (mg kg^{-1})**	**% inc.**	**ads. (mg kg^{-1})**	**% ads.**	**(g kg^{-1})**	**% Mass fraction**
Ah	20-63	42	36	85	6	15	225	149	66	76	34	516	567	110	0	0	7	7	94	0.4	6	97	
Bw1	20-63	36	30	85	5	15	118	102	86	16	14	579	288	50	291	50	9	4	38	6	62	42	15
Bw2C	20-63	25	26	104	0	0	115	89	78	25	22	578	630	109	0	0	7	2	30	5	70	26	
Ah	2-20	38	37	97	1	3	143	124	86	20	14	611	680	111	0	0	14	5	37	9	63	82	
Bw1	2-20	67	48	72	19	28	106	84	80	21	20	680	616	91	64	9	18	9	49	9	51	38	26
Bw2C	2-20	63	49	77	15	23	117	89	77	27	23	678	680	100	0	0	22	8	35	14	65	-	
Ah	0.2- <2	44	37	85	7	15	175	132	76	42	24	694	648	93	46	7	17	8	48	9	52	-	
Bw1	0.2- <2	84	64	76	29	24	123	114	93	9	7	635	816	129	0	0	24	13	53	12	47	43	3
Bw2C	0.2- <2	79	60	76	19	24	159	112	71	47	29	755	753	100	2	0	26	12	46	14	54	62	
Ah	0.02-0.2	156	-	-	-	-	1845	-	-	-	-	487	-	-	-	-	24	-	-	-	-	-	
Bw1	0.02-0.2	170	68	40	103	60	607	114	19	493	81	707	679	96	27	4	52	18	35	3	65	58	0.9
Bw2C	0.02-0.2	153	45	29	108	71	1299	142	11	1158	89	629	653	104	0	0	41	12	29	29	71	-	

Figure 1

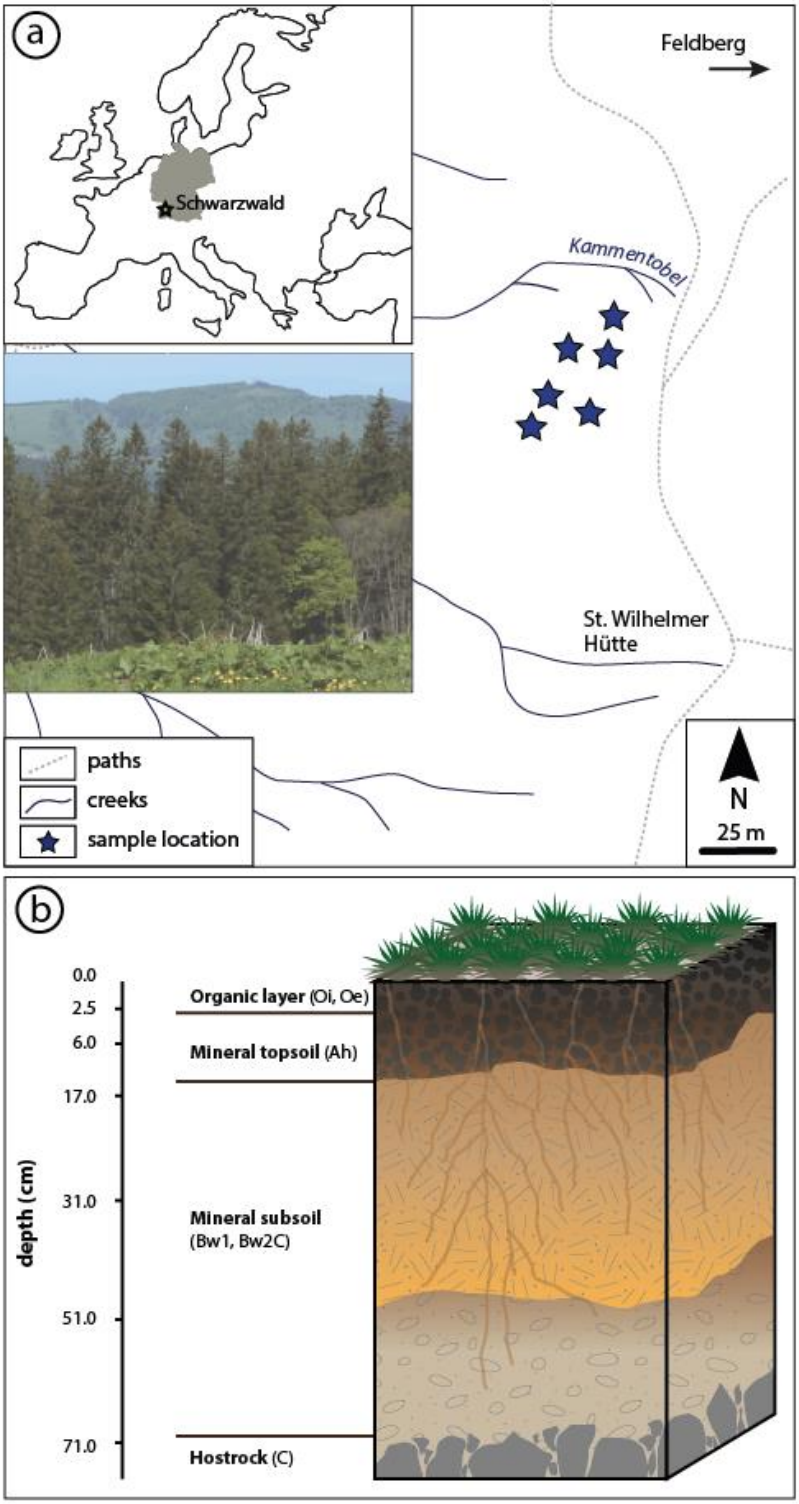
a
Schwarzwald
Feldberg
Kammentobel
St. Wilhelmer
Hütte
paths
creeks
sample location
N
25 m
b
depth (cm)
0.0
2.5
6.0
17.0
31.0
51.0
71.0
Organic layer (Oi, Oe)
Mineral topsoil (Ah)
Mineral subsoil
(Bw1, Bw2C)
Hostrock (C)

Figure 2

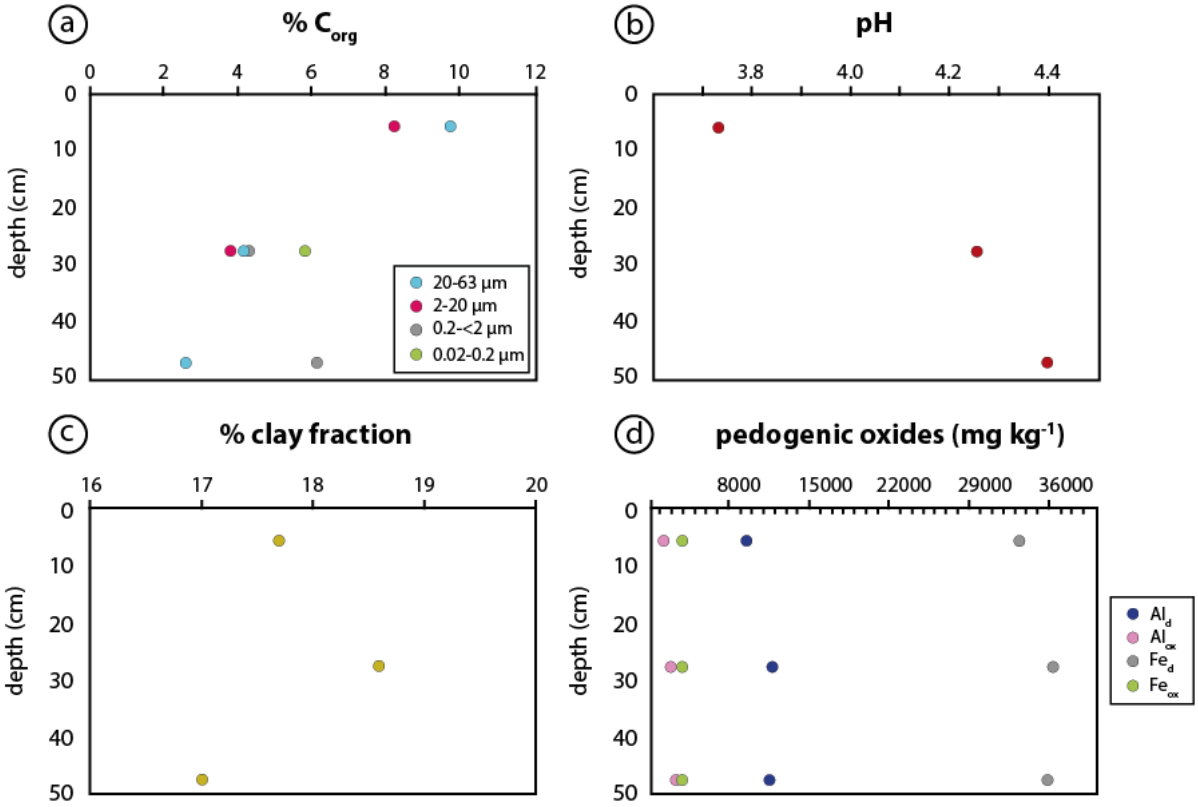
a
% C org
0
2
4
6
8
10
12
depth (cm)
0
10
20
30
40
50
20-63 µm
2-20 µm
0.2-<2 µm
0.02-0.2 µm
b
pH
3.8
4.0
4.2
4.4
c
% clay fraction
16
17
18
19
20
d
pedogenic oxides (mg kg-1)
8000
15000
22000
29000
36000
Ald
Alox
Fed
Feox

Figure 3

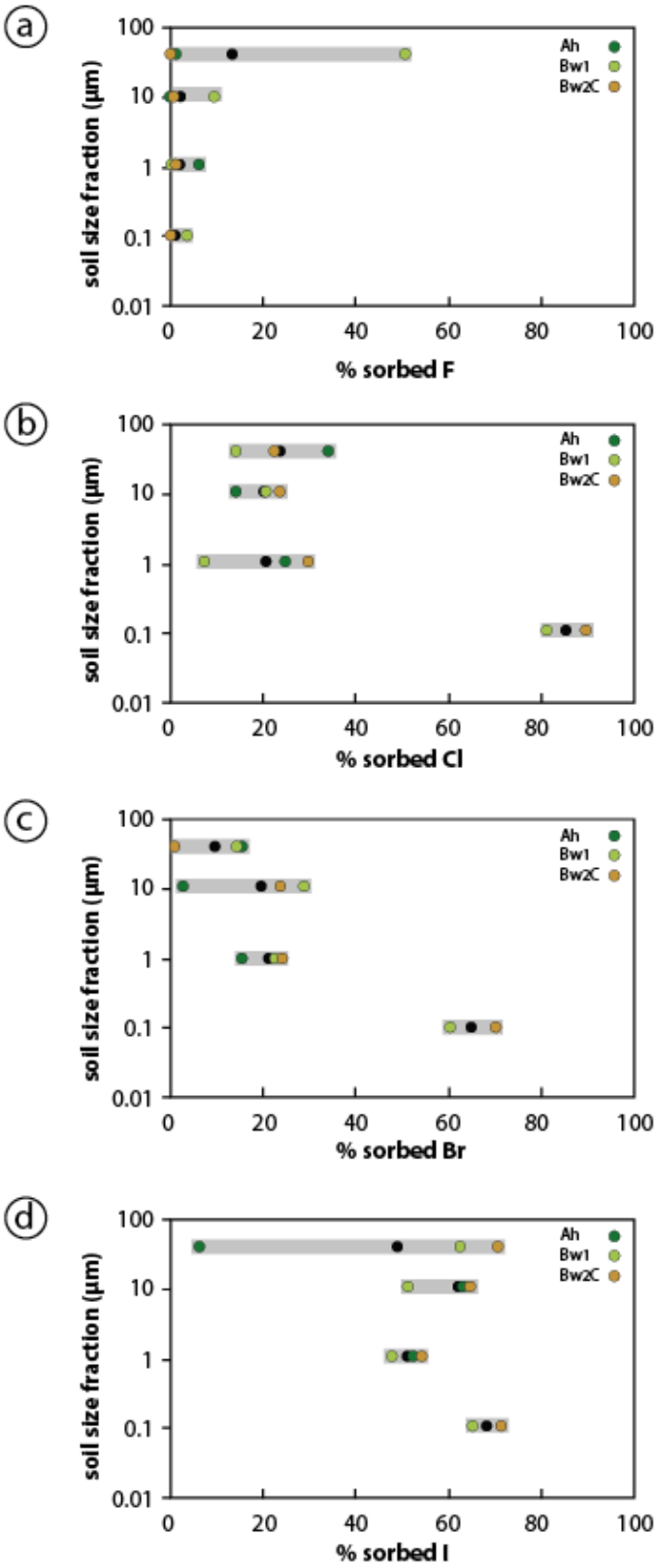
a
b
c
d
soil size fraction (µm)
100
10
1
0.1
0.01
0
20
40
60
80
100
% sorbed F
% sorbed Cl
% sorbed Br
% sorbed I
Ah
Bw1
Bw2C

Figure 4

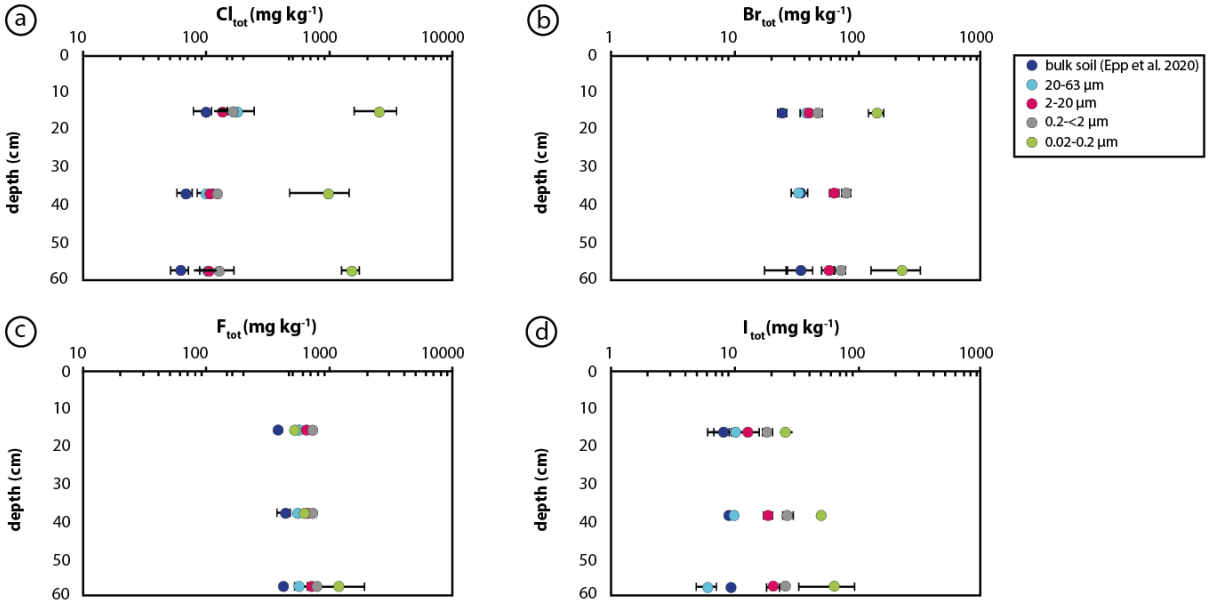
a
Cl_{tot} (mg kg^{-1})
10
100
1000
10000
depth (cm)
0
10
20
30
40
50
60
b
Br_{tot} (mg kg^{-1})
1
10
100
1000
bulk soil (Epp et al. 2020)
20-63 µm
2-20 µm
0.2-<2 µm
0.02-0.2 µm
c
F_{tot} (mg kg^{-1})
d
I_{tot} (mg kg^{-1})

Figure A1

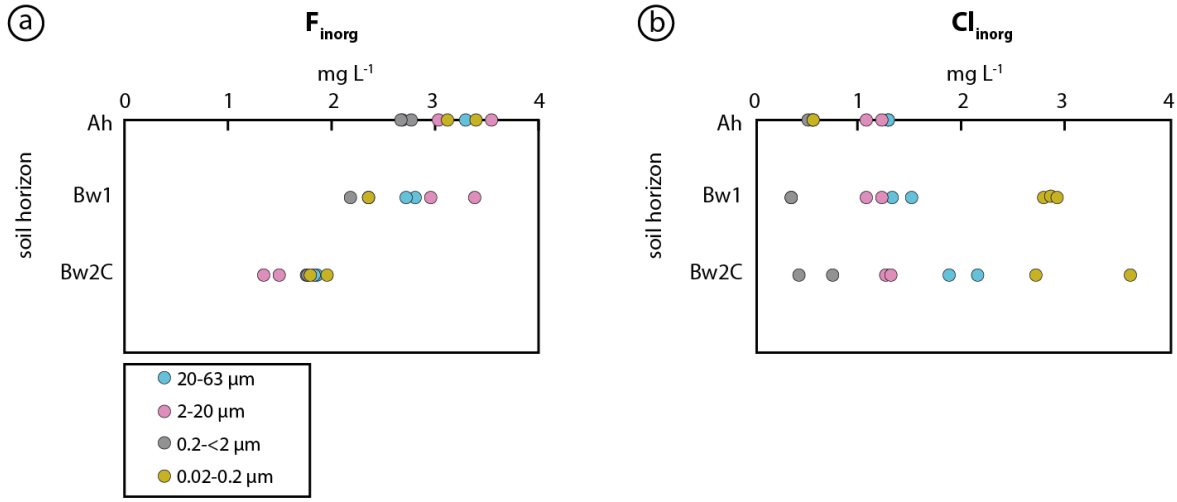
a
F inorg
mg L-1
0
1
2
3
4
Ah
Bw1
Bw2C
soil horizon
20-63 µm
2-20 µm
0.2-<2 µm
0.02-0.2 µm
b
Cl inorg
mg L-1
0
1
2
3
4
Ah
Bw1
Bw2C
soil horizon

Figure A2

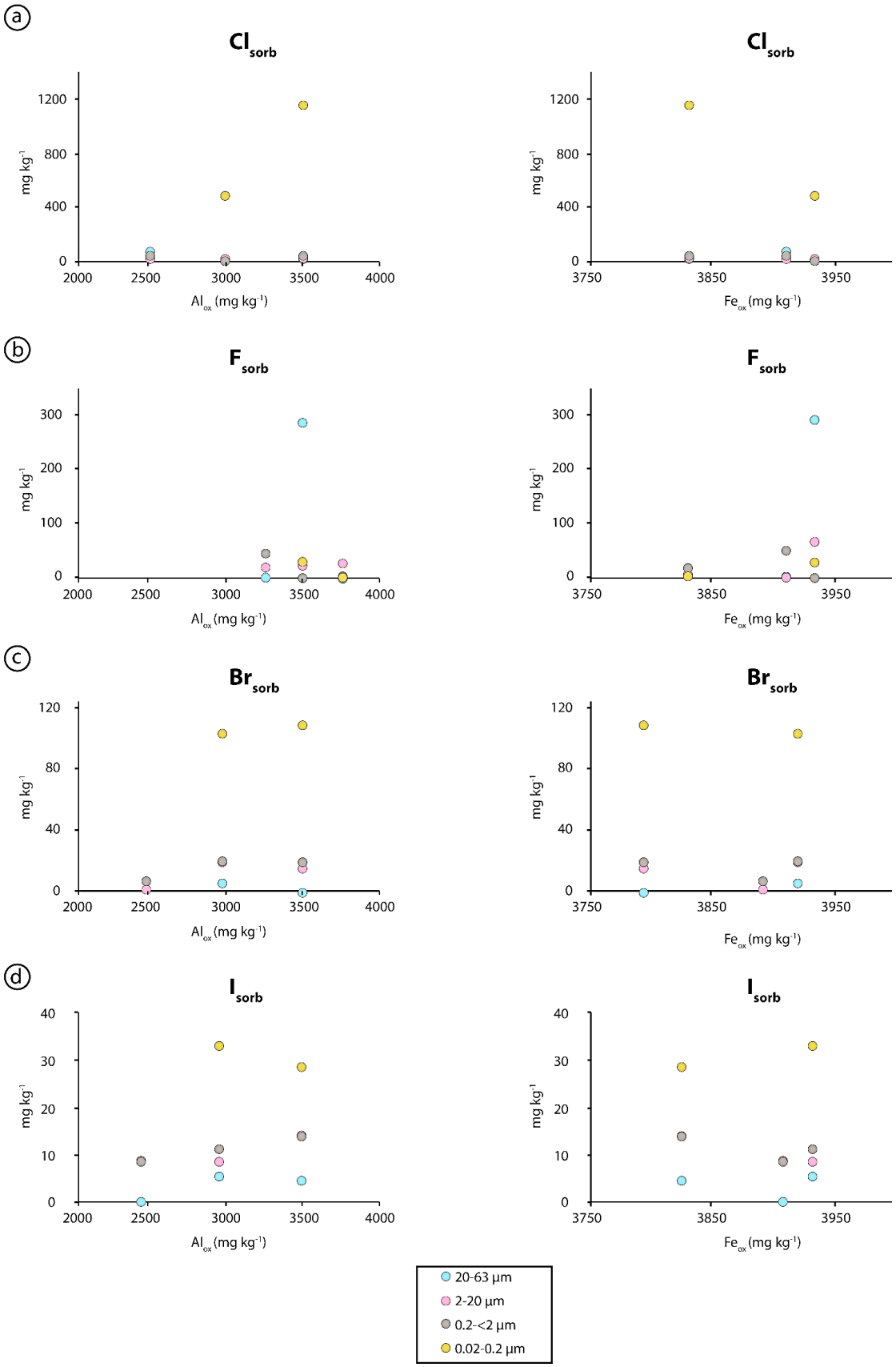
a
Cl sorb
mg kg-1
Alox (mg kg-1)
Feox (mg kg-1)
b
F sorb
c
Br sorb
d
I sorb
20-63 µm
2-20 µm
0.2-<2 µm
0.02-0.2 µm